

Title	Smart optical imaging systems with automated electronics
Authors	La Torre, Juan Pablo
Publication date	2017
Original Citation	La Torre, J. P. 2017. Smart optical imaging systems with automated electronics. PhD Thesis, University College Cork.
Type of publication	Doctoral thesis
Rights	© 2017, Juan Pablo La Torre. - <a href="http://creativecommons.org/licenses/by-nc-nd/3.0/">http://creativecommons.org/licenses/by-nc-nd/3.0/</a>
Download date	2024-05-06 18:20:00
Item downloaded from	<a href="https://hdl.handle.net/10468/5746">https://hdl.handle.net/10468/5746</a>

# SMART OPTICAL IMAGING SYSTEMS WITH AUTOMATED ELECTRONICS

Juan Pablo La Torre

B. Sc., M. Sc.



NATIONAL UNIVERSITY OF IRELAND, CORK

SCHOOL OF ENGINEERING

ELECTRICAL AND ELECTRONIC ENGINEERING

Thesis submitted for the degree of

Doctor of Philosophy

June 2017

Major Supervisor:

Professor Nabeel A. Riza



© 2017 by Juan Pablo La Torre

[j.latorre@uamail.ucc.ie](mailto:j.latorre@uamail.ucc.ie)



This is to certify that the work I am submitting is my own and has not been submitted for another degree, either at University College Cork or elsewhere. All external references and sources are clearly acknowledged and identified within the contents. I have read and understood the regulations of University College Cork concerning plagiarism.

Signature: \_\_\_\_\_ Date: \_\_\_\_\_



## ABSTRACT

In this dissertation, several novel smart electronically automated optical designs to efficiently solve existing real-world problems are proposed and demonstrated. The first half of the thesis proposes shape sensing techniques that employ the use of an Electronically Controlled Variable Focus Lens (ECVFL) within a smart optical design. These designs use a combination of discrete optical components, electronically programmable smart modules, imaging processing algorithms techniques, and automated mechanical designed moving parts. For control purposes, a programmed *ad hoc* single peripheral decisional software work alongside with each deployed optical design. Two methods, one using a point scan and one using a laser line scan, are presented for shape sensing working in unison with a custom designed inline viewpoint camera module. The achieved experimental results show a 16X per-point-scan performance improvement in shape acquisition speed when deploying the laser line illumination versus the single laser point scan based sensor. Both the sensor designs maintain the highest transverse resolution over a designed depth scan. Such feature cannot be achieved by existing commercial devices based on the geometrical working principle for distance measurement. Additionally, the proposed and tested novel optical shape sensor design is highly flexible and its main components are reengineered and electronically controlled to implement and experimentally demonstrate an automated smart projection system called Smart Art Display. The proposed projection display overcomes limitations in existing projection displays that suffer degradation of the projected image when deploying a multi-depth surface screen projection target. Thus, the proposed display guarantees the smallest spatial resolution for the designed projection distance and its use is envisioned in scenarios such as art installation presenting irregularities in their surfaces or when a major interactive experience is required.

The second part of this dissertation involves the use of the Digital Micromirror Device (DMD) as an automated spatial light modulator deployed within the proposed smart optical designs that uses discrete optical components and advanced software programming for device control and automation, image processing, and Digital Signal Processing (DSP). Initially the DMD is deployed to illustrate its use as a programmable Young's Double slit interferometer device and the achieved experimental results match the theoretically expected values. Additionally, different imaging DMD-based design ideas that use a combination of several smart modules and smart arrangement are summarized in the same chapter. Next, introduced



for the first time is a complete programmable pinhole based imager/profiler device for lasers supported by a micro-controller and a cost-effective DMD platform. Designed and implemented within this platform is a stand-alone imager device. The device is additionally supported by software implemented for DMD control purposes and synchronization between the micro-controller operations for correct and reliable data acquisition and interpretation. The adopted working principle is based on the pinhole scan Time Division Multiple Access (TDMA) mode. Starting from the developed platform, further improvements of the imager device are made, demonstrating new working principles based on Frequency Division Multiple Access (FDMA) and Coded Division Multiple Access (CDMA) coded optical modulations. Specifically, proposed are the design and implementation of the novel imaging device called Coded Access Optical Sensor (CAOS) where CAOS is capable of operating with all the aforementioned working modes. Experimentally and successfully demonstrated for the first time is the FDMA-TDMA CAOS imager mode for coherent light laser imaging and the presented results demonstrate its efficiency when compared with the TDMA-only imager mode working principle. A major improvement with the novel CAOS design is its extreme Dynamic Range (DR) performance that greatly overcomes the previously demonstrated DR obtained with the TDMA imager mode. Specifically, imaging DR improved from 22 dB to 77 dB for the laser imaging experiment. Motivated by this impressive performance, also presented in this dissertation is the CAOS imager used as an incoherent imager for the white light high dynamic range imaging scenario. The proposed CAOS imager is used in cooperation with a Complementary Metal Oxide Semiconductor (CMOS) sensor imager device forming a new smart imaging device called the CAOS-CMOS camera. When imaging conditions exceed the limited CMOS sensor DR performance, the CAOS imager is engaged to successfully image the target scenario confirming its great potential when deployed in extreme contrast imaging conditions. The CAOS imager experimental DR performance is further improved by deploying a higher quality Data Acquisition (DAQ) card having greater signal sampling characteristics and processing power compared to the cost-effective micro-controller device engaged with lower bit value analog-to-digital converters. With the improved DAQ configuration, for the first time, demonstrated are a further improvement of the obtained experimental camera DR reaching 136 dB and the reengineering of the deployed optical design for the implementation of a novel multispectral and hyperspectral CAOS imager device suitable for visible and near infrared high DR imaging scenario. Specifically, the use of a DMD based programmable CAOS-mode spectral filter is incorporated and demonstrated within the CAOS multispectral camera design.

## TABLE OF CONTENTS

ABSTRACT.....	vii
TABLE OF CONTENTS.....	ix
AUTHOR’S PUBLICATION LIST .....	xiii
LIST OF ABBREVIATIONS.....	xvii
LIST OF FIGURES .....	xxi
LIST OF TABLES.....	xxix
ACKNOWLEDGEMENTS.....	xxxiii
CHAPTER 1 – INTRODUCTION.....	1
REFERENCES .....	6
CHAPTER 2 – OPTICAL SHAPE SENSOR USING ELECTRONICALLY CONTROLLED LENS.....	9
2.1 INTRODUCTION .....	9
2.2 PROPOSED SINGLE VIEWING AXIS OPTICAL 3-D SHAPE SENSOR DESIGN.....	12
2.2.1 DERIVATION OF CAMERA DEPTH OF FIELD (DOF).....	15
2.3 EXPERIMENT .....	18
2.4 CONCLUSION.....	32
REFERENCES .....	33
CHAPTER 3 – SMART OPTICAL SHAPE SENSOR USING ELECTRONICALLY CONTROLLED LENS AND LASER LINE ILLUMINATION SCANNING .....	37
3.1 INTRODUCTION .....	37
3.2 PROPOSED LASER LINE BASED 3-D SHAPE SENSOR DESIGN .....	39
3.3 EXPERIMENT .....	44
3.4 CONCLUSION.....	54

REFERENCES .....	55
CHAPTER 4 – SMART ART DISPLAY PROJECTION SYSTEM .....	59
4.1 INTRODUCTION .....	59
4.2 PROPOSED SMART ART DISPLAY PROJECTION SYSTEM.....	61
4.3 EXPERIMENT .....	63
4.4 CONCLUSION.....	67
REFERENCES .....	68
CHAPTER 5 – AGILE WAVEFRONT SPLITTING INTERFEROMETRY AND IMAGING USING A DIGITAL MICROMIRROR DEVICE.....	69
5.1 INTRODUCTION .....	69
5.2 SLM-BASED WAVEFRONT SPLITTING INTERFEROMETER DESIGNS .....	70
5.3 EXPERIMENTAL DEMONSTRATION OF YOUNG’S DOUBLE SLIT INTERFEROMETER.....	72
5.4 IMAGING USING 3-D SCANNING APERTURES.....	78
5.5 CONCLUSION.....	85
REFERENCES .....	86
CHAPTER 6 – AN EMBEDDED SMART AGILE PIXEL IMAGER FOR LASERS.....	91
6.1 INTRODUCTION .....	91
6.2 PROPOSED EMBEDDED SYSTEM BASED SMART AGILE PIXEL IMAGER DESIGN.....	93
6.2.1 LASER BEAM IMAGING PROCESS .....	93
6.2.2 GAUSSIAN LASER BEAM .....	94
6.3 EXPERIMENTAL EMBEDDED BASED LASER BEAM IMAGER SETUP COMPONENTS .....	95
6.3.1 TI DLP LIGHTCRAFTER EVALUATION BOARD .....	96
6.3.2 MSP-EXP430FR5969 LAUNCHPAD EVALUATION KIT .....	96
6.3.3 PHOTODETECTOR .....	97
6.3.4 SYNCHRONOUS COMMUNICATION.....	97

6.4 EXPERIMENTAL DEMONSTRATION .....	98
6.5 CONCLUSION.....	101
REFERENCES .....	102
CHAPTER 7 – CODED ACCESS OPTICAL SENSOR (CAOS) IMAGER .....	105
7.1 INTRODUCTION .....	105
7.2 PROPOSED CAOS IMAGER DESIGN.....	107
7.3 EXPERIMENT .....	113
7.4 CONCLUSION.....	119
REFERENCES .....	120
CHAPTER 8 – CAOS-CMOS CAMERA.....	123
8.1 INTRODUCTION .....	123
8.2 THE CAOS-CMOS CAMERA DESIGN.....	125
8.3 EXPERIMENTAL DEMONSTRATION OF THE CAOS-CMOS CAMERA.....	130
8.4 CONCLUSION.....	144
REFERENCES .....	145
CHAPTER 9 – DEMONSTRATION OF 136 DB DYNAMIC RANGE CAPABILITY FOR A SIMULTANEOUS DUAL OPTICAL BAND CAOS CAMERA .....	149
9.1 INTRODUCTION .....	149
9.2 SIMULTANEOUS DUAL OPTICAL BAND CAOS CAMERA DESIGN.....	152
9.3 VISIBLE-NIR SIMULTANEOUS DUAL OPTICAL BAND CAOS CAMERA EXPERIMENT .....	155
9.4 CAOS CAMERA EXTREME DYNAMIC RANGE ANALYSIS AND EXPERIMENT .....	167
9.5 CONCLUSION.....	174
REFERENCES .....	176
CHAPTER 10 – CONCLUSIONS .....	181



## AUTHOR'S PUBLICATION LIST

### THESIS PUBLICATIONS

#### JOURNALS

1. J. P. La Torre, M. J. Amin, B. Thompson, and N. A. Riza, "Optical shape sensor using electronically controlled lens," *IEEE Sensors Journal*, vol. 16, no. 12, pp. 4776-4785, (2016).

*Chapter 2*

2. J. P. La Torre, B. Bornemann, and N. A. Riza, "Smart optical shape sensor using electronically controlled lens and laser line illumination scanning," *IEEE Sensors Journal*, vol. 17, no. 4, pp. 1005-1012, (2016).

*Chapter 3*

3. J. P. La Torre, N. Mayes, and N. A. Riza, "Laser display system for multi-depth screen Projection Scenarios," *Applied Optics*, (in press), (2017).

*Chapter 4*

4. N. A. Riza, M. J. Amin and J. P. La Torre, "Coded Access Optical Sensor (CAOS) imager," *Journal European Optical Society - Rapid Publications*, vol. 10, 15021, (2015).

*Chapter 7*

5. N. A. Riza, J. P. La Torre and M. J. Amin, "CAOS-CMOS camera," *Optics Express*, vol. 24, no. 12, pp. 13444-13458, (2016).

*Chapter 8*

6. N. A. Riza and J. P. La Torre, "Demonstration of 136 dB dynamic range capability for a simultaneous dual optical band CAOS," *Optics Express*, vol. 24, no. 26, pp. 29427-29443, (2016).

*Chapter 9*

## CONFERENCES

1. J. P. La Torre, N. Mayes, and N. A. Riza, “Smart art display projection system,” in Photonics Ireland, Ireland, (2017).

*Chapter 4*

2. J. P. La Torre, M. J. Amin and N. A. Riza, “Agile wavefront splitting interferometry and imaging using a digital micromirror device,” SPIE Photonics Europe - Optics, Photonics and Digital Technologies for Imaging Applications Conference, 98960B, Belgium, (2016).

*Chapter 5*

3. J. P. La Torre, M. J. Amin, M. Magno and N. A. Riza, “An embedded smart agile pixel imager for lasers,” 6th European Embedded Design in Education and Research Conference (EDERC), pp. 230-234, Italy, (2014).

*Chapter 6*

4. N. A. Riza and J. P. La Torre, “Multispectral and Hyperspectral CAOS Camera,” in Light, Energy and the Environment, OSA, paper HM2E.5, Germany, (2016).

*Chapter 9*

## **ADDITIONAL PUBLICATIONS**

### **JOURNALS**

1. M. J. Amin, J. P. La Torre and N. A. Riza, “Embedded optics and electronics single digital micromirror device-based agile pixel broadband imager and spectrum analyzer for laser beam hotspot detection,” *Applied Optics*, vol. 54, no. 12, pp. 3547-3559, (2015).





## LIST OF ABBREVIATIONS

$\lambda$	Wavelength
$\pi$	Pi
1-D	One-Dimension
2-D	Two-Dimensions
3-D	Three-Dimensions
ADC	Analog-to-Digital Converter
AOTF	Acousto-Optical Tunable Filters
ASIC	Application Specific Integrated Circuit
BS	Beam Splitter
CAOS	Coded Access Optical Sensor
CCD	Charge Coupled Device
CDMA	Code-Division Multiple Access
CMOS	Complementary Metal Oxide Semiconductor
CPS	Cyber-Physical Systems
CS	Compressive Sensing
dB	Decibel
DLP	Digital Light Processing
DMA	Direct Memory Access
DMD	Digital Micromirror Device
DOF	Depth-of-Field
DR	Dynamic Range
DSP	Digital Signal Processing
ECVFL	Electronically Controlled Variable Focus Lens
EM	Electromagnetic
EVM	Evaluation Module

f	Frequency (Hertz)
F	Focal Length
FDMA	Frequency Division Multiple Access
FFT	Fast Fourier Transform
FOV	Field-of-View
FT	Fourier Transform
GUI	Graphical User Interface
He-Ne	Helium-Neon
HDR	High Dynamic Range
Hz	Hertz
LCr	LightCrafter
LED	Light Emitting Diode
LM	Laser Module
LS	Laser Source
LSD	Laser Scanning Display
M	Mirror
MO	Microscope Objective
MEMS	Micro Electro Mechanical Systems
ND	Neutral Density
NEP	Noise Equivalent Power
OAD	Optical Array Device
OCT	Optical Coherence Tomography
OD	Optical Density
P	Pinhole
PBS	Polarizing Beam Splitter
PC	Personal Computer
PD	Photodetector

PDA	PhotoDetector Assembly
PPD	Point Photodetector
QWP	Quarter Wave Plate
R	Receiver
RF	Radio Frequency
SLM	Spatial Light Modulator
SF	Spatial Filter
SM	Smart Module
SNR	Signal to Noise Ratio
T	Transmitter
TDMA	Time Division Multiple Access
TF	Tunable Filter
TI	Texas Instruments, Inc.
TIM	Timer
TOF	Time-of-Flight
T/R	Transmitter/Receiver
VGA	Variable Gain Amplifier
WLI	White Light Interferometry



## LIST OF FIGURES

Fig. 2.1. (a) Operation of a prior art triangulation geometry-based 3-D shape sensor, and (b) scenario shows how the 3-D shape sensing triangulation technique fails in the presence of occlusions such as for solid 3-D objects with complex internal structures. .... 10

Fig. 2.2. (a) Deployment scenario of the proposed single viewing axis optical 3-D shape sensor, (b) proposed high transverse resolution single viewing axis optical 3-D shape sensor using electronically controlled optical lens, and (c) camera design used for image acquisition within the proposed 3-D shape sensor. .... 12

Fig. 2.3. Optical ray diagram of a single lens imaging system illustrating the concept of Depth of Field. .... 15

Fig. 2.4. Flow chart diagram sensor that shows the relationship among the designed working range  $h$  and DOF. .... 20

Fig. 2.5. Flow chart diagram illustrating the sequential steps of the proposed 3-D shape sensor, highlighting the steps implemented in the imaging processing algorithm. .... 21

Fig. 2.6. (a) Laboratory setup of the proposed 3-D shape sensor including the mirrors  $M_1$  and  $M_2$  deployed for beam alignment, (b) experimental 3-D sensor depth  $h$  calibration data versus ECVFL drive current values  $i$  for the designed 40 mm depth measurement range, and (c) 3-D shape sensor x-y transverse resolution calibration curve for spot diameter  $2w_{\min}$  versus depth  $h$  values obtained during the sensor calibration phase. A comparison between experimental (dots) and theoretical (line) values is shown. .... 22

Fig. 2.7. (a) Side view of the custom made boreholes solid block that is assembled by stacking two separate blocks, (b) top view of the assembled boreholes solid block, and (c) solid block 3-D borehole depth reconstructions using the proposed ECVFL-based sensor. .... 23

Fig. 2.8. (a) Top view of the TSSOP IC package with scanned regions A and B. Region B has two pins removed, and (b) side view of the TSSOP IC package. Notice the pin angular orientation on the highlighted pin region. .... 26

Fig. 2.9. (a) 2-D optical intensity map obtained for the A region of the TSSOP IC using the proposed ECVFL-based sensor, (b) 2-D optical intensity map obtained for the B region of the TSSOP IC using the proposed ECVFL-based sensor, (c) 1-D normalized intensity plot for zone A of the IC component obtained using the proposed ECVFL-based sensor showing the presence of all pins, and (d) 1-D normalized intensity plot for zone B of the IC component

obtained using the proposed ECVFL-based sensor showing the locations of the two missing pins.....	27
Fig. 2.10. (a) Fokker aircraft part used in the 3-D shape sensing experiment, (b) 3-D point cloud map of the Fokker aircraft part obtained using the proposed 3-D shape sensor, and (c) 1-D plot of $h$ versus $O_L$ , outlining the shape profile of the aircraft part shown in (a).....	28
Fig. 2.11. (a) Proposed laser line source-based 3-D shape sensor optical design, and (b) top view of a laser line pattern with 4 lines illuminating a target for the proposed ECVFL-based 3-D shape sensor.....	30
Fig. 3.1. (a) Proposed optical design of a single viewing axis laser line illumination based 3-D shape sensor. (b) Proposed camera module design used for image acquisition. (c) Camera module optical ray diagram. ....	38
Fig. 3.2. (a) Side view ray optics diagram of the ECVFL and LLM cylindrical lens $L_c$ based two lens system. TP: Target Plane. (b) Laser line illumination behavior due to different ECVFL focal length values. In this illustration, the optimum ECVFL value for is given by $F_{e,0}$ . ....	41
Fig. 3.3. (a) Experimental setup and (b) view of the proposed 3-D shape sensor using a laser line illumination.....	45
Fig. 3.4. Flowchart diagram for that shows the relationship among the designed working range $h_R$ , DOF, and FOV. ....	46
Fig. 3.5. (a) Laser line illumination width camera snapshot for an unfocused (left) and a focussed (right) beam. (b) Laser line illumination intensity versus CMOS sensor pixel location along $y$ -direction for an unfocused (dotted line) and a focussed (solid line) laser line beam. (c) Experimentally measured laser line thickness (in CMOS sensor pixel count) versus ECVFL drive current for a given depth $h_i = 10$ mm. (d) Laser line illumination falling over a cube shaped object. (e) Laser line illumination divided in $n$ segments. ....	48
Fig. 3.6. Experimental calibration depth $h$ versus ECVFL drive current $i$ for the designed 40 mm depth range. Raw data (dots) and the best fit curve (solid line) are shown. The curve fitting operation was performed using MATLAB. ....	50
Fig. 3.7. (a) Abstract representation of the two cubes deployed for the experimental demonstration (b) Sample delrin block made by two cubes having 1 cm and 2 cm heights, respectively. (c) 3-D profile obtained with the proposed 3-D shape sensor.....	51
Fig. 3.8. (a) Staircase sample delrin block having 10 mm, 20 mm, 30 mm, and 40 mm height for each step respectively. (b) Complete object 3-D profile obtained with proposed 3-D shape sensor. ....	51

Fig. 3.9. (a) Sample having a narrow crevice with a 15 mm depth and 7 mm width. (b) Partial cut-section 3-D profile reconstruction using the laser line shape sensor.....52

Fig. 4.1. Example projection scenarios using a dual-depth screen and various projection technologies such as (a) Standard LCD/DLP projector with limited depth-of-focus; (b) Classic Laser Scanning Display (LSD) which presents image distortion; and (c) Proposed Smart Art Display which produce a high resolution image with no image distortion.....60

Fig. 4.2. (a) Side view ray optics diagram of the ECVFL and LLM cylindrical lens  $L_c$  based two lens system. TP: Target Plane. (b) Laser line illumination behavior due to different ECVFL focal length values. The optimum ECVFL value for distance measurement is given by  $F_{e,0}$ .....62

Fig. 4.3. Smart Art Display embedded distance sensor calibration data of localized screen distance  $L$  versus ECVFL1 current when observing the smallest laser spot on the projection screen that is covering a projection screen depth variation of  $h=65$  cm.....64

Fig. 4.4. Two sample “CAOS” lettering projections produced using two different laser pen thicknesses for text writing. Shown are also various pen thicknesses. ....65

Fig. 4.5. Multi-distance screen projection test for two side-by-side screens with front screen  $L1$  located at 20 cm position and back screen  $L2$  located at 70 cm depth position. Projected circle images are shown using (a) Standard DLP Projector and (b) Smart Art Display. In (b) shown is the laser beam spot compensation operation for the projected circle shape using the Smart Art Display that results in a non-distorted sharp and high resolution image projection at both  $L1$  and  $L2$  show casing the power of the Smart Art Display.....65

Fig. 5.1. Proposed agile electronically programmable wavefront splitting interferometer designs using a Spatial Light Modulator (SLM) such as (a) a transmissive SLM, (b) a DMD SLM and (c) a Beamsplitter with a DMD SLM. Original version of the shown diagrams can be found in [34].....71

Fig. 5.2. Experimental optical designs (a) and (b) used to demonstrate the proposed DMD-based Young’s double slit interferometers. ....73

Fig. 5.3. (a) (left) Computer generated image of a double slit that is transferred onto the DMD chip to create two horizontal slits separated by  $64.8 \mu\text{m}$  and the (right) corresponding far-field interference pattern produced on the CCD sensor when a 633 nm collimated laser beam is incident on DMD chip. (b) (left) Computer generated image of double slit that is transferred onto the DMD chip to create 2 horizontal slits separated by  $129.6 \mu\text{m}$  and the (right) corresponding far-field interference pattern produced on the CCD sensor when a 633 nm collimated laser beam is incident on DMD chip.....75



Fig. 5.4. (a) (left) Computer generated image transferred onto the DMD chip representing all the micromirrors that deviates the light towards the screen direction to visualize on screen the diffraction order spots (right).(b) (left) Computer generated image of double slit that is transferred onto the DMD chip to create two diagonally oriented slits at  $+45^\circ$  separated by  $61.09 \mu\text{m}$  and the (right) corresponding far-field interference pattern produced on the CCD sensor when a  $633 \text{ nm}$  collimated laser beam is incident on DMD chip. (c) (left) Computer generated image of double slit that is transferred onto the DMD chip to create two diagonally oriented slits at  $+45^\circ$  separated by  $247.38 \mu\text{m}$  and the (right) corresponding far-field interference pattern produced on the CCD sensor when a  $633 \text{ nm}$  collimated laser beam is incident on DMD chip. ....77

Fig. 5.5. Block diagram of a 3-D imager design using electronic beam 3-D scan/position controls and a single point photo-detector and optical illumination source. Original version of the shown diagrams can be found in [40]. ....79

Fig. 5.6. Schematic block diagram of a module for implementing smart camera for 3-D imaging with focus and aperture size control via an ECVFL-SLM combination and single point photo-detection. Options of (a) Reflective SLM and (b) Transmissive SLM. Original version of the shown diagrams can be found in [40]. ....80

Fig. 5.7. Schematic block diagram of a module for implementing combined projector and camera module for 3-D imaging with single point photo-detection. Original version of the shown diagrams can be found in [40]. ....82

Fig. 5.8. Schematic block diagram of a module for implementing a lens-based aperture controlled camera with a digital 2-D SLM and 2-D detector array. Original version of the shown diagrams can be found in [40]. ....83

Fig. 5.9. Schematic block diagram of a module for implementing a lens-less pinhole camera with a digital 2-D SLM and 2-D detector array. Original version of the shown diagrams can be found in [40]. ....84

Fig. 6.1. Proposed embedded smart agile pixel imager block diagram. ....93

Fig. 6.2. (a) A simulated 1-D Gaussian beam intensity distribution showing the  $1/e^2$  beam width  $2w$ , (b) A simulated 2-D cross-section of a Gaussian laser beam intensity distribution using (a) for orthogonal axes of irradiance map. ....95

Fig. 6.3. Detailed experimental block diagram of proposed embedded imager. ....95

Fig. 6.4. (a) Experimental setup with the imaging plane (DMD plane) at  $d_0 = 50 \text{ cm}$  away from the laser source. (b) MATLAB plot of embedded agile pixel imager acquired 2-D beam

irradiance map obtained using an agile pixel size of 3x3 micromirrors during the imaging process.....	98
Fig. 6.5. Lens having 20 cm focal length incorporated in setup stated in Fig. 6.4(a). Distance $d_1$ is kept fixed at 30 cm, while $d_2$ is changed to values of 21 cm, 26 cm and 31 cm. ....	99
Fig. 6.6. Embedded imager acquired 1-D plots showing imaging capability for different distances along beam propagation path. Imaging is carried out at $d_2$ values of (a) 21 cm, (b) 26 cm and (c) 31 cm. The approximate $1/e^2$ threshold is also shown in each plot with a horizontal line. ....	100
Fig. 7.1. CAOS imager implementation (side view). ....	107
Fig. 7.2. CAOS imager signal flow chart.....	110
Fig. 7.3. (a) CAOS imager optical experimental setup. (b) Schematic representation of (a).....	113
Fig. 7.4. (a) Coded 1-D time signal produced by the PD for three agile pixels on the DMD chip. (b) FFT signal processing decoding of the three micromirror agile pixel irradiances $I_1$ , $I_2$ , and $I_3$ that are proportional to the normalized spectral values computed by the FFT operation. ....	115
Fig. 7.5. (a) 2-D irradiance of 2160 agile pixels data from the experimental CAOS imager using 60 1-D line scans across DMD chip. (b) (Left) The optical irradiance distribution representation of a laser spot incident on an example 6 pixels (in a column) by 9 pixels (in a row) DMD chip.(Right) The total pixel-by-pixel optical irradiance on the chip is represented in a single 1-D plot, which includes the optical irradiance contributions of each row of the DMD chip. ....	117
Fig. 7.5. (c) Zoomed version of Fig. 7.5(a) irradiance data to estimate the average null or noise floor in the imager (d) The fully decoded 2-D irradiance map produced by CAOS Imager showing raw (i.e., unprocessed) intensity values, normalized to 1. (e) Comparison of central cross-section data of the CAOS imager acquired laser beam image (dots) vs. laser manufacturer provided theoretically expected Gaussian beam envelope (dashed line). ....	118
Fig. 8.1. The CAOS-CMOS Camera design.....	125
Fig. 8.2. Snapshot of the CAOS-CMOS camera experimentally setup in the laboratory.....	131
Fig. 8.3. Field of View of the target scene as viewed from the CAOS-CMOS camera in the experimental demonstration.....	132
Fig. 8.4. Images of the scene viewed using the CMOS mode of the CAOS-CMOS camera. (a) Unsaturated scene with a torch off, (b) saturated scene due to torch lighting, (c) scene of (b) attenuated by a factor of 1,000, (d) scene of (b) attenuated by a factor of 3,200, (e) scene of	

(b) attenuated by a factor of 10,000, and (f) logarithmic scale image of the irradiance data from image (e).....	134
Fig. 8.5. 2-D image reconstruction of the target scene using the CAOS mode of the CAOS-CMOS camera. (a) scaled irradiance map $I(x,y)$ is shown, (b) scaled irradiance map of the logarithm of $I(x,y)$ values is shown, and (c) same plot as in (b) but with additional labels of regions R1, R2, R3 and R4 as well as location of traces T1, T2 and T3 used for quantitative image analysis purposes.....	138
Fig. 8.6. The frequency domain plots of chosen CAOS acquired signals at regions (a) R1 covering a segment of the torch, (b) R2 covering the filament, (c) R3 covering the traffic sign, and (d) R4 covering the black background. Note that only $ S(f) $ peaks at frequencies $f_1 = 133.4$ Hz and $f_2 = 200.2$ Hz indicate the scaled relative optical irradiance at the corresponding agile pixels. The peak at 150 Hz appearing in each plot is due to the 3 <sup>rd</sup> harmonic of the 50 Hz electricity mains supply. ....	140
Fig. 8.7. Plots showing the measured scaled irradiances along Fig. 8.5(c) labeled traces (a) T1, (b) T2, and (c) T3. ....	141
Fig. 9.1. Proposed simultaneous dual optical band CAOS imager design. ....	152
Fig. 9.2. Shown is the Visible-NIR bands target scene created using 3 visible LEDs and 1 NIR LED. Photos show LEDs off (left) and LEDs on (right). These photos are taken with a Nikon D3300 DLSr visible camera.....	156
Fig. 9.3. (a) Visible scaled irradiance map obtained using the CAOS visible-NIR simultaneous dual optical band imager visible channel. (b) NIR scaled irradiance map obtained using the CAOS camera infrared channel.....	159
Fig. 9.4. Narrower spectral channel CAOS visible-NIR simultaneous dual optical band imager scaled irradiance maps at (a) $\lambda = 450$ nm with FWHM of 40 nm, (b) $\lambda = 550$ nm with FWHM of 40 nm and (c) $\lambda = 620$ nm with FWHM of 10 nm. ....	160
Fig. 9.5. Shown is the normalized optical irradiance plotted versus agile pixel scan distance as the agile pixel conducts a line-by-line scan over the DMD1 plane making 442 agile pixels. Plot in (a) is generated from PD2 (NIR channel) while plot in (b) is generated from PD1 (Visible channel). Note that (b) is obtained unrolling in a 1-D array the 2-D array shown in Fig. 9.4(b).....	161
Fig. 9.6. (a) Shown is the design of the DMD2-based TF1 module used in Channel 1 of the CAOS camera that implements CAOS-mode narrower wavelength optical spectral detection. (b) Photograph of the DMD2 plane spatially distributed visible spectrum produced by light coming from the DMD1 programmed CAOS-mode white light agile pixel. ....	163

Fig. 9.7. Shown are the detected RF spectrum peaks  $|S(f)|$  for different visible band spectral selections programmed by the CAOS-mode of DMD2 in TF1. (a)  $|S(f = f_0)| = 49.68 \times 10^{-4}$  obtained when the entire DMD2 is programmed to direct all spectral components of the white light agile pixel at  $f = f_0 = 400$  Hz CAOS-mode to PD1. (b)  $|S(f_0 + f_3)| = 0.4581 \times 10^{-4}$  obtained when DMD2 is programmed to direct only the red color spectral band light to PD1 using a  $f_3 = 50$  Hz CAOS-mode. (c)  $|S(f_0+f_2)| = 1.091 \times 10^{-4}$  obtained when DMD2 is programmed to direct only the green color spectral band light to PD1 using a  $f_2 = 62.5$  Hz CAOS-mode. (d)  $|S(f_0+f_3)| = 0.4597 \times 10^{-4}$  and  $|S(f_0 + f_1)| = 1.074 \times 10^{-4}$  obtained when DMD2 is programmed to simultaneously direct the red and blue color spectral band light components to PD1 using  $f_3 = 55.5$  Hz (red) and  $f_1 = 83.3$  Hz (blue) CAOS-mode. .... 165

Fig. 9.8. Highlighted are the detected peak  $|S(f_1)|$  for different optical attenuation, DAQ voltage range configuration, and sampling duration time. (a)  $|S(f_1)| = 1.228$  obtained for a 10 V DAQ range setting when no optical attenuation is used and  $t_s = 5$  s. (b)  $|S(f_1)| = 1.43 \times 10^{-5}$  obtained for a 10 V DAQ range setting when ND filter is equal to  $OD = 5$  and  $t_s = 5$  s. (c) Peak at  $f_1$  buried in system noise floor for a 10 V DAQ range setting when ND filter is equal to  $OD = 5.5$  and  $t_s = 5$  s. (d)  $|S(f_1)| = 3.56 \times 10^{-6}$  obtained for a 200 mV DAQ range setting when ND filter is equal to  $OD = 5.5$  and  $t_s = 5$  s. .... 171

Fig. 9.9. (a)  $|S(f_1)| = 1.902 \times 10^{-6}$  obtained for a 200 mV DAQ range setting when ND filter is equal to  $OD = 6$  and  $t_s = 5$  s. (b) Peak at  $f_1$  buried in system noise floor for a 200mV volts DAQ range setting when ND filter is equal to  $OD = 6.3$  and  $t_s = 5$  s. (c)  $|S(f_1)| = 6.371 \times 10^{-7}$  obtained for a 200 mV DAQ range setting when ND filter is equal to  $OD = 6.3$  and  $t_s = 60$  s. (d)  $|S(f_1)| = 3.662 \times 10^{-7}$  obtained for a 200 mV DAQ range setting when ND filter is equal to  $OD = 6.6$  and  $t_s = 60$  s. (e) Peak at  $f_1$  buried in system noise floor for a 200mV volts DAQ range setting when ND filter is equal to  $OD = 6.9$  and  $t_s = 60$  s..... 173



## LIST OF TABLES

Table 2.1. Experimental solid block borehole depth values obtained with the proposed 3-D shape sensor and a vernier caliper. ....	25
Table 5.1. Experimental versus theoretical fringe separation.....	78
Table 6.1. Experimental data showing $1/e^2$ beam radii estimates extracted using MATLAB and micro-controller for different $d_2$ values and pinhole sizes. ....	99



*To my mother, Justina Aro Quispe  
and my father, Salvatore Bensi.*





## ACKNOWLEDGEMENTS

There are no words to express my profound gratitude towards my parents for the enormous support you have been giving me throughout these years. Mom, you are the most important person that I have and it is all because of you that I am here writing these few lines. All the sacrifices and privations that you have done since the beginning of my studies have allowed me to get to this stage. Brunino, many thanks for your unconditional support, it is also because of you that I was able to get to this point and accomplish this goal.

This second paragraph is a must, dedicated to the architect of this journey, Prof. Nabeel Riza. Prof. Riza gave me his unconditional trust reminding me many times along the track that the person's mind set is the most important quality that goes even beyond his numerical calculation abilities. For all the times I did stumble along the way, he taught me to start over and learn from my mistakes. Of course not everything was smooth and shiny, sometimes I did learn things the hard way but I am convinced that those little lessons are the ones that will stick with me the longest. Now we are at the end of this run and I hope I was a good student and a worthy investment. Thank you.

Junaid, I was very lucky to have the opportunity to work with you side-by-side, steal your secrets and learn from you. You are my colleague, mentor and friend, all-in-one. Thanks for all the times we stood up side-by-side to overcome the difficulties along the way. I am not forgetting your wife, Joveria Baig. I am very lucky to know her and to have tasted the best biryani ever. I wish Joveria, little Hooria, and you all the best for your future as a sweet family. No later than a few months after Dr. Junaid departed for Princeton University, Mohsin Mazhar joined the UCC photonics group. He is a young enthusiast student and I am picturing him doing well in his future career. I am very thankful to Prof. John Sheridan of University College Dublin for agreeing to be my external examiner and dedicate his valuable time for evaluating this dissertation. I am also very grateful to Dr. Kevin McCarthy and Dr. John Hayes for agreeing with no hesitation to be my internal supervisor and thesis advisor, respectively. I would like to thank the UCC staff in Electrical Engineering-School of Engineering, in particular Hillary Mansfield and James Griffiths for their useful suggestions and recommendations on electronics related topics, Michael O'Shea and Timothy Power for the realization of many custom hardware used in the experiments, the administrative staff of Claudia Cashman, Mary O' Leary and Niamh O'Sullivan, and the UCC teaching staff with a

special mention of Dr. Emanuel Popovici for playing an important role at the very beginning of my stay at UCC.

Another key person is Alessandro Bravin, my grumpy brother. Thanks a lot Ale for your many suggestions, for all the time we spent together, relaxing, playing, consulting, talking, wondering and many more. Lorenzo Gaggero is also my big brother. We have spent wonderful time all together, the three of us. Thanks Gagge, it is always fun remembering the happiness of the early years. This long Irish adventure started also with other three dear friends, Antonio Libri, Emanuele Fumeo and Gabriele Campodonico. Many good friendships were born during this period. Marianne Pellisier and Jeanne Mourre, thank you. Alessio Burlando and Frabrizio Silvestri are also great companions whom I will always remember. We all have taken different paths along the way and I thank you all for all the good times we had together and I wish you the best for the future. I will always cherish the time spent with the Erasmus 2012/2013 and 2013/2014 group; apologies if I am not listing everyone's names.

I also express my gratitude to the Gutierrez family back in Italy towards which I harbour great affection for the many years we have known each other. Many thanks to Irma Gutierrez, Zenaida Gutierrez, Delia Gutierrez, Marina Gutierrez, and Yuliana Yactayo Gutierrez. My thoughts are also with Olga Valle Moron, Kelly Romero Gutierrez, Indira Garcia, Margarita Chavez, Dalila Chavez, Emilio, Jose, Gladis and all of you. My family back in Peru is also another motivation for keeping me moving ahead. You all are in my thoughts and I wish one day to help you all to the best of my abilities.

Thanks to all the good colleagues and friends in the Electrical Engineering discipline of the School of Engineering and the UCC institution in general, and apologies if I cannot mention everyone. Thanks to Bruno Srbinovski and Alex Jaeger in particular for all the times we had deep discussions on electronics which have helped me a lot. Thanks to the Electrical Engineering soccer buddies Pietro Nardelli, Edward O'Dwyer, Conor O'Shea, Adrian O'Sullivan, Brendan Barry, Brian Murphy, Diarmaid Hogan, Daniel O'Keefe and Robert Ryan. Monday nights were awesome. Other valuable colleagues that I would like to thank are Yeny Vazquez Gutierrez, Bo Yang, Michele Magno, Oksana Semenova, Alison Ní Sheaghda, Haiyang Li, Wentao Jiang, and George O'Mahony. I would also like to thank all the good friends from the Tyndall National Institute, in particular Annamaria Fordymacka, Stefano Facchin, Prasanna Ramaswamy and Marco Dalla Danta. Thanks Aodh Quinlivan and all the UCC Staff soccer team for the three years that I have played with all you guys. Special

thanks to Walter Messina, Marco Nocita, Matteo Pusceddu, and Pietro Maccioni for the good times we had together.

Thanks to all my friends in Cork who have helped make my life more enjoyable. Elisa Zappa, for beginning a wonderful dancing partnership and for helping me in kicking things up a notch. Thanks to Marine Kurth, Linda Morichetti, Elena Lattanzi, Valentina Ambrogi, Giulia Pattarini, Cristina Libri, Emma Guerin, Charles Perumal, Lorenzo Di Marcello, Dimitris, Ignacio (Nacho) Castineiras, Han Shao, Harsh Mer, Anbu, Abdul Razzaq. Thanks also to the Salsa Cubana Cork and the Bachata Cork group, in particular Samantha, Giusy, Donnie, Francesca and Valentina for the good times I am having in this last period. Thanks to my Latin friends in Cork, namely, Andres Felipe Molina Osorio, Francisco Peña, Natalia Cañas Estrada, Juliet Haykal Libbos, Octavio and Andrea. Special thanks to Cliona Maher; it was you who introduced me to such wonderful people. Thanks to all my very good friend back in Italy: Anita, Danilo, Ylenia, Davide, and Francesco.

I am forever grateful to Hong Wu. Mia, thanks for all the times you have been patient with me. You are always there reminding me to smile even when difficulties appeared insurmountable. Thanks for your love and your continuous and unwavering support. I will never take it for granted nor will I forget what you have done for me.

With this final line I acknowledge you all and apologise if I am forgetting someone for being part of my personal life and educational career.



# CHAPTER 1

## INTRODUCTION

Photonics is the discipline that studies light and its applications. Electronics is the discipline that involves the use of electrical circuit components from massive transformers to tiny integrated circuit packages having physical dimensions that reach down to the nanoscale level. Continuous and remarkable innovations in both these disciplines are being produced by independent research groups all around the world. Such achievements motivate researchers to outperform prior solutions by presenting smarter solutions for today's engineering challenges. With this dissertation, the merging of the aforementioned disciplines is accomplished by strategically adopting key strengths of photonics and electronics for the realization of automated smart system designs. Applications that can benefit from such designs varies from non-destructive shape sensing to art centric displays to imaging systems such as laser beam mappers and incoherent light cameras. Throughout this dissertation, each chapter provides the motivation and evidence of the existing problems and then goes on to describe the robust automated designs which are implemented and tested with detailed experiments.

Chapter 2 presents the design of an optical shape sensor operating along with a computer-controlled Electronically Controlled Variable Focus Lens (ECVFL) for non-contact measurements applications [1]. The novelty introduced in the proposed optical design is the use of a single in-line viewing axis optical sensor. This new feature idea overcomes previous triangulation-based Three-Dimensional (3-D) shape sensor limitations that were caused either due to geometrical constraints or limited working range [2-4]. Sensor design analysis of aberration and diffraction effects balancing strategies are presented, including the derivation of the depth of field of the camera module used within the 3-D sensor. The proposed sensor illustrated in this chapter is experimentally demonstrated to work in an automated platform in conjunction with its dedicated Graphical User Interface (GUI), which is C++ based. The optical shape sensor is designed to work over a calibrated depth  $z$  of 40 mm with a demonstrated transverse resolution of 52  $\mu\text{m}$  over the entire  $x$ - $y$  working range of 400 mm  $\times$  400 mm. The proposed 3-D shape sensor system is successfully deployed to measure an

object presenting surface irregularities such as borehole depths in a 3-D sample. Moreover the versatile shape sensor is tested by imaging the pin region of a 16-pin Integrated Circuit (IC) Thin-Shrink Small Outline Package (TSSOP) and also used to reconstruct the shape of a 3-D aircraft part, making the 3-D shape sensor ideal for a wide range of applications.

Chapter 3 presents the design of a shape sensor that uses an ECVFL and a line illumination scanning for 3-D shape sensing and reconstruction [5]. The proposed design uses a smart single viewing axis camera module designed to work with a laser line illumination scanning principle. Image processing algorithm techniques are presented in this chapter that evaluate the acquired laser illuminated target images. The deployment of a laser line scanning illumination with respect to the Chapter 2 demonstrated single laser point scanned ECVFL based 3-D shape sensor represents a major improvement in shape sensor speed performance [1, 6]. In particular, the line illumination sensor experimentally demonstrates 16X per-point 3-D scan performance improvement when compared to the Chapter 2 presented point-scan based sensor. The proposed shape sensor is experimentally demonstrated using a liquid ECVFL and a transverse direction motion mechanical platform to successfully 3-D map 40 mm depth steep surface profile objects with a demonstrated experimental mean measurement error of <5% within the designed working range.

Chapter 4 presents a novel projection display system that is ECVFL based and called Smart art display [7]. The use of an ECVFL in the projection display design allows the projection of sharp and in-focus images over multi-distances/multi-level 3-D surfaces. In order to 3-D map the multi-depth target projection, the proposed projection system functions in unison with an embedded and non-invasive distance sensor that uses the ECVFL for both sensing and projection purposes. With respect to conventional laser scanning and Spatial Light Modulator (SLM) based projection systems, the proposed projection system offers in-focus non-distorted projection over a multi-distance screen zone with varying depths [8]. A basic computer automated experimental projection system for a screen depth variation distance ranging from 12 cm to 77 cm with respect to the edge of the projection system is demonstrated. The projection system uses a 633 nm laser beam, a 3 kHz scan speed galvo-scanning mirrors and a liquid-based ECVFL, improving on the 2011 non-automated implementation [9]. Furthermore, this chapter shows the 3-D projection capabilities of the Smart Art Display, including the projection of a non-distorted image over a two-depth screen versus a distorted image obtained via dominant prior-art projection methods.

Chapter 5 describes the proposed Digital Micromirror Device (DMD) based wavefront splitting interferometer and imager designs [10]. In 1997 Prof. Riza's group has proposed and demonstrated the use of the Texas Instrument (TI) DMD for various applications including optical switching. In 2009, Prof. Riza's group has proposed the use of the DMD to realize wavefront splitting interferometers as well as a variety of imagers [11]. Specifically, proposed are agile electronically programmable wavefront splitting interferometer designs using transmissive and reflective Spatial Light Modulator (SLM) configurations. The SLM operates with on/off or digital state pixels to control the passage/reflection of the incident light. SLM pixel locations can be spatially and temporally modulated to create custom wavefronts for near-common path optical interference at the optical detector e.g. Charge Coupled Device (CCD)/Complementary Metal Oxide Semiconductor (CMOS) sensor, a Focal Plane Array (FPA) sensor or a point-photodetector. In this chapter, the design and experimental verification of the Digital Micromirror Device (DMD) based wavefront splitting interferometer is conducted for the first time. Furthermore, its performances are illustrated showcasing its capabilities as a programmable Young's double slit interferometer device.

Chapter 6 presents the design of an embedded electronics laser beam profiler automated platform based on the use of the smart agile pixel imaging technique as proposed by Prof. N. A. Riza's group since 2002 [12-14]. This chapter describes in detail the realization, for the first time, of the design and the implementation of a fully embedded and automated laser profiler system platform [15]. It is demonstrated how laser beam techniques can be embedded through hardware and software co-design to develop an embedded system that is cost effective and compact with respect to weight and volume. Such an embedded design is desirable since in the last few years there are a growing number of laser beam industrial applications that demand characterization, tracking and measurement of the laser beam profile. The proposed automated design uses a DMD device along with a microcontroller and point photo-detectors to implement a compact system having minimum sized components. The proposed embedded laser beam profiler is successfully deployed to experimentally demonstrate its efficacy when characterizing a Gaussian laser beam. The proposed design is suitable for industrial laser based applications requiring accurate two-dimensional beam irradiance maps, without needing any attenuating components disrupting the beam under test.



Chapter 7 presents for the first time the design and implementation of the novel Coded Access Optical Sensor (CAOS) Imager/Camera [16]. High spatial resolution, low inter-pixel crosstalk, high Signal-to-Noise Ratio (SNR), adequate application dependent speed, economical and energy efficient design are common goals sought after for optical image sensors. Imagers based on pixelated imaging devices such as CCD/CMOS sensors avoid pixel-by-pixel scanning as all sensor pixels operate in parallel, but these imagers are fundamentally limited by inter-pixel crosstalk, in particular with interspersed bright and dim light zones. This chapter presents and discusses the CAOS agile pixel imager sensor design platform that can greatly alleviate the aforementioned fundamental limitations, empowering smart optical imaging for particular extreme contrast environments. Specifically, this novel CAOS imager engages an application dependent electronically programmable agile pixel platform using hybrid space-time-frequency coded multiple-access of the sampled optical irradiance map. This chapter demonstrates the foundational working principles of the first experimental electronically programmable CAOS imager using hybrid time-frequency multiple access sampling of a known high contrast laser beam irradiance test map, with the CAOS imager based on a TI DMD device. Experimentally, the CAOS imager provides imaging data that exhibits 77 dB electrical Signal-to-Noise Ratio (SNR) and the measured laser beam image irradiance specifications closely match (i.e., within 0.75% error) the laser manufacturer provided beam image irradiance radius number. The proposed CAOS imager can be deployed in many scientific and non-scientific applications where pixel agility via electronic programmability can zoom in on desired features in an irradiance map subject to the CAOS imaging operation.

Chapter 8 presents for the first time the CAOS-CMOS camera design that combines the CAOS imager platform with the CMOS multi-pixel optical sensor [17]. The chapter describes how the combination of a classic CMOS sensor light staring mode with the time-frequency-space agile pixel CAOS imager mode within one programmable optical unit is able to achieve a high dynamic range imager design for extreme light contrast conditions. The proposed CAOS-CMOS camera is built using a DMD, a silicon point photo-detector with a variable gain amplifier, and a silicon CMOS sensor with a maximum rated 51.3 dB Dynamic Range (DR). A white light imaging scenario comprising three different brightness simultaneously viewed targets is achieved by the CAOS-CMOS camera demonstrating an experimental 82.06 dB DR. To confirm the potential of the presented CAOS-CMOS camera, the image acquisition of the same scenario was shown to fail when viewed with the classic

CMOS image sensor due to the limited CMOS camera DR. The results presented in this chapter extend the coherent laser imaging performance in Chapter 7 to incoherent white light imaging [16]. Applications of the proposed novel camera include industrial machine vision, welding, laser analysis, automotive, night vision, surveillance and multispectral military systems.

Chapter 9 further extends the results provided in Chapter 7 and Chapter 8. It is shown, for the first time, the CAOS camera designs to enable simultaneous dual optical band imaging suited for extreme contrast multispectral bright target scenarios [18]. The proposed design deploys DMDs for time-frequency agile pixels CAOS-mode modulation in both the spatial and spectral domain in the image space. The design also uses two-point detectors that are spatially and spectrally isolated. This new imager can simultaneously and independently detect pixel selective image irradiance information for two different broad spectral bands, visible (VIS) and near infrared (NIR), that further undergo independent spectral image data extraction via finer-tuned wavelength filtering using all-optical or CAOS-mode electronic filters. A proof-of-concept visible-near infrared band CAOS imager is successfully demonstrated using a target scene containing LEDs having different central wavelengths and using narrowband optical filters. Furthermore, using the CAOS-mode, simultaneous colour content monitoring of a white light image target is demonstrated. For the proposed design a higher bit count Analog-to-Digital Converter (ADC) device is deployed with both range and sampling duration parameter control, allowing a wider dataset acquisition. Such considerable data set size undergoes electronic Digital Signal Processing (DSP) to extract higher DSP gain and additional noise suppression. The introduction of the aforementioned features improved the achieved experimental DR by 56 dB over the CAOS-imaging demonstration presented in Chapter 8 [17].

Finally, chapter 10 presents conclusions of the thesis by highlighting key results and suggesting future works to further improve the proposed smart module designs.

## REFERENCES

- [1] J. P. La Torre, M. J. Amin, B. Thompson, and N. A. Riza, "Optical shape sensor using electronically controlled lens," *IEEE Sensors Journal*, vol. 16, no. 12, pp. 4776-4785, (2016).
- [2] V. Lombardoa, T. Marzullib, C. Pappalettereb and P. Sforzaa, "A time-of-scan laser triangulation technique for distance measurements," *Optics and Lasers in Engineering*, vol. 39, no. 2, pp. 247-254, (2003).
- [3] J. C. Wyant, "White light interferometry," *Holography: A Tribute to Yuri Denisyuk and Emmett Leith*, SPIE Proceedings, vol. 4737, pp. 98-107, (2002).
- [4] S-W. Lee, H-W. Jeong, B-M. Kim, Y-C. Ahn, W. Jung and Z. Chen, "Optimization for axial resolution, depth range, and sensitivity of spectral domain optical coherence tomography at 1.3  $\mu\text{m}$ ," *Journal of the Korean Physical Society*, vol. 55, no. 6, pp. 2354-2360, (2009).
- [5] J. P. La Torre, B. Bornemann, and N. A. Riza, "Smart optical shape sensor using electronically controlled lens and laser line illumination scanning," *IEEE Sensors Journal*, vol. 17, no. 4, pp. 1005-1012, (2016).
- [6] N. A. Riza and S. A. Reza, "Smart agile lens remote optical sensor for three-dimensional object shape measurements," *Applied Optics*, vol. 49, no. 77, pp. 1139-1150, (2010).
- [7] J. P. La Torre, N. Mayes, and N. A. Riza, "Laser Display System for Multi-Depth Screen Projection Scenarios," *Applied Optics* (in press), (2017).
- [8] P. F. Van Kessel, L. J. Hornbeck, R. E. Meier, and M. R. Douglass, "A MEMS-based projection display," *Proceedings of the IEEE*, vol. 86, no. 8, pp. 1687-1704, (1998).
- [9] N. A. Riza and P. J. Marraccini, "Smart two-dimensional laser-based display," *IEEE Journal of Display Technology*, vol. 7, no. 2, pp. 90-95, (2011).
- [10] J. P. La Torre, M. J. Amin and N. A. Riza, "Agile wavefront splitting interferometry and imaging using a digital micromirror device," *SPIE Photonics Europe - Optics, Photonics and Digital Technologies for Imaging Applications Conference*, 98960B, Belgium, (2016).
- [11] N. A. Riza, "Agile optical image sensing, control, and measurement modules," USA Patent Application No. 61/258,344, 2009.

- [12] S. Sumriddetchkajorn and N. A. Riza, "Micro-electro-mechanical system-based digitally controlled optical beam profiler," *Applied Optics*, vol. 41, no. 18, pp. 3506-3510, (2002).
- [13] N. A. Riza, "Digital optical beam profiler," US Patent No. 6922233, (2005).
- [14] M. Sheikh and N. A. Riza, "Demonstration of pinhole laser beam profiling using a digital micromirror device," *IEEE Photonics Technology Letters*, vol. 21, no. 10, pp. 666-668, (2009).
- [15] J. P. La Torre, M. J. Amin, M. Magno and N. A. Riza, "An embedded smart agile pixel imager for lasers," 6th European Embedded Design in Education and Research Conference (EDERC), pp. 230-234, Italy, (2014).
- [16] N. A. Riza, M. J. Amin and J. P. La Torre, "Coded Access Optical Sensor (CAOS) Imager," *Journal of the European Optical Society-Rapid Publications*, vol. 10(15021), (2015).
- [17] N. A. Riza, J. P. La Torre, and M. J. Amin, "CAOS-CMOS camera," *Optics Express*, vol. 24, no. 12, pp. 13444-13458, (2016).
- [18] N. A. Riza and J. P. La Torre, "Demonstration of 136 dB dynamic range capability for a simultaneous dual optical band CAOS," *Optics Express*, vol. 24, no. 26, pp. 29427-29443, (2016).



## CHAPTER 2

### OPTICAL SHAPE SENSOR USING ELECTRONICALLY CONTROLLED LENS<sup>1</sup>

#### 2.1 INTRODUCTION

An optical 3-D shape sensor uses light to characterize an object under test to obtain depth and shape information with high accuracy. Optical 3-D shape sensors are sought after in applications where precise shape monitoring is required, such as in industrial manufacturing, cultural heritage preservation, entertainment, medical inspections, aerospace inspection, component inspection, tracking systems, position sensing and more [1-5]. Among the available 3-D shape sensing techniques described in references [6-7], the most used is the triangulation method [8]. As shown in Fig. 2.1(a), triangulation uses two Transmitter (T)/Receiver (R) points separated by a distance  $d$  to compute the depth/shape of a given object. The same working principle is used in fringe projection techniques in which patterns are projected onto an object and depth information is derived from extensive computation routines [9]. However, due to the geometry-based constraints of triangulation sensors, both classic triangulation and projection techniques do not provide accurate depth/shape measurements in the presence of occlusions such as boreholes as shown in Fig. 2.1(b). In such a scenario, a single view point 3-D shape in-line sensor is desired. Time-of-flight (ToF) and White Light Interferometer (WLI) sensing techniques are examples of single viewing axis 3-D shape sensors used for position sensing and medical inspection. ToF sensors require expensive high bandwidth electronics for short distance depth ranges ( $< 1$  m) [10]. WLI sensors are limited in measurement range (e.g., 0.4 mm) and are also an expensive sensing alternative, although they have high axial resolution [11]. Other distance sensing techniques also exist in literature. Optical Coherence Tomography (OCT) is widely used in biological research, given its high depth resolution, i.e. 5 - 15  $\mu\text{m}$ , but its depth measurement range is limited to a few millimetres making it unsuitable for various industrial applications [12]. Ultrasound is a popular technique used for automotive collision avoidance applications,

---

<sup>1</sup> J. P. La Torre, M. J. Amin, B. Thompson, and N. A. Riza, "Optical shape sensor using electronically controlled lens," IEEE Sensors Journal, vol. 16, no. 12, pp. 4776-4785, (2016).

among many others, but its transverse resolution is limited due to the divergence of the sound waves in air [13]. Chromatic Confocal sensors used for surface topography and biological sample thickness measurement provide below 500 nm axial resolution along with approximately 20  $\mu\text{m}$  transverse resolution [14-15]. However, Chromatic Confocal sensors are very expensive and have limited depth measuring range, i.e., less than 10 mm. Therefore, these aforementioned sensors are unsuitable options for the borehole scenario depicted in Fig. 2.1(b) for a depth range exceeding 15 mm. A single view-point, cost effective and high transverse resolution sensor having a depth range of the order of centimetres is desired for sensing applications such as shown in the Fig. 2.1(b) illustration.

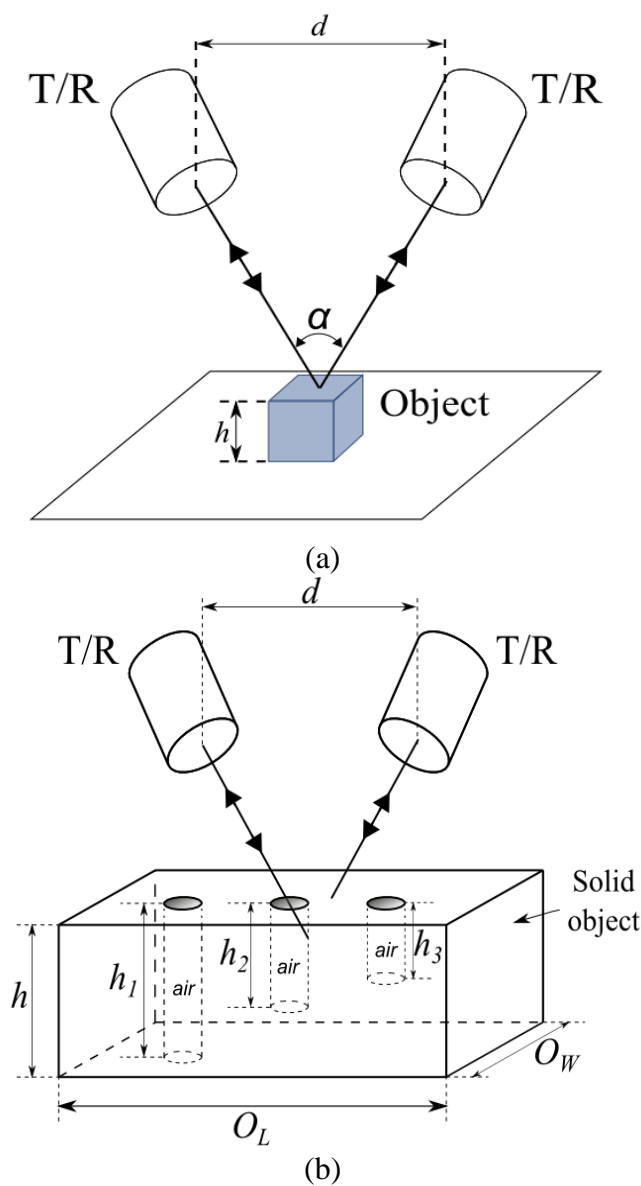


Fig. 2.1. (a) Operation of a prior art triangulation geometry-based 3-D shape sensor, and (b) scenario shows how the 3-D shape sensing triangulation technique fails in the presence of occlusions such as for solid 3-D objects with complex internal structures.

In [16-19], the use of the ECVFL for imaging, display and distance measurements has been proposed and demonstrated. Specifically, [16] demonstrates a single point distance sensor while [17] demonstrates a 3-D distance mapping sensor. The optical design in [17] includes off-axis camera viewing which inhibits the use of this 3-D shape sensor design for borehole sensing scenarios such as depicted in Fig. 2.1(b) which require a single viewing axis based sensor. Furthermore, in [17] a non-automated scan system design is proposed and demonstrated. Also, in [17] the sensor design does not allow input beam diameter control for aberration reduction resulting in a non-optimal illuminating laser beam diameter being deployed for sensing applications. In [18] is proposed a laser sampling head design for 2-D image acquisition applications. Note that [18] does not describe a 3-D shape sensor but provides an optimized optical design for 2-D image sensing with the highest transverse resolution possible for all target distances. Furthermore, in [19] it is shown how the basic ECVFL-based distance sensor can be implemented as a smart high resolution laser scanning display.

In this chapter, a computer automated 3-D scan shape sensor with on-axis camera viewing, including target illuminating beam diameter control for optimal scan transverse resolution, is designed and demonstrated for a variety of complex objects undergoing optical inspections. Specifically, proposed is a low cost single view point 3-D shape sensor for non-contact measurements that provides high transverse resolution over the designed working range and, due to the on-axis nature of the sensor design, the proposed sensor is not subject to the occlusion problem illustrated in Fig. 2.1(b). First, the chapter describes the proposed 3-D shape sensor optical design theory. Next a variety of distance measurement experiments are conducted to showcase the versatility of the proposed sensor to measure shape along One Dimensional (1-D) (e.g., multi-boreholes test part), Two Dimensional (2-D) (e.g., integrated electronic chip pin layout testing), and 3-D (e.g., aircraft 3-D part) imaging domains. The chapter concludes with an assessment of the sensor performance, features and limitations.



## 2.2 PROPOSED SINGLE VIEWING AXIS OPTICAL 3-D SHAPE SENSOR DESIGN

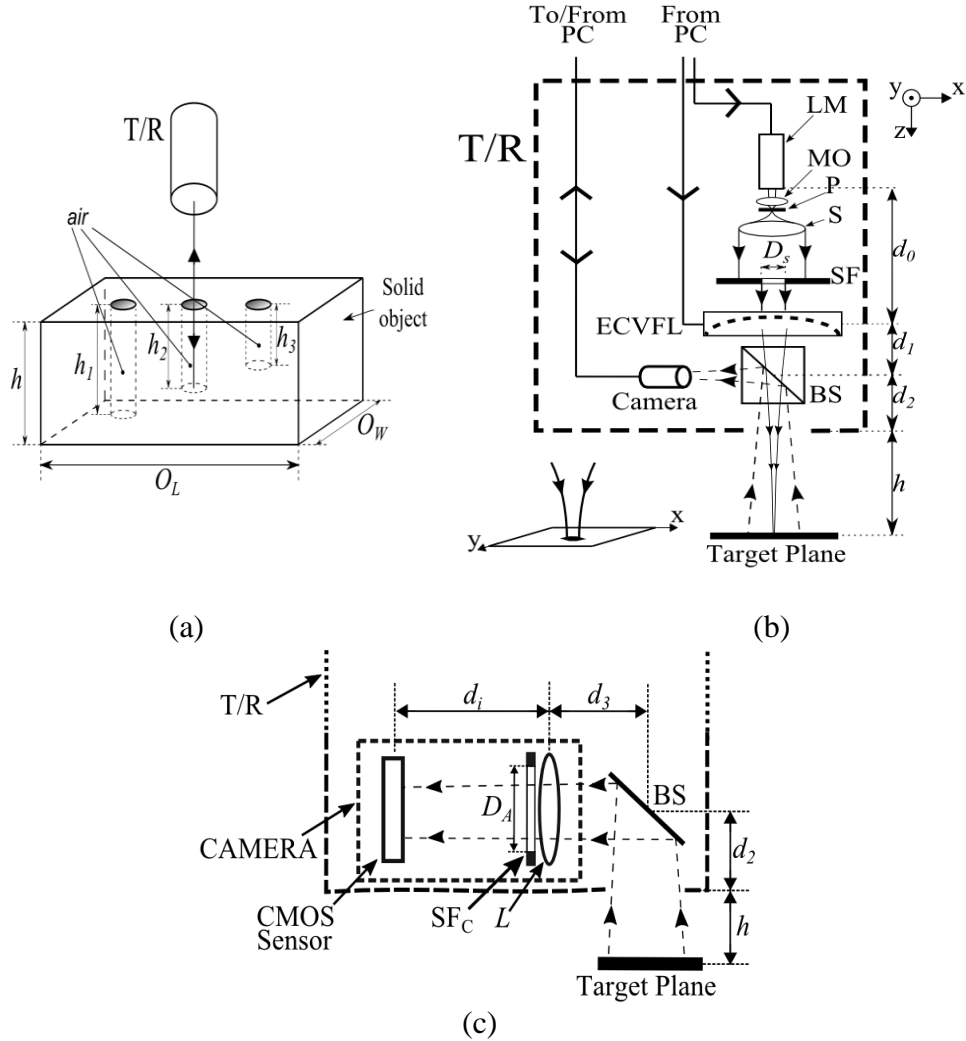


Fig. 2.2. (a) Deployment scenario of the proposed single viewing axis optical 3-D shape sensor, (b) proposed high transverse resolution single viewing axis optical 3-D shape sensor using electronically controlled optical lens, and (c) camera design used for image acquisition within the proposed 3-D shape sensor.

Fig. 2.2(a) shows the deployment of the desired in-line single viewing axis 3-D shape sensor which overcomes the limitation of triangulation-based shape sensors for scanning zones that contain small apertures such as boreholes. Specifically, Fig. 2.2(b) shows the optical design of the desired in-line single viewing axis 3-D shape sensor. Here, a Gaussian laser beam of wavelength  $\lambda$  coming out of a Laser Module (LM) propagates along the  $z$ -direction before entering a collimation setup composed of a Microscope Objective (MO), a Pinhole (P) and a collimation lens (S). The collimated laser beam passes through an electronic controllable Spatial Filter (SF) having an aperture diameter  $D_s$ , before entering an

ECVFL having a focal length  $F_e$ . The resulting beam travels through the Beam Splitter (BS) before exiting the sensor module to strike the 3-D target. The distance from the LM to the ECVFL's center is  $d_0$ , the distance between the ECVFL's center and the BS's center is  $d_1$ , the distance between the BS's center and the edge of the sensor module is  $d_2$ . The light then travels a distance  $h$  from the edge of the sensor module to any given target axial (range) plane forming a beam spot that is imaged by an on-axis camera via the BS light path. The LM, ECVFL and the camera elements are mounted on a motorized x-y stage. These elements are controlled by a Personal Computer (PC) having relevant scanning and data acquisition software.

The proposed shape sensor acquires 3-D measurements using the procedure described next. For a given depth  $h$  and a  $F_e$  value within the ECVFL's focal length range, the beam spot formed on the target plane is observed and captured by the in-line camera. The PC processes the image captured and a computer algorithm provides the beam spot diameter in pixel units. The spot diameter on the target plane is controlled by the  $F_e$  value set by the PC establishing a correlation between the spot diameter and  $F_e$ . Tuning the  $F_e$  over the full operational ECVFL's range corresponds to dynamically changing the spot size formed on the target plane. The  $F_e$  value that corresponds to the smallest spot diameter is considered the optimum ECVFL setting for a certain target depth  $h$ . Considering different depth values, it is possible to train and calibrate the sensor system linking optimum  $F_e$  values and  $h$  depth values [16-18]. For full 3-D shape recovery and reconstruction, the sensor system is programmed to move the laser sampling spot over the x-y plane scanning zone that encompasses the object transverse region under test. Thus a 3-D point cloud representing the object's 3-D reconstruction is provided by the sensor system. Compared to [17] which deployed off-axis imaging of the target illuminating laser spot, the single viewing axis nature of the Fig. 2.2(b) proposed optical design allows its use for borehole scenarios such as depicted in Fig. 2.1(b).

For any target plane located at a depth  $h$  from the sensor, the diffraction limited diameter  $2w_{diff}$  of the focussed sampling spot on the target is given by [20]:

$$2w_{diff} = 2.44 \times \lambda \times \left( \frac{F_e}{D_s} \right). \quad (2.1)$$

In a practical scenario, the achievable minimum focused spot size is affected not only by aperture-based diffraction effects but also by aberration effects in the optical system [20-

21]. For instance, a bigger optical aperture at the lens entrance creates a stronger beam spot spreading effect due to spherical aberration in the lens. Aberrations can be counterbalanced either by designing a system of aberration correcting lenses and/or by simply decreasing the input beam diameter. In the proposed design compared to the prior work [12-14], the latter solution as shown in Fig. 2.2(b) has been used where a SF controls the optical aperture  $D_s$ . Note that although decreasing the input beam diameter  $D_s$  reduces aberrations, it also increases diffraction effects that result in a larger diffraction limited beam spot diameter. In a practical scenario, these two effects need to be considered carefully and balanced to achieve the smallest possible focused spot diameter at the target plane.

Fig. 2.2(c) shows the camera design which is based on an imaging lens  $L$  with a focal length of  $F$ , a camera aperture of diameter  $D_A$  and a CMOS sensor chip. The distance from the CMOS sensor to  $L$  is denoted as  $d_i$ , the distance from  $L$  to BS is denoted as  $d_3$  and the distance from BS to the edge of the T/R module is denoted as  $d_2$ .  $h_c$  is defined as the total distance from the target plane to camera lens entrance to i.e.  $h_c = d_3 + d_2 + h$ . In order for the 3-D shape sensor to work for a chosen target depth range, the camera needs to take acceptably sharp images of the target illuminated spot over all these depth values. To ensure this condition, the camera parameters such as  $F$  and  $D_A$  need to be set carefully to allow a sufficient DOF. Section 2.2.1 describes a theoretical overview of the factors affecting the DOF of the camera to select experimental camera parameters for optimal 3-D shape sensing using the proposed system.

## 2.2.1 DERIVATION OF CAMERA DEPTH OF FIELD (DOF)

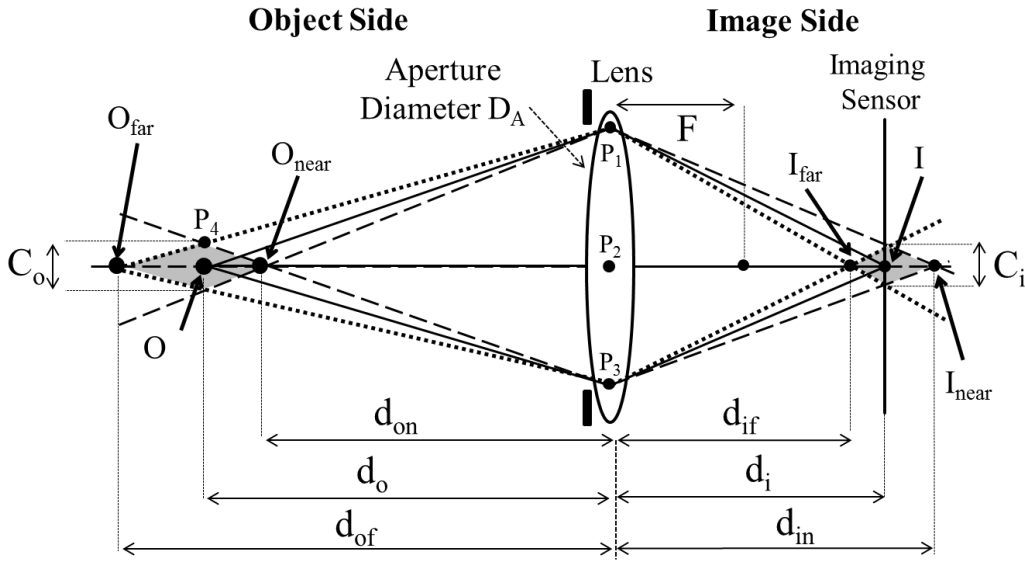


Fig. 2.3. Optical ray diagram of a single lens imaging system illustrating the concept of Depth of Field.

For optimal performance of the shape sensor, an important aspect to consider is the camera design. Specifically, the DOF of the camera needs to cover the measuring range of the 3-D shape sensor. Therefore, in order to choose the appropriate camera parameters, this section involves a derivation of the DOF which will help to determine the experimental camera parameters needed for a desired 3-D shape sensor design. The DOF of camera is defined as the range of distances on the object side over which a focussed image is formed on the imaging CMOS sensor chip. The depth of focus is defined as the range of distances on the image side over which a focused image is formed on the imaging sensor. For the single lens camera system shown in Fig. 2.3, an object  $O$  is perfectly focused onto an imaging sensor to form an image  $I$ . In Fig. 2.3,  $F$  is the lens focal length,  $D_A$  is the lens aperture diameter,  $d_o$  is the lens to object distance and  $d_i$  is the lens to image distance.  $O_{near}$  is the point on the optic axis on the object side representing the near limit of the DOF while  $O_{far}$  is the point on the optic axis on the object side representing the far limit of the DOF.  $I_{far}$  is the point on the optic axis on the image side representing the image of the point  $O_{near}$  while  $I_{near}$  is the point on the optic axis on the image side representing the image of the point  $O_{far}$ . Note that  $d_{on}$  is the lens to  $O_{near}$  distance,  $d_{of}$  is the lens to  $O_{far}$  distance,  $d_{if}$  is the lens to  $I_{far}$  distance and  $d_{in}$  is the lens to  $I_{near}$  distance.  $C_i$  is the permissible diameter of the blur circle formed on the imaging sensor

in order for an object to be considered in focus and  $C_o$  is the corresponding (conjugate) diameter in the object space. The shaded grey region on the object side represents the extent of the DOF and the corresponding depth of focus region on the image side is also shaded in grey.  $P_1, P_2, P_3$  and  $P_4$  are marked points on the diagram to aid the following DOF derivation. For an imaging system, the thin lens equation relating  $F, d_i$  and  $d_o$  is given by [20]:

$$\frac{1}{F} = \frac{1}{d_o} + \frac{1}{d_i}, \quad (2.2)$$

while the transverse magnification  $M_T$  of the camera is [16]:

$$M_T = -\frac{d_i}{d_o}. \quad (2.3)$$

In terms of an object of height  $y_o$  forming an image of height  $y_i$ ,  $M_T$  is:

$$M_T = -\frac{y_i}{y_o}. \quad (2.4)$$

Note that in Eqn. (2.4), both  $y_o$  and  $y_i$  are assumed to be positive when measured upwards from the optic axis. Now,  $C_o$  can be thought of as the object height  $y_o$  as it is measured on the object plane.  $C_i$  can be thought of as the image height  $y_i$  as  $C_i$  is measured on the image plane. Therefore,  $M_T$  can be written as:

$$M_T = -\frac{C_i}{C_o}.$$

Rearranging for  $C_o$  gives:

$$C_o = -\frac{C_i}{M_T}. \quad (2.5)$$

Combing Eqns. (2.3) and (2.5) gives:

$$C_o = \frac{C_i d_o}{d_i}. \quad (2.6)$$

Note that in Eqn. (2.6), the negative sign from Eqn. (2.3) cancels that of Eqn. (2.5). Substituting  $d_i$  from Eqn. (2.2) into Eqn. (2.6) gives:

$$C_o = \frac{C_i d_o}{\left( \frac{F d_o}{d_o - F} \right)},$$

$$C_o = \frac{C_i(d_o - F)}{F}. \quad (2.7)$$

This expression for  $C_o$  will be used later in the derivation.

In Fig. 2.3, note that angle  $\angle P_1\text{-O}_{\text{near}}\text{-P}_2$  is equal to  $\angle P_4\text{-O}_{\text{near}}\text{-O}$ , therefore the following expression is obtained using trigonometry:

$$\frac{C_o}{d_o - d_{on}} = \frac{D_A}{d_{on}}. \quad (2.8)$$

Rearranging the above expression gives:

$$d_{on} = \frac{D_A d_o}{D_A + C_o}. \quad (2.9)$$

Substituting  $C_o$  from Eqn. (2.7) into Eqn. (2.9) gives:

$$d_{on} = \frac{D_A d_o}{D_A + \frac{C_i(d_o - F)}{F}},$$

$$d_{on} = \frac{D_A d_o F}{D_A F + C_i(d_o - F)}. \quad (2.10)$$

Similarly, to derive an expression for  $d_{of}$ , note that angle  $\angle P_1\text{-O}_{\text{far}}\text{-P}_2$  is equal to  $\angle P_4\text{-O}_{\text{far}}\text{-O}$ , therefore the following expression is obtained using trigonometry:

$$\frac{C_o}{d_{of} - d_o} = \frac{D_A}{d_{of}}. \quad (2.11)$$

Rearranging the above expression gives:

$$d_{of} = \frac{D_A d_o}{D_A - C_o}. \quad (2.12)$$

Substituting  $C_o$  from Eqn. (2.7) into Eqn. (2.12), and rearranging, gives:

$$d_{of} = \frac{D_A d_o F}{D_A F - C_i(d_o - F)}. \quad (2.13)$$

Having obtained  $d_{on}$  and  $d_{of}$ , the mathematical expression for DOF can simply be written as:

$$DOF = d_{of} - d_{on}. \quad (2.14)$$

Substituting Eqns. (2.10) and (2.13) into Eqn. (2.14) gives:

$$DOF = \frac{D_A d_o F}{D_A F - C_i (d_o - F)} - \frac{D_A d_o F}{D_A F + C_i (d_o - F)}$$

$$DOF = \frac{2D_A d_o F C_i (d_o - F)}{D_A^2 F^2 - C_i^2 (d_o - F)^2} \quad (2.15)$$

Eqn. (2.15) represents the derived DOF equation which will be used to determine camera parameters needed to set a DOF over the experimental depth range. The next section describes the experimental demonstration of the proposed 3-D shape sensor.

### 2.3 EXPERIMENT

For the experiments performed, the LM along with the collimation optics is excluded from the motorized x-y platform. A 15mW Melles Griot He-Ne laser module having  $\lambda = 633$  nm is used as LM [22]. This laser source irradiates along the x-direction and strikes two mirrors labelled as  $M_1$  and  $M_2$  which are both built-in as part of the motorized platform for this demonstration for beam alignment to allow motorised motion control of the laser scanning head despite LM being excluded from the x-y platform (see Fig. 2.5(a)).  $M_1$  deflects the beam light in the y direction and  $M_2$  directs light towards the z-direction. MO is a Newport model MV-10X having numerical aperture of 0.25 and magnification of 10x, P has a diameter of 15  $\mu$ m, and lens S has 20 cm focal length.  $D_s$  is set to 4 mm which is experimentally determined to give the smallest focussed spot size, balancing out aberration and diffraction effects. The ECVFL used is an Optotune lens model EL-10-30 [23] having lens diameter equal to 10 mm. The ECVFL is current controlled by the PC through its corresponding USB lens driver controller from Optotune. The BS used is a Thorlabs model BS013.  $d_0 = 30$  cm,  $d_1 = 23.2$  mm, and  $d_2 = 55.9$  mm are the settings used in the experiment. The x-y motion, i.e., lateral motion, of the T/R module is obtained using two stepper motors. The driver card for the motors, model P700 from Astrosyn [24], is controlled by a STM32F4 microcontroller from STMicroelectronics [25]. In the x-y plane, the shape sensor, driven by the motor configuration, is designed to cover a transverse region target scan up to a 400 mm by 400 mm area. For the experiments where minor displacements along to x-y plane are required, a translation stage from Newport is used to move the object under test while maintaining the shape sensor head in a static position. In the camera, the sensor chip used is a CMOS sensor from IDS model UI-1250LE-M-GL [26]. The CMOS chip's active sensor area

is  $8.5 \text{ mm} \times 6.4 \text{ mm}$  with a pixel size of  $5.3 \text{ }\mu\text{m}$  and a pixel count of  $1600 \times 1200$  pixels. Given an experimental depth sensing range  $h$  of  $40 \text{ mm}$  adequate to scan 3-D samples in this experiment, the Eqn. (2.15) DOF expression is used to design the camera parameters needed to achieve an acceptable quality of focus within this range. The aperture diameter  $D_A$  of the camera's iris is set to  $2 \text{ mm}$  for the given experimental lighting conditions and target sample surface reflectance properties.  $L$  deployed in the camera is a single standard lens having  $F = 50 \text{ mm}$ . With regards to  $d_o$ , according to Eqn. (2.15), a higher value of  $d_o$  gives a larger DOF but this increases the system size, which is not desirable. Keeping this aspect in mind,  $d_3$  is set to  $7.91 \text{ cm}$ . Thus, using this  $d_3$  and  $d_2 = 5.59 \text{ mm}$ ,  $h_c = 7.91 + 5.69 + h = 13.5 + h$  (units of cm). This means that in terms of  $h_c$ , the desired DOF range of the camera is from  $h_c = 13.5 \text{ cm}$  to  $h_c = 17.5 \text{ cm}$  since the chosen  $h$  range is from  $0 \text{ cm}$  to  $4 \text{ cm}$ . In other words, the desired  $d_{on}$  is  $13.5 \text{ cm}$  and the desired  $d_{of}$  is  $17.5 \text{ cm}$ . In Eqn. (2.15), with  $\text{DOF} = 40 \text{ mm}$ ,  $F = 50 \text{ mm}$  and  $D_A = 2 \text{ mm}$ ,  $d_o$  and  $C_i$  still need to be calculated. With a desired DOF range from  $13.5 \text{ cm}$  to  $17.5 \text{ cm}$ , a starting value of  $d_o$  for Eqn. (2.15) is chosen to be the midpoint of this range, i.e.,  $d_o = 15.5 \text{ cm}$ . This gives a  $C_i$  value of  $0.121 \text{ mm}$ . However, when using  $C_i = 0.121 \text{ mm}$ ,  $F = 50 \text{ mm}$ ,  $D_A = 2 \text{ mm}$  and  $d_o = 15.5 \text{ cm}$ ,  $d_{on}$  is computed using Eqn. (2.10) to be  $13.75 \text{ cm}$  which is larger than our desired  $d_{on}$  of  $13.5 \text{ cm}$ . To bring  $d_{on}$  closer to  $13.5 \text{ cm}$ , different values of  $d_o < 15.5 \text{ cm}$  are iterated over, calculating  $C_i$  and subsequently  $d_{on}$  for each  $d_o$ , until  $d_{on}$  equals  $13.5 \text{ cm}$ . This occurs when  $d_o = 15.24 \text{ cm}$  giving a  $C_i = 0.126 \text{ mm}$ .



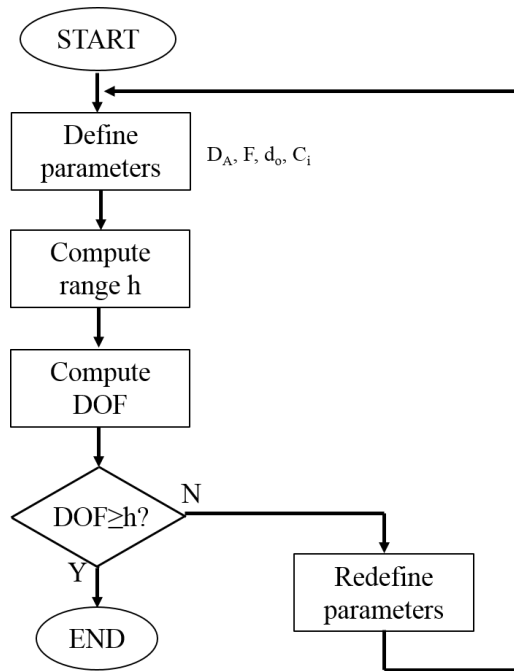


Fig. 2.4. Flow chart diagram that shows the relationship between the designed working range  $h$  and the DOF.

In Fig. 2.4 is shown a flow chart diagram that summarizes the operations that are involved for the correct evaluations of the parameters so far described. To summarize, using  $D_A = 2 \text{ mm}$  and  $F = 50 \text{ mm}$ , a DOF of  $40 \text{ mm}$  is achieved between  $h = 0 \text{ mm}$  to  $h = 40 \text{ mm}$  (same as  $h_c = 13.5 \text{ cm}$  to  $h_c = 17.5 \text{ cm}$ ) only when the permissible diameter of the blur circle  $C_i$  is taken as  $0.126 \text{ mm}$ . A  $C_i$  of  $0.126 \text{ mm}$  means that at the periphery of the chosen depth sensing range, i.e., closer to  $h = 0 \text{ mm}$  and  $h = 40 \text{ mm}$ , the image of a focussed point spot on the target can be as large as  $0.126 \text{ mm}$  and still be considered an acceptably focussed image. From the 3-D shape sensor operation point of view, the system is robust to this high value of  $C_i$  since the image processing relies on the relative change seen in spot size for different values of ECVFL current. The system does not rely on the absolute size of the spot's image formed on the CMOS, thereby allowing an extended DOF for 3-D shape sensing applications.

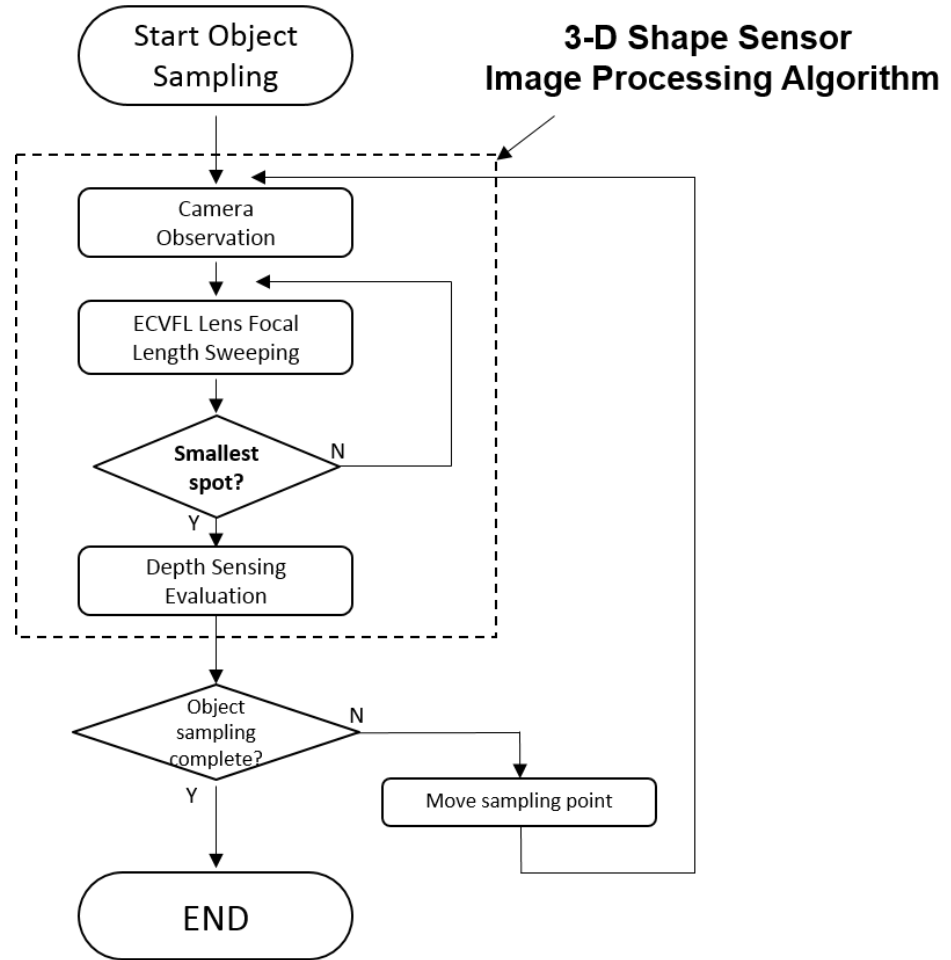
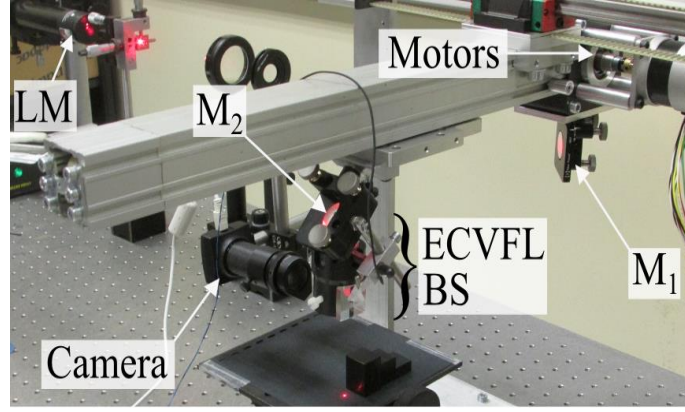
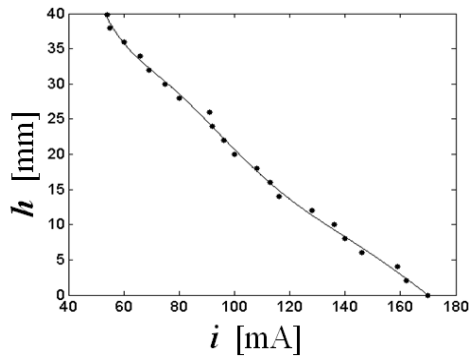


Fig. 2.5. Flow chart diagram illustrating the sequential steps of the proposed 3-D shape sensor, highlighting the steps implemented in the imaging processing algorithm.

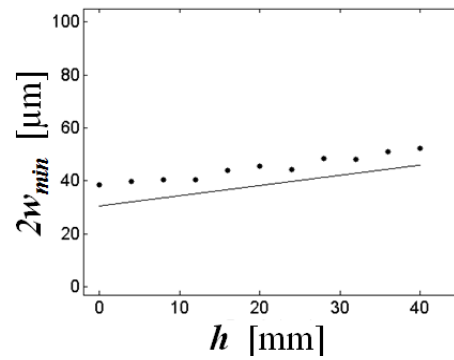
Moreover, to automate the system, a Graphic User Interface (GUI), developed in C++/CLI language, controls the camera in real-time, ECVFL current (hence focal length), x-y motorized stage and the synchronization of the components. The GUI is also responsible for the image processing part of the depth sensing routine. The spot diameter (in pixels) of the captured image is found by transforming the image captured into a two-level binary image (1 bit per depth) and counting the number of white pixels above a certain intensity threshold. The result of the counting routine is proportional to the spot size. Therefore, the optimum  $F_e$  value corresponding to the smallest spot size allows depth information recovery by consulting the calibration curve obtained during the training phase of the system. The aforementioned operations are all summarized in Fig. 2.5.



(a)



(b)



(c)

Fig. 2.6. (a) Laboratory setup of the proposed 3-D shape sensor including the mirrors  $M_1$  and  $M_2$  deployed for beam alignment, (b) experimental 3-D sensor depth  $h$  calibration data versus ECVFL drive current values  $i$  for the designed 40 mm depth measurement range, and (c) 3-D shape sensor x-y transverse resolution calibration curve for spot diameter  $2w_{min}$  versus depth  $h$  values obtained during the sensor calibration phase. A comparison between experimental (dots) and theoretical (line) values is shown.

The Fig. 2.2(b) design is experimentally implemented in the laboratory facility as shown in Fig. 2.6(a). Since  $F_e$  and current  $i$  values are proportional, the calibration curve obtained in the training phase is shown in Fig. 2.6(b) which plots depth  $h$  versus current  $i$ . Given the experimentally chosen  $h$  range of 40 mm, the theoretical diffraction limited spot diameter  $2w_{diff}$  derived from Eqn. (2.1) is plotted versus depth  $h$  and shown as a solid curve in Fig. 2.6(c). Figure 2.6(c) also shows the experimental x-y transverse resolution data of the 3-D shape sensor obtained by placing the CMOS sensor chip on the target plane and then implementing image processing on the CMOS sensor chip provided beam spot pattern.

To assess the transverse resolution performance of the demonstrated shape sensor, the data sheet of a commercially available micro-epsilon model ILD 1700-40 triangulation-based sensor with a similar depth range is studied. This micro-epsilon sensor provides a spot

diameter of no less than  $210\ \mu\text{m}$  in the  $40\ \text{mm}$  operational range [27]. Therefore, in terms of the transverse resolution, the demonstrated shape sensor has a spot diameter that is approximately four times smaller than the micro-epsilon triangulation sensor.

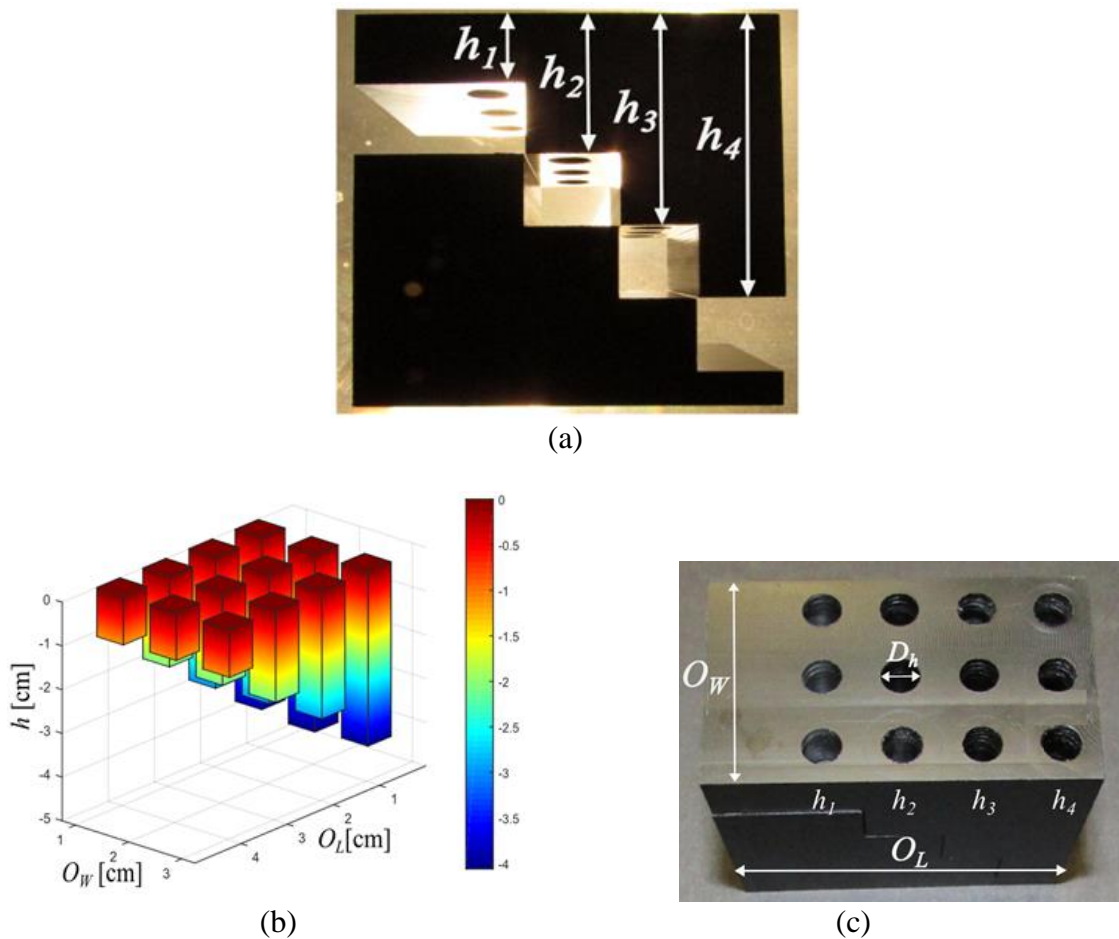


Fig. 2.7. (a) Side view of the custom-made boreholes solid block that is assembled by stacking two separate blocks, (b) top view of the assembled boreholes solid block, and (c) solid block 3-D borehole depth reconstructions using the proposed ECVFL-based sensor.

To demonstrate the versatility of the calibrated shape sensor, three types of shape sensing experiments are performed. As illustrated in Fig. 2.2(a), the proposed sensor is first used to map the depths of the sample with multiple boreholes. Figure 2.7(a) shows the solid block sample obtained by joining two custom delrin material made parts having matte dark surfaces. The two separated block 3-D sample design allows one to check that the borehole bases are flat and a vernier caliper can be used to measure borehole depths. Note that in this experiment, the vernier caliper is used as a reference for subsequent 3-D shape sensor

measurement data. Figure 2.7(b) shows the solid block hole structure which is organized in a  $3 \times 4$  matrix where the 4 depths columns are labelled as  $h_1$ ,  $h_2$ ,  $h_3$ , and  $h_4$ . For calibration purposes, the 2 parts of the block are separated and depths are measured with a vernier caliper, giving the depth values shown in Table 2.1. For each borehole, the diameter  $D_h$  is equal to 5 mm and the distance between each neighbouring hole center is 10 mm. Note that for each hole in the block, a single point scan at the center of the hole is performed using the proposed 3-D shape sensor and the corresponding measured depth values are presented and compared with the calliper measured depth values in Table 2.1. As shown in Table 2.1, the measured depth values are close to the reference vernier readings. More precisely, Table 2.1 includes the mean measurement error (in mm) of the measurements compared to the vernier readings which are 0.84 mm, 0.58 mm, 0.44 mm and 0.50 for depth columns  $h_1$ ,  $h_2$ ,  $h_3$  and  $h_4$ , respectively.

These mean errors are all within  $\pm 0.5$  mm of the corresponding vernier depth values. For each column depth  $h_1$ ,  $h_2$ ,  $h_3$  and  $h_4$ , the 95 % confidence interval of the true mean depth value is calculated using the statistical t-test [28] and presented in Table 2.1. The average error of the system (in mm) is the average of the individual mean measurement errors of the depth columns, which is 0.59 mm having a standard deviation of 0.17 mm. To evaluate the mean percentage error of the system, each of these mean measurement error values (in mm) are divided by its corresponding vernier reading and multiplied by 100. This gives a percentage error for each depth columns  $h_1$ ,  $h_2$ ,  $h_3$  and  $h_4$ . The mean percentage error of the system is the mean of these individual percentage errors, which is approximately  $\pm 3\%$  when compared to measurements from the vernier caliper. Fig. 2.7(c) shows the 3-D view of the reconstructed solid block holes depth map.

Table 2.1. Experimental solid block borehole depth values obtained with the proposed 3-D shape sensor and a vernier caliper. When using the shape sensor, one measurement is taken for each hole approximately at its base centre point.

	$h_1$ [mm]	$h_2$ [mm]	$h_3$ [mm]	$h_4$ [mm]
<b>Vernier Caliper</b>	10.16±0.01	20.32±0.22	30.06±0.05	40.18±0.063
<b>3-D Shape Sensor</b>	11.20 10.90 10.90	20.70 21.00 21.00	30.01 29.62 29.24	39.32 40.60 39.95
<b>Mean Measurement Error</b>	+0.84	+0.58	-0.43	-0.50
<b>Mean</b>	11	20.9	29.62	39.95
<b>95% Confidence Interval via t-test</b>	11±0.42	20.9±0.42	29.62±0.94	39.95±1.58

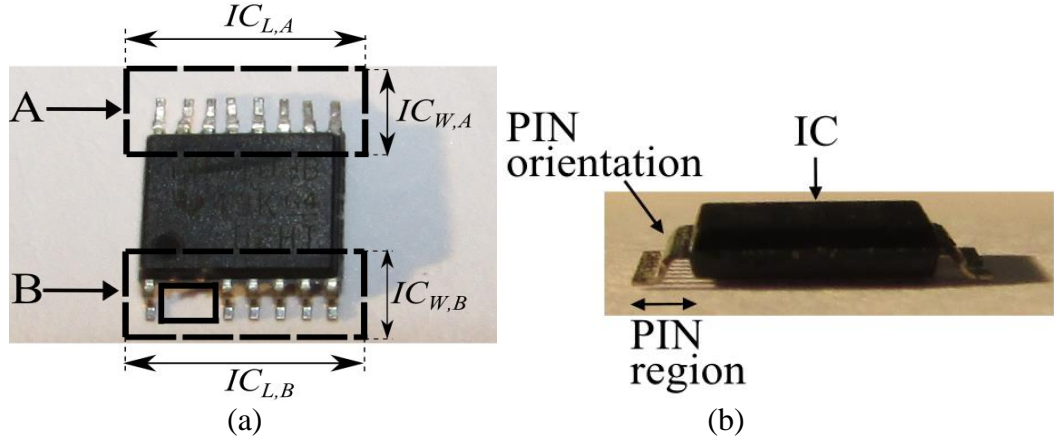


Fig. 2.8. (a) Top view of the TSSOP IC package with scanned regions A and B. Region B has two pins removed, and (b) side view of the TSSOP IC package. Notice the pin angular orientation on the highlighted pin region.

The next experiment emphasizes the 3-D shape sensor's high transverse resolution. The proposed 3-D shape sensor is used as a position sensing sensor to verify pin position in an IC having a TSSOP package shown in Fig. 2.8(a) and in Fig. 2.8(b). The IC is placed at a depth value of  $h=0$  mm and a top view inspection of the two zones marked as A and B shown in Fig. 2.8(a) is performed using a fixed focused beam having  $40\ \mu\text{m}$  spot diameter. The IC package dimensions are  $(5\pm 0.1)\ \text{mm} \times (6.4\pm 0.2)\ \text{mm}$  on which the pin width is  $245\pm 55\ \mu\text{m}$  and each pin is separated by  $650\ \mu\text{m}$ . The scanned area considered is limited by the line segments  $IC_{L,A}=IC_{L,B}=5.4\ \text{mm}$  and  $IC_{W,A}=IC_{W,B}=1.5\ \text{mm}$  for the two zones A and B. The scan motion is implemented using an x-y translation stage with a step resolution of  $50\ \mu\text{m}$ . The 3-D shape sensor returns the IC intensity map representing the scattered light produced when the laser light strikes the IC. A strong scattered laser spot captured by the camera indicates to the PC software the presence of a metallic pin. To simulate a faulty side, two pins from the IC were removed in the B zone.

Figure 2.9(a) and Fig. 2.9(b) illustrate the results obtained when scanning the A and B zones for a normal and a faulty IC side, respectively. Note that due to the incline pin orientation as shown in Fig. 2.8(b), the intensity map in Fig. 2.9(a) and Fig. 2.9(b) has light starved areas because pin reflected light is not caught by the camera. Figure 2.9(c) and Fig. 2.9(d) are 1-D cross section plots of Fig. 2.9(a) and Fig. 2.9(b), respectively. Both cross-sections in Fig. 2.9(c) and Fig. 2.9(d) are taken at  $IC_{W,B} = 350\ \mu\text{m}$  in the context of Figs. 2.9(a) and 2.9(b), respectively. The two missing pins in zone B of Fig. 2.8(a) are clearly distinguished by the absence of peaks in Fig. 2.9(d). This type of plot is helpful in automated

processing routines where pin verification can be performed by looking at the presence or absence of peaks.

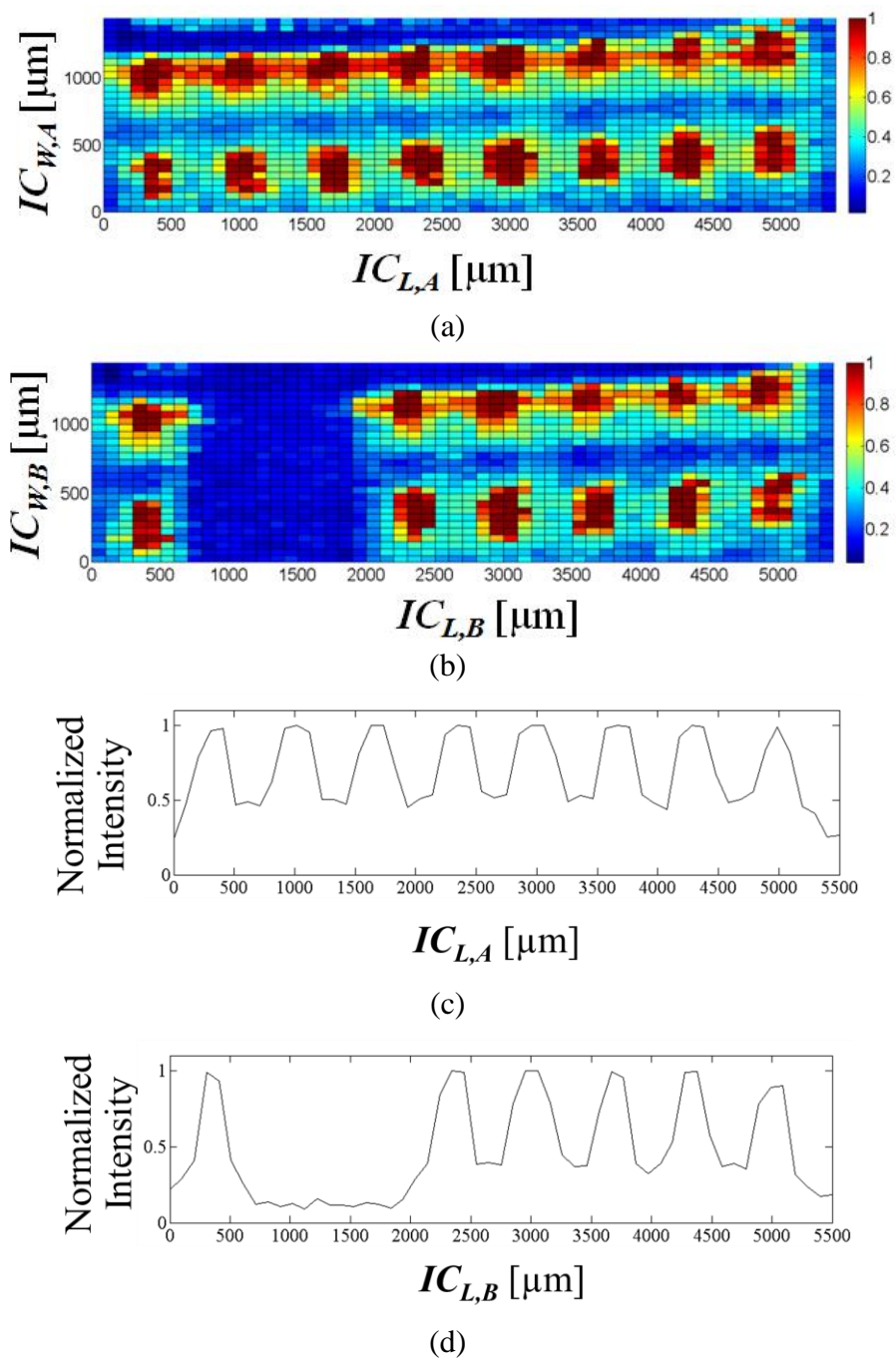


Fig. 2.9. (a) 2-D optical intensity map obtained for the A region of the TSSOP IC using the proposed ECVFL-based sensor, (b) 2-D optical intensity map obtained for the B region of the TSSOP IC using the proposed ECVFL-based sensor, (c) 1-D normalized intensity plot for zone A of the IC component obtained using the proposed ECVFL-based sensor showing the presence of all pins, and (d) 1-D normalized intensity plot for zone B of the IC component obtained using the proposed ECVFL-based sensor showing the locations of the two missing pins.



Next, the proposed 3-D shape sensor is deployed to generate a complete 3-D point cloud map of a Fokker aircraft part having volumetric containment dimensions of  $35\text{ cm} \times 8\text{ cm} \times 4\text{ cm}$ . This 3-D part has conformal non-uniform surfaces making standard contact measurement techniques unusable for 3-D mapping. The aircraft part shape acquisition is experimentally carried out by utilizing a motorized stage covering an area  $O_W=32\text{ cm}$  by  $O_L=4\text{ cm}$  in the x-y plane with a step side resolution of  $5\text{ mm}$  for a total of 504 points in the 3-D point cloud. As shown in Fig. 2.10(a), the part surface varies from being mostly flat in the middle region to having two asymmetric slopes on the sides. Figure 2.10(b) shows the point cloud map obtained for the scanned aircraft part under test via the proposed shape sensor revealing the non-uniform surface regions optimized for aerodynamic air flow operations. Figure 2.10(c) shows a 1-D plot of  $h$  versus  $O_L$  across the Fig. 2.10(a) aircraft part. 1-D traces such as Fig. 2.10(c) can be used as a quick inspection check for locating defects in shape profiles before carrying out a detailed 2-D scan. In order to obtain a  $360^\circ$  FOV coverage 3-D point cloud of a generic 3-D part, independent 3-D point clouds using different Field of Views (FOVs) must be acquired. These different point cloud datasets must be combined via software to obtain the complete 3-D object point cloud.

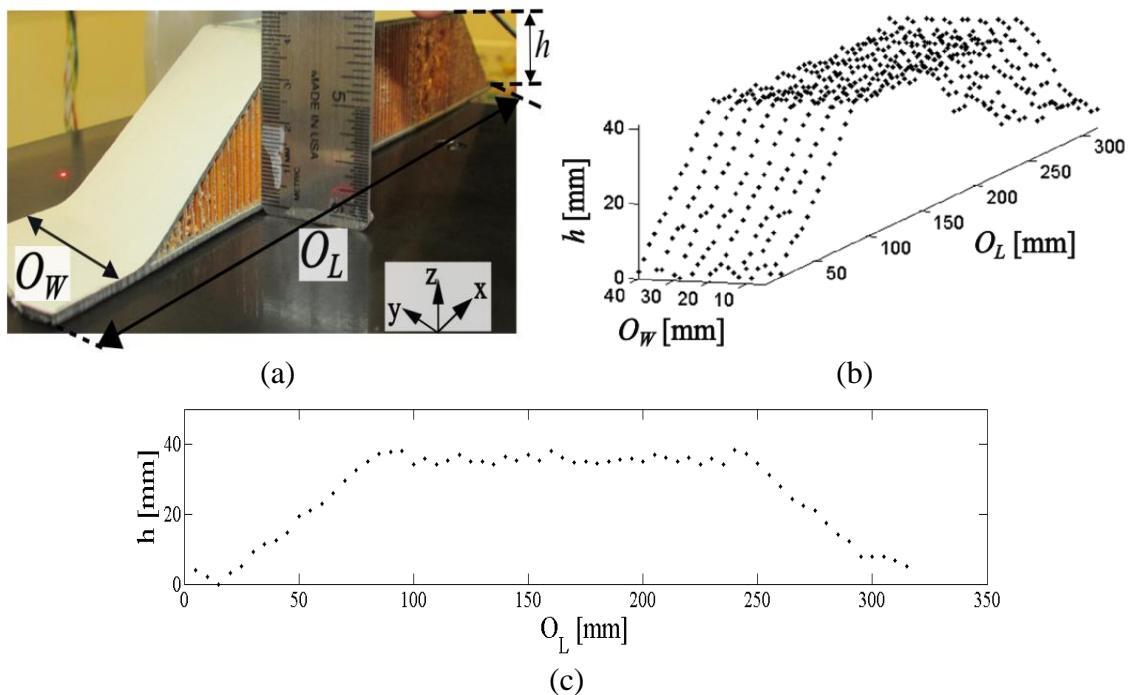


Fig. 2.10. (a) Fokker aircraft part used in the 3-D shape sensing experiment, (b) 3-D point cloud map of the Fokker aircraft part obtained using the proposed 3-D shape sensor, and (c) 1-D plot of  $h$  versus  $O_L$ , outlining the shape profile of the aircraft part shown in (a).

Note that the shape mapping time of the proposed shape sensor varies according to the application requirements. The scan area and the x-y step resolution are application specific factors which influence the time needed to complete the shape reconstruction process. Other factors include ECVFL response time, image processing algorithm efficiency and camera image acquisition time. For the Optotune ECVFL deployed in the experiment, it is recommended to permit a settling time of a minimum 15 ms for every new focal length value. Therefore, by considering 200 mA current range and using a 1 mA step, the time required to complete the current sweep in the ECVFL is 3 seconds. Since real-time image processing is involved for each acquired optical image of the scan laser spot, 10 seconds are required to scan a single depth value in the described experimental demonstrations. The total scan time can be optimized by using ultra-fast scanning technology. For example, the programmable high-speed Polarization Multiplexed Optical Scanner (PMOS) lens [29] having a reset time of a few microseconds (in the visible spectrum) can be deployed in conjunction with any other ECVFL device, such as the Varioptic Lenses having a 7.5 ms reset time [30], Optotune EL-10-30 having a 15 ms reset time [23] or the TAG Lens 2.0 [31] by TAG Optics having a 20  $\mu$ s response time. To estimate a single depth scan time for a system made up of a combination of the PMOS lens and the TAG Lens 2.0, assuming 20 different focal length settings are needed to evaluate the depth, a single scan point takes approximately 1 ms with this 1 ms including the time needed for efficient image processing. Coupled with high speed scanning mirror technology, for example, the excelliSCAN mirror from ScanLab [32] having a 280  $\mu$ s positioning time, a 50x50 resolution scan takes less than 2.5 seconds. In addition, compressive sensing techniques [33] can be deployed using the proposed 3-D shape sensor for sparse sampling zones to further reduce scan times and scan resolution required for adequate shape reconstruction. Furthermore, use of a laser line source rather than a laser point sampling tip for 3-D shape reconstruction can introduce parallel optical and electronic processing and can greatly reduce total scan time.

For example, Fig. 2.11(a) shows a proposed laser line source-based 3-D shape sensor. The single line is scanned across the 3-D target to acquire multiple 2-D point clouds that are stitched together to form a 3-D point cloud. Note that for faster data generation, multiple such line-based 3-D shape sensors can be combined to form a multi-line 3-D shape sensor. Furthermore, Fig. 2.9(b) shows an inter-line shift method that can be applied to produce a high resolution 3-D point cloud. In this method, all lines are shifted to multiple locations between a line pitch interval to acquire 3-D point clouds that are combined to produce a high spatial resolution 3-D point cloud data set.

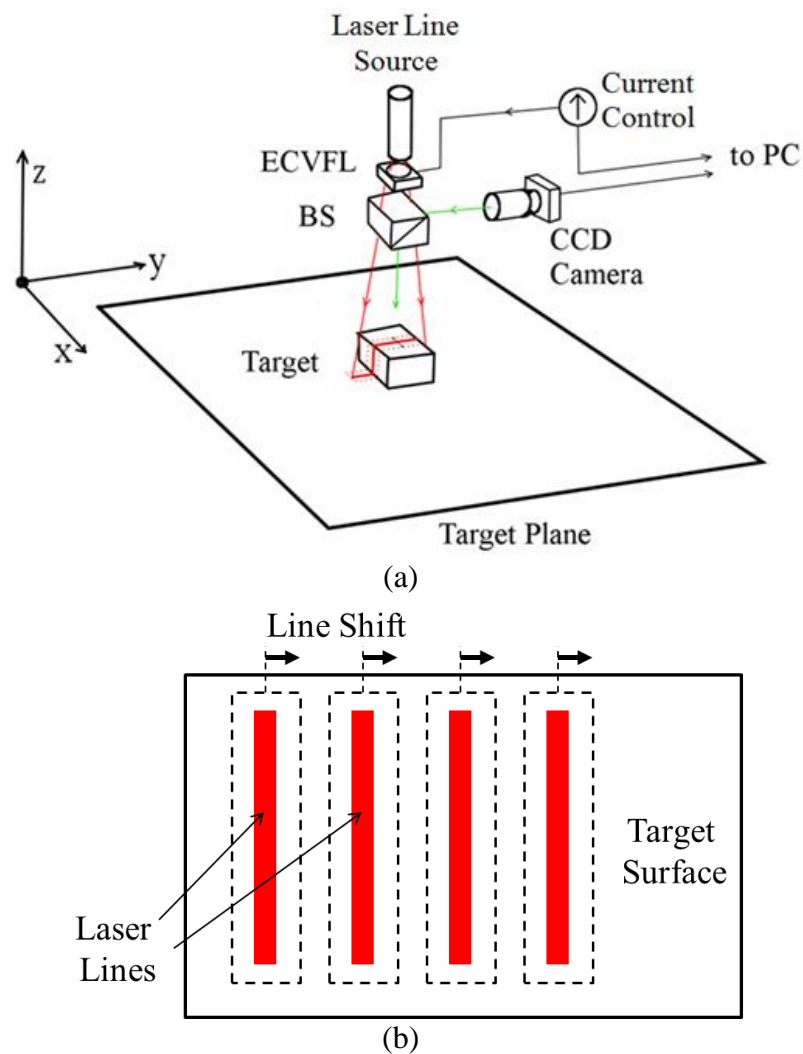


Fig. 2.11. (a) Proposed laser line source-based 3-D shape sensor optical design, and (b) top view of a laser line pattern with 4 lines illuminating a target for the proposed ECVFL-based 3-D shape sensor.

Note that all distance sensors such as OCT [12], chromatic confocal [14] and WLI [11] have measurement uncertainties. Given that every system is different, a number of factors affect a system's performance, e.g., OCT is sensitive to laser coherence stability and ToF is sensitive to timing jitter in hardware. For the proposed sensor experiment, there are also various sources of measurement uncertainty. Commercial ECVFLs such as Optotune EL-10-30 containing optical fluids are affected by temperature changes, which result in the focal length versus drive current calibration curves to vary over time. The axial resolution of the 3-D shape sensor is affected by a number of parameters. Fundamentally, it is limited by the by  $\lambda/4$  Rayleigh criterion based focal depth resolution. However, the finite-sized current step of the ECVFL, the difficulty of camera image-processing algorithms to identify the image containing the smallest spot and the drifting of the ECVFL calibration curve over time affect measurement uncertainty. To reduce measurement uncertainties, both hardware and software robustness need to be developed. However, also note that the proposed 3-D shape sensor acquires each depth value for a focal length setting which focusses the beam to the smallest possible diffraction limited (and aberration reduced) sampling tip over the complete depth range, i.e., at every depth location, the sampling spot that used is the smallest possible. Prior-art 3-D sensors do not provide this capability over the 4 cm depth range demonstrated for the proposed sensor.

The proposed 3-D shape sensor can be optimised for targets having varying degrees of optical reflectivity. For example, smooth target surfaces result in minimal scattering of the target illuminating laser spot. Difficulty in viewing laser spots striking such surfaces can be overcome by increasing the optical irradiance sensitivity parameter of the deployed camera sensor. Furthermore, noting that the sensor takes depth readings corresponding to the smallest focussed spot incident on the target, the high optical power density as well as spatial frequency spectrum of the focussed beam spot increases optical scattering [34], thereby increasing the spot's likelihood of being imaged by a sensitive camera.

## **2.4 CONCLUSION**

In conclusion, the design of a novel 3-D shape sensor having high transverse resolution, single viewing axis and computer controlled 3-D spatial scanning is proposed and successfully demonstrated. Due to its unique in-line single view point design, and high transverse sampling resolution enabled by variable aperture-based input beam diameter control of focusing beam and ECVFL-based beam focus/defocus control, the proposed shape sensor is suitable for a variety of applications from 1-D borehole depth reconstruction to 2-D high resolution imaging to 3-D complex object reconstruction. This versatility and adaptability to different scenarios makes the proposed 3-D shape sensor an all-in-one device for micro-scale to macro-scale sensing applications. The use of a single laser spot for spatial sampling limits the operational speed of the proposed sensor and smart programming of scan regions is required to reduce scan times based on the user's specific needs. Future work involves using a laser line source instead of a single laser point to introduce parallel processing and decrease shape sensing processing time.

## REFERENCES

- [1] Son, H. Park and K. H. Lee, "Automated laser scanning system for reverse engineering and inspection," *International Journal of Machine Tools and Manufacture*, vol. 42, no. 8, pp. 889-897, (2002).
- [2] R. Usamentiaga, J. Molleda and D. F. García, "Fast and robust laser stripe extraction for 3D reconstruction in industrial environments," *Machine Vision and Applications*, vol. 23, no. 1, pp. 179-196, (2012).
- [3] M. Levoy, K. Pulli, B. Curless, S. Rusinkiewicz, D. Koller, L. Pereira, M. Ginzton, S. Anderson, J. Davis, J. Ginsberg, J. Shade and D. Fulk, "The digital Michelangelo project: 3D scanning of large statues," in *Proceedings of the 27th Annual Conference on Computer Graphics and Interactive Techniques (SIGGRAPH '00)*, pp. 131-144, (2000).
- [4] J. Smisek, M. Jancosek and T. Pajdla, "3D with Kinect," *Computer Vision Workshops (ICCV Workshops), 2011 IEEE International Conference*, pp.1154-1160, (2011).
- [5] S. Zhang, "Recent progresses on real-time 3D shape measurement using digital fringe projection techniques," *Optics and Lasers in Engineering*, vol. 48, no. 2, pp. 149-158, (2010).
- [6] G. Häusler and F. Willomitzer, "A stroll through 3D imaging and measurement," *ICO Newsletter*, no. 104, (2014).
- [7] E. Stoykova, A. Alatan, P. Benzie, N. Grammalidis, S. Malassiotis, J. Ostermann, S. Piekh, V. Sainov, C. Theobalt, T. Thevar and X. Zabulis, "3-D time-varying scene capture technologies - A survey," *IEEE Transactions on Circuits and Systems for Video Technology*, vol. 17, no. 11, pp. 1568-1586, (2007).
- [8] V. Lombardoa, T. Marzullib, C. Pappalettereb and P. Sforzaa, "A time-of-scan laser triangulation technique for distance measurements," *Optics and Lasers in Engineering*, vol. 39, no. 2, pp. 247-254, (2003).
- [9] R. Anchini, G. Di Leo, C. Liguori and A. Paolillo, "A new calibration procedure for 3-D shape measurement system based on phase-shifting projected fringe profilometry," *IEEE Transactions on Instrumentation and Measurement*, vol. 58, no. 5, pp. 1291-1298, (2009).
- [10] J. Roels, W. Van der Tempel, D. Van Nieuwenhove, R. Grootjans, M. Kuijk, D. Van Thourhout and R. G. Baets, "Continuous Time-of-Flight ranging using a MEMS

- diffractive subwavelength period grating (de)modulator,” *IEEE Photonics Technology Letters*, vol. 20, no. 22, pp. 1827-1829, (2008).
- [11] J. C. Wyant, “White light interferometry,” *Holography: A Tribute to Yuri Denisyuk and Emmett Leith*, SPIE Proceedings, vol. 4737, pp. 98-107, (2002).
- [12] S-W. Lee, H-W. Jeong, B-M. Kim, Y-C. Ahn, W. Jung and Z. Chen, “Optimization for axial resolution, depth range, and sensitivity of spectral domain optical coherence tomography at 1.3  $\mu\text{m}$ ,” *Journal of the Korean Physical Society*, vol. 55, no. 6, pp. 2354-2360, (2009).
- [13] R.Przybyla, I. Izyumin, M. Kline, B. Boser and S. Shelton, “An ultrasonic rangefinder based on an AlN piezoelectric micromachined ultrasound transducer,” *IEEE Sensors Journal*, pp.2417-2421, (2010).
- [14] H. J. Tiziani and H.-M. Uhde, “Three-dimensional image sensing by chromatic confocal microscopy,” *Applied Optics*, vol. 33, no. 10, (1994).
- [15] Chromatic Confocal Point Sensor Systems, Edmund Optics Inc., USA. URL: <https://www.edmundoptics.com/document/download/396298> (visited on 03/10/2017).
- [16] N. A. Riza and S. A. Reza, “Non-contact distance sensor using spatial signal processing,” *Optics Letters*, vol. 34, no. 4, pp. 434-436, (2009).
- [17] N. A. Riza and S. A. Reza, “Smart agile lens remote optical sensor for three-dimensional object shape measurements,” *Applied Optics*, vol. 49, no. 77, pp. 1139-1150, (2010).
- [18] M. J. Amin and N. A. Riza, “Smart laser scanning sampling head design for image acquisition applications,” *Applied Optics*, vol. 52, no. 20, pp. 4991-4996, (2013).
- [19] N. A. Riza, *Photonics signals and systems: An introduction*, McGraw-Hill, (2013).
- [20] E. Hecht, *Optics (4th Edition)*, Pearson Addison-Wesley, (2002).
- [21] M. Born and E. Wolf, *Principles of optics (7th Edition)*, Cambridge University Press, Cambridge, (1999).
- [22] He-Ne Laser Model 05-LHP-991 datasheet, Melles Griot, USA. Datasheet URL: [https://www.global-optosigma.com/en/page\\_pdf/05-LPL.pdf](https://www.global-optosigma.com/en/page_pdf/05-LPL.pdf) (visited on 03/10/2017).
- [23] EL-10-30 datasheet, Optotune, Switzerland. Product description available at URL: <http://www.optotune.com/products/focus-tunable-lenses?task=view&id=97> (visited on 03/10/2017).
- [24] Astrosyn P700 datasheet, England, URL: <http://www.astrosyn.com/p700-stepper-motor-drive-technical-datasheet> (visited on 03/10/2017).

- [25] STM32D4, Discovery Evaluation Board, Switzerland, STMicroelectronics, URL: <http://www.st.com/en/evaluation-tools/stm32f4discovery.html> (visited on 03/10/2017).
- [26] IDS  $\mu$ Eye LE camera datasheet, IDS, Germany. Product description available at URL: <https://en.ids-imaging.com/store/products/cameras/usb-2-0-cameras/ueye-le.html> (visited on 03/10/2017).
- [27] Laser Triangulation Displacement Sensors, OptoNCTD, ILD 1700-40, Micro-Epsilon, Germany. Product description available at URL: <http://www.micro-epsilon.com/download/manuals/man--optoNCDT-1700--en.pdf> (visited on 03/10/2017).
- [28] W. D. Zimmerman, "A note on interpretation of the paired-samples T Test," *Journal of Educational and Behavioral Statistics*, vol. 22, no. 3, pp. 349-360, (1997).
- [29] N. A. Riza and S. A. Khan, "Programmable high-speed polarization multiplexed optical scanner," *Optics Letters*, vol. 28, no. 7, pp. 561-563, (2003).
- [30] B. Burger, S. C. Meimon, C. Petit and M. Chau Nguyen, "Improvement of varioptic's liquid lens based on electrowetting: how to obtain a short response time and its application in the design of a high resolution iris biometric system," *Proceedings SPIE 9375, MOEMS and Miniaturized Systems XIV, 93750S*, (2015).
- [31] TAG Lens 2.0 datasheet, TAG Optics Inc, P.O. Box 1572, Princeton, NJ, USA. Product description available at URL: <http://www.tag-optics.com/TL2ProductLine.php> (visited on 03/10/2017).
- [32] excelliSCAN datasheet, SCANLAB AG, Germany. Product description available at URL: <http://www.scanlab.de/en/products/scan-systems/excelliscan> (visited on 03/10/2017).
- [33] E. J. Candes, J. Romberg, and T. Tao, "Robust uncertainty principles: exact signal reconstruction from highly incomplete frequency information," *IEEE Transactions on Information Theory*, vol. 52, no. 2, pp.489-509, (2006).
- [34] N. M. Lawandy, R. M. Balachandran, A. S. L. Gomes and E. Sauvain, "Laser action in strongly scattering media," *Nature*, vol. 368, pp. 436-438, (1994).





## CHAPTER 3

### SMART OPTICAL SHAPE SENSOR USING ELECTRONICALLY CONTROLLED LENS AND LASER LINE ILLUMINATION SCANNING<sup>2</sup>

#### 3.1 INTRODUCTION

Light-based provides 3-D shape sensing with high spatial resolution and remote access with minimal physical contact affects. Applications for optical 3-D sensors include industrial manufacturing, cultural heritage preservation, medical and aerospace inspection, tracking systems, and position sensing [1-9]. Optical 3-D shape sensors have advantages and disadvantages based on particular application scenarios [10, 11]. Over the years, we have proposed and demonstrated the use of the ECVFL for several applications ranging from distance measurement [12-15], surface profiling [16], biological microscopy [17], vision testing [18], optical wireless [19], microwave signal processing [20], fibre-optic attenuation [21], laser beam analysis [22], optical beam steering [23], and others [24]. Specifically, in [15] it is introduced and demonstrated an ECVFL-based 3-D optical shape sensor that used laser point scanning to 3-D map objects with irregularities in shape that are difficult to measure using common shape sensor techniques. A feature of the ECVFL-based method is its optimized high transverse resolution for all target depths as well as the use of low temporal bandwidth signal processing (i.e., avoids high temporal bandwidth processing needed in laser radar-based distance sensing). However, the shape sensor described in [15] is limited in speed as it is based on laser point scanning to map an object 3-D shape contour. To improve the proposed optical shape sensor speed, in this chapter we propose and demonstrate a novel optical 3-D shape sensor design that combines the ECVFL with a scanning laser line illumination used along with line thickness measurement image processing. This single viewing optical axis sensor is designed to provide a high transverse resolution for all the target distance values within the sensor working depth range. This chapter describes the basic

---

<sup>2</sup> J. P. La Torre, B. Bornemann, and N. A. Riza, "Smart optical shape sensor using electronically controlled lens and laser line illumination scanning," *IEEE Sensors Journal*, vol. 17, no. 4, pp. 1005-1012, (2016).

principles of the proposed sensor, showcasing experimental results that demonstrates the improved sensor performance including a faster speed of operation.

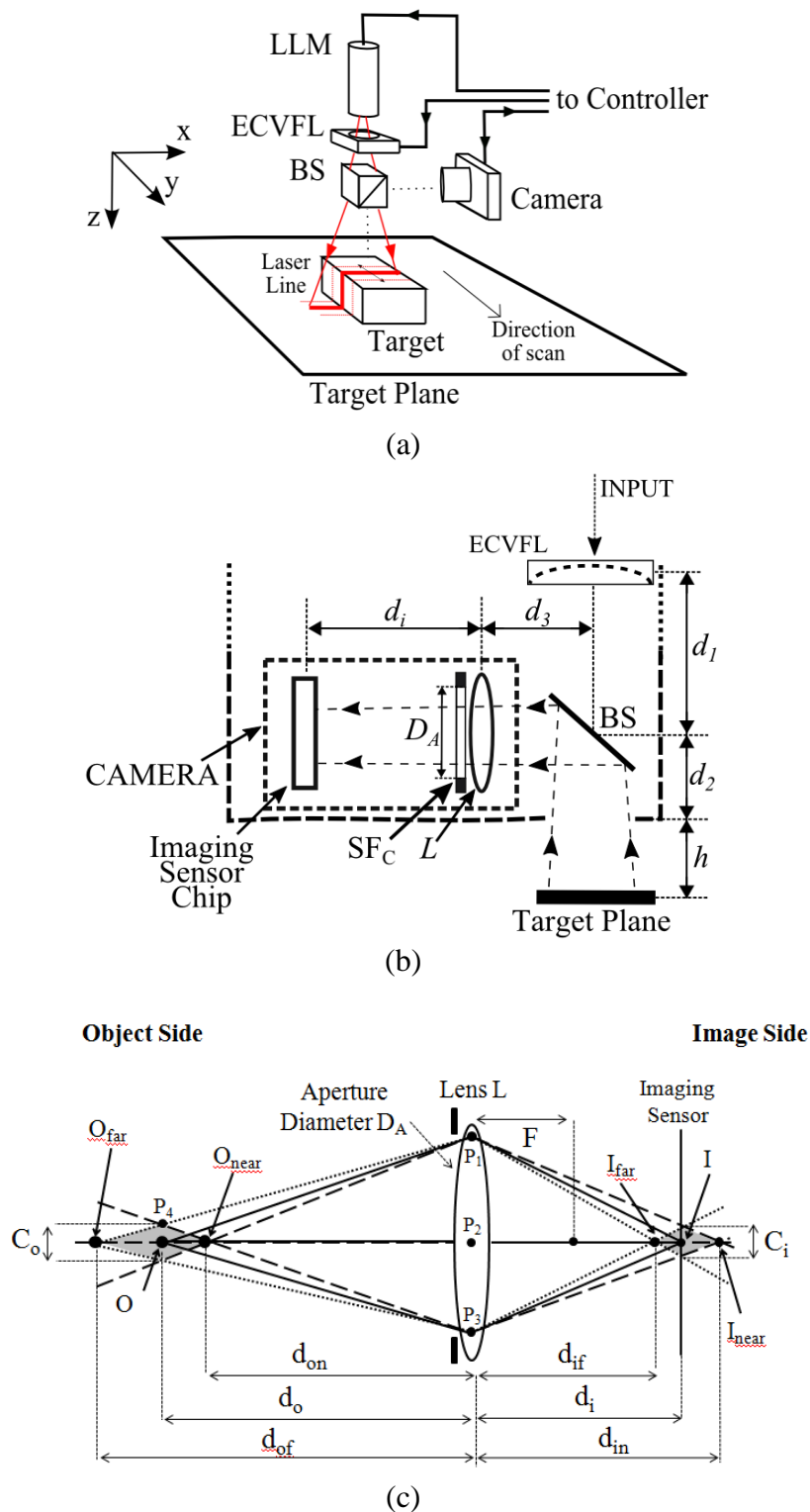


Fig. 3.1. (a) Proposed optical design of a single viewing axis laser line illumination based 3-D shape sensor. (b) Proposed camera module design used for image acquisition. (c) Camera module optical ray diagram.

### 3.2 PROPOSED LASER LINE BASED 3-D SHAPE SENSOR DESIGN

Figure 3.1(a) shows the proposed 3-D shape that uses a laser line module (LLM) as the light source. The LLM arrangement contains a point laser source (diode) and a cylindrical lens of focal length  $F_c$  that is responsible for focussing the laser light along one dimension (e.g., transverse y-direction) in free-space to form a line illumination along the x-direction. This laser line illumination propagates along the z-direction. The light from the LLM passes through the ECVFL having an electronically controlled focal length  $F_e$ . Next, the light after the ECVFL travels through a Beam Splitter (BS) which divides the light optical path into two directions namely, the x-direction and the z-direction. Light along the z-direction propagates to strike the target object. The line shaped illumination falling over the target object is imaged by an on-axis camera module through the BS. The sensor is calibrated to work over a working distance defined as  $h_R$ . The LLM, ECVFL and camera module are mounted on an x-y motion motorized stage, with all these components interfaced to a Personal Computer (PC) having dedicated software for the sensor controls. In our prior works, a single laser spot was used as the sensing probe [12-15]. Using the same basic principle of light focusing for a line illumination, the width diameter  $2w_{diff}$  of the line illumination on the target plane is given by [14, 25]:

$$2w_{diff} = 2.44 \times \lambda \times \left( \frac{F_e}{D_c} \right), \quad (3.1)$$

where  $\lambda$  is the laser source wavelength and  $D_c$  is the input beam diameter at the entrance of the cylindrical lens. As the ECVFL with the LLM cylindrical lens forms a two-lens imaging system, its net focal length  $F_{net}$  is given by [14,26]:

$$\frac{1}{F_{net}} = \frac{1}{F_e} + \frac{1}{F_c} - \frac{d_s}{F_e F_c}, \quad (3.2)$$

where  $d_s$  is the distance between the ECVFL and the LLM cylindrical lens. The  $2w_{diff}$  value dictates the 3-D sensing transverse resolution  $\Delta y$  along the y-direction. The x-direction transverse resolution  $\Delta x$  of the sensor is dictated by the pixel pitch of the deployed image sensor viewing the laser line illumination. In addition, fundamentally, the axial resolution of the 3-D shape sensor is limited by the Rayleigh axial resolution limit  $d$  of the focusing beam given by [12]:

$$d \approx 2\lambda \left( \frac{F_{net}}{D_c} \right)^2. \quad (3.3)$$

Figure 3.1(b) shows the proposed design of the camera module used in the 3-D shape sensor. An imaging lens  $L$  with a focal length  $F$ , a camera aperture labeled as  $SF_C$  having diameter  $D_A$ , and an imaging sensor chip constitute the camera module. The distance from the imaging sensor to  $L$  is denoted as  $d_i$ ,  $d_3$  is the distance from  $L$  to the BS, and  $d_2$  is the distance from the BS to the edge of the sensor module. Acceptably sharp images of the target illuminated laser line are necessary over all the depth values within the sensor working range. Hence  $F$  and  $D_A$  camera parameters need to be chosen carefully to allow a sufficient Depth of Field (DOF) interval value which will guarantee sharp in-focus subjects within the designed camera DOF. A detailed view of camera imaging lens operation is illustrated in Fig. 3.1(c) where the optical ray diagram is shown.  $F$  is the lens  $L$  focal length,  $D_A$  is the lens aperture diameter,  $d_o$  is the lens to object distance, and  $d_i$  is the lens to image distance.  $O_{near}$  is the point on the optic axis on the object side representing the near limit of the DOF.  $O_{far}$  is the point on the optic axis on the object side representing the far limit of the DOF.  $I_{far}$  and  $I_{near}$  are the points on the optic axis on the image side that are the images of the points  $O_{near}$  and  $O_{far}$  respectively.  $d_{on}$  is the lens to  $O_{near}$  distance while  $d_{of}$  is the lens to  $O_{far}$  distance.  $d_{if}$  is the lens to  $I_{far}$  distance, and  $d_{in}$  is the lens to  $I_{near}$  distance.  $C_i$  is defined as the permissible diameter of the blur circle formed on the imaging sensor in order for an object to be considered sufficiently in focus while  $C_o$  is the corresponding (conjugate) diameter in the object space. In Fig. 3.1(c) the shaded grey region on the object side represents the extent of the DOF. Using geometry, the DOF equation which is used to determinate the camera parameters is written as:

$$DOF = \frac{2D_A d_o F C_i (d_o - F)}{D_A^2 F^2 - C_i^2 (d_o - F)^2}. \quad (3.4)$$

The detailed and rigorous derivation of Eqn. (3.4) is fully described in [15]. Note that the Eqn. (3.4) expression represents the DOF of the camera module, and not the DOF of the target illuminating beam. Additionally, to correctly design and verify the camera parameters involved, the thin lens equation is used which is defined as [26]:

$$\frac{1}{F} = \frac{1}{d_o} + \frac{1}{d_i}, \quad (3.5)$$

and following Eqn. (3.5), the imaging system magnification factor  $M$  is defined as [26]:

$$M = -\frac{d_i}{d_o}. \quad (3.6)$$

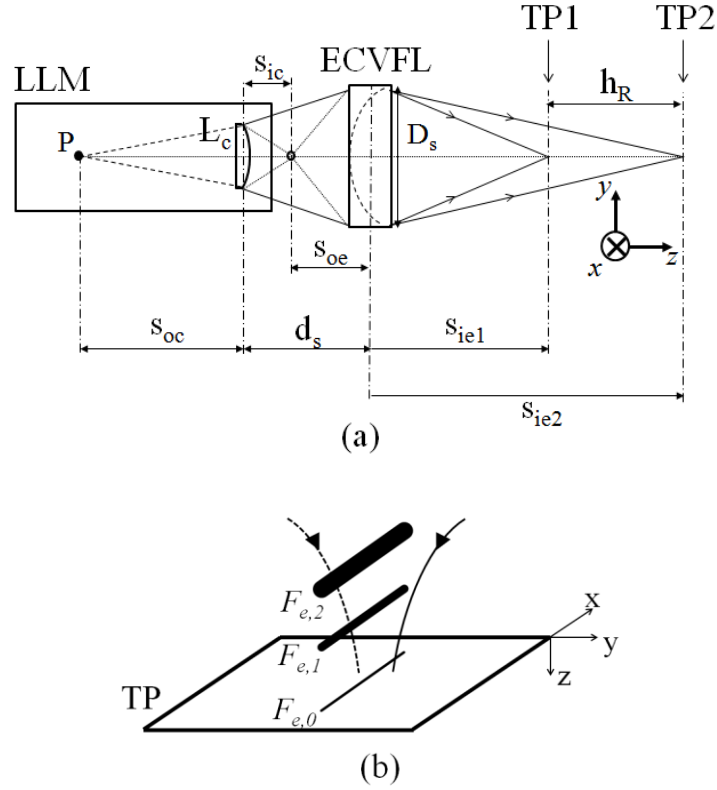


Fig. 3.2. (a) Side view ray optics diagram of the ECVFL and LLM cylindrical lens  $L_c$  based two lens system. TP: Target Plane. (b) Laser line illumination behavior due to different ECVFL focal length values. In this illustration, the optimum ECVFL value for is given by  $F_{e,0}$ .

To compute the sensor working distance  $h_R$ , the classic ray-optics thin lens imaging Eqn. (3.5) and the  $F_{net}$  Eqn. (3.2) are deployed for the two-lens system (see Fig. 3.2(a)) formed by the LLM and ECVFL. In Fig. 3.2(a), the point P is the back-projected laser virtual point source seen inside the LLM. The combined cylindrical lens-ECVFL lens system performs the thin-lens imaging operation between the target plane and the back-projected point P. By applying Eqn. (3.5) for the cylindrical lens  $L_c$ , one can write:

$$\frac{1}{F_c} = \frac{1}{s_{oc}} + \frac{1}{s_{ic}}, \quad (3.7)$$

where  $s_o = s_{oc}$  is the lens-object distance and  $s_i = s_{ic}$  is the lens-image distance. Rearranging Eqn. (3.7) gives:

$$s_{ic} = \frac{s_{oc} F_c}{s_{oc} - F_c}. \quad (3.8)$$

Using geometry, the ECVFL object distance  $s_{oe}$  is:

$$s_{oe} = d_s - s_{ic}. \quad (3.9)$$

Inserting Eqn. (3.8) into Eqn. (3.9) gives:

$$s_{oe} = d_s - \frac{s_{oc}F_c}{s_{oc} - F_c}. \quad (3.10)$$

Next, using Eqn. (3.5) for the ECVFL gives:

$$\frac{1}{F_c} = \frac{1}{s_{oe}} + \frac{1}{s_{ie}}, \quad (3.11)$$

where  $s_i = s_{ie}$  is the ECVFL-image distance. Rearranging Eqn. (3.11) gives:

$$s_{ie} = \frac{s_{oe}F_e}{s_{oe} - F_e}. \quad (3.12)$$

Inserting Eqn. (3.9) into Eqn. (3.12) gives:

$$s_{ie} = \frac{(d_s - s_{ic})F_e}{[(d_s - s_{ic}) - F_e]}. \quad (3.13)$$

Next, inserting Eqn. (3.8) into Eqn. (3.13) gives:

$$s_{ie} = \frac{\left(d_s - \frac{s_{oc}F_c}{s_{oc} - F_c}\right)F_e}{\left[\left(d_s - \frac{s_{oc}F_c}{s_{oc} - F_c}\right) - F_e\right]}. \quad (3.14)$$

Rearranging Eqn. (3.14), one can write:

$$s_{ie} = \frac{\frac{[d_s(s_{oc} - F_c) - s_{oc}F_c]F_e}{s_{oc} - F_c}}{\frac{d_s(s_{oc} - F_c) - s_{oc}F_c - F_e(s_{oc} - F_c)}{s_{oc} - F_c}},$$

$$s_{ie} = \frac{[d_s(s_{oc} - F_c) - s_{oc}F_c]F_e}{d_s(s_{oc} - F_c) - s_{oc}F_c - F_e(s_{oc} - F_c)}. \quad (3.15)$$

Using Eqn. (3.15), the working distance  $h$  measured from the edge of the shape sensor module to the target is given by:

$$h = s_{ie} - (d_1 + d_2), \quad (3.16)$$

where from Fig. 3.3 the distance  $d_1+d_2$  is the distance between the ECVFL and the edge of the shape sensor module.  $s_{ie}$  from Eqn. (3.15) is substituted into Eqn. (3.16) giving:

$$h = \frac{[d_s(s_{oc} - F_c) - s_{oc}F_c]F_e}{d_s(s_{oc} - F_c) - s_{oc}F_c - F_e(s_{oc} - F_c)} - (d_1 + d_2). \quad (3.17)$$

Using Eqn. (3.17) and Eqn. (3.18), the sensor distance range  $h_R$  is:

$$h_R = s_{ie2} - s_{ie1}, \quad (3.18)$$

where

$$s_{ie1} = \frac{[d_s(s_{oc} - F_c) - s_{oc}F_c]F_{e-\min}}{d_s(s_{oc} - F_c) - s_{oc}F_c - F_{e-\min}(s_{oc} - F_c)}, \quad (3.19)$$

and

$$s_{ie2} = \frac{[d_s(s_{oc} - F_c) - s_{oc}F_c]F_{e-\max}}{d_s(s_{oc} - F_c) - s_{oc}F_c - F_{e-\max}(s_{oc} - F_c)}. \quad (3.20)$$

Note that  $s_{ie} > d_1+d_2$  so that the targeting beam is outside the sensor enclosure. As a sensor design example, consider the following optical design parameters to compute  $h_R$ , i.e.,  $s_{oc} = 3.13$  cm,  $F_c = 2.7$  cm,  $d_s = 2$  cm, maximum ECVFL focal length  $F_{e-\max} = 12.5$  cm, minimum ECVFL focal length  $F_{e-\min} = 6.4$  cm. In this case,  $h_R = 4$  cm.

To determine the proposed shape sensor's depth control sensitivity  $\Delta h$ , one can write:

$$\Delta h = \left( \frac{dh}{dF_e} \right) \Delta F_e, \quad (3.21)$$

where  $\Delta F_e$  is the step change in  $F_e$  introduced by changing the current  $i$  applied to the ECVFL, and  $dh/dF_e$  is obtained by differentiating the Eqn. (3.17) expression with respect to  $F_e$ . Note that depending on the ECVFL device technology, its  $\Delta F_e$  is limited by the device's opto-electro-mechanical characteristics plus its electronic driver's current resolution  $\Delta i$  which in turn limits the  $\Delta h$  of the sensor. Finally, as previously mentioned, the sensor cannot spatially resolve a target depth change if it is smaller than the Rayleigh axial resolution limit of the focusing beam.



Figure 3.2(b) illustrates the working principle of the laser line illumination based 3-D shape sensor. The laser line illumination width varies with the ECVFL's  $F_e$ . This changing line illumination width is observable along the y-direction using the sensor camera. In particular, the laser line illumination width control is done by changing the ECVFL drive current  $i$ , or voltage, within the admissible ECVFL's operational range. Different  $F_e$  values correspond to different depth distances  $h$ . An optimum  $F_e$  value (and its relevant current  $i$ ) is one that returns the thinnest illumination line on the camera while tuning the ECVFL  $F_e$ . Thus, using the sensor calibration map of  $h$  versus  $i$ , the measured optimum  $i$  value provides the target depth  $h$  value within the working range of the sensor as also successfully demonstrated in [12-15].

### 3.3 EXPERIMENT

A detailed view of the experimental design is given in Fig. 3.3. The distance from the LLM's edge to the ECVFL's center is  $d_0$ , the distance between the ECVFL's center to the BS's center is  $d_1$ , and the distance between the BS's center to the edge of the sensor module is  $d_2$ . The sensor module is mounted on an x-y motorized platform designed to cover up to a  $400 \text{ mm} \times 400 \text{ mm}$  scan area. A 5 mW ProPhotonix model 3D Pro laser is used as the LLM and has a  $\lambda = 660 \text{ nm}$  [27]. For this LLM, the approximate parameters are:  $s_{oc} = 3.13 \text{ cm}$  and  $F_c = 2.7 \text{ cm}$ . An Optotune EL-6-18 lens [28] having a aperture diameter  $D_s$  of 6 mm is used as the ECVFL. The ECVFL is current  $i$  controlled by the PC through its corresponding USB lens driver interface from Optotune. The BS used is a Thorlabs model BS013. The parameter distances in the experiment are  $d_s = 2 \text{ cm}$ ,  $d_0 = 1.54 \text{ cm}$ ,  $d_1 = 2.6.5 \text{ cm}$  and  $d_2 = 2.84 \text{ cm}$ . The designed working range value of  $h_R = 40 \text{ mm}$  is adequate to scan the 3-D samples used in the experiments. This is consistent with the design example discussed in the previous section. Do note that as described in [14], by using an appropriate bias lens within the targeting system, the sensor working range can be further extended. The lateral transverse motion of the sensor module in the x-y plane is achieved using two stepper motors. The model P700 from Astrosyn driver card for the motors is controlled by a STM32F4 microcontroller from STMicroelectronics. The chosen steps of 2 mm resolution of the motors is sufficient to characterize the objects under test. The motors require in average 2 seconds to be relocated in a different scan position in the x-y plane. The CMOS sensor chip model UI-1250LE-M-GL

[29] used in the camera module is provided by IDS. The CMOS chip's active sensor area is  $8.5 \text{ mm} \times 6.4 \text{ mm}$  with a pixel size  $p$  of  $5.3 \text{ }\mu\text{m}$  and pixel count of  $1600 \times 1200$  pixels.

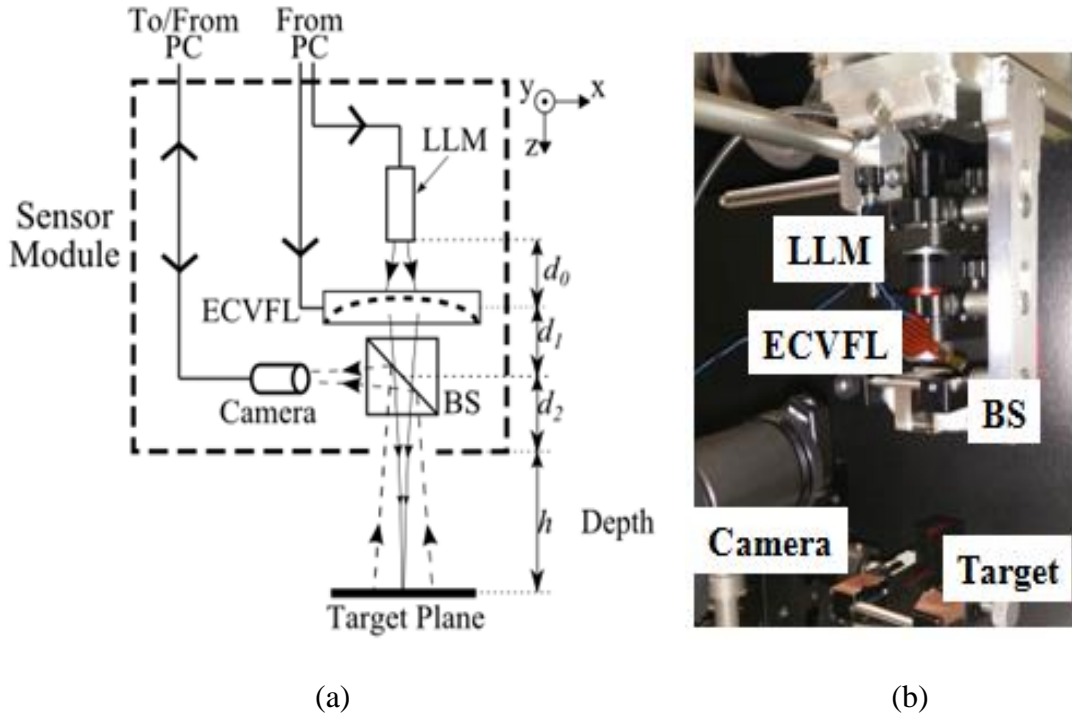


Fig. 3.3. (a) Experimental setup and (b) view of the proposed 3-D shape sensor using a laser line illumination.

Equation (3.4) is employed to evaluate the theoretical DOF value; thus, parameters involved in the camera design need to be chosen in order to guarantee the DOF constraint plus an acceptable focus quality within the designed 40 mm range. In Fig. 3.1(c),  $D_A = 1 \text{ mm}$ , considering the experimental lighting conditions and target sample surface reflectance properties. The  $L$  used has  $F = 50 \text{ mm}$ ,  $d_2 = 28.4 \text{ mm}$ ,  $d_3 = 111.6 \text{ mm}$ , and the object distance  $d_o = 160 \text{ mm}$ , with  $d_o = d_2 + d_3 + h/2$ , where  $h/2$  is the mid range working distance value. Substituting  $d_o$  and  $F$  in Eqn. (3.4),  $d_i = 72.7 \text{ mm}$ . Considering a blur circle  $C_i$  of  $80 \text{ }\mu\text{m}$  and using the formula in Eqn. (3.3), the resulting DOF range is equal to 58.12 mm, a value that guarantees the correct operation of the 3-D shape sensor in the designed working range  $h_R$  of 40 mm. The experimental Field of View (FOV) for the camera module is determined by the distances used in the optical design, i.e., the lens  $L$  focal length and the CMOS imaging sensor chip active area. For the proposed 3-D shape sensor, the experimental FOV along the x-direction  $\text{FOV}_x$  at the longest working distance range plane of  $d_{h0} = 180 \text{ mm}$  is calculated as follows. The imaging sensor along the line direction has a pixel count of 1200. Knowing

the imaging sensor pixel size  $p$ , the sensor dimension is equal to  $1200 \times 5.3 \mu\text{m} = 6.36 \text{ mm}$ . Using Eqn. (3.5), the  $FOV_x$  value is calculated as:

$$FOV_x = \frac{6.36 \times d_{ho}}{d_i} = \frac{6.36 \times 180}{72.7} = 16 \text{ mm}. \quad (3.22)$$

Note that if required, the camera optics can be designed to cover a wider FOV. In Fig. 3.4 it is shown a flow chart that highlights the constraints in the design as described previously.

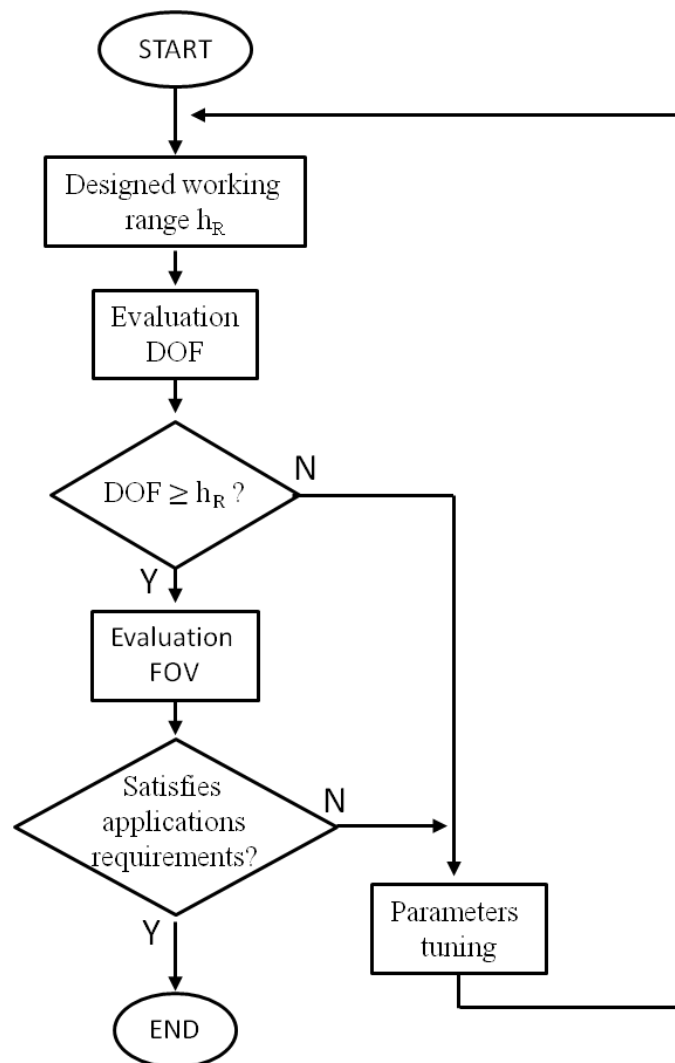


Fig. 3.4. Flowchart diagram for that shows the relationship among the designed working range  $h_R$ , DOF, and FOV.

The sensor system is programmed to operate along with an in-house software Graphic User Interface (GUI) developed in C++/CLI language which controls in real-time the 3-D shape sensor operations. The GUI is responsible for synchronization operations and interprets the commands that are sent to the ECVFL from the lens driver controller. The GUI also manages the communication between the microcontroller and the motors and implements the designed image processing algorithm.

The minimum laser line illumination width is dictated by the optimum  $F_e$  value which is linked to the current  $i$  applied to the ECVFL. Given a laser line illumination spread along the x-direction (row direction) as shown in Fig. 3.5(a), it is possible to determine a net irradiance value for a row of pixels in the image. This operation is done by adding the individual optical irradiances of each pixel in a row. Figure 3.5(b) shows an example irradiance distribution for the case of focussed and unfocussed illumination lines. Note in particular how a focused laser line translates into a sharp peak intensity profile. The measured profile intensity data experimentally obtained is used to measure the line illumination width. Figure 3.5(c) shows the result obtained with the described method. Similar results are obtained during the calibration training phase of the sensor over the experimental working distance. The average laser line illumination width  $w_{px}$  value is 20 pixels in the CMOS sensor. Using Eqn. (3.6) and the distances involved in the optical design,  $M$  at the mid range working distance is computed as  $M = -d_i/d_o = -(72.7 / 160) = -0.454$ . Knowing  $M$  and by multiplying the imaging sensor pixel pitch size  $p$  with the line illumination width size in pixel unit  $w_{px}$ , the line illumination width value  $w_L$  at the mid range working distance plane is computed as:

$$w_L = -\frac{(p \times w_{px})}{M} = \frac{5.3 \times 20}{0.454} = 233 \mu m, \quad (3.23)$$

which is the experimental line illumination width value at the mid range working distance. This value represents the experimental transverse resolution along the y-direction of the proposed 3-D shape sensor.

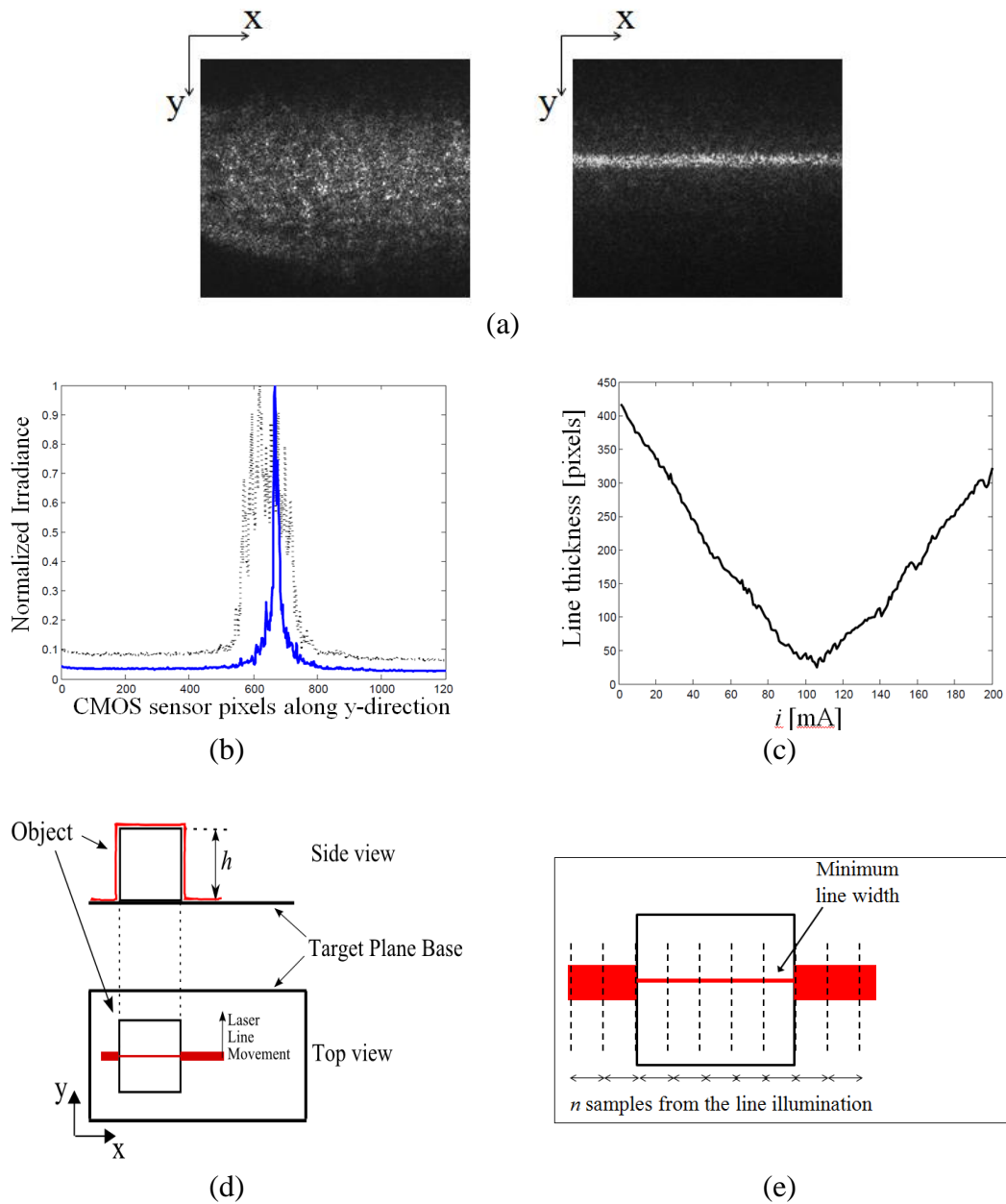


Fig. 3.5. (a) Laser line illumination width camera snapshot for an unfocused (left) and a focussed (right) beam. (b) Laser line illumination intensity versus CMOS sensor pixel location along y-direction for an unfocused (dotted line) and a focussed (solid line) laser line beam. (c) Experimentally measured laser line thickness (in CMOS sensor pixel count) versus ECVFL drive current for a given depth  $h_i = 10$  mm. (d) Laser line illumination falling over a cube shaped object. (e) Laser line illumination divided in  $n$  segments.

The line illumination scenario shown in Fig. 3.5(a) occurs only when the target depth profile is uniform along the line direction. A typical scenario could be the one shown in Fig. 3.5(d) where the laser line illumination falls over an object having different heights with respect to the base of the target plane. In such scenarios, the laser line is programmed to have a minimum line width only in a portion of the overall laser line for a single ECVFL value  $F_e$ . As shown in Fig. 3.5(e) scenario, the illumination line is divided into  $n$  segments representing  $n$  independent illumination lines. This is done in order to individually evaluate each line segment. According to the object depth  $h$ , the  $n$ -th segment will have a unique line illumination width with respect to a particular ECVFL focal length. The tuning operation of the ECVFL  $F_e$  focal length affects all the  $n$  segments at the same time. Nevertheless, the recovery of the optimum  $F_e$  values for each segment is still possible, by observing the line width illumination behavior at each segment independently. As mentioned earlier for Fig. 3.5(a), the line irradiance estimation operation along the x-direction was performed over the entire line length. For Fig. 3.5(e), the line irradiance estimation along the x-direction is performed only for the length of a given segment. This is done so one finds  $n$  optimum  $F_e$  values corresponding to the thinnest line segment. Knowing the corresponding optimum  $F_e$  values for each segment and using the calibration map obtained for the 3-D shape sensor, the depth information for each segment can be found. The value  $n$  needs to be chosen carefully according to the experimental conditions. Not only is  $n$  related to an increase in algorithm complexity, it is also sensitive to optical speckle. Specifically, when a laser light interacts with the target surface, optical speckle is created and recorded by the imaging sensor. An improper value of  $n$  negatively affects the line width evaluation due to the contribution of the coherently scattered light. For the experiment different values of  $n$  were considered to establish an  $n$  value that offers the best compromise in terms of depth measurement error and sensor performance for the adopted working range. A value of  $n = 16$  was used in algorithm implementation. The  $n$  value also dictates the experimental transverse resolution along the x-direction which is also correlated to the camera field of view. With the experimental parameters settings used, the transverse resolution along the x-direction is experimentally shown to be equal to 1 mm.

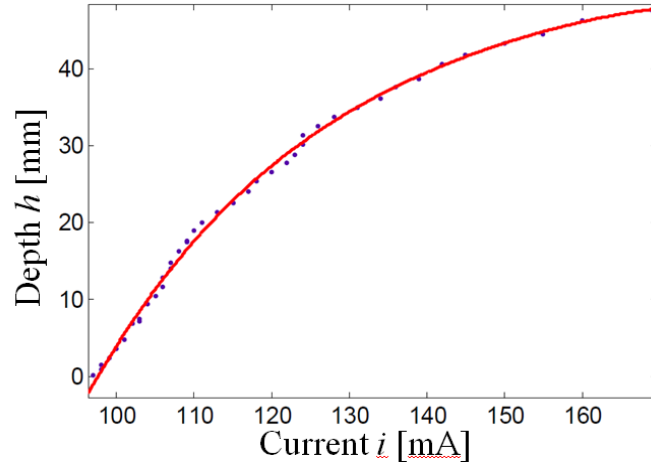


Fig. 3.6. Experimental calibration depth  $h$  versus ECVFL drive current  $i$  for the designed 40 mm depth range. Raw data (dots) and the best fit curve (solid line) are shown. The curve fitting operation was performed using MATLAB.

By experimentally compiling the 3-D sensor calibration map over the full designed working range using the optimum  $F_e$  values, the Fig. 3.6 sensor calibration curve is obtained. The calibration points are acquired with a resolution of 2 mm in depth covering the complete designed 40 mm depth range and a best line fit is drawn through the points. With the calibration map available it is possible to pursue the line scanning operation of the entire 3-D target placed on the target plane. For a given x-y location, a series of images are acquired while sweeping through the ECVFL  $F_e$  over the desired depth range. Once the  $F_e$  sweeping is complete, the image processing algorithm evaluates all the images captured and extracts the laser line illumination width data (i.e., for all  $n$  segments). As mentioned earlier, the minimum width dimension extraction relative to the  $n$ -th segment is performed considering the optimum  $F_e$  value for each segment. Finally, the optimum  $F_e$  values obtained are evaluated using the calibration curve, thus obtaining the target depth value for the considered x-y location for each line segment. This process is repeated for a number of x-y positions using the programmed x-y motors step resolution to scan the object over the entire x-y plane.

The accuracy of the calibration method for this experiment is dictated by factors such as the stability of the ECVFL optical and electrical properties over its focal length range, the optical spatial stability of the line illumination, the mechanical stability of the 2 mm step change motion stage, image corruption due to speckles in the observed illumination line, and ultimately the signal processing quantization noise in the image processing algorithm.

Several test scans were made to evaluate the performance of the proposed sensor. Shown in Fig. 3.7 (a) is an abstract representation of the cube deployed in the experimental demonstration. Figure 3.7(b) shows the delrin material object having two heights of 1 cm and 2 cm and Fig. 3.7(c) shows the profile obtained using the 3-D shape sensor with a 5 mm x-y motor step resolution. All the measurements obtained were within  $\pm 2$  mm with respect to the actual target depth, giving an error of less than 5% in the designed working range. Figure 3.8(a) shows a delrin material object having a stair-case shape with 4 levels and a step height of 10 mm. The four different levels are at heights of 10 mm, 20 mm, 30 mm, and 40 mm. To 3-D map the entire object, a 5 mm x-y motor step resolution is chosen. Experimentally a worst case  $\pm 2$  mm depth measurement deviation (see Fig. 3.8(b)) compared to the actual target height values is observed. Again, the depth measurement error is  $< 5\%$ . Next the shape sensor is used to map a delrin object material having a narrow crevice of 7 mm width and 15 mm depth.

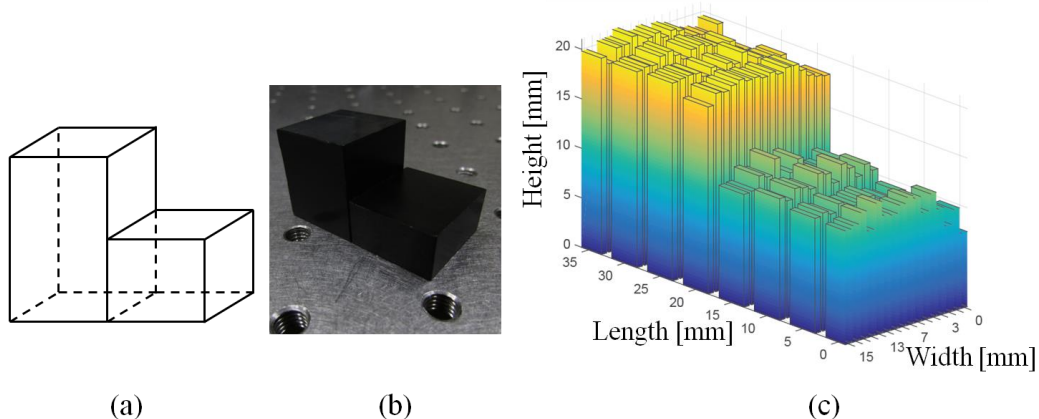


Fig. 3.7. (a) Abstract representation of the two cubes deployed for the experimental demonstration (b) Sample delrin block made by two cubes having 1 cm and 2 cm heights, respectively. (c) 3-D profile obtained with the proposed 3-D shape sensor.

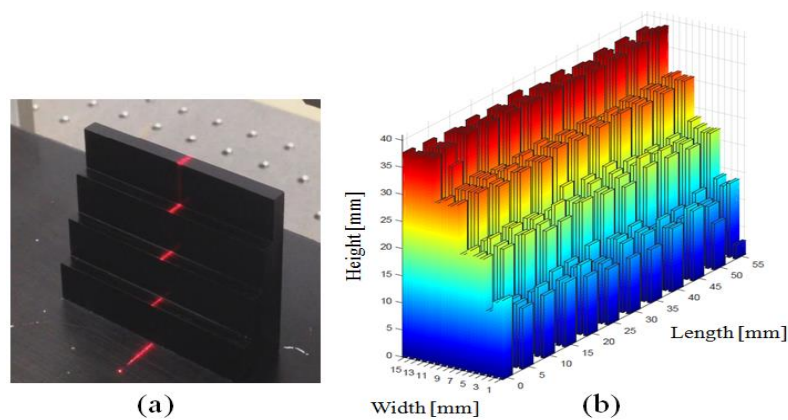


Fig. 3.8. (a) Staircase sample delrin block having 10 mm, 20 mm, 30 mm, and 40 mm height for each step respectively. (b) Complete object 3-D profile obtained with proposed 3-D shape sensor.



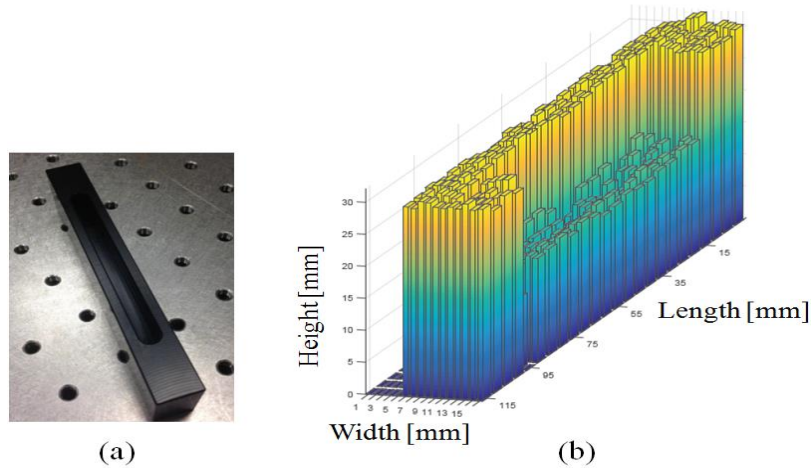


Fig. 3.9. (a) Sample having a narrow crevice with a 15 mm depth and 7 mm width. (b) Partial cut-section 3-D profile reconstruction using the laser line shape sensor.

As shown in Fig. 3.9(a), the crevice is custom manufactured inside a solid block 30 mm tall and 15 mm wide. Using the shape sensor in the 3-D scanning mode, a total of 26 individual scans are obtained, in other words, using  $n = 16$ , 416 individual data points. The reconstructed 3-D object (see Fig. 3.9(b)) gives a worst case  $\pm 2$  mm deviation from the actual target depth values, giving a less than 5% deviation error within the 40 mm designed depth working range. For visualization purposes a cut-section along the widest direction of the object is presented in Fig. 3.9(b) where the narrow crevice in the object is highlighted.

Next, examined is the proposed sensor speed performance when compared to our ref. 15 single laser spot scanning based 3-D sensor. In both sensors, the processing time depends on three factors, namely, the ECVFL settling time, the transverse motor step scan size and the laser line illumination width measurement algorithm execution time. The algorithm processing time is dependent on the PC processor power. This processing time for most modern electronics can be considered to be fast (near real-time) since the functions performed in the algorithm are not computationally demanding. For sake of simplicity, the time required to re-position the sensor using the motors in a new scan point can be excluded for both sensors comparison. This is appropriate since both sensors have the same motor configuration, therefore same re-positioning time. Regarding the ECVFL, it is necessary that before acquiring a laser line snapshot with the camera module, one allows a safe settling time for the device. The optical fluid contained in the Optotune ECVFL needs an average of 10 ms for this ECVFL model to adjust its position from a different current setting. For instance, the ECVFL can be programmed to operate using 100 distinct  $F_e$  values in the designed working

range. Therefore, allowing a total of 50 ms for the camera module to capture the image and sweeping the  $F_e$  for a total of 100 values implies an acquisition time of 5 seconds for each motor position. In the Fig. 3.9(a) target sample case, 26 scans are made to cover the entire target which takes about 2 minutes. With respect to ref. 15 where a different ECVFL, model EL-10-30 by Optotune, having 15 ms settling time was used, 10 seconds were required to cover a single depth scan position. Excluding the time for the motor to reach a different position, mapping the entire object with a single sampling laser spot implies an execution time of over 60 minutes. That being said, the improvement introduced with this new approach is significantly consistent, rated as 16 points per second versus 0.3 points per seconds, in other words, a 53 times per-point acquisition time improvement in terms of speed performance versus the ref. 15 3-D shape sensor. This time can be further improved by using commercially available high speed motorized x-y stage having faster re-position time. For instance, the ILS-LM Motor series by Newport provides motors having up to 500 mm/s maximum speed [30] compared to the 1 mm/s motor speed used in the described experiment.

For the proposed sensor, the limitations are mainly related to the inevitable speckle that is generated when a laser light source interacts with the target material. An excess in speckle complicates the correct determination of the minimum line width. The solution for this problem is to use an optical diffuser with moving components to average out the unwanted effect [31, 32]. For example, Optotune manufactures a controllable laser speckle reducer that can be easily integrated in the proposed optical design such as the LSR-3010 model [33]. Improvements can also be made in the image processing algorithm implementation. Note that for a given ECVFL focal length setting, the proposed algorithm computes the smallest possible diffraction limited (and aberration reduced) width of the illumination line for every given depth  $h$  of the target object within the designed working range. Therefore the use of an efficient and robust image processing evaluation algorithm that incorporates speckle reduction is key for minimizing experimental depth errors for the proposed 3-D shape sensor. Additionally, the development of efficient algorithms that are able to interface continuously with the scanning object and with the motor movement position can significantly improve the scanning time.

### **3.4 CONCLUSION**

In conclusion, proposed and demonstrated is the design of a novel single viewing axis laser line illumination based 3-D shape sensor that uses an ECVFL combined with line shape image processing to provide high transverse resolution imaging. The use of the laser line illumination scan method allows parallel target shape depth processing which results in an experimentally demonstrated 53 times per-point acquisition time improvement with respect to our previously demonstrated single laser point scanning based 3-D shape sensor. The sensor is deployed to successfully map objects having steep slope surfaces as well as internal cavities, such as crevices having narrow openings. The average experimental measurement error is computed to be less than 5% within the designed sensor working range of 40 mm. Speckle reduction strategies implementation as well as efficient decisional algorithms can further improve the performance of the proposed 3-D shape sensor. The proposed sensor can be deployed where traditional 3-D shape sensor techniques have limited performance due to off-axis placement constraints or where costs should be minimized without sacrificing imaging transverse resolution.

## REFERENCES

- [1] S. Son, H. Park and K. H. Lee, "Automated laser scanning system for reverse engineering and inspection," *International Journal of Machine Tools and Manufacture*, vol. 42, no. 8, pp. 889-897, (2002).
- [2] R. Usamentiaga, J. Molleda and D. F. García, "Fast and robust laser stripe extraction for 3D reconstruction in industrial environments," *Machine Vision and Applications*, vol. 23, no. 1, pp. 179-196, (2012).
- [3] M. Levoy et al., "The digital Michelangelo project: 3D scanning of large statues," in *Proc. 27th Annual Conference Computer Graphics Interactive Techniques (SIGGRAPH)*, pp. 131-144, (2000).
- [4] S. Zhang, "Recent progresses on real-time 3D shape measurement using digital fringe projection techniques," *Optics and Lasers in Engineering*, vol. 48, no. 2, pp. 149-158, (2010).
- [5] S. J. Nute, and J. P. Moss, "Three-dimensional facial growth studied by optical surface scanning," *Journal of Orthodontics*, vol. 24, no. 1, pp. 31-38, (2000).
- [6] J. P. Moore and M. D. Rogge, "Shape sensing using multi-core fiber optic cable and parametric curve solutions," *Optics Express*, vol. 20, no. 3, pp. 2967-2973, (2012).
- [7] T. Kanade, *Three-Dimensional Machine Vision*, Kluwer Academic, Boston, MA, (1987).
- [8] P. Cong, Z. Xiong, Y. Zhang, S. Zhao, and F. Wu, "Accurate dynamic 3D sensing with Fourier-assisted phase shifting," *Journal of Selected Topics in Signal Processing*, vol. 9, no. 3, pp. 396-408, (2015).
- [9] L. Zhang, D. Haiwei, and A. El Saddik, "From 3D sensing to printing: a survey," *ACM Transactions on Multimedia Computing, Communications and Applications (TOMM)*, vol 12, no.2, (2016).
- [10] G. Häusler and F. Willomitzer, "A stroll through 3D imaging and measurement," *ICO Newsletter*, no. 104, (2015).
- [11] G. Sansoni, M. Trebeschi, and F. Docchio, "State-of-the-art and applications of 3D imaging sensors in industry, cultural heritage, medicine, and criminal investigation," *Sensors*, vol. 9, no. 1, pp. 568-601, (2009).
- [12] N. A. Riza and S. A. Reza, "Non-contact distance sensor using spatial signal processing," *Optics Letters*, vol. 34, no. 4, pp. 434-436, (2009).

- [13] N. A. Riza and S. A. Reza, "Smart agile lens remote optical sensor for three-dimensional object shape measurements," *Applied Optics*, vol. 49, no. 77, pp. 1139-1150, (2010).
- [14] M. J. Amin and N. A. Riza, "Smart laser scanning sampling head design for image acquisition applications," *Applied Optics*, vol. 52, no. 20, pp. 4991-4996, (2013).
- [15] J. P. La Torre, M. J. Amin, B. Thompson, and N. A. Riza, "Optical shape sensor using electronically controlled lens," *IEEE Sensors Journal*, vol. 16, no. 12, pp. 4776-4785, (2016).
- [16] S.A Khan and N. A. Riza, "Demonstration of a no-moving-parts axial scanning confocal microscope using liquid crystal optics," *Optics Communication*, vol. 265, no. 2, pp. 461-467, (2006).
- [17] N. A. Riza, M. Sheikh, G. Webb-Wood, and P. G. Kik, "Demonstration of three-dimensional optical imaging using a confocal microscope based on a liquid-crystal electronic lens", *Optical Engineering*, vol. 47, no. 6, 063201, (2008).
- [18] N. A. Riza, M. J. Amin, and M. N. Riza, "Eye vision testing system and eyewear using micromachines," *Micromachines*, vol. 6, no. 11, pp. 1690-1709, (2015).
- [19] N. A. Riza and P. J. Marraccini, "Power smart in-door optical wireless link applications," 8th International Wireless Communication Mobile Computation. Conference (IWCMC) IEEE, 2012.
- [20] N. A. Riza, S. A. Reza, and P. J. Marraccini, "Electronically controlled agile lens-based broadband variable photonic delay line for photonic and radio frequency signal processing," *Applied Optics*, vol. 49, no. 35, pp. 6718-6725, (2010).
- [21] S. A. Reza and N. A. Riza, "A liquid lens-based broadband variable fiber optical attenuator," *Optics Communication*, vol. 282, no. 7, pp. 1298-1303, (2009).
- [22] M. A. Sheikh and N. A. Riza, "Motion-free hybrid design laser beam propagation analyzer using a digital micromirror device and a variable focus liquid lens," *Applied Optics*, vol. 49, no. 16, pp. D6-D11, (2010).
- [23] S. A. Khan and N. A. Riza, "Demonstration of 3-dimensional wide angle laser beam scanner using liquid crystals," *Optics Express*, vol. 12, no. 5, pp. 868-882, (2004).
- [24] N. A. Riza, *Photonics Signals and Systems: An Introduction*. McGraw-Hill, 2013.
- [25] M. Born and E. Wolf, *Principles of Optics (5th Edition)*, Cambridge University Press, Cambridge, 1975, Chapter 8: Elements of the Theory of Diffraction, pp. 414-418.
- [26] E. Hecht, *Optics (4th Edition)*, Pearson Addison-Wesley, 2002, Chapter 5: Geometrical Optics, pp. 149-156.

- [27] Laser Line Module, ProPhotonix 3D Pro, ProPhotonix, USA. Product description available at URL: <http://www.prophotonix.com/products/laser-structured-light/3dprolaser.aspx> (visited on 03/10/2017).
- [28] EL-6-18 datasheet, Optotune, Switzerland. Product description available at URL: <http://www.optotune.com/images/products/Optotune%20EL-6-18.pdf> (visited on 03/10/2017).
- [29] IDS  $\mu$ Eye LE camera datasheet, IDS, Germany. Product description available at URL: <https://en.ids-imaging.com/store/products/cameras/usb-2-0-cameras/ueye-le.html> (visited on 03/10/2017).
- [30] ILS-LM Series High-Performance Motor Stages, Newport, USA. Product description available at URL: [https://www.newport.com/medias/sys\\_master/images/images/hca/h2f/8797115645982/ILS-LM-Data-Sheet.pdf](https://www.newport.com/medias/sys_master/images/images/hca/h2f/8797115645982/ILS-LM-Data-Sheet.pdf) (visited on: 05/10/2017).
- [31] L. Wang, T. Tschudi, T. Halldorsson, and P. R. Petursson, "Speckle reduction in laser projection systems by diffractive optical elements," *Applied Optics*, vol. 37, no. 10, pp. 1770–1775, (1998).
- [32] Y. Kuratomi, K. Sekiya, H. Satoh, T. Tomiyama, T. Kawakami, B. Katagiri, Y. Suzuki, and T. Uchida, "Speckle reduction mechanism in laser rear projection displays using a small moving diffuser," *Journal Optical Society America A*, vol. 27, no. 8, pp. 1812–1817, (2010).
- [33] LSR-3010 Laser Speckle Reducer datasheet, Optotune, Switzerland. Product description available at URL: <http://www.optotune.com/products/laser-speckle-reducers/eap-lsr/lsr-3010-series> (visited on: 05/10/2017).



# CHAPTER 4

## SMART ART DISPLAY PROJECTION SYSTEM<sup>3,4</sup>

### 4.1 INTRODUCTION

Displaying information is an integral part of the modern world of entertainment, education, medicine, augmented reality, automotive, advertising, and art installations [1-3]. Front projection systems are often required for these mentioned applications. The most popular front projection display technologies include Laser Scanning Displays (LSDs) [4], Liquid Crystal Displays (LCDs) [5] and Digital Light Processing (DLP) technology displays using a Digital Micromirror Device (DMD) [6]. Advantages of the LSD based solution over the LCD and DMD based projection display solutions are the improved depth of focus, contrast ratio and bright colour generation. One common limitation associated with current front projection technologies such as the market dominant LCD/DMD based projectors is their basically fixed in-focus projection distance within a fixed projected spatial frame. Specifically, there is image blurring and image distortion if the screen distance is not located within the depth-of-focus of the deployed projection imaging lens. To counter these depth-of-focus limitations, one can deploy the classic LSD technology to create variable range in-focus variable frame projection. But this LSD technology also has its fundamental limitations. Specifically, as the projection distance varies, the pixel size in the projected image also varies resulting in a degradation of picture viewing quality, particularly for increasing screen distances. Furthermore, both LSD and LCD/DMD based projectors cannot operate with multi-depth conformal surface screens where they create severe projected image distortion.

In this chapter, proposed for the first time is the Smart Art Display that aims to address the need for a front projection technology that will allow for non-distorted projection onto a multi-distance 3-D conformal surface [7]. In 2011, Prof. Riza's research group has demonstrated the basic principles of a smart LSD for 2-D projection that deployed an ECVFL

---

<sup>3</sup> J. P. La Torre, N. Mayes, and N. A. Riza, "Smart art display projection system," in Photonics Ireland, Ireland, (2017).

<sup>4</sup> J. P. La Torre, N. Mayes, and N. A. Riza, "Laser display system for multi-depth screen Projection Scenarios," Applied Optics, (under review), (2017).



to produce the smallest focused beam spot size possible at a specified 2-D screen location, allowing for an improved variable screen distance range with minimal reduction in display spatial resolution and image quality [8]. In 2013, a further step was made by conducting another proof-of-concept study using an ECVFL-based LSD that showed a 2-D screen variable distance range of up to 800 cm with a laser spot (image pixel) radius of less than 1 mm over the variable screen distance range [9]. This chapter extends the smart LSD work idea. In fact, designed and tested is a first fully automated Smart Art Display for multi-depth screen applications such as found in artistic scenarios so the laser spot size and location is optimized for best artistic viewing with the 3-D multi-depth conformal screen. Additionally, the proposed system design incorporates a novel built-in embedded depth sensor for 3-D mapping of the screen projection surface to enable adaptive control of projected laser spot (pixel) to suit the specific screen distance for best artistic effects.

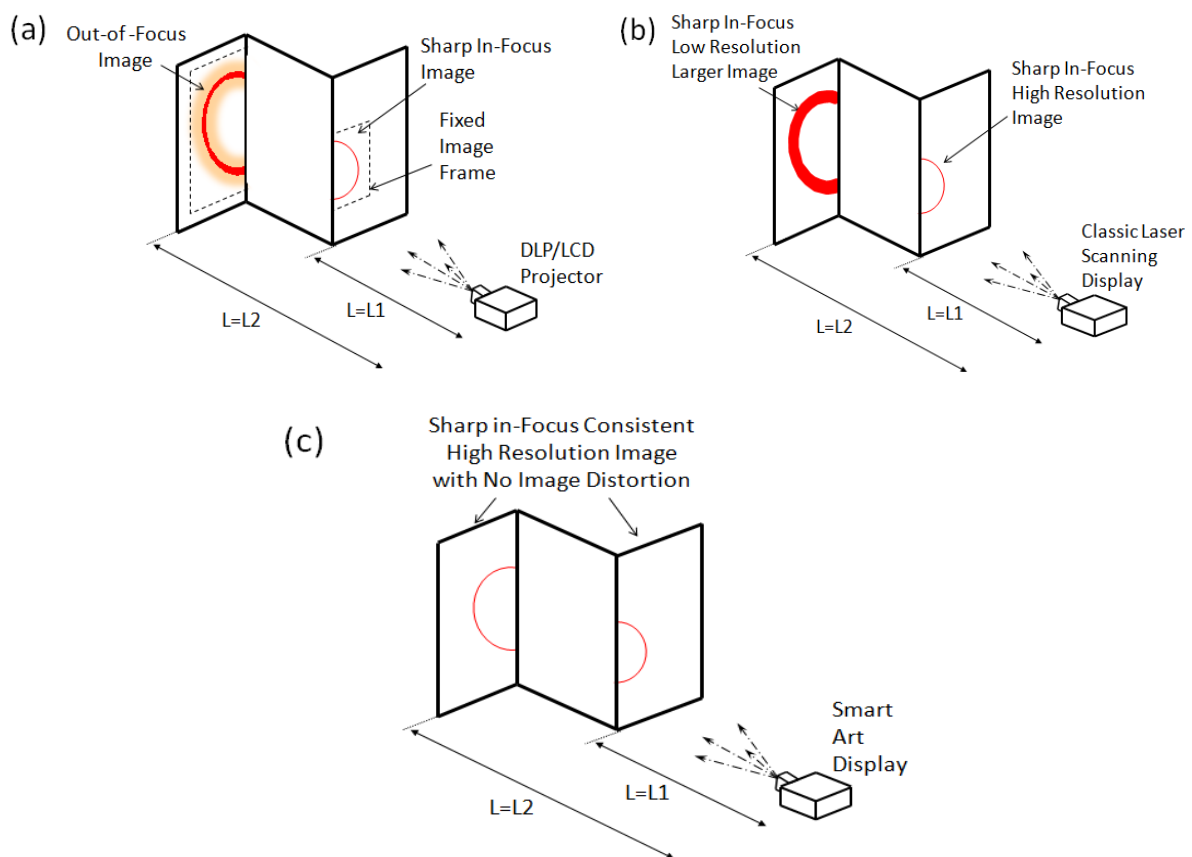


Fig. 4.1. Example projection scenarios using a dual-depth screen and various projection technologies such as (a) Standard LCD/DLP projector with limited depth-of-focus; (b) Classic Laser Scanning Display (LSD) which presents image distortion; and (c) Proposed Smart Art Display which produce a high resolution image with no image distortion.

## 4.2 PROPOSED SMART ART DISPLAY PROJECTION SYSTEM

To appreciate the impact of the proposed projection system, Fig. 4.1(a, b) show the limitations of LSD and LCD/DMD-based projection systems when projecting images onto a multi-distance screen surface. For the sake of simplicity, a two-level multi-distance projection screen scenario is presented in Fig. 4.1 with a near screen surface located at distance  $L_1$  and the far screen surface located at a distance  $L_2$ . Figure 4.1(a) uses an LCD/DLP projector that shows a clear and sharp high resolution image displayed at the location  $L_1$  while at location  $L_2$  is present an image that is blurred and has lost its sharpness. In effect, at the  $L_2$  screen distance there is a degradation of the projected image spatial resolution with some distortion. These effects are due to the limited in-focus projection range known also as the projector's depth-of-focus. Note that as the separation between the two screens increases, the resulting image projection on the far screen will progressively deteriorate. For LCD/DMD image projection, the SLM is programmed to spatially modulate the incident light falling on its entire surface creating a fixed image frame in the projected image. This aspect is also highlighted in Fig. 4.1(a) with a dashed contour area. If a projection application such as an artistic scenario requires projection onto a custom shaped screen located in brightly lit studio conditions, not only is a powerful light source required to power the projector as much light is wasted outside the shaped screen aperture, the projection system is also more complex and energy inefficient given laser and electronics cooling requirements. To counter some of these issues, Fig. 4.1(b) shows how a LSD has a different impact on the multi-depth screen scenario. Namely, the LSD projects only the spatial information required for image formation on the custom shaped screen leading to better energy usage. In Fig. 4.1(b), it is assumed that the projection optics in the deployed LSD is best suited to display a clear and sharp image at a screen located at a distance  $L_1$ . If that is the case, inevitably the projected output image at  $L_2$  will be affected by the natural divergence of the laser beam used. Shown in Fig. 4.1(c) is the multi-distance projection scenario using the proposed Smart Art Display. Notice that at both the near and far planes, the projected image is always sharp and in-focus at the same time thus illustrating the power of the proposed smart art projection system. Additionally, as with the classic LSD, there is smart and efficient usage of light energy since no fixed format image frame is present at the projection screen making the Smart Art Display suitable for many artistic 2-D, 3-D and even 4-D (3D plus time) scenarios.

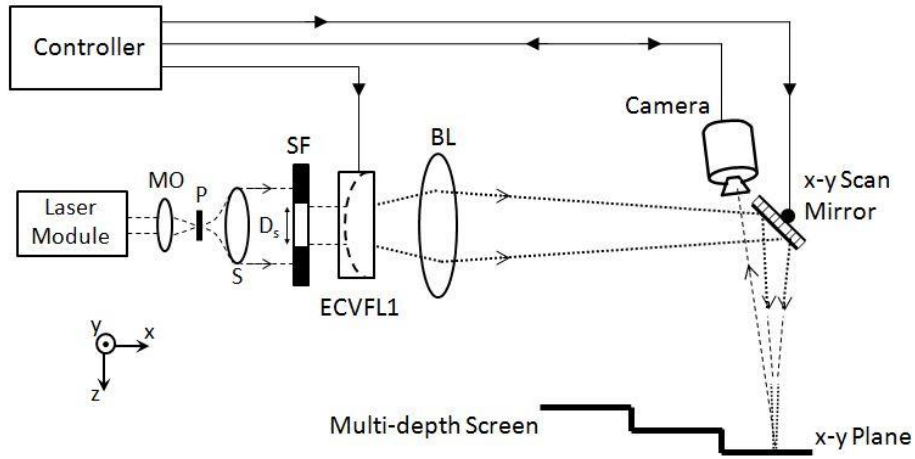


Fig. 4.2. (a) Side view ray optics diagram of the ECVFL and LLM cylindrical lens  $L_c$  based two lens system. TP: Target Plane. (b) Laser line illumination behavior due to different ECVFL focal length values. The optimum ECVFL value for distance measurement is given by  $F_{e,0}$ .

Figure 4.2 shows the design of the proposed Smart Art Display projection system. The design includes the use of a collimated laser beam that is obtained using the combination of a Gaussian laser module of wavelength  $\lambda$ , a Microscope Objective MO, a Pinhole P, and a collimation lens S. The collimated light passes through a Spatial Filter SF and a two lens system configuration consisting of ECVFL1 with  $F_1$  focal length and a Bias Lens BL. Finally, the light travels from the BL to the x-y scan mirror that is used for projecting the laser beam on the x-y plane of the screen. The ECVFL1 drive signal is varied to match the designed projection working range  $h$  for the given multi-depth screen. ECVFL1 undergoes a focal tuning operation which allows the realization of a variable beam spot size at the observation screen. For different screen distances, there is an optimum ECVFL1 focal length value that produces the highest spatial resolution viewing corresponding to the smallest focussed spot size on the screen location. From the observation of absolute changes in spot size using the viewing camera, a calibration map that correlates ECVFL1 focal length values versus screen distances is obtained implementing a screen distance sensing operation within the display hardware [8-10]. Thus the projection of a sharp and in-focus image at a certain known screen distance is obtained when this optimum ECVFL1 focal length value is used for the known screen distance. With fast focal sweep operations of ECVFL1, projected beam spots (or pixels within an image seen by the human eye) can be programmed for a multi-depth screen within the designed screen depth range of  $h$ . The deployed ECVFL1 is used in a two lens system configuration where the combined focal length  $F_{net}$  is computed as:

$$F_{net} = \frac{F_1 F_b}{F_1 + F_b - d_s}, \quad (4.1)$$

where  $F_b$  is the Bias Lens BL focal length and  $d_s$  is the separation distance between ECVFL1 and BL. Using a collimated laser beam, one can calculate the distance  $L$  from BL to the observation screen where the smallest spot will be generated. Starting from the two-lens system equation,  $L$  can be computed as [11]:

$$L = \frac{F_b(F_1 - d_s)}{F_1 + F_b - d_s}, \quad (4.2)$$

A near in-line camera containing ECVFL2 observes the projected laser light spot on the screen localized 2-D spatial position. The screen distance  $L$  at this localized 2-D spatial position is measured within the Smart Art Display hardware that as mentioned earlier intrinsically forms an embedded distance sensor. Specifically, the in-line camera images the laser beam spot on the screen and by sweeping the ECVFL1 focal length and measuring the camera observed spot size, the display measures  $L$ . In this case, the camera needs to take in-focus sharp images of the illuminated laser spot so the camera parameters should be designed such that the camera Depth-of-Field (DOF) is sufficient to have in-focus images. The Smart Art Display is expected to work with multi-depth screens; hence, ECVFL2 is placed inside the camera module to provide a larger camera DOF. For 3-D screen contour mapping of wide conformal surfaces, the deployed camera must have a wide enough field of view given the x-y scan mirrors are engaged to scan the laser spot over the 3-D multi-depth screen platform.

### 4.3 EXPERIMENT

The proposed Fig. 4.2 Smart Art Display prototype system is implemented with a 15 mW Melles Griot laser beam of wavelength  $\lambda=632$  nm which is collimated using a 10X magnification MO, a 10  $\mu$ m pinhole P, and a 20 cm focal length lens S. SF has a 4 mm aperture diameter  $D_s$  which limits the incident light aperture on ECVFL1 which is a model EL-6-18 from Optotune with a 6 mm clear aperture diameter. The focal length of ECVFL1 is controlled by an Optotune electrical lens driver which is connected to the controller. The BL has a focal length of 20 cm and is positioned at a distance  $d_s=12$  cm from ECVFL1. The x-y scan mirror is the GVS002 scanning galvo system from Thorlabs with independent x-scan and y-scan mirrors. Each mirror's angle orientation is controlled by an electrical signal that is

provided by a Data Acquisition (DAQ) Card model 6211 from National Instruments. The Smart Art Display uses a near in-line embedded camera module for distance sensing. The imaging lens used within the camera module is labelled as ECVFL2 and is model EL-10-30 from Optotune with a clear aperture diameter of 10 mm. The ECFVL2 focal length is also controlled using an Optotune electrical lens driver controller. ECVFL2 is positioned at a distance  $d_i=8.33$  cm away from the CMOS sensor chip. To implement the imaging condition, the classical thin lens equation is used to design the ECVFL2 focal length for a given screen distance within the experimental projection range  $h$  of 65 cm.

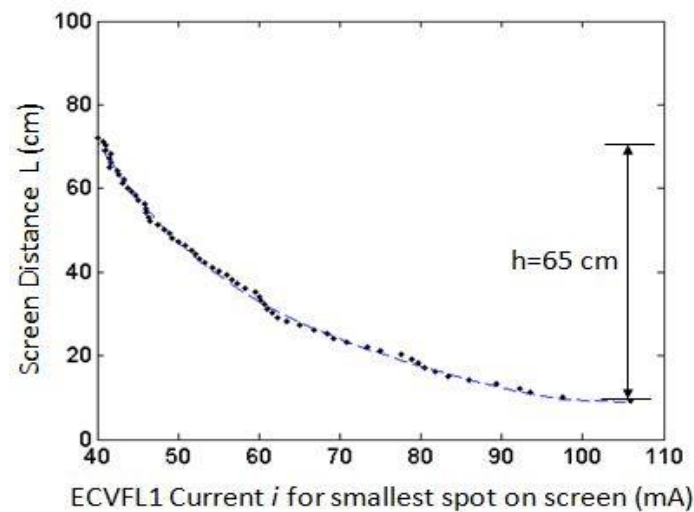


Fig. 4.3. Smart Art Display embedded distance sensor calibration data of localized screen distance  $L$  versus ECVFL1 current when observing the smallest laser spot on the projection screen that is covering a projection screen depth variation of  $h=65$  cm.

Figure 4.3 shows the screen distance versus ECVFL1 drive current calibration dataset (shown as dots) for a designed 65 cm range  $h$ . Each dot corresponds to the ECVFL1 current when the smallest laser spot was recorded on the CMOS sensor chip surface placed at a test screen location. The scanning galvo, DAQ card, ECVFL1, and camera module (including ECVFL2) are connected to a processor that controls the entire display operation. A MATLAB Graphic User Interface (GUI) is implemented to control beam spot size as well as beam scans to generate desired graphics display on a given multi-depth screen.

Shown in Fig. 4.4 is a text sample output displaying information using 2 different line thicknesses. This indicates how an artist using this display can optically draw with changing laser pen widths depending on the application. Here the shown view size is 6 cm height by 11 cm width, and the information is displayed on a flat screen.



Fig. 4.4. Two sample “CAOS” lettering projections produced using two different laser pen thicknesses for text writing. Shown are also various pen thicknesses.

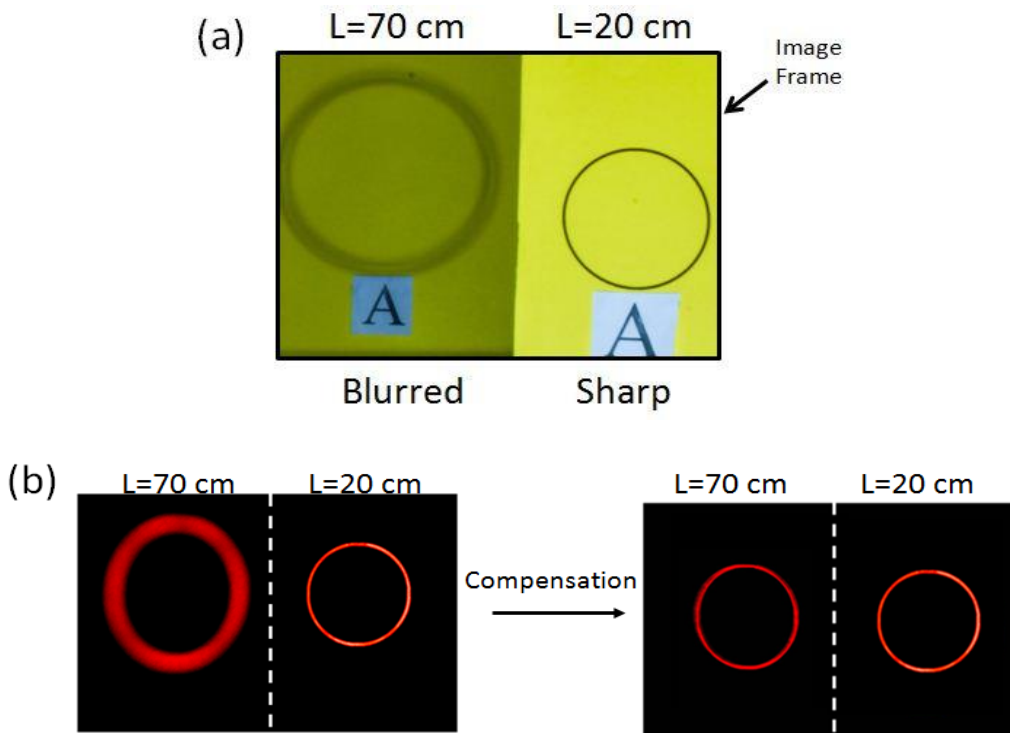


Fig. 4.5. Multi-distance screen projection test for two side-by-side screens with front screen L1 located at 20 cm position and back screen L2 located at 70 cm depth position. Projected circle images are shown using (a) Standard DLP Projector and (b) Smart Art Display. In (b) shown is the laser beam spot compensation operation for the projected circle shape using the Smart Art Display that results in a non-distorted sharp and high resolution image projection at both L1 and L2 show casing the power of the Smart Art Display.

Figure 4.5 shows the true Smart Art Display potential when compared with standard LCD/DMD based projectors. For the experimental demonstration, a Dell DLP projector model 2300-NP is used. Two circle shapes of identical geometrical dimensions are projected using the DLP projector onto a multi-distance screen with screen 1 located at  $L_1=20$  cm and screen 2 located at  $L_2=70$  cm. Fig. 4.5(a) shows the snapshot of the viewed scene (13 cm height by 15 cm width) created by the DLP projector. At the same time, two target letters are

positioned at the screen distances L1 and L2 and are used to show that the viewing camera used to obtain the Fig. 4.5(a) snapshot has a sufficient depth-of-field as both target letter “A”’s are in focus. Fig. 4.5(a) shows that while the DLP projector created circle image projected at L1 is clear and sharp, the circle projected at L2 is not only out-of-focus and blurred but larger in size. This is because of the limited in-focus projection range of the DLP projector. On the contrary, when deploying the Smart Art Display in a similar scenario, these problems are eliminated. To project the circle shape at L1, a suitable ECVFL1 focal length value is used to display a clear and sharp projection image output. At the same time, the projected in-focus circle image at L2 due to the uncompensated Smart Art Display results in a bigger size image as the same settings for the galvanometer mirrors angles are used creating a lower resolution image as the laser spot has been optimized for L1 and not L2. However, with the proposed Smart Art Display, it is possible to control both image distortion and image resolution for projection over a multi-distance screen distance using electronically programmable optical components. This image distortion compensation operation is also shown in Fig. 4.5(b) where the circle displayed at L2 is compensated using an optimized focal length value. In other words, the in-focus undistorted human eye-based visualization of both circles is possible having the best resolution although located at different multi-distance screen depths. This optimized observation of images on a multi-depth screen can be performed by providing synchronization of the elements involved, the knowledge of the screen localized depth data, as well as by use of a sufficient fast focal sweep of the ECFVL1 focal length value. Finally note that in Fig. 4.5(b), the compensation operation not only takes care of the output image resolution but it also adjusts the geometrical dimensions of the circle shape located at L2 to be comparable to the geometrical dimension at L1. In fact, depending on observer’s view point, different visual effects for different applications can be obtained by control of both the ECFVL1 as well as the galvo mirrors.

As mentioned earlier, at the start of the Smart Art Display operations, a 3-D depth and contour map of the deployed multi-depth screen should be conducted. To achieve this operation, for a localized screen depth position, ECVFL1 is tuned to generate the smallest spot viewed by the camera with ECVFL2 focal length tuned to observe an in-focus image of the spot. Such observed spot is subject to image processing and then screen depth calculation using a prior recorded ECVFL1 current versus L calibration curve. For the proposed experiment, an evaluation test for 7 different screen distances is performed. with actual L values of 15 cm, 25 cm, 35 cm, 45 cm, 55 cm, 65 cm, and 75 cm. An algorithm based on

small spot detection evaluated the spot size change for each ECVFL1 focal length tuning operation. The optimum focal length value corresponding to the smallest spot was obtained, and using the calibration map of ECVFL1 current versus the distance  $L$  (Fig. 4.3), the estimate of the screen distance  $L$  is computed. The experimental values obtained for this test with the embedded distance sensor were 12.8 cm, 24 cm, 34 cm, 42 cm, 53 cm, 63 cm, and 71 cm with a measurement error that increased with  $L$ . As we have shown, distance sensing methods based on single spot size observation have limitations if a non-robust image processing algorithm is used [9]. However, better methods can be deployed to increase the distance sensing performance in the proposed display such as by using multi-image acquisition [11] and machine learning algorithms or engaging time of flight laser radar techniques.

#### **4.4 CONCLUSION**

In conclusion, proposed and demonstrated is a novel projection display called a Smart Art Display suitable for projection over multi-distance conformal screen. The system counters issues of loss of resolution, blurring, and distortion when using LSD and DLP/LCD projectors for multi-depth screens. The proposed system includes the use of an ECVFL for in-focus projection within a designed screen depth working range and an embedded distance sensor used for 3-D mapping of the screen projection surface profile. The proposed display can be deployed in artistic creations and art installations where an interaction between the displayed information within a 3-D screen platform and the human observer is desired for a better visual perception. Ultimately, viewers could even create an augmented reality interactive experience with real-time feedback to the display system. Future work includes the use of the robust methods for efficient distance sensing and the implementation of the Smart Art Display in a larger scale all-colour installation.



## REFERENCES

- [1] O. Bimber, A. Emmerling and T. Klemmer, "Embedded entertainment with smart projectors," IEEE Computer Society, vol. 38, no. 1, pp. 48-55, (2005).
- [2] R. Ben-Mrad and D. Pasiliao, "A MEMS micromirror based head-up display system," Symposium on Design, Test, Integration and Packaging of MEMS/MOEMS (DTIP), pp. 1-4 (2015).
- [3] X. C. Wang, S. C. Kong, and R. H. Huang, "Influence of digital equipment on interaction quality in technology-rich classroom," IEEE International Conference on Advanced Learning Technologies (ICALT), pp. 455-459, (2016).
- [4] J. Tauscher , W. O. Davis, D. Brown, M. Ellis, Y. Ma, M. E. Sherwood, D. Bowman, M. P. Helsel, S. Lee, and J. W. Coy, "Evolution of MEMS scanning mirrors for laser projection in compact consumer electronics," SPIE Proceedings, MOEMS and Miniaturized Systems IX, 75940A, (2010).
- [5] Y. Ishii, "The world of liquid-crystal display TVs - Past, present, and future," Journal of Display Technology, vol. 3, no. 4, pp. 351-360, (2007).
- [6] P. F. Van Kessel, L. J. Hornbeck, R. E. Meier, and M. R. Douglass, "A MEMS-based projection display," Proceedings of the IEEE, vol. 86, no. 8, pp. 1687-1704, (1998).
- [7] N. A. Riza, Compressive Optical Display and Imager, US Patent 8,783,874 B1, July 22, 2014.
- [8] N. A. Riza and P. J. Marraccini, "Smart two dimensional laser-based display," Journal of Display Technology, vol. 7, no. 2, pp. 90-95, (2011).
- [9] M. J. Amin and N. A. Riza, "Smart laser scanning sampling head design for image acquisition applications," Applied Optics, vol. 52, no. 20, pp. 4991-4996, (2013).
- [10] J. P. La Torre, B. Bornemann, and N. A. Riza, "Smart optical shape sensor using electronically controlled lens and laser line illumination scanning," IEEE Sensors Journal, vol. 17, no. 4, pp. 1005-1012, (2017).
- [11] N. A. Riza and M. J. Amin, "Multi-image acquisition-based distance sensor using agile laser spot beam," Applied Optics, vol. 53, no. 25, pp. 5807-5814, (2014).

# CHAPTER 5

## AGILE WAVEFRONT SPLITTING INTERFEROMETRY AND IMAGING USING A DIGITAL MICROMIRROR DEVICE<sup>5</sup>

### 5.1 INTRODUCTION

An optical interferometer is a powerful tool used in sensing, measurement and imaging applications. Ideally, an interferometer should be optically phase stable, operate over broadband spectrum (e.g., 350 nm to 2500 nm), and possess spatial and temporal programmability to enable the highest fringe contrast ratio optical interferometric detection. Because of its near common-path nature, the classical wavefront splitting interferometer is an ideal interferometer from a phase stability point-of-view [1-2]. One such wavefront splitting interferometer is the Young's double slit interferometer. Earlier, Prof. Riza's research group has proposed and demonstrated the use of the Texas Instrument (TI) Digital Micromirror Device (DMD) for various non-display applications such as variable delay lines, optical switching, wavelength equalization, imaging, RF photonics, etc [3-33].

In 1997, Prof. Riza's research group has proposed using programmed gratings on the DMD to steer laser light [3]. More recently in 2009, our group proposed the use of the DMD to realize wavefront splitting interferometers as well as a variety of imagers [34]. Very recently, this DMD-based Young's double slit interferometer design has been used to measure spatial coherence of a light source [35] and optical field values at a sample plane [36]. In this chapter, described is an SLM-based interferometer and several imager designs showing also basic experimental results from the [34] DMD-based Young's double slit interferometer design.

---

<sup>5</sup> J. P. La Torre, M. J. Amin and N. A. Riza, "Agile wavefront splitting interferometry and imaging using a digital micromirror device," SPIE Photonics Europe - Optics, Photonics and Digital Technologies for Imaging Applications Conference, 98960B, Belgium, (2016).

## **5.2 SLM-BASED WAVEFRONT SPLITTING INTERFEROMETER DESIGNS**

Shown in Fig. 5.1 is the proposed agile electronically programmable wavefront splitting interferometer designs using a Spatial Light Modulator (SLM) such as (a) a transmissive SLM labelled in Fig. 5.1 with the number 855, (b) a DMD SLM labelled with the number 850 and (c) a Beamsplitter numbered 902 with a DMD SLM numbered as 950. Component numbering notation from the patent application in [34] is maintained to keep the originality of the dated works in [34].

These SLMs operate with on/off or digital state pixels, much like a black and white state optical window to control passage/reflection of incident light. Specifically, SLM pixel locations can be spatially and temporally modulated to create custom wavefronts for near-common path optical interference at an optical detector such as a CCD/CMOS sensor 805, a Focal Plane Array (FPA) sensor or a point photo-detector (PD). Figures 5.1 (a) and (b) show classic Young's double slit (or point) implementations that generate fringes on the optical detection plane. These slit or point light sources on the DMD plane can be placed anywhere on its 2-D SLM plane and can also have different shapes and sizes to optimize fringe visibility.

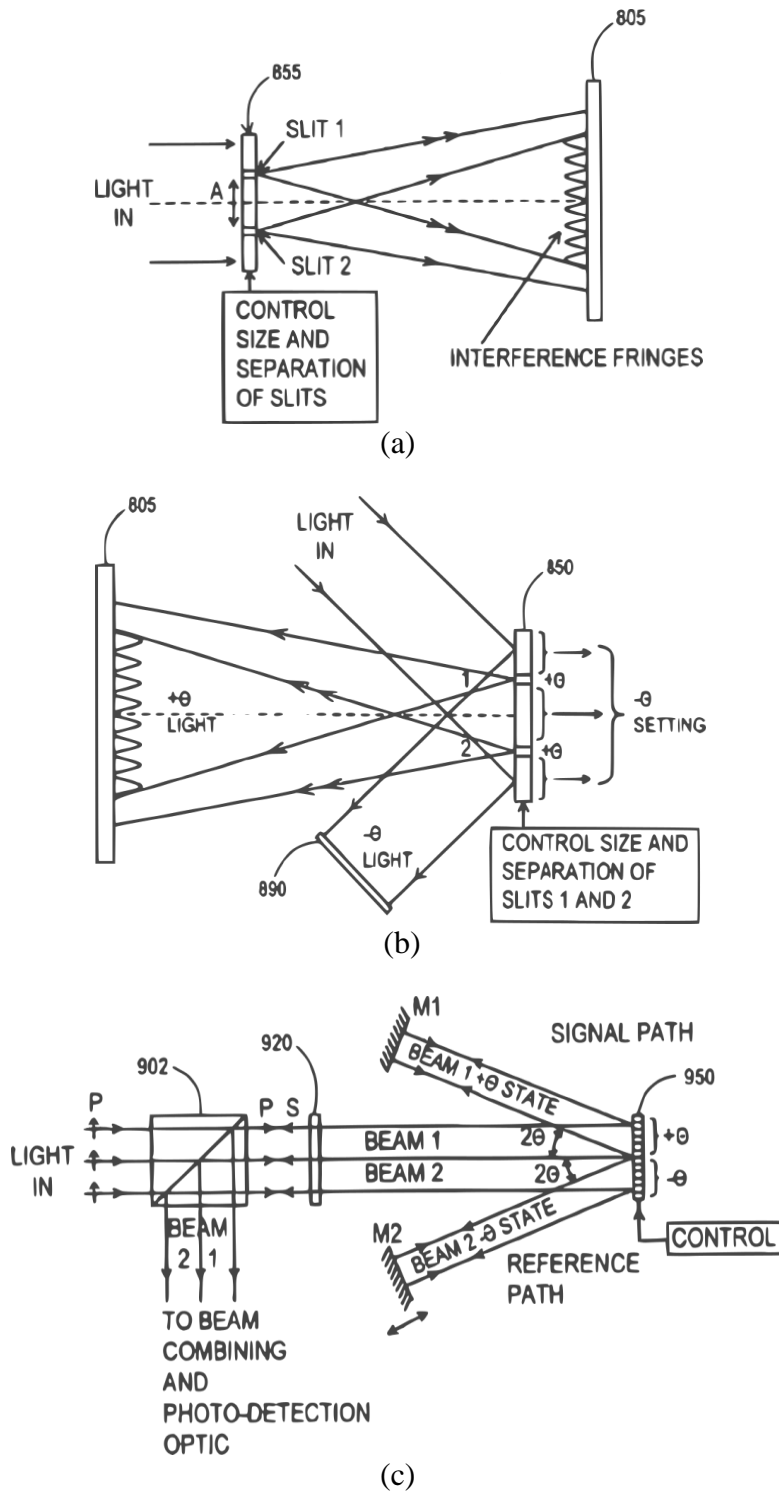


Fig. 5.1. Proposed agile electronically programmable wavefront splitting interferometer designs using a Spatial Light Modulator (SLM) such as (a) a transmissive SLM, (b) a DMD SLM and (c) a Beamsplitter with a DMD SLM. Original version of the shown diagrams can be found in [34].

It is well known that interferometry can not only be used to study the radiation in one of the paths of the interferometer but the system can also be used to study the coherence properties of the light source used to operate the interferometer. Fig. 5.1(c) shows a programmable wavefront splitting interferometer where a collimated horizontally or p-polarized light representing a full wavefront enters a Polarizing Beam Splitter (PBS) and then passes through a Quarter Wave Plate (QWP) to strike the DMD at normal incidence. The DMD is used to produce two separate wavefronts of programmable beam sizes. Each beam follows a separate beam path striking separate mirrors M1 and M2 with M1 in the interferometer signal path and M2 in the reference path. Reflected light from M1 and M2 strikes the DMD which redirects the reflected signal and reference light to the QWP and the PBS. Both light beams now being vertically or s-polarized get deflected by the PBS to enter beam combining and photo-detection optics. For example, the beam combining optics can be a lens and the photo-detection optics can be a point PD. Other types of beam combining optics can also be used such as a beam combining grating optic or a prism and mirror assembly, both engaged with 2-D CCD/CMOS sensor photo-detection. The mirror M2 can also be moved to produce phase shifts such as for scanned Fourier transform spectroscopy, for example, via a Lamellar grating produced by programming alternate pixels of the DMD, one pixel to go to M1 while the adjacent pixel is directed toward M2. Each 2 pixel beam can be combined on its return path via the DMD 950 with a lenslet array to form a multichannel interferometer. Note that it is not necessary that the two beams be side by side. Also, any wavefront division format can be delivered by programming the DMD to control beam powers, shapes, sizes and time duration.

### **5.3 EXPERIMENTAL DEMONSTRATION OF YOUNG'S DOUBLE SLIT INTERFEROMETER**

The programmable Young's double slit interferometer is experimentally implemented in the laboratory using the different setups shown in Fig. 5.2. A 15 mW Melles Griot He-Ne laser having a wavelength of  $\lambda = 633$  nm is used along with collimation optics comprising of a Newport microscope objective model MV-10x having numerical value of 0.25 and magnification of 10x, a 15  $\mu$ m diameter pinhole aperture, and a collimation lens having a 20 cm focal length. The resulting collimated laser beam strikes the SLM at a normal incidence. In particular, the SLM used is the DLP3000 DMD chip which has a pixel pitch of 7.637  $\mu$ m

and a pixel count of 608 by 684 micromirrors that are arranged in a diamond shape structure. Each individual micromirror is programmable and can change its  $\theta = \pm 12^\circ$  tilt orientation angle with respect to the DMD normal. To draw and display the agile Young's slits, the DMD chip is interfaced with a processor.

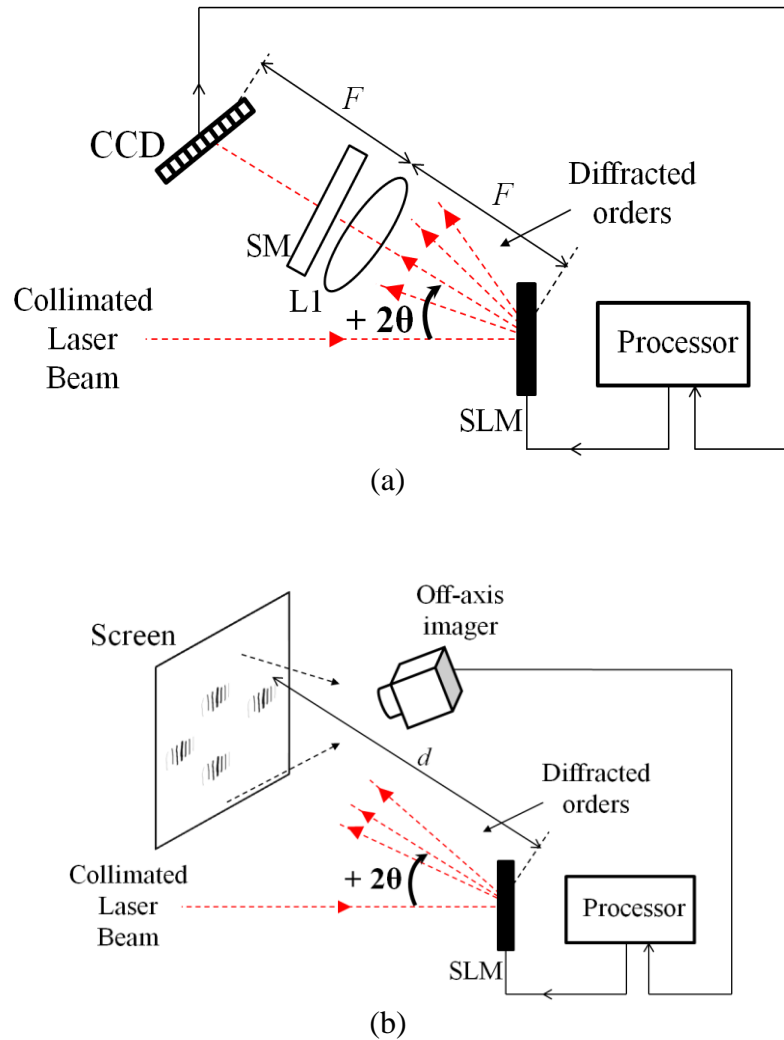


Fig. 5.2. Experimental optical designs (a) and (b) used to demonstrate the proposed DMD-based Young's double slit interferometers.

In the first setup shown in Fig. 5.2(a), a convex lens L1 having focal length  $F_{L1} = 5$  cm is located at a distance  $F = F_{L1}$  from the SLM device and is positioned along the  $+2\theta$  direction. Along the same direction, a target imaging plane represented by a CCD sensor is placed at a distance  $F$  from the lens L1. In such a configuration, the CCD plane represents the Fourier (spatial frequency) transform plane where the SLM is the signal space plane. Additional generic optical module, labelled as Smart Module (SM) as illustrated in Fig. 5.2(a) can be used in the proposed optical design if required. For instance, the SM component used

for this experiment is an optical Neutral Density (ND) filter used to attenuate the light intensity that strikes the CCD sensor in order to avoid saturation issues. The second experimental setup of Fig. 5.2(b) does not use a capturing lens or CCD sensor. Instead, a target screen is deployed for visualization purposes located at a distance  $L = 20$  cm away from the SLM device. An off-axis imager device is used to capture an instant screen shot of the interference pattern on the screen. The imager deployed for the experiment is a commercial Nikon D3300 reflex camera.

A collimated laser beam striking the SLM generates diffraction orders due to the grating nature of the DMD chip. If two slits are displayed/ programmed on the SLM, each of the orders diffracted in the  $+2\theta$  direction contain a corresponding interference pattern due to diffraction at the slits. Such interference patterns can be visualized directly on a CCD sensor as in Fig. 5.2(a) or on the screen as in Fig. 5.2(b). It is important to note here that there are two sets of diffractions occurring simultaneously. One is due to the grating nature of the DMD and the other is due to presence of the programmable slits. In this experiment, the latter, i.e., the interference due to the slits, is of interest.

The flexibility and programmability of the DMD chip deployed as the SLM allows different degrees of freedom in terms of slit dimensions, slit shape, slit separation distance, slit orientation, and number of slits to use. First, the Fig. 5.2(a) setup is implemented in the laboratory. Fig. 5.3 shows a representation of the slits displayed on the DMD and its corresponding interference pattern on the CCD sensor obtained when the slit separation distance  $d$  is equal to  $64.8 \mu\text{m}$  (Fig. 5.3(a)) and  $129.6 \mu\text{m}$  (Fig. 5.3(b)). The thickness of each slit is  $21.6 \mu\text{m}$ . It can be seen in Fig. 5.3 that the location of the diffraction orders due to the grating nature of DMD chip stay the same, but only the interference pattern within each of these orders changes when the slit separation  $d$  is changed.

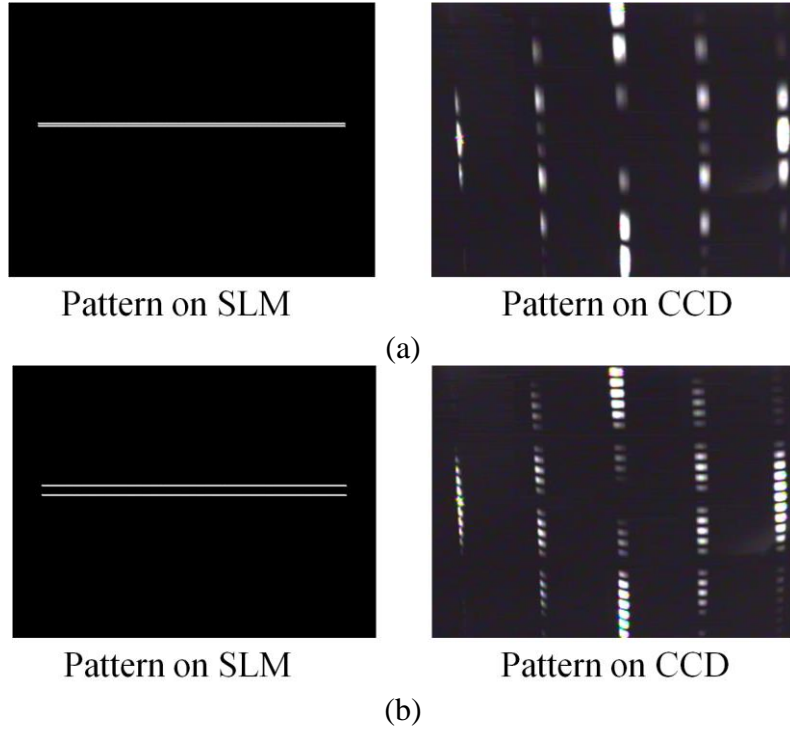


Fig. 5.3. (a) (left) Computer generated image of a double slit that is transferred onto the DMD chip to create two horizontal slits separated by  $64.8 \mu\text{m}$  and the (right) corresponding far-field interference pattern produced on the CCD sensor when a  $633 \text{ nm}$  collimated laser beam is incident on DMD chip. (b) (left) Computer generated image of double slit that is transferred onto the DMD chip to create 2 horizontal slits separated by  $129.6 \mu\text{m}$  and the (right) corresponding far-field interference pattern produced on the CCD sensor when a  $633 \text{ nm}$  collimated laser beam is incident on DMD chip.

Next, the Fig. 5.2(b) setup is deployed. Here, the DMD chip is programmed to display slits having  $d$  values of  $61.09 \mu\text{m}$ ,  $122.19 \mu\text{m}$ ,  $183.29 \mu\text{m}$  and  $244.38 \mu\text{m}$ . The thickness (i.e., width) of each slit is  $30.55 \mu\text{m}$ . Due to the diamond arrangement of the micromirrors on the DMD chip, the programmed slits deployed are oriented following the natural DMD chip structure, i.e. they are diagonally oriented at  $45^\circ$  angle from the DMD chip horizontal. Both slit orientations of  $+45^\circ$  and  $-45^\circ$  are used.

The following equation to evaluate the fringe separation is deployed for the analysis of the Fig. 5.2(b) setup [37]:

$$\lambda = \frac{xd}{nL} \tag{5.1}$$



where  $\lambda$  is the wavelength of the light source,  $x$  represents the distance from the central fringe (which is the one containing the zeroth-order associated to the brightest diffraction spot),  $d$  is the distance between the slits displayed in the SLM device and  $n$  is the order of the fringe.

The Fig. 5.2(b) experimental setup results are displayed in Fig. 5.4. Figure 5.4(a) shows a completely blank pattern programmed on SLM with all micromirrors reflecting light towards the  $+2\theta$  direction and its corresponding off-axis view of the interference pattern striking the screen. Note that this diffraction pattern is only due to the grating nature of the DMD. A ruler is positioned on the screen to aid subsequent measurements. Notice that subsequent interference pattern will appear at each of the order location shown in Fig. 5.4(a) when slits are programmed on the DMD. Figure 5.4(b) shows the programmed diagonally oriented double slit at  $+45^\circ$  on the SLM having  $d = 61.09 \mu\text{m}$  and its corresponding interference pattern on the screen. As expected, an interference pattern due to the programmed double slit is present in each diffraction order of the DMD grating diffraction pattern. Figure 5.4(c) shows the programmed diagonally oriented double slit at  $+45^\circ$  on the SLM having  $d = 247.38 \mu\text{m}$  and its corresponding interference pattern on the screen.

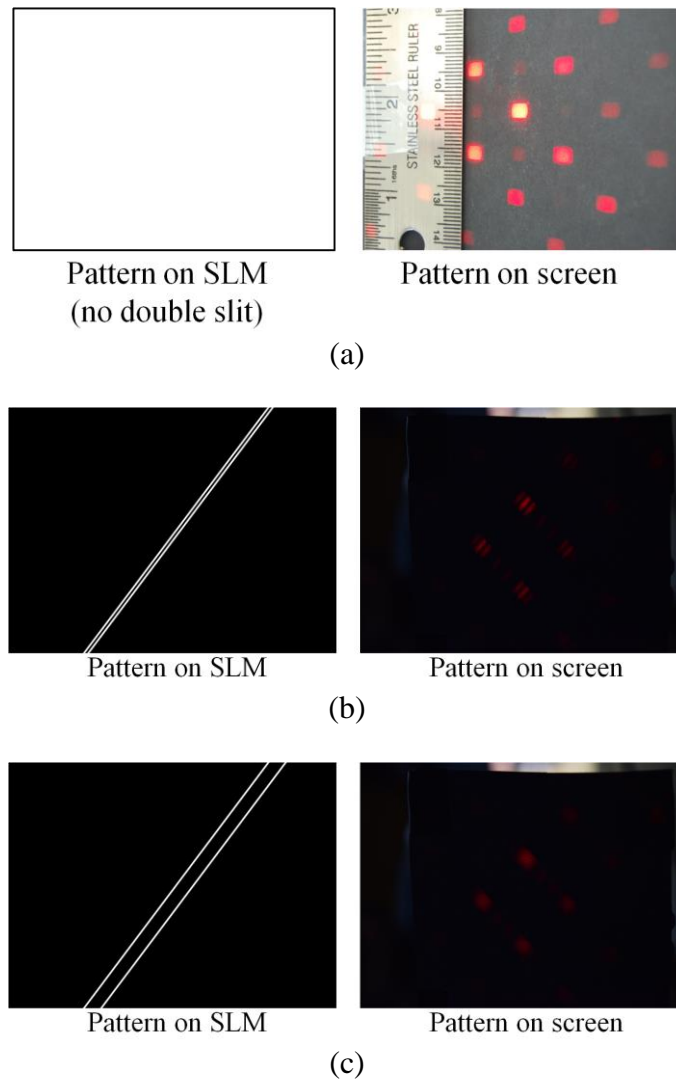


Fig. 5.4. (a) (left) Computer generated image transferred onto the DMD chip representing all the micromirrors that deviates the light towards the screen direction to visualize on screen the diffraction order spots (right). (b) (left) Computer generated image of double slit that is transferred onto the DMD chip to create two diagonally oriented slits at  $+45^\circ$  separated by  $61.09 \mu\text{m}$  and the (right) corresponding far-field interference pattern produced on the CCD sensor when a  $633 \text{ nm}$  collimated laser beam is incident on DMD chip. (c) (left) Computer generated image of double slit that is transferred onto the DMD chip to create two diagonally oriented slits at  $+45^\circ$  separated by  $247.38 \mu\text{m}$  and the (right) corresponding far-field interference pattern produced on the CCD sensor when a  $633 \text{ nm}$  collimated laser beam is incident on DMD chip.

From the experimental findings and by using Eqn. (5.1), a comparison is conducted between the theoretical fringe spacing  $x_{th}$  and the actual experimental fringe spacing  $x_{exp}$  for both diagonal orientations. This comparison is summarized in Table 5.1.

Table 5.1. Experimental versus theoretical fringe separation.

<b>Slit Separation <math>d</math></b>	<b>Theoretical Fringe spacing <math>x_{th}</math></b>	<b>Experimental fringe spacing <math>x_{exp, +45^\circ}</math></b>	<b>Experimental fringe spacing <math>x_{exp, -45^\circ}</math></b>
<b>[<math>\mu\text{m}</math>]</b>	<b>[mm]</b>	<b>[mm]</b>	<b>[mm]</b>
61.09	2.0721	2.1587	2.1746
122.19	1.0361	1.1429	1.0794
183.29	0.6907	0.7619	0.6984
244.38	0.5108	0.5873	0.5397

The results shown in Table 5.1 prove the effectiveness of the programmable SLM device as a programmable Young's double slit interferometer even though the uncertainty error introduced by the measuring tool is evident when increasing the slit separation distance  $d$ . Specifically, one notes that as the fringe separation decreases, the uncertainty of the fringe separation measurement increases.

## 5.4 IMAGING USING 3-D SCANNING APERTURES

As shown in Fig. 5.5 and described earlier [38-40], Three Dimensional (3-D) optical scanners with a laser object illumination source and a single-point detector including the use of optical amplification in the signal processing Transmitter/Receiver chain can be used for active or laser-based imaging of 3-D objects. Here an Electronically Controlled Variable Focus Lens (ECVFL) can be used to electronically translate a scanning pixel along the light propagation axis providing for 3-D image depth information.

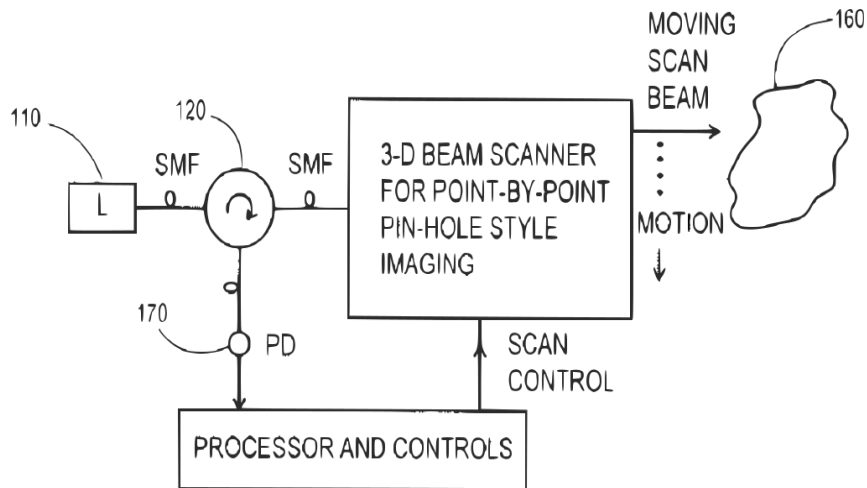


Fig. 5.5. Block diagram of a 3-D imager design using electronic beam 3-D scan/position controls and a single point photo-detector and optical illumination source. An original version of the shown diagram can be found in [40].

Figure 5.6(a) and Fig. 5.6(b) show the module design for implementing a smart camera for 3-D imaging via single point photo-detection and with focus and aperture size control via an ECVFL-SLM combination. The cascaded ECVFL 420 and DMD 450 devices are engaged within a novel design to deliver the powers of a specific application, in this case, a 3-D imager. As shown in Fig. 5.6(a), various transverse image planes at different axial directions (along beam direction) of a 3-D object 460 are imaged on to the DMD plane using a cascade of a fixed lens 430 and the ECVFL 420. Thus, by changing the ECVFL focal length by electronic control 440, a sequence of 2-D images of the object 460 at different axial depths (along the optic-axis of the system) are acquired using pin-hole profiling control of the DMD 450 and the focus/beam collection lens 433 and the single large area point photo detector 470. Thus, the DMD forms a moving pin-hole on the projected 2-D image plane/DMD plane where the object 2-D image occurs for a given axial/depth position of the 3-D object 460.

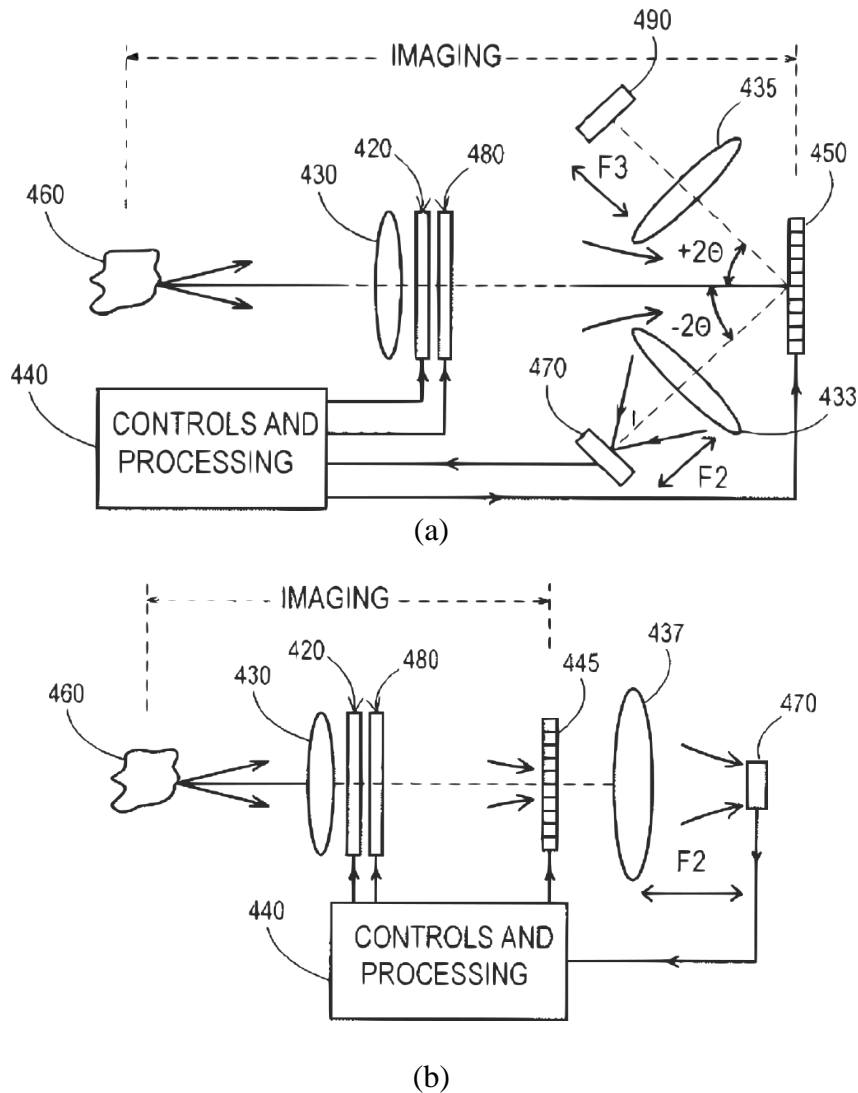


Fig. 5.6. Schematic block diagram of a module for implementing smart camera for 3-D imaging with focus and aperture size control via an ECVFL-SLM combination and single point photo-detection. Options of (a) Reflective SLM and (b) Transmissive SLM. An original version of the shown diagram can be found in [40].

The distance between focus/beam collection lens 433 and photo detector 470 is the focal length  $F2$  of focus/beam collection lens 433. Object light enters at normal incidence on the DMD so the object image forms on the flat DMD plane, ideal for pin-hole sampling of the object 2-D image at a given ECVFL focus. The DMD 450 has  $\pm\theta$  state micromirrors. As shown, the pinhole is formed by assigning the  $-\theta$  state to a select number of micromirrors in a given zone on the DMD 450 so that selected light from the object image is directed to focus/beam collection lens 433 where all this light is captured by photo detector 470 to represent light from a given part of the image zone. All the other micromirrors are set to the  $+\theta$  state so all this light off the projected object image is directed to focus/beam collection lens 435 and physically blocked by a spatial block 490. A color filter 480 cascaded to the

ECVFL 420 can be used to sample object image data on a per color (e.g., red, green, blue) basis. Spatial block 490 can be an electronically controlled LC color filter.

As the DMD 450 can be programmed by an electronic controller 440, the pinhole on the projected image can be made to move across the entire image to form a 2-D point sampler, thus having photo detector 470 produce point-by-point object irradiance data that can be used by the processing electronics 440 to reconstruct the given 2-D image slice. Given the ECVFL varies its focus, plural object 2-D image slices can be reconstructed to make a 3-D image of object 460 and hence realize a 3-D camera. The smallest pin-hole size is a single micromirror while bigger pinhole sizes and needed shapes can be used depending on the object type and imaging quality needed.

Figure 5.6(b) shows a transmissive 3-D camera module design using a liquid crystal LC SLM 445 instead of the DMD shown in Fig. 5.6(a) although the working principles are similar. In this case, light entering the system is linearly polarized for proper LC SLM operations. Typically, the LC SLM 445 consists of two polarizers with LC material layer sandwiched in-between so that no separate external polarizer is needed in some cases of LC SLMs. In this embodiment, the entire 3-D camera is controlled by an electronic controller 440 for optical power detection by the photodetector 470, SLM 445, color filter 480, and ECVFL control, and image processing at the processing and controller electronics 440.

A typical SLM can have 1 million pixels implying 1 million pin-holes can sample a typical projected image falling on the flat SLM surface. Typically, pixels are square or rectangular design, so one can program the SLM to form a variety of pinhole shape such as hexagons, circles, ellipses, etc, to form the point-sampling head/delta function. Fixed lens 430 can be replaced by a mechanically spinning head containing a variety of fixed but different focal length lenses to give more focus power to the 3-D camera module.

Figure 5.7 is a schematic diagram showing the module for implementing combined projector and camera module for 3-D imaging with single point photo-detection. The basic design is the same as Fig. 5.6, except the spatial block 490 is replaced by a light source L1 505 that feeds the DMD projection system. To act as a DMD image projector, a digital image is fed to the DMD 550. Light for projection that carries the chosen image is directed through the path containing the imaging lens combination of fixed lens 530 and ECVFL 520. To generate a 3-D image, one can change the ECVFL focal length to a direct image plane in the 3-D object plane.

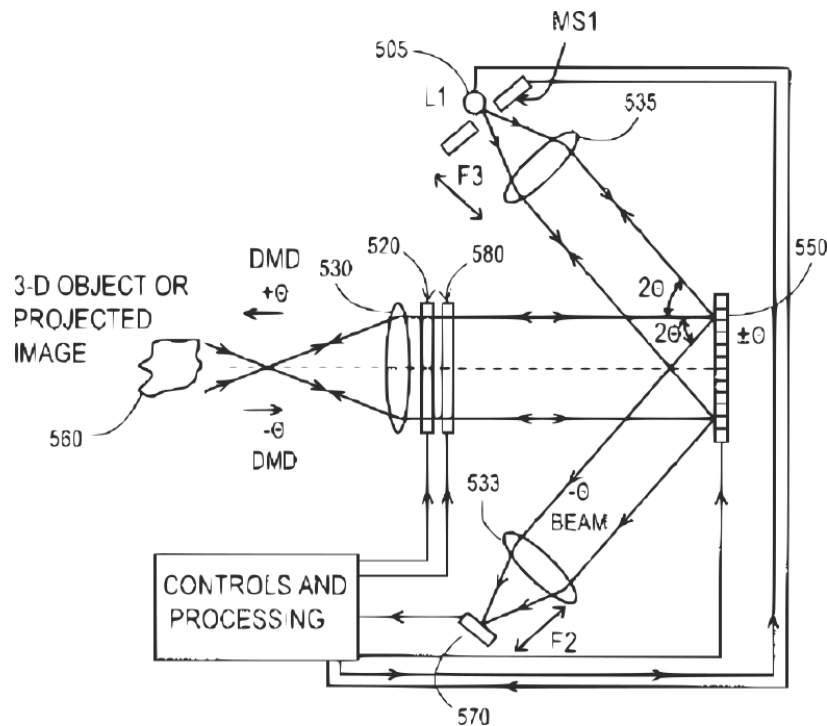


Fig. 5.7. Schematic block diagram of a module for implementing combined projector and camera module for 3-D imaging with single point photo-detection. An original version of the shown diagram can be found in [40].

To actually see a 3-D object, the image planes must get independently illuminated such as via use of a special material that lights up when in this in-focus image plane. To send light through the image projection path, the DMD 550 micromirrors need to be set to their  $+\theta$  state, and any  $-\theta$  state indicates dark parts of the projected image that occur as light is rejected and sent into the collection lens 533 arm where it is collected by photo detector 570. In this projector operation case, photo detector 570 output is inactive or not used for processing. The color filter 580 is set in sequence to the appropriate colors for each image on the DMD 550 to complete the color projection operation.

Alternatively, the color filter 580 can be removed and use three separate color sources in parallel with independent time modulation to generate the design color for the image. To operate the Fig. 5.7 module as a 3-D camera, the light source 505 is turned off and photo detector 570 is turned on to collect the light from the image on the DMD 550 with the DMD operated as a scanning pin-hole to sample the image point-by-point as done in the Fig. 5.6 camera module. The rejected light is directed to collection lens 535 and falls on L1 505. One can also deploy a mechanical shutter MS1 in front of the L1 505 to act as a beam block like spatial block 490 in Fig. 5.6. Thus, the module forms both a 3-D camera and a 3-D image

projector. In its basic mode with ECVFL inactive, the module forms both a 2-D camera via a point detector and a 2-D image projector.

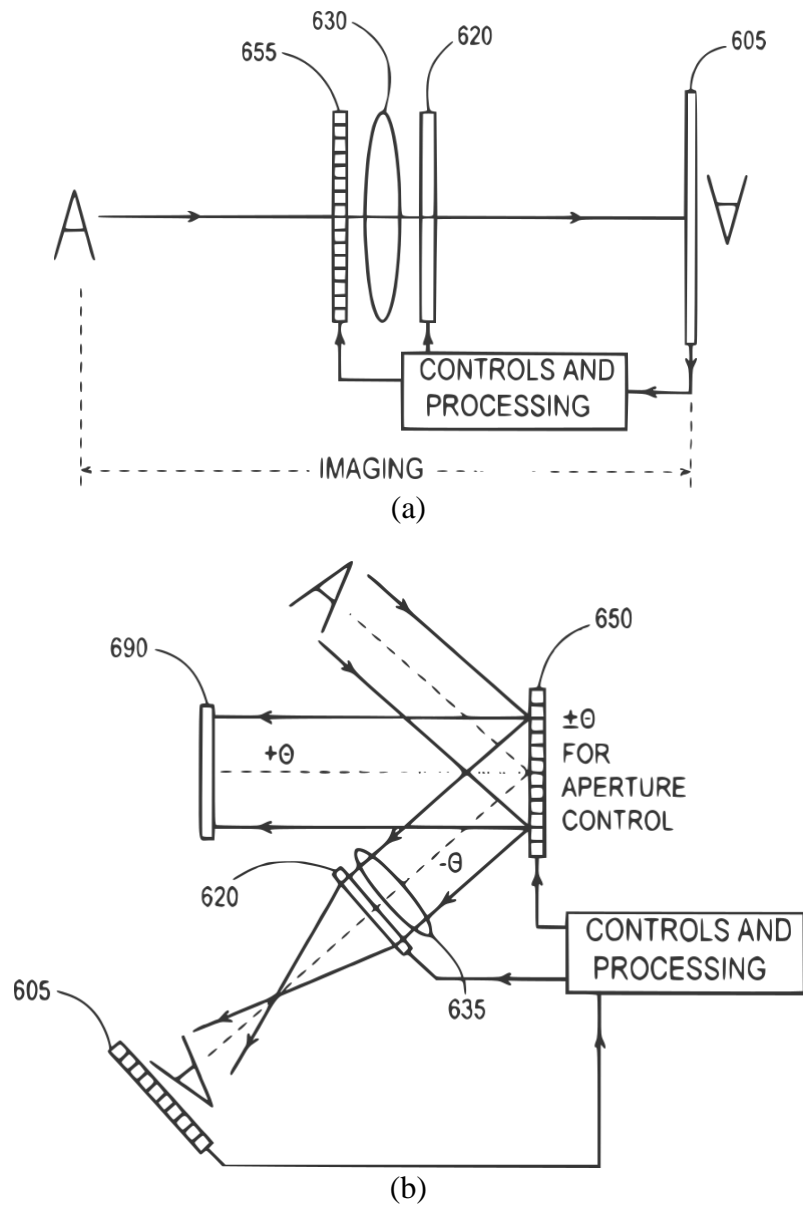


Fig. 5.8. Schematic block diagram of a module for implementing a lens-based aperture controlled camera with a digital 2-D SLM and 2-D detector array. An original version of the shown diagram can be found in [40].

Figures 5.8(a) and 5.8(b) shows the proposed module for implementing a classic lens-based aperture controlled camera with a digital 2-D SLM and 2-D detector array. Figure 5.8(a) uses a transmissive LC SLM 655 cascaded with a fixed imaging lens 630 and an ECVFL 620. The SLM 655 produces a controlled aperture for the imaging camera 605 to



control light throughput. The ECVFL 620 provides image focus control. Fixed lens 630 with the ECVFL 620 acts as the imaging lens that transfer the object plane to the CCD imager plane. The CCD 605 is a 2-D detector array. Figure 5.8(b) shows a similar aperture controlled camera module as Fig. 5.8(a) apart from the fact that the SLM 655 is a reflective DMD 650 and the optical design is reflective.

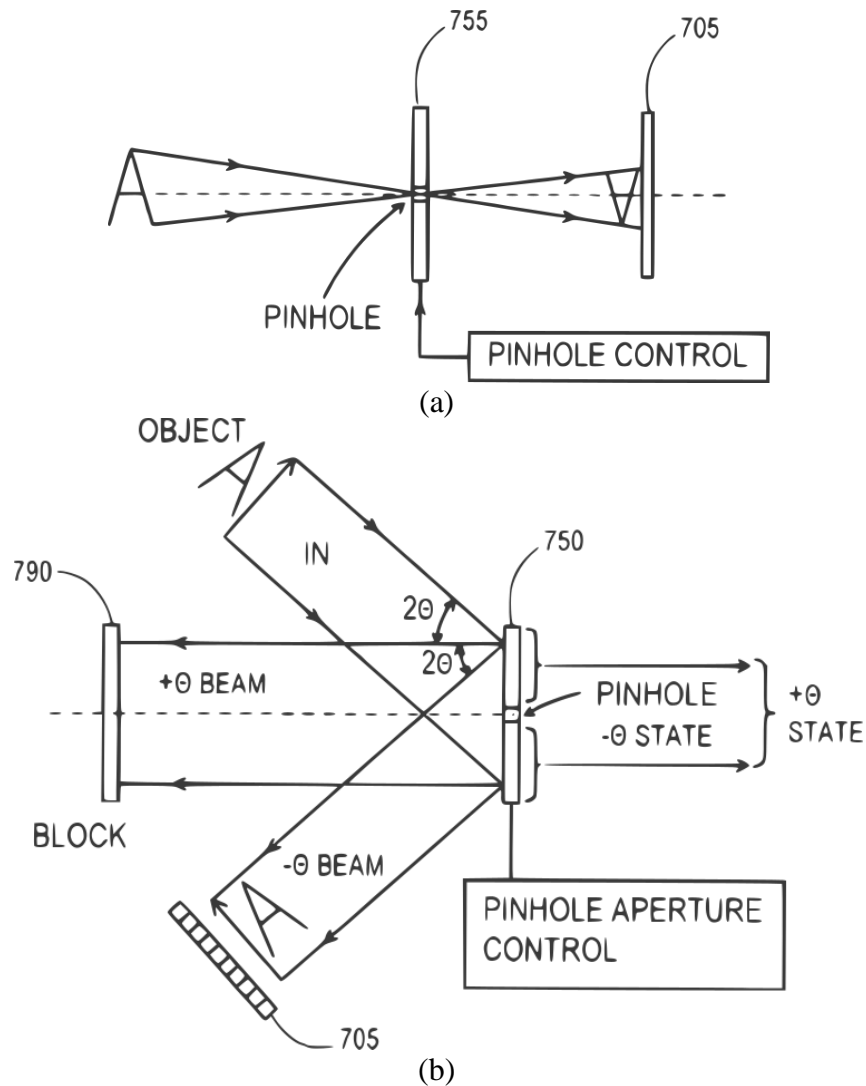


Fig. 5.9. Schematic block diagram of a module for implementing a lens-less pinhole camera with a digital 2-D SLM and 2-D detector array. An original version of the shown diagram can be found in [40].

Figure 5.9 is a schematic diagram showing the module for implementing a classic lens-less pinhole camera with a digital 2-D SLM and 2-D detector array. Unlike the Figs. 5.8(a) and 5.8(b) modules, the Fig. 5.9(a) and 5.9(b) configurations contain no lens for

imaging. The imaging operation is produced by using the LC SLM 755 as a controlled size pinhole at the center of the SLM 655, making a classic Al-Hazen pinhole camera [41], but with an electronically programmable pinhole size to produce the best quality image in terms of focus, Field-of-View, etc. The Fig. 5.9(a) lens-less pinhole camera module uses a LC SLM 755 and CCD 705 while the Fig. 5.9(b) module design includes a DMD 750, CCD 705, and spatial block 790. The LC SLM 755 has polarizers, much like a LC display to act a light on/off shutters on a SLM pixel basis. The DMD 750 uses the  $-\theta$  state of micromirrors to represent the pinhole that then directs the light coming from the object to travel to the CCD 705. The remaining micromirrors are set to the  $+\theta$  state to send light away from the CCD 705 and to the light block 790.

Do note that for all the presented modules that use timed photo-detection to integrate light, the DMD can also operate as a timed on/off shutter due to its fast programming speeds. Hence, apart from controlling the speed of the photo-detector integration times, the DMD can also be engaged to modulate the light signals in time to produce powerful image processing effects.

## 5.5 CONCLUSION

Proposed is the design of a programmable SLM-based wavefront splitting interferometer such as a Young's double slit interferometer. Using the DMD as the SLM, demonstrated is a programmable Young's double slit interferometer that offers complete programmability over slit properties such as slit size, slit shape, slit width, slit time and number of slits. Other advantages of the demonstrated interferometer is its 100% spatial repeatability of the slits and the ability for the DMD to handle high power broad spectrum incident light. Given the demonstrated interferometer's cost effectiveness and operational reliability, it can serve as a demonstration unit for optics education in schools and universities. This chapter has also presented several imager designs using 3-D scanning apertures. Specifically, these imager designs are empowered by using a combination of components including SLMs, ECVFLs, lenses, apertures, colour filters, CCD/CMOS sensors, and single point photo-detectors. Future work relates to the design and experimental demonstration of the proposed design modules for agile interferometry and imaging.

## REFERENCES

- [1] M. Francon, *Optical Interferometry*, Academic Press, New York & London, 1966.
- [2] P. Hariharan, *Optical Interferometry*, Academic Press, San Diego & London, 2003.
- [3] N. A. Riza, "Coherent techniques and deformable-mirror device (DMD)-based switched photonic time delay control for high frequency antenna arrays," *SPIE Conference on Optical Technology for Microwave Applications VIII*, vol. 3160, pp. 97-105, (1997).
- [4] N. A. Riza and S. Sumriddetchkajorn, "Fault tolerant dense multi-wavelength add/drop filter using a two dimensional digital micromirror device," *Applied Optics-LP*, vol. 37, no. 27, (1998).
- [5] N. A. Riza and S. Sumriddetchkajorn, "Fault tolerant polarization insensitive photonic delay line architectures using two dimensional digital micromirror devices," *Optics Communications*, vol. 160, pp. 311-320, (1999).
- [6] N. A. Riza and S. Sumriddetchkajorn, "Digitally controlled fault tolerant multiwavelength programmable fiber-optic attenuator using a two dimensional digital micromirror devices," *Optics Letters*, vol. 24, no. 5, (1999).
- [7] N. A. Riza and S. Sumriddetchkajorn, "Small tilt micromirror device-based multiwavelength three dimensional 2x2 fiber-optic switch structures," *Optical Engineering*, vol.39, no. 2, pp. 379-386, (2000).
- [8] N. A. Riza and S. Sumriddetchkajorn, "Micromechanics-based wavelength-sensitive photonic beam control architectures and applications," *Applied Optics*, vol. 39, no. 6, pp. 919-932, (2000).
- [9] S. Sumriddetchkajorn and N. A. Riza, "Fault-tolerant three-port fiber-optic attenuator using small tilt micromirror device," *Optics Communications*, vol. 205, no. 1-3, pp. 77-86, (2002).
- [10] S. Sumriddetchkajorn and N. A. Riza, "Micro-electro-mechanical system-based digitally controlled optical beam profiler," *Applied Optics-LP*, vol. 41, no. 18, (2002).
- [11] N. A. Riza and M. J. Mughal, "Broadband optical equalizer using fault tolerant digital micromirrors," *Optics Express*, vol. 11, pp. 1559-1565, (2003).
- [12] N. A. Riza and M. A. Arain, "Programmable broadband radio-frequency transversal filter with compact fiber-optics and digital microelectromechanical system-based optical spectral control," *Applied Optics*, vol. 43, no. 15, pp. 3159-3165, (2004).

- [13] N. A. Riza and F. N. Ghauri, "Hybrid analog digital MEMS fiber optic variable attenuator," *IEEE Photonic Technology Letters*, vol. 17, no. 1, pp. 124-126, (2005).
- [14] N. A. Riza and F. N. Ghauri, "Super resolution variable fiber-optic attenuation instrument using digital micromirror device," *AIP Review of Scientific Instruments Journal*, vol. 76, no. 1, (2005).
- [15] N. A. Riza and F. N. Ghauri, "Super resolution hybrid analog-digital optical beam profiler using digital micro-mirror device," *IEEE Photonics Technology Letters*, vol. 17, no. 7, pp. 1492-1494, (2005).
- [16] M. A. Arain and N. A. Riza, "Optoelectronic approach to adaptive radio frequency transversal filter implementation with negative coefficients by using optical spectrum shaping," *Applied Optics*, vol. 45, no. 11, (2006).
- [17] S. A. Khan and N. A. Riza, "Demonstration of a MEMS digital micromirror device-based broadband reconfigurable optical add-drop filter for dense wavelength division multiplexing systems," *IEEE Journal of Lightwave Technology*, vol. 25, no. 2, pp. 520-526, (2007).
- [18] N. A. Riza and S. A. Reza, "Hybrid analog-digital design microelectromechanical systems spectral processor for simultaneous gain slope and channel equalization controls," *Optical Engineering*, vol. 46, no. 3, (2007).
- [19] N. A. Riza and S. A. Reza, "Smart value-added fiber-optic modules using spatially multiplexed processing," *Applied Optics*, vol. 46, no. 18, pp. 3800-3810, (2007).
- [20] N. A. Riza and S. A. Reza, "Broadband all-digital variable fiber-optic attenuator using digital micro-mirror device," *IEEE Photonics Technology Letters*, vol. 19, no. 21, pp. 1705-1707, (2007).
- [21] N. A. Riza and F. N. Ghauri, "High resolution tunable microwave filter using hybrid analog-digital controls via an acousto-optic tunable filter and digital micromirror device," *IEEE Journal of Lightwave Technology*, vol. 26, no. 17, pp. 3056-3061, (2008).
- [22] N. A. Riza and S. A. Reza, "High-dynamic-range hybrid analog-digital control broadband optical spectral processor using micromirror and acousto-optic devices," *Optics Letters*, vol. 33, no. 11, pp. 1222-1224, (2008).
- [23] M. Sheikh and N. A. Riza, "Demonstration of pinhole laser beam profiling using a digital micromirror device," *IEEE Photonics Technology Letters*, vol. 21, no. 10, (2009).

- [24] S. A. Reza and N. A. Riza, "High dynamic range variable fiber optical attenuator using digital micromirrors and opto-fluidics," *IEEE Photonics Technology Letters*, vol. 21, no. 13, pp. 845-847, (2009).
- [25] M. Sheikh and N. A. Riza, "Motion-free hybrid design laser beam propagation analyzer using a digital micro-mirror device and a variable focus liquid lens," *Applied Optics*, vol. 49, no. 16, pp. D6-D11, (2010).
- [26] N. A. Riza, S. A. Reza and P. J. Marraccini, "Digital micro-mirror device-based broadband optical image sensor for robust imaging applications," *Optics Communications*, vol. 284, no. 1, pp. 103-111, (2011).
- [27] P. J. Marraccini and N. A. Riza, "Multimode laser beam analyzer instrument using electrically programmable optics," *AIP Review Scientific Instruments Journal*, vol. 82, no. 12, 123107, (2011).
- [28] N. A. Riza, P. J. Marraccini, and Cody Baxley, "Data efficient digital micromirror device-based image edge detection sensor using space-time processing," *IEEE Sensors Journal*, vol. 12, no. 5, pp. 1043-1047, (2012).
- [29] N. A. Riza, "Application intelligence-based imaging using programmable photonics," *Photonics Ireland Conference Proceedings*, Belfast, (2013).
- [30] J. P. La Torre, M. J. Amin, M. Magno and N. A. Riza, "An embedded smart agile pixel imager for lasers," *6th European Embedded Design in Education and Research Conference (EDERC)*, pp. 230-234, (2014).
- [31] M. J. Amin, J. P. La Torre, and N. A. Riza, "Embedded optics and electronics single digital micromirror device-based agile pixel broadband imager and spectrum analyser for laser beam hotspot detection," *Applied Optics*, vol. 54, no. 12, pp. 3547-3559, (2015).
- [32] N. A. Riza, M. J. Amin, and J. P. La Torre, "Coded Access Optical Sensor (CAOS) Imager," *Journal of the European Optical Society (JEOS) Rapid Publications*, vol. 10, 15021, (2015).
- [33] N.A. Riza and P.J. Marraccini, "Programmable optic-based robust underwater/free-space optical data transfer link designs for applications using high power lasers," *Photonics Ireland Conference Proceedings*, (2015).
- [34] N. A. Riza, "Agile optical image sensing, control, and measurement modules," *USA Patent Application no. 61/258,344*, (2009).
- [35] H. Partanen, J. Turunen, and J. Tervo, "Coherence measurement with digital micromirror device," *Optics Letters*, vol. 39, no. 4, (2014).

- [36] G. Vdovin, H Gong, O Soloviev, P Pozzi and M Verhaegen, "Lensless coherent imaging by sampling of the optical field with digital micromirror device," UK IOP Journal of Optics, vol. 17, 122001, pp.1-5, (2015).
- [37] E. Hecht, Optics, 4<sup>th</sup> Edition, Pearson, 2002. Chapter 10: Diffraction.
- [38] N. A. Riza, "BOPSCAN technology: A methodology and implementation of the billion point optical scanner," Proceedings SPIE 3482, International Optical Design Conference (IODC), 572, (1998).
- [39] N. A. Riza and Yu Huang, "High speed optical scanner for multi-dimensional beam pointing and acquisition," in LEOS IEEE Annual Meeting Conference Proceedings, vol. 1, pp. 184-185, (1999).
- [40] N. A. Riza, "Multiplexed optical scanner technology," Patent No. 6 687 036, Feb. 3, 2004.
- [41] A. Mark Smith, "Alhacen's theory of visual perception: A critical edition" Transactions of the American Philosophical Society New Series, vol. 91, no. 4, (2001).



## CHAPTER 6

### AN EMBEDDED SMART AGILE PIXEL IMAGER FOR LASERS<sup>6</sup>

#### 6.1 INTRODUCTION

Over the years, the contribution of laser beams in shaping our everyday lives has increased dramatically. They are used in aircraft, automobile, construction, and security industries for a variety of applications. These include manufacturing, cutting, drilling, sensing, and tracking applications key to the design of many products of modern systems. In order to use laser beams effectively in these applications, it is important to know exactly the properties and characteristics of a particular laser beam. For a Gaussian laser beam which is commonly used in industries, these properties may include the  $1/e^2$  width of the laser beam. As a Gaussian beam propagates through an optical system, the beam width, and possibly the beam transverse intensity distribution depends on optical components, and changes with respect to distance. It is important to track and measure these developments in beam profile so that the laser beam can be optimized and tailored to suit potential applications.

There is extensive literature on various techniques deployed over the years to characterise a laser beam's transverse profile [1-8]. Common techniques used for laser imaging purposes include mechanical knife edge profiling, slit profiling and image sensors such as using a CMOS or CCD chip placed at the laser beam cross-section. Issues of repeatability, resolution and consistency arise in mechanical motion based profilers such as the moving knife-edge and slit profilers. Knife-edge profilers assume the laser beam is perfectly Gaussian and Slit profilers suffer from data interpolation uncertainty as the acquired slices of optical irradiance maps are image processed to predict the viewed laser beam profile. CMOS chip or CCD based profilers require a laser beam to be attenuated in order for the sensors to avoid saturation or damage. This may cause unwanted effects on the beam

---

<sup>6</sup> J. P. La Torre, M. J. Amin, M. Magno and N. A. Riza, "An embedded smart agile pixel imager for lasers," 6th European Embedded Design in Education and Research Conference (EDERC), pp. 230-234, Italy, (2014).



profile as a result of placing attenuating optical components. For high power lasers, i.e. >100 mW, these sensors are less effective in giving an accurate and exact profile due to the large amount of beam attenuation required.

A new imaging technique based on the use of a Digital Micromirror Device (DMD) has been proposed and demonstrated in the knife edge and pinhole scan modes [9-12]. This imager is able to withstand high laser powers without the need of attenuation or disruptions in the beam path, and has demonstrated high repeatability and accuracy in providing two dimensional (2-D) laser beam irradiance at any cross section along the beam propagation axis. In this chapter, an embedded version of the imager for laser beam mapping is presented.

Embedded systems have been recognised as a fundamental enabling technology for a wide range of Cyber-Physical System (CPS) applications such as healthcare, security, entertainment industrial domains and others, due especially to the capability to perform real time digital signal processing in small size devices. Each device embodies an embedded general purpose processor that integrates computing, analog/digital converters and several other peripherals in order to collect and process data from the external world, generally collaborating to coordinate activities with other devices.

Combining embedded device advances with mature techniques to monitor and detect laser beam profiles allows the development of high accuracy, low cost and small size devices [13-16]. In this chapter, presented is the design and implementation of a low cost and low power embedded system to achieve a high accuracy smart agile pixel imager for laser beam profiling. The proposed approach significantly extends the state-of-the-art with respect to embedded hardware and software co-design of such systems, combining an ultralow power microcontroller from Texas Instruments (TI) with a TI DMD chip through the novel integration of state-of-the-art profiling techniques directly processed on board. This innovation to the best of our knowledge is notable as it is the first such embedded digital processing system proposed in the literature.

This chapter is organized as follows. The architecture of the system along with a brief description of the Gaussian laser beam is presented in section 6.2. Section 6.3 focuses on the description of individual experimental components used for the proposed embedded systems based profiler demonstration, as well as the experimental setup and results. Finally, section 6.4 states the conclusions and the applications of the proposed embedded system based imager.

## 6.2 PROPOSED EMBEDDED SYSTEM BASED SMART AGILE PIXEL IMAGER DESIGN

A basic block diagram representing the proposed embedded system based imager is shown in Fig. 6.1. Light from a test laser strikes a DMD chip consisting of a 2-D array of micromirrors which offer high reflectivity to incoming light. The orientation of each micromirror can be individually programmed to either a  $+\theta$  direction, reflecting light towards Photodetector 1 (PD1), or  $-\theta$  direction to reflect light towards PD2. Light striking the photodetectors generates a current proportional to the amount of light intensity falling on them. This current is translated to a voltage in the PD circuitry block shown in Fig. 6.1. The two voltage values, one for each PD, are read into a micro-controller via its Analog-to-Digital Converter (ADC) ports. The micro-controller is responsible for programming the micromirror orientation on the DMD chip, detecting the PD circuitry generated voltage, and analysing the acquired data to extract meaningful results. This acquired data is stored for further processing using a Personal Computer (PC). A detailed account of the system is presented in section 6.3 which discusses experimental implementation of the proposed Fig. 6.1 imager. A brief overview of the imaging procedure is stated next.

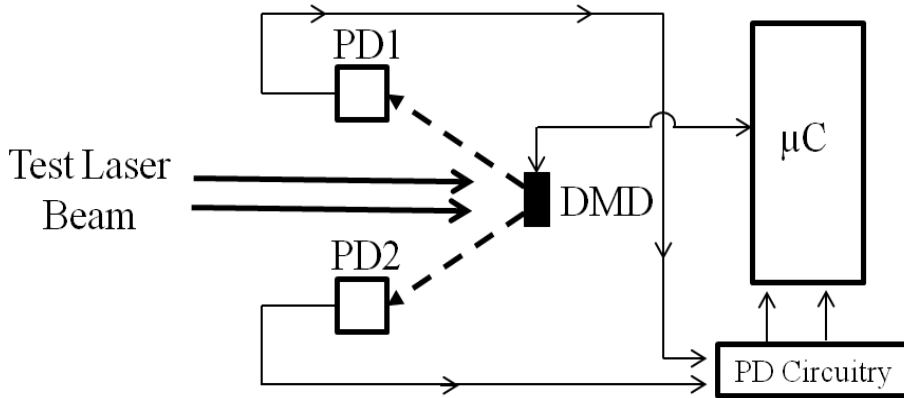


Fig. 6.1. Proposed embedded smart agile pixel imager block diagram.

### 6.2.1 LASER BEAM IMAGING PROCESS

With a test laser beam falling on the micromirror array, the DMD chip is programmed such that only one micromirror set (can be composed of multiple individual micromirrors) out of the 2-D micromirror array is oriented at  $+\theta$  direction, while all the other micromirrors in the chip are in the  $-\theta$  state. PD1 will detect light falling on just this micromirror set, or agile pixel, in  $+\theta$  state. This PD1 reading is assigned as the intensity falling onto that micromirror set coordinate on the chip. Next, a different micromirror pixel set is oriented to

+ $\theta$  direction, while the remaining are in  $-\theta$  state. In other words, the agile pixel is at a different location. PD1 records the laser intensity for this different micromirror set only, thereby allowing the micro-controller to assign this new PD1 value to this second coordinate on the grid. This process, i.e., orientating each micromirror, and detecting and storing corresponding light intensity via micro-controller, is repeated for all micromirrors giving a complete 2-D irradiance pattern of the laser beam representing the beam cross section at the imaging plane (plane of the DMD chip). Such a scan is known as a pinhole scan, reminiscent of a moving pinhole or agile pixel across the DMD chip. With no need of attenuating components, and the ability to acquire the actual 2-D laser beam intensity profile instead of a 1-D profile (e.g., via slit or knife-edge methods), this proposed laser imaging technique gives the true irradiance values in the beam cross section.

### 6.2.2 GAUSSIAN LASER BEAM

Gaussian laser beams are commonly used in laser based industrial applications. This type of beam's cross section beam intensity is  $I(x, z)$ , where  $x$  is the transverse coordinate and  $z$  is the propagation distance, it is approximated by a Gaussian function and is given in one dimension (1-D) by [17]:

$$I(x, z) = A(z) \exp\left[-\frac{2(x - x_0)^2}{w(z)^2}\right], \quad (6.1)$$

where  $A(z)$  is the amplitude and  $w(z)$  is the  $1/e^2$  beam radius at a particular  $z$ . A 1-D plot representing a Gaussian beam transverse profile with normalized amplitude is given in Fig. 6.2(a). Note that the  $1/e^2$  diameter  $2w$  stated in Fig. 6.2(a) is an important feature of a transverse Gaussian beam profile at a given distance. A 2-D transverse profile of a Gaussian beam is simulated and plotted in MATLAB [18] and shown in Fig. 6.2(b). From an industrial manufacturing point of view, the intensity distribution of a laser at the cutting/drilling plane needs to be shaped a certain way, in order to reduce unwanted optical power and material losses to give the required performance. If a Gaussian laser is used, it is important for the shape and width of the Gaussian beam to be verified before initiating any manufacturing process. In the next section, an experimental prototype imager is presented which is tailor made for exactly this purpose.

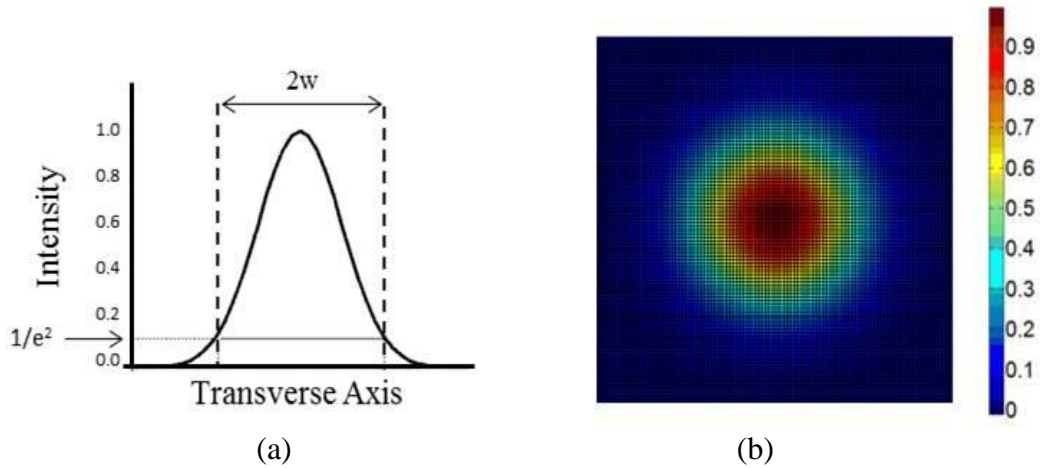


Fig. 6.2. (a) A simulated 1-D Gaussian beam intensity distribution showing the  $1/e^2$  beam width  $2w$ , (b) A simulated 2-D cross-section of a Gaussian laser beam intensity distribution using (a) for orthogonal axes of irradiance map.

### 6.3 EXPERIMENTAL EMBEDDED BASED LASER BEAM IMAGER SETUP COMPONENTS

An experimental prototype of the proposed embedded based laser beam imager is shown in Fig. 6.3. The different components used in this experimental setup are stated below and described in detail.

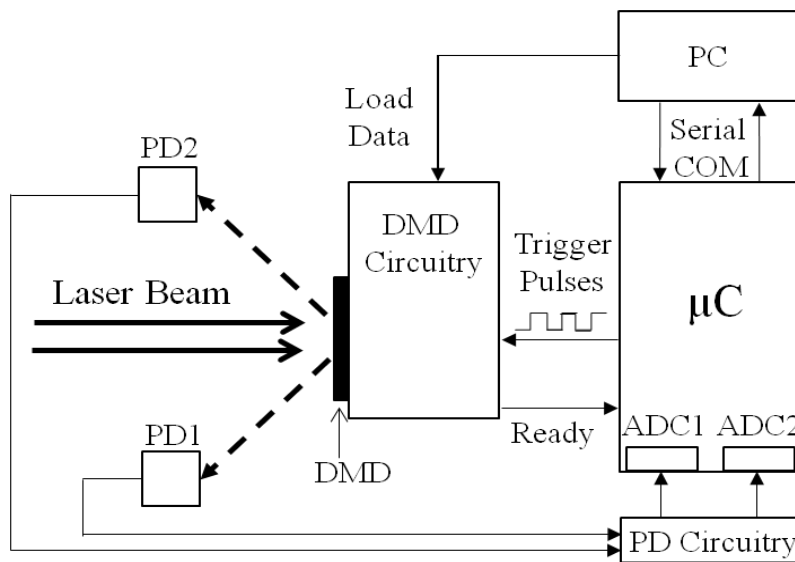


Fig. 6.3. Detailed experimental block diagram of proposed embedded imager.

### **6.3.1 TI DLP LIGHTCRAFTER EVALUATION BOARD**

Texas Instrument (TI) DLP LightCrafter evaluation board is used as the DMD Chip with model number DLP3000. The chip itself has physical dimensions of 3.7 mm (height) per 6.6 mm (width). In terms of micromirrors, the chip has 608 x 684 micromirrors. These micromirrors are arranged in a diamond arrangement over the chip, with each micromirror being 7.64  $\mu\text{m}$  x 7.64  $\mu\text{m}$ . The chosen coordinate system for this diamond configuration has its x and y axes rotated 45 degrees with respect to the horizontal edge of the chip. A Graphical User Interface (GUI) programmed in the PC loads images onto the DMD via the LightCrafter TCP/IP interface. The nature of these images dictates the orientation of the micromirrors. Black pixels in the image cause corresponding micromirrors to point to  $+\theta$  direction while white pixels correspond to micromirrors in the  $-\theta$  state. Once a series of images are loaded onto the LightCrafter on-board memory, the micro-controller is able to cycle (scan) through them and collect corresponding PD readings. Note that these images need to be carefully chosen to complete the imaging process described earlier within the practical limitations of the hardware such as the on board memory on the LightCrafter dictating the amount of images allowed to be stored.

### **6.3.2 MSP-EXP430FR5969 LAUNCHPAD EVALUATION KIT**

The micro-controller used in the experimental setup is the MSP430FR5969, in particular, the FR5969 LaunchPad evaluation module (EVM) that has on it several ADC channels, each featuring 12 bits of resolution. For profiling purposes, only two of them are used, one for each PD. An important function of the micro-controller in the setup is managing the synchronisation between the running through images on the DMD and acquiring PD voltage via ADC ports. The microcontroller is programmed to send to the LightCrafter evaluation board a certain number of pulses that correspond to the total number of images that are to be displayed on the DMD chip. This number is set using the GUI developed. In order to avoid damage to the ADC ports, the analog input signal from the PD circuitry cannot exceed the saturation voltage of the micro-controller. A buffer configuration block has been included in the voltage signal's path through PD circuitry with the gain set to 1, before the signal is taken up by the ADC. The operational amplifier used for the buffer configuration does not allow the PD voltage to exceed the micro-controller saturation voltage threshold. An additional advantage of the buffer configuration is to provide impedance isolation between the PD and the micro-controller.

### **6.3.3 PHOTODETECTOR**

For the experimental prototype system, two Thorlabs SM05PD1A silicon based photodiodes are deployed as PDs. Each of them has a spectral response range from 350nm to 1100nm. The output voltage level given by the PD circuitry depends on the input laser optical power on the chip and the load resistance chosen in the deployed PD circuit.

### **6.3.4 SYNCHRONOUS COMMUNICATION**

A Direct Memory Access (DMA) ensures synchronous communication between the scanning of images on the DMD chip and the PD voltage acquisition by the micro-controller ADC. The DMA is controlled by a timer (TIM) which has its frequency set by the GUI. The same TIM in this scenario controls both the ADC sampling time and the image frame speed in the LightCrafter (DMD). TIM properties such as pre-scaler and period are initially set accordingly by the GUI. The image frame rate of the LightCrafter limits the overall profiling speed of the system. In this case, the frame rate on the DMD is set to 50 Hz to guarantee correct operation and allow a large amount of images. Moreover, during the ADC sampling execution process, another task managed by the system is serial communication. Data relating to the beam profile is sent through a serial port into a peripheral such as a PC where the GUI is designed to receive this data and eventually execute post processing operations. Powerful tools such as MATLAB can be used to perform analyses of the data received and plotting actions.

## 6.4 EXPERIMENTAL DEMONSTRATION

For the experimental demonstration of the prototype embedded systems based imager, a Helium-Neon 05-LHP-991 Melles Griot laser is used, having a wavelength of 632.8 nm and optical power of 15 mW. Initially, a beam profile is captured using the proposed imager at a distance of  $d_0 = 50$  cm from the exit of the laser module, as shown in Fig. 6.4(a). The 2-D irradiance map at  $d_0 = 50$  cm is acquired using a 3 x 3 micro-mirrors set pinhole size, scan rate of 50 Hz and a total number of 5,306 images, and is shown in Fig. 6.4(b). By fitting Gaussian beam equations in MATLAB onto this acquired irradiance map, the  $1/e^2$  beam diameters in both x and y dimensions are found to be 887.6  $\mu\text{m}$  and 897.8  $\mu\text{m}$ , respectively. The theoretically predicted value of the beam radius for this distance is 906 microns. Next, as part of the demonstration, a lens of focal length 20 cm is inserted in the laser path, and placed at a distance  $d_1 = 30$  cm from the exit of the laser module as shown in Fig. 6.5. The lens concentrates or focuses the optical power of the laser at around  $d_2 = 20$  cm, before the laser diverges as  $d_2$  is increased.

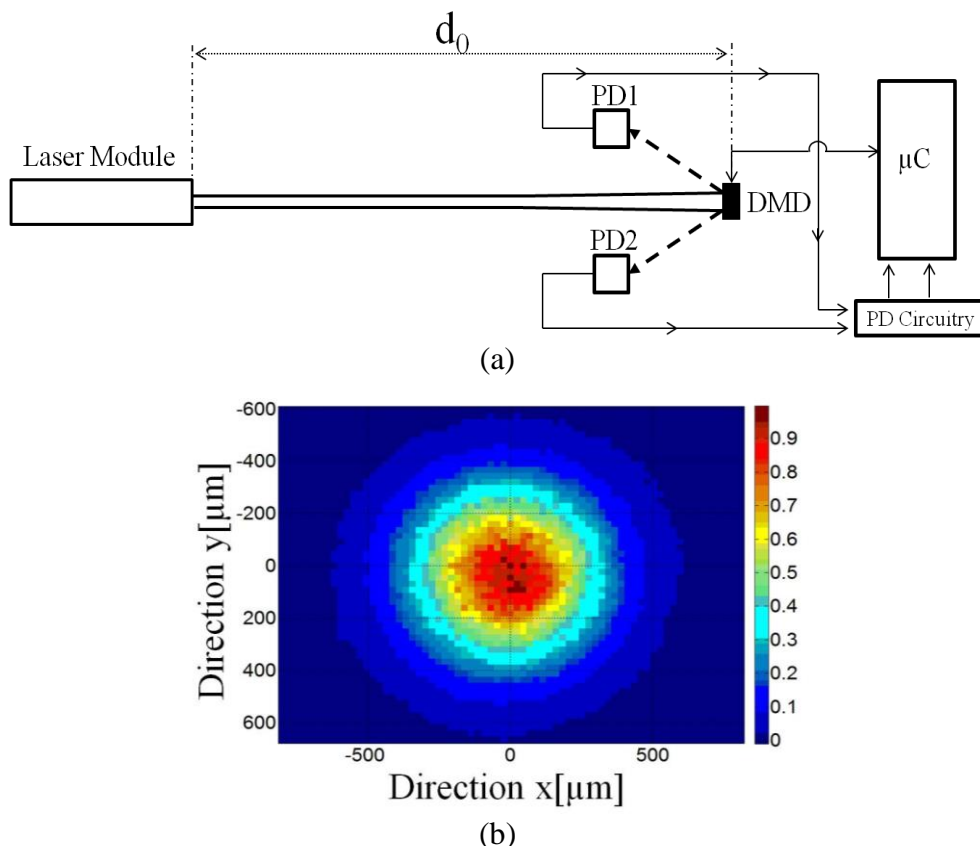


Fig. 6.4. (a) Experimental setup with the imaging plane (DMD plane) at  $d_0 = 50$  cm away from the laser source. (b) MATLAB plot of embedded agile pixel imager acquired 2-D beam irradiance map obtained using an agile pixel size of 3x3 micromirrors during the imaging process.

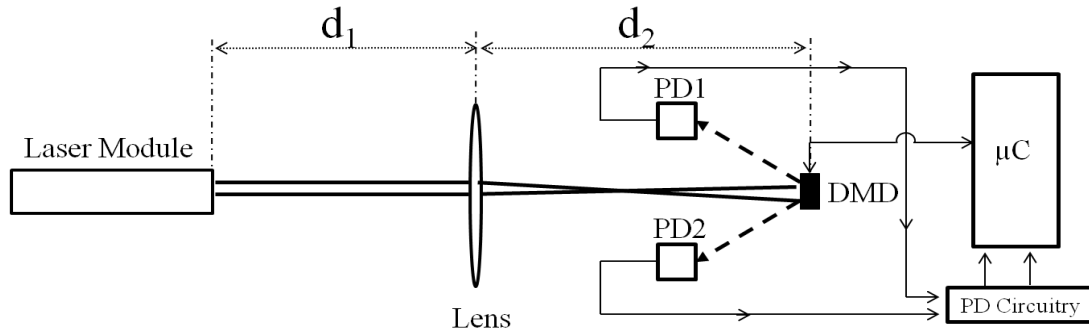


Fig. 6.5. Lens having 20 cm focal length incorporated in setup stated in Fig. 6.4(a). Distance  $d_1$  is kept fixed at 30 cm, while  $d_2$  is changed to values of 21 cm, 26 cm and 31 cm.

Table 6.1. Experimental data showing  $1/e^2$  beam radii estimates extracted using MATLAB and micro-controller for different  $d_2$  values and pinhole sizes.

Pinhole Size [micromirrors]	Distance $d_2$ [cm]	MATLAB $1/e^2$ radius		Micro-controller $1/e^2$ radius [ $w_\mu$ ]
		$w_x$ [ $\mu\text{m}$ ]	$w_y$ [ $\mu\text{m}$ ]	
3x3	21	126.4	125.0	126.0
	26	143.2	141.4	145.8
	31	194.7	195.4	194.4
5x5	21	126.4	125.0	126.0
	26	143.2	141.4	145.8
	31	194.7	195.4	194.4

Table 6.1 shows data acquired using the agile pixel imager for distances  $d_2$  values of 20 cm, 25 cm and 30 cm. Pinhole sizes of 3 x 3 and 5 x 5 micromirrors sets are used for each  $d_2$ . Using MATLAB fitting operations, beam radii  $w_x$  and  $w_y$  are computed corresponding to the diamond arrangement x and y coordinates, respectively. The last column of Table 6.1 shows the  $1/e^2$  values,  $w_\mu$ , computed within the micro-controller that are calculated by finding the transverse axis distance between the two  $1/e^2$  crossing points of the 1-D intensity curve. These values have an error offset from the MATLAB fitted ones since each micromirror is 7.64 microns wide, and 3 x 3 and 5 x 5 micromirror pinhole sizes represent the actual physical step size during the scanning process. When the micro-controller internally locates the physical location of the fitted irradiance corresponding to the  $1/e^2$  beam intensity, error arises due to these large scanning step sizes. This difference in MATLAB curve-fitted estimates and micro-controller calculated values can be minimized by programming



interpolation and fitting algorithms within the micro-controller software. Fig. 6.6 displays 1-D cross section MATLAB obtained plots for each of the  $d_2$  distances i.e.,  $d_2 = 20$  cm, 25 cm and 30 cm. The  $1/e^2$  threshold is marked using a black colored horizontal line on each plot. Table 6.1 and Fig. 6.6 show that for focused beams, with concentrated optical power, the embedded system based imager is able to adequately give beam profiles representing actual 2-D beam irradiance.

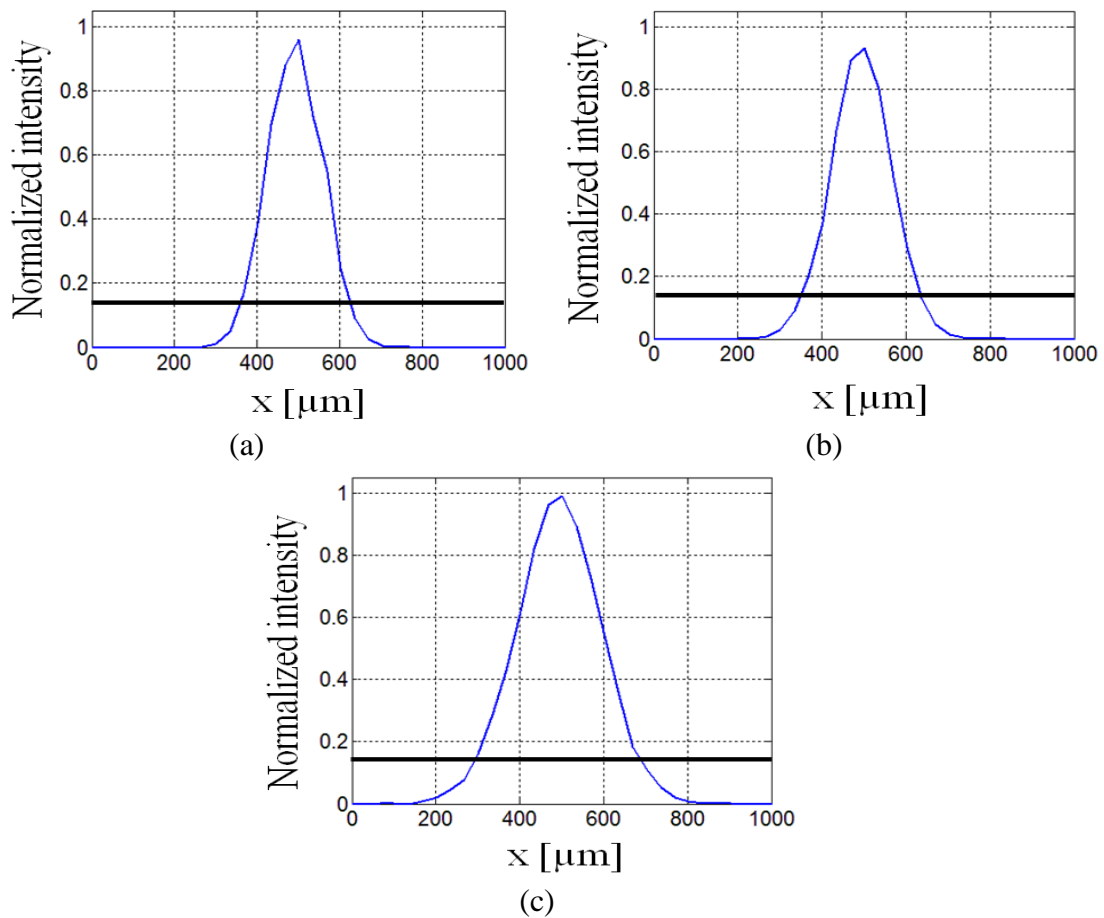


Fig. 6.6. Embedded imager acquired 1-D plots showing imaging capability for different distances along beam propagation path. Imaging is carried out at  $d_2$  values of (a) 21 cm, (b) 26 cm and (c) 31 cm. The approximate  $1/e^2$  threshold is also shown in each plot with a horizontal line.

## 6.5 CONCLUSION

Presented is an embedded platform based agile pixel imager suitable for industrial laser beam profiling applications. The design uses a DMD chip along with embedded electronics including a micro-controller which orchestrates the imaging process and acquires data through its ADC ports. The experimental prototype is demonstrated for Gaussian laser beam profiling displaying accurate high resolution 2-D irradiance maps of beam cross section, enabling  $1/e^2$  beam computation as well as file transfer to a PC for further analyses. Applications include high optical power laser beam profiling in industrial manufacturing and laser quality testing sector. Future work will address improvements in the micro-controller computed  $1/e^2$  radii values via implementation of curve-fitting algorithms within the micro-controller.

## REFERENCES

- [1] H. Ditlbacher, J. R. Krenn, A. Leitner, and F. R. Aussenegg, "Surface plasmon polariton-based optical beam profiler," *Optics Letters*, vol. 29, no. 12, pp. 1408-1410, (2004).
- [2] J. A. Arnaud, W. M. Hubbard, G. D. Mandeville, B. de la Clavière, E. A. Franke, and J. M. Franke, "Technique for fast measurement of gaussian laser beam parameters," *Applied Optics*, vol. 10, no. 12, pp. 2775-2776, (1971).
- [3] M. Katto, R. Matsumoto, K. Kurosawa, W. Sasaki, Y. Takigawa, and M. Okuda, "Laser beam profiler in the vacuum ultraviolet spectral range using photostimulable phosphor," *Review of Scientific Instruments - American Institute of Physics Journals*, vol. 64, no. 2, pp. 319-324, (1993).
- [4] A. Rose, Y.-X. Nie, and R. Gupta, "Laser beam profile measurement by photothermal deflection technique," *Applied Optics*, vol. 25, no. 11, pp. 1738-1741, (1986).
- [5] P. J. Shayler, "Laser beam distribution in the focal region," *Applied Optics*, vol. 17, no. 17, pp. 2673-2674, (1978).
- [6] Z. Liangmin, "Intensity spatial profile analysis of a gaussian laser beam at its waist using an optical fiber system," *Chinese Physics Letters*, vol. 27, no. 5, p. 054207, (2010).
- [7] J. A. Arnaud, "Apparatus for locating and measuring the beam-waist radius of a gaussian laser beam," US Patent 3617755 A, 02-Nov-1971.
- [8] N. A. Riza and D. Jorgesen, "Minimally invasive optical beam profiler," *Optics Express*, vol. 12, no. 9, pp. 1892-1901, (2004).
- [9] S. Sumriddetchkajorn and N. A. Riza, "Micro-electro-mechanical system-based digitally controlled optical beam profiler," *Applied Optics*, vol. 41, no. 18, pp. 3506-3510, (2002).
- [10] M. Sheikh and N. A. Riza, "Demonstration of pinhole laser beam profiling using a digital micromirror device," *IEEE Photonics Technology Letters*, vol. 21, no. 10, pp. 666-668, (2009).
- [11] N. A. Riza, S. A. Reza, and P. J. Marraccini, "Digital micro-mirror device-based broadband optical image sensor for robust imaging applications," *Optics Communication*, vol. 284, no. 1, pp. 103-111, (2011).
- [12] N. A. Riza, "Digital optical beam profiler," US Patent 6922233 B2, 26-Jul-2005.

- [13] M. Mubashir, L. Shao, and L. Seed, "A survey on fall detection: Principles and approaches," *Neurocomputing*, vol. 100, pp. 144-152, (2013).
- [14] T. Ma, M. Hempel, D. Peng, and H. Sharif, "A survey of energy-efficient compression and communication techniques for multimedia in resource constrained systems," *IEEE Communications Surveys & Tutorials*, vol. 15, no. 3, pp. 963-972, (2013).
- [15] U. Kacar, M. Kirci, M. Kus, and E. O. Gunes, "An embedded biometric system," in *2013 16th International Conference on Information Fusion (FUSION)*, pp. 736-742, (2013).
- [16] M. Magno, F. Tombari, D. Brunelli, L. Di Stefano, and L. Benini, "Multimodal abandoned/removed object detection for low power video surveillance systems," in *Sixth IEEE International Conference on Advanced Video and Signal Based Surveillance, (AVSS)*, pp. 188-193, (2009).
- [17] H. Kogelnik and T. Li, "Laser beams and resonators," *Applied Optics*, vol. 5, no. 10, pp. 1550-1567, (1966).
- [18] MATLAB Release 2009b, The MathWorks, Inc., Natick, Massachusetts, USA.



# CHAPTER 7

## CODED ACCESS OPTICAL SENSOR (CAOS) IMAGER<sup>7</sup>

### 7.1 INTRODUCTION

Imaging of Electromagnetic (EM) radiation is of fundamental importance to medical, manufacturing, astronomy, aerospace, arts, entertainment, forensics, education, research, and defense sectors. For large scale deployment and impact from optical imagers, it is not only highly desirable to have the features mentioned earlier, but also important to realize portability, low energy consumption, and security of operations. Over the last 65 years, there have been tremendous technological advances in optical image sensor design including optoelectronic photo-detection CCD and CMOS sensor chips and their custom precision interface optics, as well as advances in coding and imaging techniques like Stimulated Emission Depletion (STED) using fluorescence to achieve spatial resolutions beyond the diffraction limit [1-11]. Nevertheless, these and other prior imager designs approached the optical imaging sensor challenge from a mainly fixed space-time-frequency pixel view point that to a large extent have increased system complexity and limitations, particularly when relying on fluorescence materials, wavelength sensitive coherent sources, detectors, and optics, as well as pixel-scale sensitive mechanical alignments and iterative image processing and recovery methods.

Today, the airwaves are filled with trillions of human-made EM signals emanating from radiating static and mobile platforms ranging from very large to ultra-small such as cell phones, computers, airplanes, earth orbiting satellites, and ground-based radars. Each of these EM electronic devices has the remarkable capability to sift through trillions of different EM signals simultaneously incident on the device and to extract the unique EM signal directed specifically to the device. For example, each cell phone has its specific phone number that acts as its unique identifier code which is deployed in the sifting process. This amazing feat

---

<sup>7</sup> N. A. Riza, M. J. Amin and J. P. La Torre, "Coded Access Optical Sensor (CAOS) imager," Journal European Optical Society - Rapid Publications, vol. 10, 15021, pp. (2015).

of very weak EM signal detection buried in wideband EM noise (created by all the unwanted EM signals) is achieved using highly sensitive Radio Frequency (RF) electronics with powerful on-chip encoding and decoding via analog and Digital Signal Processing (DSP) within energy efficient and compact high speed hardware [12, 13].

Earlier we have proposed and extensively demonstrated an agile pixel DMD-based imager that functions basically as the proposed CAOS imager, but with the agile pixels programmed in a limited SNR operations starring mode which acquires irradiance (i.e., intensity) data without any time-frequency modulation [14-20]. With present-day RF/optical communications and a robust fully programmable smart image sensor design in mind, proposed is the CAOS imager design that has the potential to deliver high SNR images by uniquely exploiting the time-frequency signaling domain of agile pixels-based spatially distributed optical radiation that is received by one easy to align optical antenna with a single RF output [21]. Specifically, the proposed CAOS imager uses image optical irradiance agile pixel position coding via time-frequency modulation codes implemented by a programmable Two Dimensional (2-D) Optical Array Device (OAD) interfaced with a single point optical receive antenna called a point Photo-Detector (PD). Each agile pixel position with its corresponding irradiance value in the multi-agile pixels optical irradiance map has its unique time-frequency code, thereby unleashing the extreme sensitivity and processing power of electrical domain analog and digital signal post-processing implemented by modern electronic chip technologies [22].

This chapter starts by providing the design and working principles of the CAOS imager, including the key features and capabilities of the imager. An experimental CAOS imager demonstration is implemented based on using a visible band DMD as the OAD. The experimental CAOS system imaging quality is tested and compared using a commercial system laser beam with the laser manufacturer providing the accurate Gaussian laser beam irradiance map specifications [23]. In addition, significant performance improvement of the demonstrated CAOS imager SNR is compared with our previously demonstrated limited SNR agile pixel DMD-based starring mode imager [19, 20]. The chapter concludes with a summary of the key CAOS imager design and experimental results.

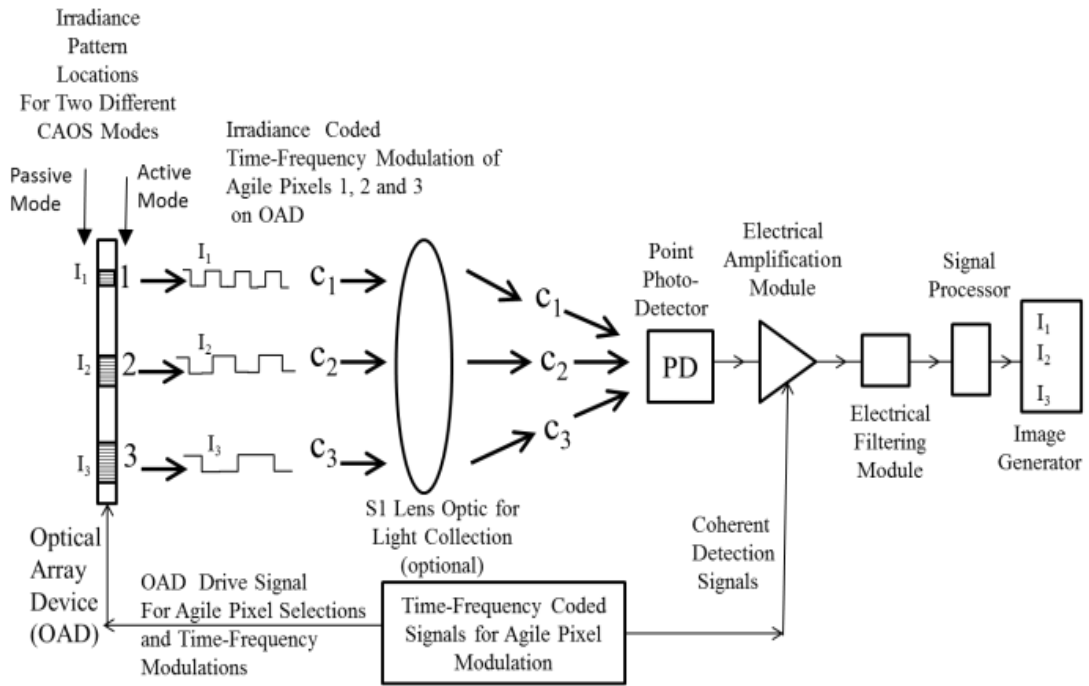


Fig. 7.1. CAOS imager implementation (side view).

## 7.2 PROPOSED CAOS IMAGER DESIGN

Figure 7.1 shows a possible implementation of the CAOS imager that can operate in two modes of imaging, i.e., passive mode and active mode. The passive mode of CAOS imager operation occurs when irradiance to be imaged comes from an external radiation source and falls on the OAD agile pixels-plane. The active mode of operation occurs when the OAD acts as an internal pixelated radiation source that illuminates the object undergoing imaging that for near-field imaging is placed at or adjacent to the OAD agile pixels-plane. The OAD is an electronically programmable device that allows one to select the location, shape, and size of any given  $n^{\text{th}}$  agile pixel plus its time-frequency modulation characteristics to suit the particular imaging scenario. The pixel is called an agile pixel as its agility comes both in the spatial domain and time-frequency coding domain and can be electronically optimized for a given imaging scenario. The number of agile pixels  $N$  deployed is also application dependent. As an example, Fig. 7.1 shows  $N = 3$  pixels each having a unique code  $c_n(t)$  defined by its time-frequency modulation characteristics, i.e., the irradiance  $I_1$  due to agile pixel 1 (i.e.,  $n = 1$ ) is modulated at a higher temporal frequency (shown as a digital on/off time sequence) than the irradiance  $I_2$  due to agile pixel 2, which in turn is modulated at a higher temporal frequency than the irradiance  $I_3$  due to agile pixel 3. Lens S1 (or concave mirror optic) is positioned to collect the individually coded optical irradiance signals on the



OAD and deliver them to the point PD for optical-to-electrical signal conversion. Depending on the light's coherence properties as well as the physical aperture sizes of the OAD, S1, PD, and agile pixel set, S1 can simply act as an imaging optic between the OAD and PD planes or operate in a focus mode or a combination of the two. It is important to note that when operating with coherent light, the PD aperture being large enough does a fringe averaging operation that washes out any optical interference effects, leaving the photo-current to represent the desired sum of the agile pixel irradiance values. Note that in some cases, optical signal amplification can be deployed before the light reaches the point PD. The light collection optic S1 is not required to have an exceptional optical quality so it can spatially resolve a pixel size on the OAD. In fact, if the OAD and PD have similar active area cross-sections, they can be placed directly adjacent to each other, making an ultra-compact lens-less imager design. The PD generated electrical signal can be written as:

$$i(t) = K \sum_{n=1}^N c_n(t) I_n(x_n, y_n), \quad (7.1)$$

where K is a constant depending on various photo-detection factors including the PD quantum efficiency. For the  $n^{\text{th}}$  agile pixel on the OAD,  $x_n$ ,  $y_n$  are the pixel central coordinates,  $I_n$  is the pixel irradiance, and  $c_n(t)$  is the pixel time-frequency code. The PD generated electrical signal containing the temporally coded pixel irradiance data set (e.g., 3 pixels for Fig. 7.1) next undergoes electrical amplification. This amplification operation can be stand-alone, i.e., electrically incoherent where simply the PD generated signal is electrically amplified by a fixed factor  $G_A$  giving an amplified signal  $i_A(t) = G_A i(t)$ . Another option is to implement electrically coherent amplification where the time-base reference frequency signal  $r(t)$  used to generate the different pixel temporal codes for the OAD also provides an electrical phase-reference for the electrical mixing operation inside a phase-locked amplifier to produce an output signal  $i_C(t) = G_A r(t) i(t)$ , similar to some extent to a super-heterodyne radio receiver. In both cases, the amplified signal undergoes RF filtering to block out the undesired frequency spectrum and retain the high gain signal containing the coded pixel irradiance values.

Next the amplified and filtered electrical signal is fed to a signal processor module where it undergoes time/frequency domain signal transform analysis such as Fourier spectrum analysis or correlation analysis that is used to recover each agile pixel irradiance value given the known identifier code for the given agile pixel. Take the simple case where

pure frequency codes are deployed for the agile pixel coding, so  $c_n(t)=\cos(2\pi f_n t)$  and incoherent electrical detection is used in the imager. In this case, simple time domain spectrum analysis or Fourier Transform (FT) in the  $f$  Hz frequency space can be conducted on the processed PD signal  $i_A(t)$  with the signal processor output signal  $S(f)$  given by:

$$S(f) = FT\{i_A(t)\} = FT\left\{G_A K \sum_{n=1}^N c_n(t) I_n(x_n, y_n)\right\} = FT\left\{G_A K \sum_{n=1}^N \cos(2\pi f_n t) I_n(x_n, y_n)\right\}. \quad (7.2)$$

Assuming single sideband spectrum analysis and  $G$  being a fixed spectrum analysis gain factor, one can write Eqn. (7.2) as:

$$S(f) = G G_A K \sum_{n=1}^N I_n(x_n, y_n) \delta(f - f_n)$$

$$S(f) = G G_A K \{I_1(x_1, y_1)\delta(f - f_1) + I_2(x_2, y_2)\delta(f - f_2) + I_3(x_3, y_3)\delta(f - f_3) + \dots + I_N(x_N, y_N)\delta(f - f_N)\}. \quad (7.3)$$

In Eqn. (7.3), one is assuming that a single frequency spectral code appears as a Delta function of zero 3-dB bandwidth in the  $f$  Hz frequency space. In reality, each finite time duration real code signal has some finite 3-dB spectral bandwidth in Hz. The key for very low inter-pixel crosstalk in the Eqn. (7.3) CAOS operation is to choose code frequencies not closely positioned in the instantaneous frequency space for the  $N$  simultaneously sampled agile pixels. As shown by the Eqn. (7.3) FT spectral output  $S(f)$  produced by the signal processor, a complete irradiance map at the time-frequency coded spatial locations on the OAD is generated by the CAOS system. In practice, the number of agile pixels processed simultaneously is application dependent as well as CAOS deployed hardware and software dependent. For the case of more complex  $c_n(t)$  codes, time domain correlation processing can be implemented to decode the sampled pixel irradiances values. In fact, to unleash the full power of high speed DSP, the PD provided signal can undergo immediate digitization with all signal post-processing operations handled in the all-digital space.

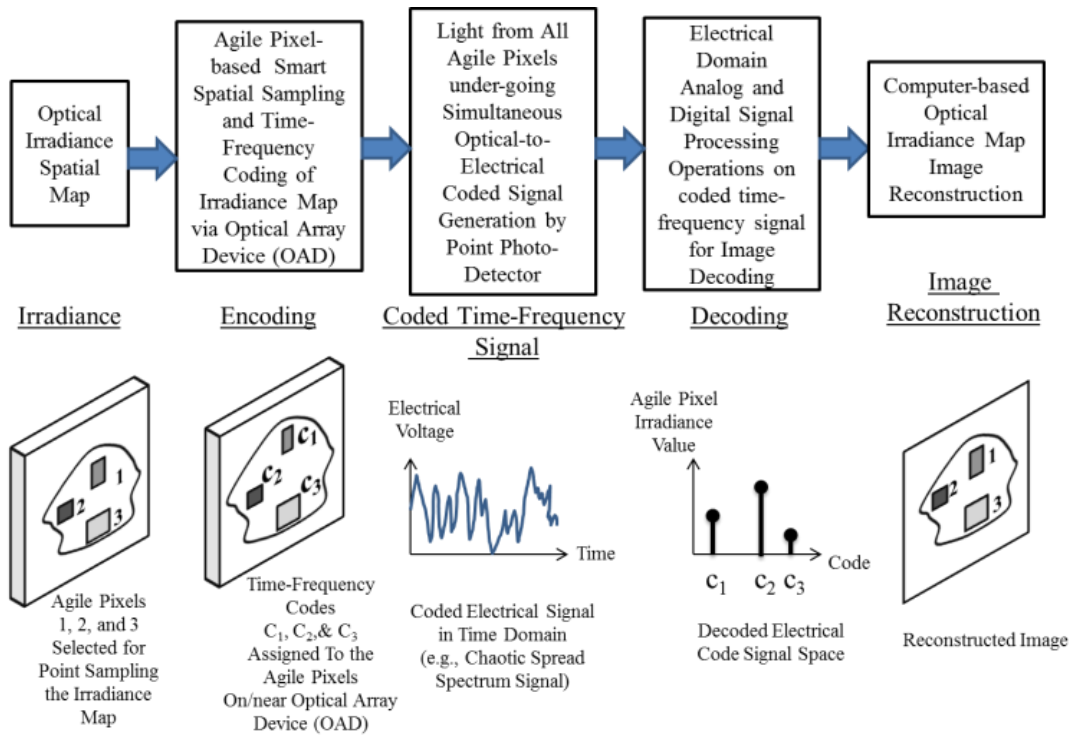


Fig. 7.2. CAOS imager signal flow chart.

To further elaborate on the signal flow workings of the Fig. 7.1 CAOS imager implementation, Fig. 7.2 shows a signal flow chart where shown are 3 different sizes, shapes, and positions of the agile pixels labelled as 1, 2, and 3 that are coded with codes  $c_1$ ,  $c_2$ , and  $c_3$ , respectively. All the time-frequency coded optical signals engage simultaneously on the PD. This optical analogy is similar to the cell phone scenario where numerous EM signals incident on the RF antenna is equivalent to the many optical agile pixels in the irradiance map incident simultaneously on the point PD. Decoding of agile pixel position based irradiance values is implemented by using the PD generated temporally varying electrical signal and subjecting it to high speed analog and digital electronics-based one Dimensional (1-D) coherent (i.e., electrical phase locked) or incoherent signal processing. With the agile pixel-based irradiance values recovered from what looks like a chaotic RF signal, computer-based non-iterative image processing (2-D) and reconstruction techniques are used to stitch together the 2-D optical irradiance map observed by the CAOS Imager. Do note that the selected sizes, shapes, and locations of the agile pixels within a given sampling time slot can also be optimized to extract the desired image features with maximum SNR based on application specific intelligence.

Complete electronic programmability gives the CAOS imager powerful attributes both as a smart spatial sampler of irradiance maps and also for electronic processing to enable high performance encoding and decoding of the agile pixel irradiance map. Much like wireless and wired communication networks, the agile pixel can operate in different programmable time-frequency coding modes like Frequency Division Multiple Access (FDMA), Code-Division Multiple Access (CDMA), and Time Division Multiple Access (TDMA) [22], [24-26]. CDMA and FDMA will produce spread spectrum RF signals from the PD while TDMA is the staring-mode operation of the CAOS imager, one agile pixel at a time producing a DC signal. For full impact of the CAOS imager, agile pixel codes should include CDMA, FDMA or mixed CDMA-FDMA codes that produce not only PD signals on a broad RF spectrum but also engage sophisticated analog, digital, and hybrid information coding techniques to provide isolation (e.g., minimum cross-correlation) and robustness amongst time-frequency codes used for OAD pixel coding [27]. As pointed out earlier, coherent high sensitivity detection in the electrical domain can be used for decoding of the agile pixels. For example, high SNR correlation operations can be run in parallel using the code set to decode the pixel irradiances. These correlation operations can be implemented in physical hardware that forms a bank of 1-D time signal correlators or in a software-based DSP system or even a hybrid of the two approaches.

The CAOS platform instantaneously brings the following unique features when compared to prior-art imagers: (a) the agile pixel space-time-frequency characteristics can be programmed to suit the imaging scenario with adaptive control deployed as needed; (b) staring mode PDs such as CCD/CMOS sensors naturally produce a photo-detection electrical noise spectrum that is dominant around the DC and lower frequency components [28]. The CAOS imager produces its photo-detected signal at a temporal frequency band that is away from the noisy part of the PD output near DC, thus creating a higher SNR signal for decoding signal processing. All electronics are fundamentally subjected to  $1/\text{frequency}(f)$  or  $1/f$  noise. By having the output signal frequency band for the PD in the CAOS imager away from DC, the  $1/f$  noise in the signal processing electronics chain is also lower as  $f$  can be from many tens of Hertz to many GHz [29]. In addition, it has been known for many years that when using a single photo-detector for spatial light capture, simultaneous detection of light from different sampled spatial zones versus single zone light capture can lead to improved SNR of the time modulated photo-detected output signal [30]; (c) after photo-detection, electrical domain coherent detection such as with electronic mixing plus phased locked amplification

and filtering can provide detection of extremely weak signals buried in noise. The CAOS imager can exploit this coherent detection and processing feature in the robust electrical domain versus in a vibration/optical phase sensitive domain of optical interferometry; (d) the spatial imaging resolution of the CAOS imager is determined by the size of the agile pixel selected for time-frequency coded modulation on the OAD and not by the optical quality of the diffraction limited optic S1. For passive mode of operations, the OAD is a transmissive (or reflective) Spatial Light Modulator (SLM) device. In this case, the smallest size of the time-frequency modulating agile pixel is the smallest size of the programmable pixel in the SLM. Various SLM technologies can be deployed such as using optical MEMS/NEMS, liquid crystals, Multiple Quantum Wells, and nano-photonic devices. Optically addressed pixel structure-free SLMs can also be deployed as the OAD. In the case of imager active mode operations, the OAD is a light source array device like a 2-D optical display device, e.g., a 2-D laser array, a 2-D LED array, or a light source array coupled waveguide/fibre array device. Depending on the OAD technology, in the near future one can even envision a pixel size as small as an atomic radiator, thus easily beating the optical diffraction limit when deploying an active mode near-field CAOS imager. Because all agile pixel positions and their irradiances on the OAD are encoded in time-frequency and decoding of pixel information no longer depends on the optical diffraction limits of the lens optics in the imager, exceptionally low inter-pixel crosstalk levels can be achieved via the electronic signal processing operations even when the pixel sizes are much smaller than the Abbe diffraction limit [31]; (e) the optical signal incident on the PD as well as the PD generated electrical signal look chaotic and are inherently secure as the image cannot be recovered without the pixel codes needed for decoding at the receiver; (f) the CAOS platform is extendable to Three Dimensional (3-D) imaging techniques including light sheet, confocal, and wavelength diversity-based methods [32, 37], by also applying time-frequency coding to pixels in the third spatial dimension. In addition, the CAOS imager can be combined with classical 2-D CCD/CMOS-based imagers to interrogate sub-2-D image zones in the full 2-D image space where sub-critical data must be extracted from the image scene.

### 7.3 EXPERIMENT

For a first demonstration of the basics of the CAOS imager, the 2-D irradiance map of a CW visible laser beam is chosen for imaging as it is well specified by the commercial laser system manufacturer and also showcases both extreme brightness zones and dim light zones. The CAOS imager is set-up in the lab as shown in Fig. 7.3. A TI DMD is deployed as the OAD. Components used in the present experiment are: TI DLP LightCrafter (LCr) evaluation board with pico DMD chip micro-mirror binary tilt states of  $+12^\circ$  and  $-12^\circ$ , the  $12^\circ$  state beam directed to PD, aluminium visible band coated square pixels of  $7.64\ \mu\text{m}$  sides aligned in a diagonal geometry with a total micromirror count of  $608 \times 684$  and deployed frame rate up-to 400.4 Hz; Lens S1 with 4 cm focal length; Point PD is a Thorlabs silicon visible band model SM05PD1A; A STM32F4 is the micro-controller with a 12-bit Analog-to-Digital Converter (ADC) is used to control the DMD and interface with the Personal Computer (PC); A 15mW  $\lambda = 633\ \text{nm}$  Melles-Griot single-mode Gaussian laser beam is used for imager testing where the data sheet indicates the beam characteristics [23].

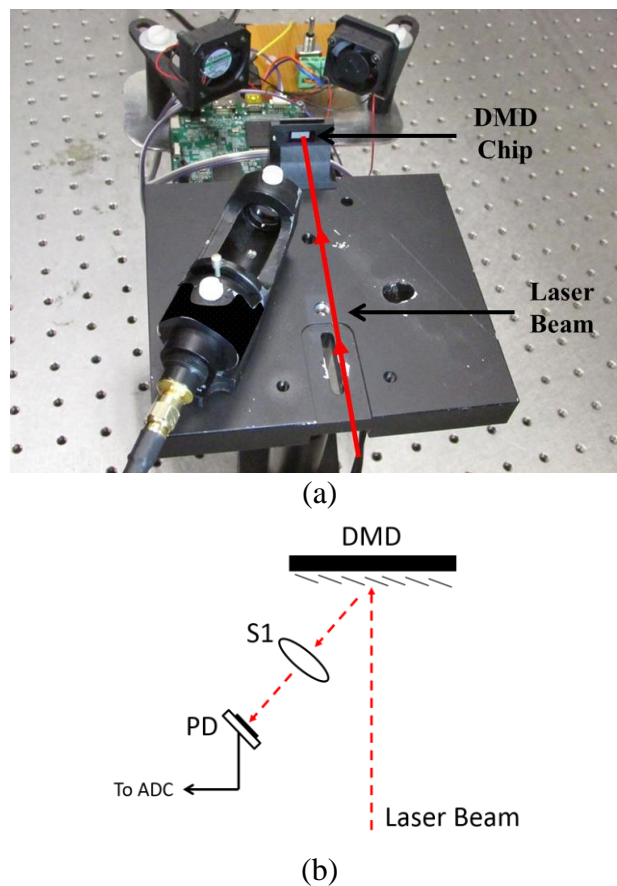
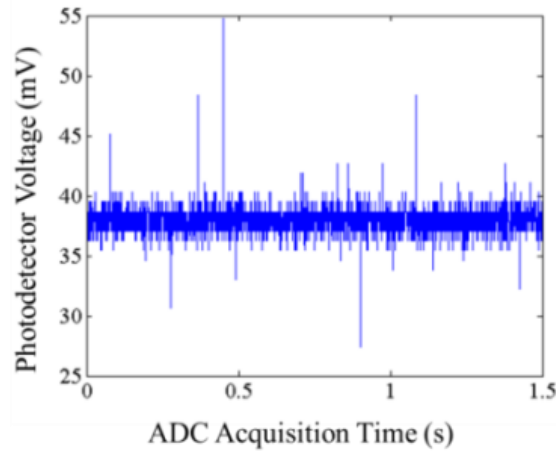
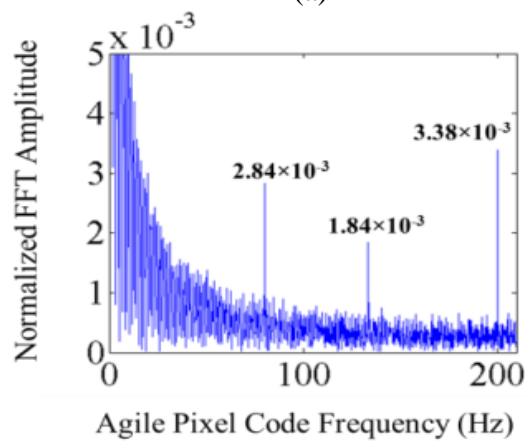


Fig. 7.3. (a) CAOS imager optical experimental setup. (b) Schematic representation of (a).

Because of the slow data transfer speed and significant memory limitations of this low cost TI LCr board built for pico-projectors, the full image of the incident laser beam irradiance is generated by operating the CAOS imager agile pixel in a hybrid FDMA plus TDMA mode by scanning 3 agile pixels in a raster format line scan. For example, agile pixels 1, 2 and 3 modulate at frequency codes  $f_1$ ,  $f_2$  and  $f_3$  Hz. After the irradiance data is recorded, agile pixels 4, 5 and 6 are also set to modulate at  $f_1$ ,  $f_2$  and  $f_3$  Hz and the subsequent irradiance data is recorded, and so on. Furthermore, in-coherent stand-alone electrical detection of the PD acquired electrical signal data is used to generate the post-processing signal that contains the coded pixel irradiance values. The PD electrical signal is digitized using the ADC of the micro-controller and fed to the PC where it is subject to DSP via a Fast Fourier-Transform (FFT) operation in MATLAB. As mathematically indicated in the earlier section, the agile pixel irradiance values are proportional to the FFT spectral peak values and are obtained directly from the frequency domain of the FFT data. Specifically, the imager operation 2-D scan parameters are: 2160 agile pixels time modulating via FDMA coding in sets of three with each set modulating for 6.24 seconds followed by a 14 seconds delay before the next set modulates to ensure synchronisation between PC, micro-controller and LCr DMD board. The size of each agile pixel is  $6 \times 6$  micromirrors and the sampling rate of the ADC is set to 2.4 kHz to acquire the PD signal. A total of 720 (2160/3) text files having coded irradiance map data are generated from the PD signal ADC data. With the available processing unit, a program in MATLAB which takes 5 seconds to run, implements the FFT algorithm on the 720 files and extracts the relevant electrical spectral peak values which represent the normalized optical irradiances of the agile pixel sampled laser beam map. Using this decoded data, the 2-D irradiance map is plotted and an inbuilt 2-D Gaussian fitting function in MATLAB is used to estimate the  $1/e^2$  beam radius.



(a)



(b)

Fig. 7.4. (a) Coded 1-D time signal produced by the PD for three agile pixels on the DMD chip. (b) FFT signal processing decoding of the three micromirror agile pixel irradiances  $I_1$ ,  $I_2$ , and  $I_3$  that are proportional to the normalized spectral values computed by the FFT operation.

Figure 7.4(a) shows the coded 1-D time signal produced by the PD and recorded by the ADC for three agile pixels at the DMD chip plane coded with on/off modulations of  $f_1 = 80.1$  Hz,  $f_2 = 133.4$  Hz, and  $f_3 = 200.2$  Hz resulting from the two-tilt state nature of the DMD chip micromirrors. Figure 7.4(b) shows the FFT signal processing decoding of the three agile pixel irradiances  $I_1$ ,  $I_2$ , and  $I_3$  at the DMD chip plane that were coded with the FDMA-TDMA coding. Because in theory, there are no FFT frequency spectral peak overlaps between the 3 coded agile pixels (i.e., when one assumes that each FFT spectral peak resembles a narrow spectral Delta function with no frequency content outside its main spectral lobe), one can consider that there is very low optical crosstalk between the 3 agile pixel decoded irradiances, a fundamental feature of the CAOS imager. In reality, when operating in this FDMA only mode, one must choose the coding frequencies to have minimal instantaneous spectrum overlap and with additional filtering, one can pluck spectral/optical irradiance data with

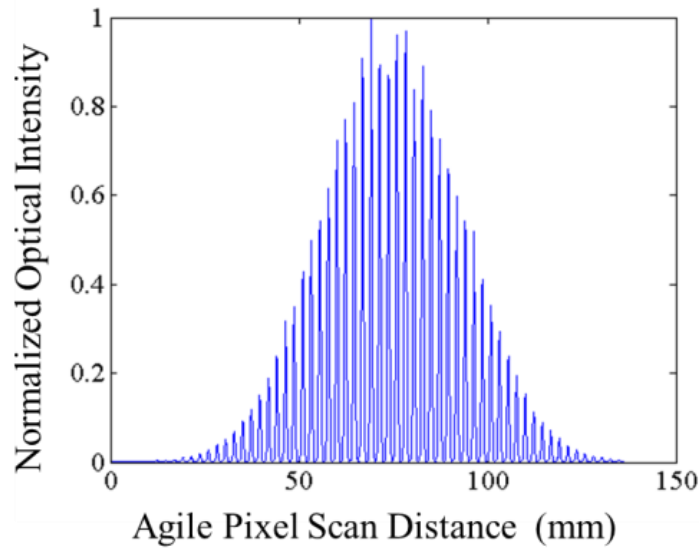


essentially minimal inter-pixel crosstalk. Figure 7.5(a) shows the 2-D irradiance of 2160 agile pixels data ( $60 \times 36 = 2160$ ) from the experimental CAOS imager using 60 1-D line scans across the DMD chip with each line scan consisting of 36 agile pixels. Specifically, Fig. 7.5(a) shows the normalized optical intensity versus distance in mm covered during the 1-D line-by-line scanning process using 3 simultaneous and side-by-side placed agile pixels moving along each scan line. Figure 7.5(a) is explained using Fig. 7.5(b). Figure 7.5(b) on the left side shows the optical irradiance distribution incident on a simulated DMD chip having a micromirror grid of 6 rows and 9 columns. Figure 7.5(b) on the right side shows the pixel-by-pixel irradiance map over the simulated chip beginning with the irradiance contribution from row 1 and onwards. In Fig. 7.5(a), the inter-pixel pitch in the line scan direction is 64.8 microns ( $6 \times$  micromirror diagonal of  $10.8 \mu\text{m}$ ). Note that in the line scan plot, the maximum value of the coded electrical spectral component obtained via the FFT corresponding to a particular agile pixel in the scan is normalized and given a value of 1. Figure 7.5(c) shows a zoom of the FFT acquired decoded irradiance data to estimate the average null or noise floor in the imager giving an estimated normalized average minimum noise floor of 0.00014267 leading to an imager electrical SNR of 77 dB. This is equivalent to a 38.5 dB optical irradiance SNR with optical SNR computed as:

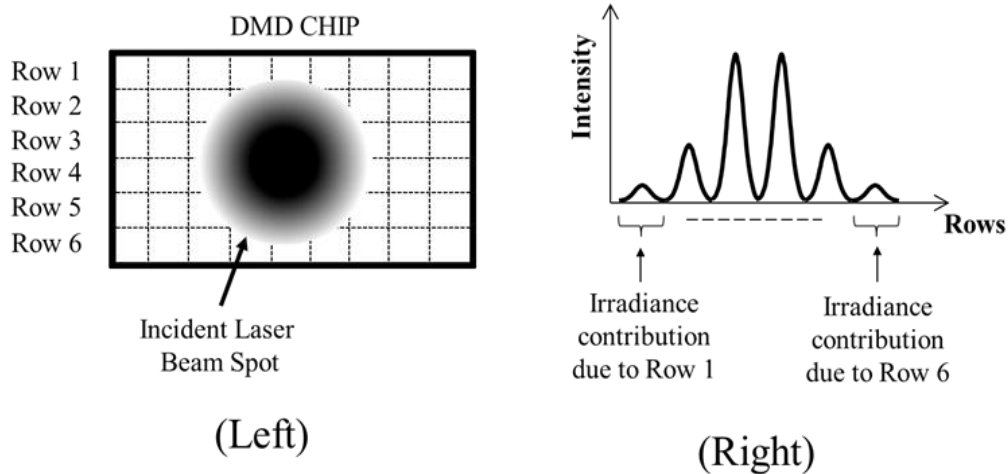
$$SNR = 10 \log \left( \frac{MaxFFT\text{spectralvalue}}{FFT\text{spectralnoise floor}} \right) = 10 \log \left( \frac{1}{0.00014267} \right). \quad (7.4)$$

Imager electrical SNR is two times the optical SNR. Note that previously we have proposed and demonstrated a DMD-based staring mode agile pixel optical imager that demonstrated an optical SNR of 10.7 dB, resulting in an image electrical SNR of 21.4 dB [19, 20]. Our present results point to the greatly improved SNR of the CAOS imager, even though coherent detection is not deployed in the electronics of the decoder to achieve image decoding. Figure 7(d) shows the full decoded 2-D irradiance map produced by the CAOS imager using the FFT decoding data. Using the acquired CAOS imager-based irradiance 2-D spatial beam map and 2-D Gaussian fitting in MATLAB, obtained are  $1/e^2$  laser beam waist radii of  $w_x = 526.0 \mu\text{m}$  and  $w_y = 530.1 \mu\text{m}$ . In comparison, using Gaussian laser beam propagation theory and the laser manufacturer data sheet  $325 \mu\text{m}$  minimum beam waist radius and 67.5 cm beam travel distance to DMD, one gets  $w_x = w_y = 529.9 \mu\text{m}$ . This manufacturer specified beam radius value is within 0.75% error (i.e.,  $100\% (529.9 - 526)/529.9$ ) of the CAOS imager Fig. 7.5(d) data provided 2-D Gaussian fitting measurement

[23]. A 1-D comparison of the central cross-section of the measured laser beam image with the expected Gaussian beam envelope using manufacturer's values is presented in Fig. 7.5(e). The marker dots show normalized raw (i.e., unprocessed) CAOS imager acquired experimental irradiance data while the dashed curve, which matches well with the dots, is the theoretically expected 1-D Gaussian normalized irradiance envelope at the same propagation distance.

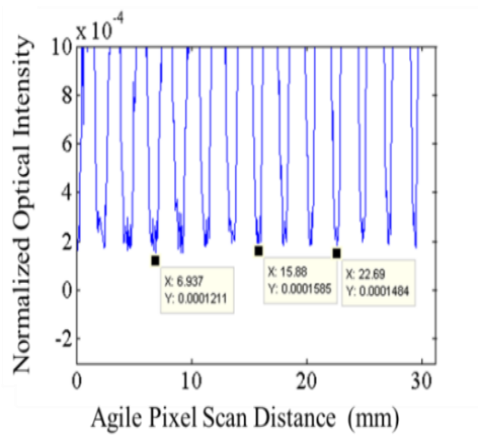


(a)

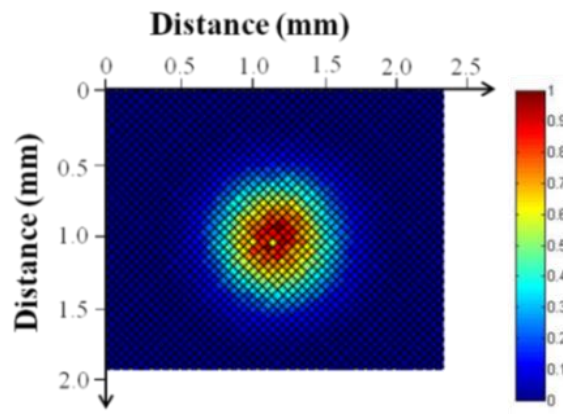


(b)

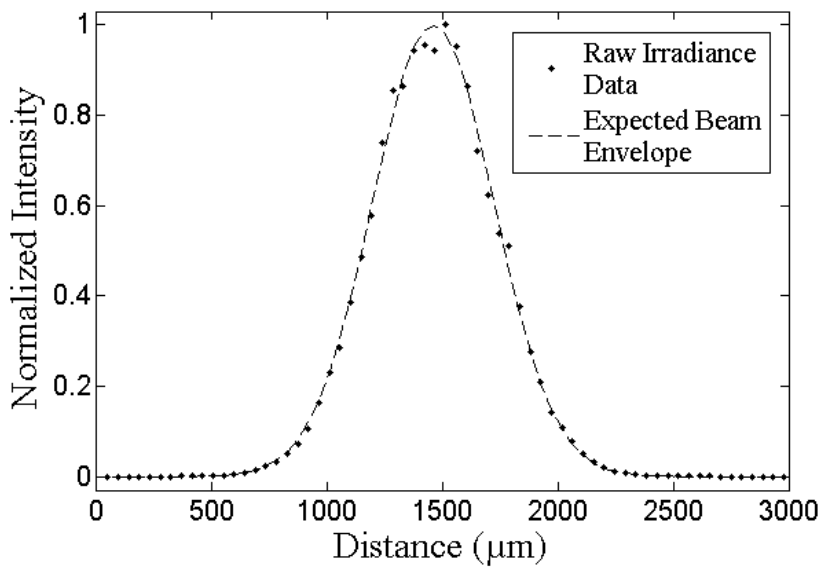
Fig. 7.5. (a) 2-D irradiance of 2160 agile pixels data from the experimental CAOS imager using 60 1-D line scans across DMD chip. (b) (Left) The optical irradiance distribution representation of a laser spot incident on an example 6 pixels (in a column) by 9 pixels (in a row) DMD chip.(Right) The total pixel-by-pixel optical irradiance on the chip is represented in a single 1-D plot, which includes the optical irradiance contributions of each row of the DMD chip.



(c)



(d)



(e)

Fig. 7.5. (c) Zoomed version of Fig. 7.5(a) irradiance data to estimate the average null or noise floor in the imager (d) The fully decoded 2-D irradiance map produced by CAOS Imager showing raw (i.e., unprocessed) intensity values, normalized to 1. (e) Comparison of central cross-section data of the CAOS imager acquired laser beam image (dots) vs. laser manufacturer provided theoretically expected Gaussian beam envelope (dashed line).

## 7.4 CONCLUSION

In conclusion, presented is the CAOS imager agile pixel platform for optical imager design that engages an electronically programmable OAD to enable agile pixel coded multiple access of an optical irradiance map subjected to the imaging operation. The CAOS imager can electronically adapt to the specific imaging application and its specific needs to sift out desired image information, including under extreme lighting conditions. As a proof-of-concept demonstration, a CAOS imager is demonstrated using a low cost DMD as the OAD with a laser test beam map providing the extreme contrast imaging zone. Image data acquired for the laser beam map shows an excellent 77 dB electrical SNR with a 0.75% spatial beam measurement error, illustrating the power of the CAOS platform where time/frequency domain signal processing of photo-detected data can deliver excellent SNR properties. Compared to our previous starrng-mode agile pixel DMD imager, the CAOS imager has demonstrated a near 55 dB or over 5 orders of magnitude improvement in electrical SNR. The CAOS platform can also be configured to engage polarization diversity, optical field modulation/encoding and coherent optical detection with DSP decoding to deliver advanced sensing capabilities. In addition, CAOS enables direct image content manipulations using both optical and electronic information processing. It is important to note that in order to realize the full potential of the CAOS imager, dedicated high speed OAD, PD, and chip-scale control and signal processing hardware and software must be developed and optimized. Given the maturity and pace of development of today's electronics, laser array, nano-phonic, nano-mechanical and optical modulation and display technologies including high speed parallel drive optoelectronic devices and pipelined processor architectures, this goal is feasible and can lead to creating critical impact via the CAOS agile pixel space-time-frequency programmable smartness platform matched for certain imaging environments.

## REFERENCES

- [1] M. J. E. Golay, "Multi-slit spectrometry," *JOSA* 39, pp. 437-444, (1949).
- [2] S. J. Katzberg, F. O. Huck, and S. D. Wall, "Photosensor aperture shaping to reduce aliasing in optical-mechanical line-scan imaging systems," *Applied Optics*, vol. 12, pp. 1054-1060, (1973).
- [3] E. E. Fenimore, "Coded aperture imaging: predicted performance of uniformly redundant arrays," *Applied Optics*, vol. 17, pp. 3562-3570, (1978).
- [4] N. A. Riza, M. M. Howlader, and Madamopoulos, "Photonics security system using spatial codes and remote coded coherent optical communication," *Optical Engineering*, vol. 35, no. 9, pp. 2487-2498, (1996).
- [5] P. M. Blanchard and A. H. Greenaway. "Simultaneous multiplane imaging with a distorted diffraction grating," *Applied Optics* vol. 38, pp. 6692-6699, (1999).
- [6] W. T. Cathey, and E. R. Dowski. "New paradigm for imaging systems," *Applied Optics*, vol. 41, pp. 6080-6092, (2002).
- [7] N. A. Riza and M. Arain, "Code multiplexed optical scanner," *Applied Optics*, vol. 42, pp. 1493-1502, (2003).
- [8] B. Laude-Boulesteix, A. De Martino, B. Drévilion and L. Schwartz, "Mueller polarimetric imaging system with liquid crystals," *Applied Optics*, vol. 43, pp. 2824-2832, (2004).
- [9] B. Javidi, S. Hong, and O. Matoba. "Multidimensional optical sensor and imaging system," *Applied Optics*, vol. 45, pp. 2986-2994, (2006).
- [10] E. Rittweger, K. Y. Han, S. E. Irvine, C. Eggeling, and S. W. Hell, "STED microscopy reveals crystal colour centres with nanometric resolution," *Nature Photonics*, vol. 3, pp. 144-147, (2009).
- [11] N. Waltham, "CCD and CMOS sensors: Observing photons in space," (Springer New York, pp. 423-442, 2013).
- [12] Springer and R. Weigel, "RF microelectronics for W-CDMA mobile communication systems," *Electronics and Communication Engineering Journal*, vol. 14, no. 3, pp. 92-100, (2002).
- [13] J. Tsui, *Digital techniques for wideband receivers*, SciTech Publishing, 2004.
- [14] S. Sumriddetchkajorn and N. A. Riza, "Micro-electro-mechanical system-based digitally controlled optical beam profiler," *Applied Optics*, vol. 41, no. 18, pp. 3506-3510, (2002).

- [15] M. Sheikh and N. A. Riza, "Demonstration of pinhole laser beam profiling using a digital micromirror device," *IEEE Photonics Technology Letters*, vol. 21, no. 10, pp. 666-668, (2009).
- [16] N. A. Riza, S. A. Reza and P. J. Marraccini, "Digital micro-mirror device-based broadband optical image sensor for robust imaging applications," *Optics Communications*, vol. 284, no. 1, pp. 103-111, (2011).
- [17] P. J. Marraccini and N. A. Riza, "Multimode laser beam analyzer instrument using electrically programmable optics," *Review of Scientific Instruments*, vol. 82, no. 12, 123107, (2011).
- [18] N. A. Riza, P. J. Marraccini and C. Baxley, "Data efficient digital micromirror device-based image edge detection sensor using space-time processing," *IEEE Sensors Journal*, vol. 12, no. 5, pp. 1043-1047, (2012).
- [19] J. P. La Torre, M. J. Amin, M. Magno and N. A. Riza, "An embedded smart agile pixel imager for lasers," 6th IEEE TI European Embedded Design in Education and Research Conference (EDERC), pp. 230-234, (2014).
- [20] M. J. Amin, J. P. La Torre and N. A. Riza, "Embedded optics and electronics single digital micromirror device-based agile pixel broadband imager and spectrum analyser for laser beam hotspot detection," *Applied Optics*, vol. 54, no. 12, pp. 3547-3559, (2015).
- [21] N. A. Riza, Compressive optical display and imager, USA Patent 8,783,874, July 22, 2014.
- [22] W. C. Y. Lee and C. H. Kang, *Mobile communications*, John Wiley & Sons, 1993.
- [23] Laser Model 05-LHP-991 datasheet, Melles Griot, USA. Datasheet URL: [https://www.global-optosigma.com/en/page\\_pdf/05-LPL.pdf](https://www.global-optosigma.com/en/page_pdf/05-LPL.pdf) (visited on 03/10/2017).
- [24] N. A. Riza, J. E. Hershey, and A. A. Hassan, "A signalling system for multiple access laser communication and interference protection," *Applied Optics*, vol. 32, no. 11, pp. 1965-1972, (1993).
- [25] N. A. Riza, "Universal optical code division multiple access (O-CDMA) encoders/decoders," *Proceedings SPIE* 6, pp. 179-190, (2003).
- [26] N. Karafolas and D. Uttamchandani, "Optical fiber code division multiple access network: a review," *Optical Fiber technology*, vol. 2, no. 2, pp. 149-168, (1996).
- [27] T. Richardson and R. Urbanke, *Modern coding theory*, Cambridge University Press, 2008.

- [28] M. Johnson, Photodetection and measurement: Maximizing performance in optical systems, McGraw-Hill, 2003.
- [29] T. H. Wilmshurst, Signal recovery from noise in electronic instrumentation, Second Edition, CRC Press, 1990.
- [30] P. Gottlieb, "A television scanning scheme for a detector-noise-limited system," IEEE Transactions on Information Theory, vol. 14, pp. 428-433 (1968).
- [31] M. Born and E. Wolf, Principles of Optics, Cambridge University Press, 1997.
- [32] P. A. Santi, "Light sheet fluorescence microscopy: a review," Journal of Histochemistry and Cytochemistry, vol. 59, no. 2, pp. 129-138, (2011).
- [33] J. Pawley, Handbook of biological confocal microscopy, Springer, 2010.
- [34] N. A. Riza and A. Bokhari, "Agile optical confocal microscopy instrument architectures for high flexibility imaging," BIOS Proceedings SPIE 5324, 14, (2004).
- [35] N. A. Riza, M. Sheikh, G. Webb-Wood and P. G. Kik, "Demonstration of three-dimensional optical imaging using a confocal microscope based on a liquid-crystal electronic lens," Optical Engineering Journal, vol. 47, no. 6, 063201 - 063201-9, (2008).
- [36] N. A. Riza, "Multiplexed Optical Scanner Technology," US Patent 6,687,036 (2004).
- [37] Z. Yaqoob and N. A. Riza, "High-speed scanning wavelength-multiplexed fiber-optic sensors for biomedicine," Proceedings of IEEE Sensors Conference, vol. 1, pp. 325-330, (2002).

## CHAPTER 8

### CAOS-CMOS CAMERA<sup>8</sup>

#### 8.1 INTRODUCTION

Depending on the application, imaging systems are called scanners, profilers, cameras, imagers, and optical sensors. Classic state-of-the-art optical imager designs in a variety of applications deploy photo-detector arrays such as the Charge Coupled Devices (CCDs) and the Complementary Metal Oxide Semiconductor (CMOS) optical sensor devices. In 2014, a new Global Shutter Sony Pregius model IMX174 CMOS sensor was introduced that has a 72.94 dB dynamic range [1]. In addition, recent CMOS sensor research devices from major commercial manufacturers are showing 80 dB dynamic ranges [2]. Techniques and sensor architectures used to achieve these high dynamic ranges are diverse and include pixel level light integration time control, pixel level electronic gain control including non-linear conversion gain control, and doubling pixel size for large quantum well size in the rolling shutter mode [3]. Nevertheless, there exists a strong need for an alternative imager design that operates under extreme contrast and brightness conditions (i.e., irradiance contrast levels  $> 10^4:1$  requiring over 80 dB camera dynamic range). Such an imager which ideally has the ability to provide a large quantum well capacity with time-space pixel agility, optical spectrum flexibility, and exceptional inter-pixel crosstalk control and suppression. Starting in 2001, we proposed and extensively demonstrated (using a DMD: Digital Micromirror Device) an agile pixel Spatial Light Modulator (SLM)-based optical imager based on single pixel and dual pixel photodetection with a large quantum well capacity that is suited for operations with both coherent and incoherent light across broad spectral bands, i.e., 337 nm - 2500 nm [4-11]. This imager design operates with the agile pixels programmed in a limited Signal-to-Noise Ratio (SNR) operations starring time-multiplexed mode where acquisition of image irradiance (i.e., intensity) data is done one agile pixel at a time across the SLM plane where the desired incident image radiation is present. In effect, the agile pixel electronically

---

<sup>8</sup> N. A. Riza, J. P. La Torre and M. J. Amin, "CAOS-CMOS camera," *Optics Express*, vol. 24, no. 12, pp. 13444-13458, (2016).



adapts in a deterministic way to the imaging scenario to extract the user desired image data. This imager does not use pseudo-random spatial coding of the optical radiation with iterative computational signal processing of the detected photo-current to produce an estimated “*computational*” image as some imagers do. Our imager physically samples and detects the true optical irradiance information and then deploys computer processing to stitch the agile pixel data to produce the user desired image map. This imager can operate adaptively to electronically reprogram its user specified agile pixel settings to improve the desired imaged data quality. To put things in context, it is important to note that imaging with a single pixel (or single point detector) goes back to the late 1960’s when the USSR space program and NASA explored robust imager designs for space missions [12,13]. Today, our proposed SLM-based agile pixel imager design [4] is being called by some as a single pixel imager/camera (as one point photo-detector can be used for light detection versus a multi-element detector array). This basic imager has been engineered to implement Compressed Sensing (CS) based imaging [14] where the DMD imparts pseudo-random spatial codes on the light irradiance under observation and spatial correlation methods and iterative imaging processing are deployed to create an estimate of the true image that is considered of sparse spatial content. Note that we are not proposing an imager having the same compressive sensing working principle. Interestingly, essentially the same optical design as our proposed SLM-based imager has been used to form a ghost computational [15] and ghost compressive imager [16], but in this case, the SLM codes the light before it strikes the object to be imaged. It is also important to note that coding of optical radiation for designing a variety of single photo-detector optical instruments has been around for over 50 years and has been deployed in a variety of ways (moving 2-D binary spatial codes) to extract spectral and spatial information [17-21]. For example, in [17] a single pixel spectrometer encodes infrared optical spectra with two dimensionally patterned rotating gratings while in [21] a single pixel active 3-D imager (using a laser) deploys 2-D spatial codes (of CDMA variety) to encode and decode scanned object pixel irradiances in the 3-D sample space. In addition, the DMD has also been used with classic CCD/CMOS cameras to realize imaging spectrometers [22] and control camera blooming [23], Field of View (FOV) and pixel level irradiance integration times [24].

Motivated by modern day advances in RF wireless, optical wired communications and ultra-high speed electronic signal processing and photonic device technologies and using our prior-art SLM-based imager design [4], recently proposed and demonstrated is a new and

improved imager design platform called Coded Access Optical Sensor (CAOS) [25-27] that has the ability to provide high dynamic range low inter-pixel crosstalk images using time-frequency-space coded agile pixels. Presented in this chapter is a novel hybrid imager design that combines the CMOS/CCD sensor or any photo-detector array (PDA) sensor with the CAOS imager platform within one fully programmable optical camera unit. Specifically, the CAOS-CMOS/CCD imager functions as a smart high dynamic range image information sifter that is guided by raw image data generated from a CCD/CMOS PDA sensor. This chapter for the first time describes the implemented optical design and operations of a CAOS-CMOS camera including an experiment demonstrating the powers of its high dynamic range to decipher objects under extreme contrast and brightness conditions.

## 8.2 THE CAOS-CMOS CAMERA DESIGN

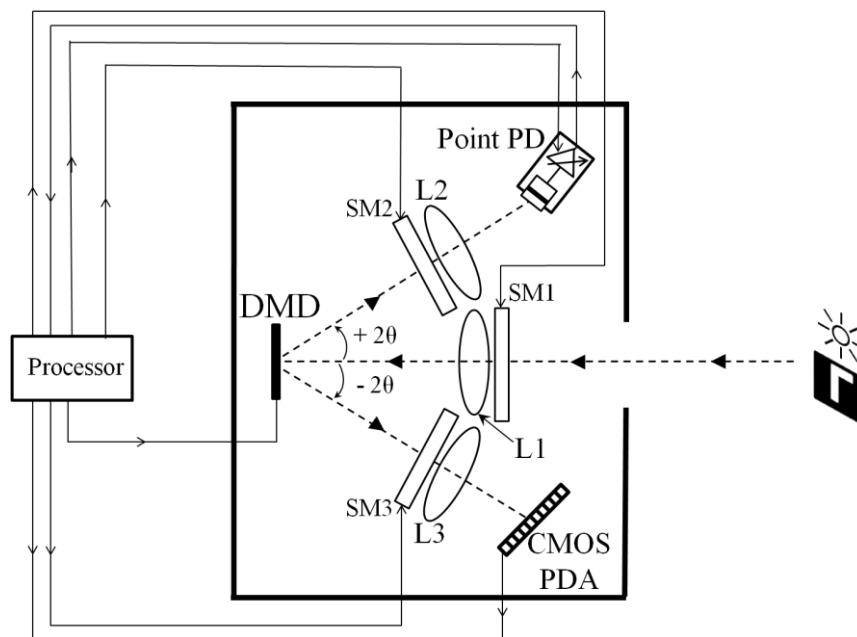


Fig. 8.1. The CAOS-CMOS Camera design.

Figure 8.1 shows the design of the proposed CAOS-CMOS imager. Lens L1 directs the irradiance to be imaged from an external light distribution plane onto the agile pixels-plane of the programmable Two Dimensional (2-D) DMD. The point PD engaged with the DMD via the lens L2 operating in the Scheimpflug [28] imaging condition forms the CAOS imaging platform. In contrast, the CMOS PDA engaged with the DMD via the lens L3

operating in the Scheimpflug imaging condition forms the CMOS imager. The DMD consists of a multi-pixel grid of micromirrors. Each micromirror is electronically programmable and has two distinct tilt states, i.e.,  $\pm\theta$  digital tilt states. In the proposed hybrid CAOS-CMOS imager design, the DMD provides two functions. First, it performs a spatial routing function for camera platform selection by forming a programmable beam splitter that directs chosen target scene irradiance pixels to either the point PD port or the CMOS PDA port. Second, the DMD imparts CAOS mode temporal modulation to certain pixels in the target scene irradiance map. Specifically, these selected agile pixels on the DMD can operate in different time-frequency coding modes like Frequency Division Multiple Access (FDMA), Code-Division Multiple Access (CDMA), and Time Division Multiple Access (TDMA). CDMA and FDMA will produce spread spectrum electrical signals from the point PD while TDMA is the staring-mode operation of the CAOS platform with one agile pixel at a time producing a DC signal per agile pixel position (same as our original DMD-imager). For full impact of the CAOS platform, agile pixel codes should include CDMA, FDMA or mixed CDMA-FDMA codes that produce not only a point PD signal with a broad electrical spectrum (that looks like a chaotic electrical signal), but also incorporates advanced information coding techniques to provide isolation (e.g., minimum cross-correlation) and robustness amongst the simultaneously deployed time-frequency codes. The proposed Fig. 8.1 design also shows the placement of optional Smart Modules (SM) labelled as SM1, SM2, and SM3 in the system. Depending on the camera application, each SM can contain a variety of electronically programmable optical conditioning elements such as variable apertures, on/off shutters, variable focus lenses, spectral filters, polarizers, and variable attenuators. When engaged with electronic post-processing, the SMs can improve imaging performance parameters including limiting saturation of the point PD and PDA. The choice of point PD and PDA also depends on the application. For example, a variety of point PDs can be used such as avalanche PDs, bolometers and photo-multiplier tubes while PDA's can be CMOS/CCD and Focal Plane Array (FPA) devices. Note that a silicon CMOS PDA with a limited spectral range can be modified for broader band operations using heterogeneous integration of thin film detectors on silicon CMOS circuitry [29,30]. As shown in Fig. 8.1, the point PD can also be combined with a Variable Gain Amplifier (VGA) module with phase-locking operations. All electronically programmable components are controlled by the camera processor that can adapt component drive conditions to deliver the desired camera imaging performance.

The CAOS-CMOS camera high dynamic range operation can be explained using the following example. Imagine the camera focussed on a given far field scene using controlled SM1 parameters with all DMD micromirrors set to their  $-\theta$  state to direct all the imaged scene irradiance to the CMOS PDA. Now imagine that the scene happens to contain a high brightness target called target 1 as well as an extremely low brightness target called target 2. Furthermore, assume that the difference in irradiance between the target 1 maximum irradiance pixel and target 2 maximum irradiance pixel exceeds the dynamic range capability of the CMOS sensor. In such a high contrast imaging scenario, the CMOS sensor will fail to register the target 2 in the viewed scene. In fact, if target 1 pixels have significant optical irradiance due to being a high brightness target, all the CMOS sensor pixels can saturate causing a full white image to be seen as the output of the CMOS sensor. In such a scenario, a variable optical attenuator in SM1 and/or SM3 can be engaged to start attenuating the optical irradiance reaching the CMOS sensor. The assumption here is that such an attenuation process does not spoil the final quality of the viewed image. Given adequate attenuation, the irradiance value of the maximum irradiance pixel in target 1 can be brought down to the level just below saturation of the CMOS pixel. At this stage, target 1 becomes visible to the CMOS sensor providing a within CMOS sensor dynamic range limit gray-scale image of target 1. Target 2 remains undetected by the CMOS sensor. Also, as the camera processor has determined the location and pixel-based irradiances of target 1, the target free zones in the CMOS sensor viewed scene are recorded. Next, the CAOS mode of the camera is engaged by turning on the  $\pm \theta$  state temporal coded modulations for the DMD pixels in the target free zones. The point PD now provides a coded electrical signal that can undergo electronic signal processing (e.g., Fourier Transform when using FDMA codes) to decode and recover the relative irradiance values of the pixels from the target 1 free zones. In general, the point PD gives a time-frequency encoded current  $i(t)$  which can be written as:

$$i(t) = K \sum_{n=1}^N c_n(t) I_n(x_n, y_n). \quad (8.1)$$

For the  $n^{\text{th}}$  agile pixel on the DMD,  $I_n$  is the pixel irradiance at the pixel central coordinates  $(x_n, y_n)$ ,  $c_n(t)$  is its time-frequency code,  $N$  is the total number of simultaneously coded agile pixels and  $K$  is a constant depending on various photo-detection factors. The next stage of signal conditioning is amplification where  $i(t)$  can be electrically amplified by a fixed factor  $G_A$  giving  $i_A(t)$ :

$$i_A(t) = G_A i(t). \quad (8.2)$$

Electrical coherent amplification using a phase-locked amplifier can also be deployed for weak optical irradiance signal amplification. The signal  $i_A(t)$  next undergoes time-frequency domain processing such as the Fourier Transform (FT) to recover the optical irradiance value at each agile pixel using the known agile pixel FDMA modulation codes. Using Eqns. (8.1) and (8.2), and assuming pure frequency codes  $c_n = \cos(2\pi f_n t)$  are used for agile pixel coding where  $f_n$  is the frequency code for the  $n^{\text{th}}$  agile pixel, the output  $S(f)$  of the Fourier Transform of  $i_A(t)$  is written as:

$$S(f) = FT\{i_A(t)\},$$

$$S(f) = FT\left\{G_A K \sum_{n=1}^N c_n(t) I_n(x_n, y_n)\right\},$$

$$S(f) = FT\left\{G_A K \sum_{n=1}^N \cos(2\pi f_n t) I_n(x_n, y_n)\right\}. \quad (8.3)$$

The Eqn. (8.3) expression can be simplified further. Assuming single sideband spectrum analysis and using  $G$  as a fixed spectrum analysis gain factor, Eqn. (8.3) can be reformulated as:

$$S(f) = G G_A K \sum_{n=1}^N I_n(x_n, y_n) \delta(f - f_n),$$

$$S(f) = G G_A K \{I_1(x_1, y_1) \delta(f - f_1) + I_2(x_2, y_2) \delta(f - f_2) + \dots$$

$$\dots + I_N(x_N, y_N) \delta(f - f_N)\}. \quad (8.4)$$

Equation (8.4) assumes that a single frequency spectral code appears as a delta function. In reality, each finite time duration signal has a finite spectral bandwidth. The Eqn. (8.4) expression indicates that the  $n^{\text{th}}$  agile pixel coded irradiance (having a unique identifier frequency code) separates out into a spectral peak in the frequency domain at  $f = f_n$  having an amplitude proportional to  $I_n(x_n, y_n)$ . Note that if FDMA codes are used, the simultaneously sampled agile DMD pixels need to be programmed with these unique frequency codes to enable decoding of the optical irradiances at these pixel locations in the resulting spectral

domain. The FDMA frequency codes need to be chosen carefully to avoid interference/crosstalk due to inter-modulation products and frequency harmonics between chosen frequency codes. Using Eqn. (8.4), the irradiance map of the image at the DMD plane can be reconstructed by sampling the amplitude of  $S(f)$  at each coded frequency location, and then assigning each amplitude to its corresponding agile pixel location, allowing a complete 2-D image reconstruction. Because the point PD combined with the VGA, SM1/SM2 control, and electronic decoding can avoid point PD optical saturation and produce high computational signal processing gain, target 2 will register in the viewed camera image when using the CAOS mode. To calibrate the low brightness target 2 relative to the high brightness target 1, the CAOS mode is also applied to at least the maximum irradiance zone of the known target 1 zone so a relative irradiance map for both targets can be generated. In effect, the CAOS-CMOS camera via smart camera processing operations can produce a true image from a high brightness and high contrast imaging scenario.

How the camera sifts through the viewed pixels in the scene in the CAOS mode depends on the camera application and optical scene characteristics. In other words, the size, location and temporal characteristics of the coded agile pixel as well as the number of simultaneous agile pixels used during sifting is determined by the camera processor in collaboration with the CMOS sensor gathered real-time images plus machine learning parameters acquired via prior training of the application deployed camera. In effect, speed of acquisition of full images via the proposed camera is not only hardware and software dependent, but also application dependent with trade-offs between agile pixel sizes and sampled pixel total count versus camera response time.

### 8.3 EXPERIMENTAL DEMONSTRATION OF THE CAOS-CMOS CAMERA

For a first demonstration of the basics of the CAOS-CMOS imager, the experimental setup implemented in the laboratory is shown in Fig. 8.2. L1, L2, and L3 have a diameter of 2.54 cm while the focal lengths of L1, L2 and L3 are 7.5 cm, 2.5 cm, and 4.0 cm, respectively. The DMD used is Texas Instrument's DLP 3000 DMD chip having a micromirror pitch of 7.637  $\mu\text{m}$ , a 608 $\times$ 684 micromirror array arranged in a diamond configuration and a micromirror tilt angle  $\theta = \pm 12^\circ$  with respect to the DMD normal. The CMOS PDA sensor deployed is IDS UI-1250LE-M-GL monochrome CMOS camera module which uses the sensor EV76C570ABT with a dynamic range of 51.3 dB, having a pixel size of 4.5  $\mu\text{m}$ , an exposure time of 87.2 ms, a frame-rate of 11.5 frames per second and a pixel count of 1600 $\times$ 1200 pixels [31]. The Dynamic Range (DR) of an optical image sensor is given by [1, 32]:

$$\begin{aligned}
 DR &= 20 \log \left( \frac{\text{Full Well Charge Storage Capacity of the Photo-Cell (electrons)}}{\text{Noise Charge (electrons)}} \right) = \\
 &= 20 \log \left[ \frac{i_{sat} (\text{Saturation})}{i_N (\text{Dark Noise})} \right] = 20 \log \left( \frac{P_{max}}{P_{min}} \right),
 \end{aligned}
 \tag{8.5}$$

where  $P_{max}$  and  $P_{min}$  are the photo-cell (i.e., sensor pixel) maximum detected optical power and the noise-limited minimum detected optical power, respectively.

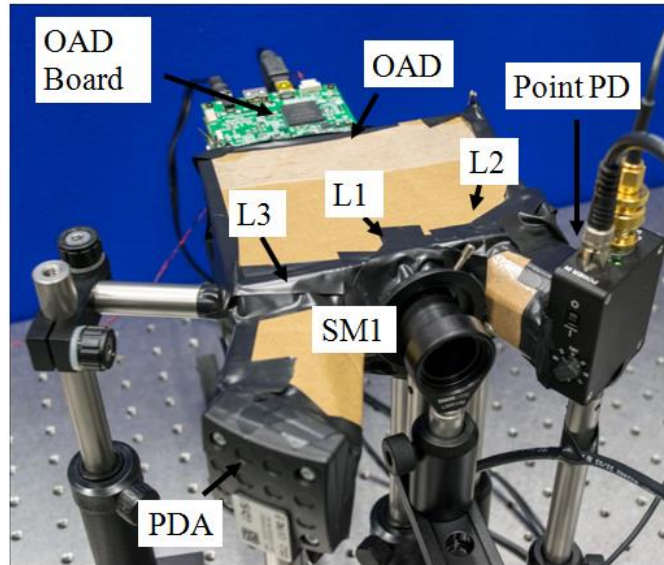


Fig. 8.2. Snapshot of the CAOS-CMOS camera experimentally setup in the laboratory.

The distance between the centers of L1 and the DMD chip is 7.9 cm, the distance between the centers of the DMD and L2 is 8.4 cm, the distance between the centers of the L2 and the PD is 3.7 cm, the distance between the centers of the DMD and L3 is 8.8 cm, and the distance between the centers of the L3 and the CMOS sensor is 7.3 cm. The SM1 deployed consists of a controllable aperture set to a diameter of 1.85 cm for the complete duration for the experiment. Note that for this demonstration, SM2 and SM3 are not deployed. The processor block in Fig. 8.2 consists of dedicated circuitry to control the DMD, a PD circuit for PD current-to-voltage conversion, a Laptop and a microcontroller ( $\mu\text{C}$ ) STM32F4 from STMicroelectronics comprising of a 12-bit Analog-to-Digital Converter (ADC). The PD voltage from the PD circuit is acquired by the ADC which is then real time transferred to the Laptop using a USB communication serial interface. Note that this voltage is limited to 3 V which is the maximum limit of the ADC deployed in the experiment. The Laptop is also connected to the DMD circuitry via USB to control the tilt states of the individual DMD micromirrors. The size, shape and time-frequency codes of the agile pixels on the DMD chip are completely programmable. The CMOS sensor is interfaced with the Laptop directly via a USB connection. A custom designed Graphical User Interface (GUI) is developed in C++/CLI language using Visual Studio 2012 in the Laptop to manage CAOS-CMOS camera operations.



Shown in Fig. 8.3 is the observed image scene acquired with a commercial Nikon D3300 camera in ambient light conditions. The Fig. 8.3 target scene consists of Rolson's 5W Aluminium Z2 LED Torch with a head diameter of 53 mm and luminosity of 180 lumens, a custom-made traffic sign and an incandescent light bulb with a line filament. The torch represents a bright light source, the traffic sign is a dim passive target while the filament in the light bulb is a current controlled variable brightness target. All three targets lie in the same plane located at a distance 1.38 m from L1. To ensure adequate lighting of the target scene, particularly of the passive traffic sign region, ambient room light is turned on. In addition, the target scene is also illuminated using two LED work lights (model Streetwize multi-purpose rechargeable torch/work light), providing adequate scene lighting. Note that the Fig. 8.3 image field of view is analogous to the field of view of the CAOS-CMOS camera.

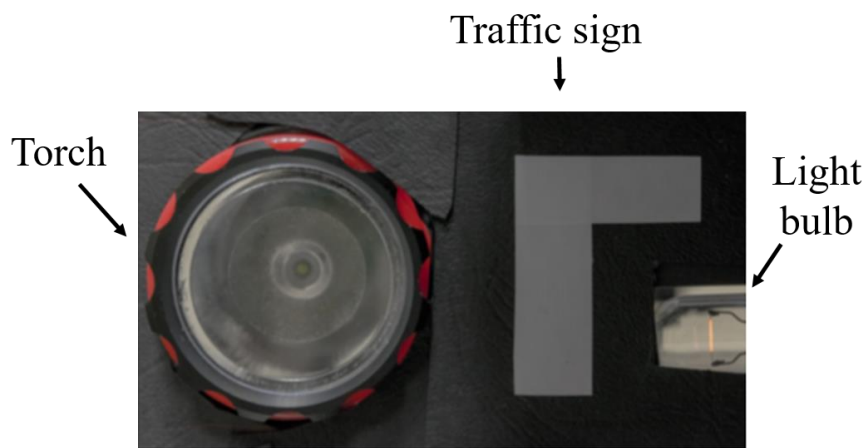


Fig. 8.3. Field of View of the target scene as viewed from the CAOS-CMOS camera in the experimental demonstration.

The point PD (i.e., photo-cell) in the experiment is a Silicon Switchable Gain Detector PDA36A by Thorlabs [33] having an active area of  $13 \text{ mm}^2$  ( $3.6 \text{ mm} \times 3.6 \text{ mm}$ ). This point PD is operated at its in-built 70 dB gain setting and the output is terminated to a  $50 \Omega$  resistor. In this setting, the PD provides a gain  $G_A$  of  $2.38 \times 10^6 \text{ V/A}$ , a maximum voltage output  $V_{\max}$  of 5 V and a Bandwidth (BW) = 5 kHz. The rise time  $t_r$  of the PD is computed as  $t_r = 0.35/\text{BW} = 70 \mu\text{s}$  [34]. Since the ADC used has a maximum input voltage limit of 3 V,  $V_{\max}$  is limited to 3 V. The maximum current output  $i_{\max}$  can be found from  $i_{\max} = V_{\max}/G_A = 3/(2.38 \times 10^6) = 1.26 \times 10^{-6} \text{ A}$ . Using a wavelength responsivity  $R(\lambda)$  of 0.35 A/W at  $\lambda = 550 \text{ nm}$  (central

wavelength of the visible range), the maximum detectable optical power  $P_{\max}$  of the PD is computed as:

$$P_{\max} = \frac{i_{\max}}{R(550nm)} = \frac{1.26 \times 10^{-6}}{0.35} = 3.6 \times 10^{-6} \text{ W}. \quad (8.6)$$

To compute the dynamic range of the point PD, it is desirable to compute its minimum detectable optical power  $P_{\min}$ . For that, the Noise Equivalent Power (NEP) [35] of the PD is used. NEP is the optical power incident on the detector that needs to be applied to equal the noise power from all sources in the detector. For the PD in the experiment, the wavelength dependent  $NEP(\lambda)$  at  $\lambda = 950 \text{ nm}$  is  $2.10 \times 10^{-12} \text{ W}/\sqrt{\text{Hz}}$ .  $R(950 \text{ nm})$  is also known to be  $0.65 \text{ A/W}$  from the point PD datasheet. Since the point PD is operated in the visible range,  $NEP(550 \text{ nm})$  is required and is computed as:

$$NEP(\lambda) = NEP_{\min} \times \left[ \frac{R_{\max}}{R(\lambda)} \right], \quad (8.7)$$

where in this setting,  $NEP_{\min} = NEP(950 \text{ nm})$  and  $R_{\max} = R(950 \text{ nm})$ . Thus,  $NEP(550 \text{ nm})$  can be computed as:

$$NEP(550 \text{ nm}) = NEP(950 \text{ nm}) \times \frac{R(950 \text{ nm})}{R(550 \text{ nm})} = 4.01 \times 10^{-12} \text{ W}/\sqrt{\text{Hz}}. \quad (8.8)$$

Since the PD BW is  $5 \text{ kHz}$  at the  $70 \text{ dB}$  setting,  $P_{\min}$  can be computed as:

$$P_{\min} = NEP(\lambda) \times \sqrt{BW} = NEP(550 \text{ nm}) \times \sqrt{5 \times 10^3} = 2.84 \times 10^{-10} \text{ W}. \quad (8.9)$$

Therefore, the point PD electrical Dynamic Range (DR), defined earlier [1, 32] as  $20 \log(P_{\max}/P_{\min})$ , is computed to be  $82.0668 \text{ dB}$  at the settings used in the experiment. This designed DR value for the point PD will be compared to the experimentally demonstrated CAOS mode camera DR.

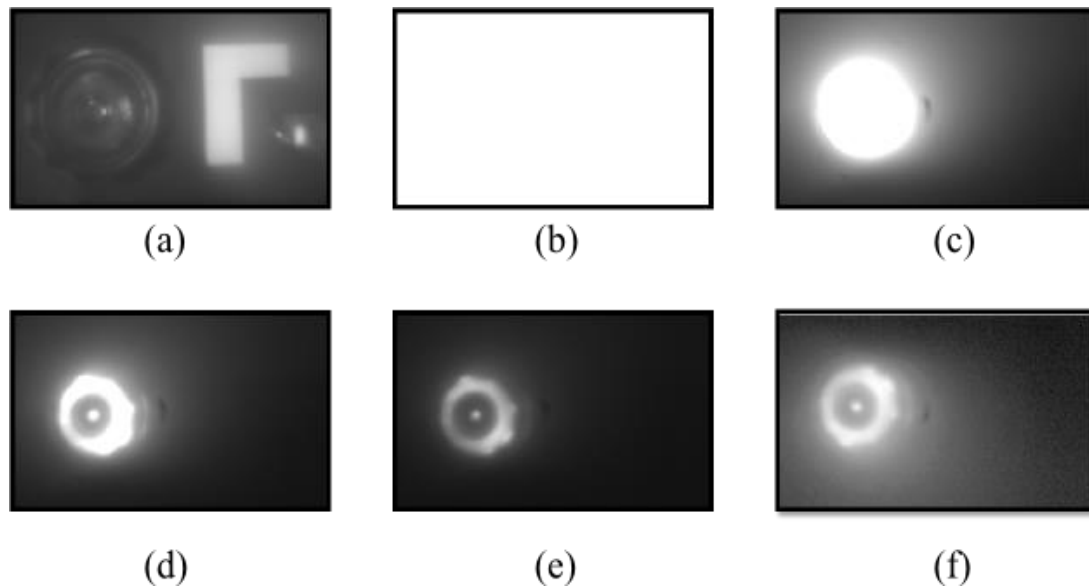


Fig. 8.4. Images of the scene viewed using the CMOS mode of the CAOS-CMOS camera. (a) Unsaturated scene with a torch off, (b) saturated scene due to torch lighting, (c) scene of (b) attenuated by a factor of 1,000, (d) scene of (b) attenuated by a factor of 3,200, (e) scene of (b) attenuated by a factor of 10,000, and (f) logarithmic scale image of the irradiance data from image (e).

To begin the experimental demonstration, the CMOS mode of the CAOS-CMOS camera is deployed. With the torch off and the bulb on, an image of the scene is acquired using the CMOS mode and shown in Fig. 8.4(a). All three of the torch, traffic sign and bulb's filament are clearly seen in Fig. 8.4(a). Next, the torch is turned on, causing the CMOS sensor to saturate completely due to the high light intensity, as shown in Fig. 8.4(b). To combat CMOS sensor saturation, Thorlabs Neutral Density (ND) filters are incorporated into SM1. Attenuating the optical irradiance from the scene by a factor of 1,000 compared to Fig. 8.4(b) results in the image shown in Fig. 8.4(c). The Fig. 8.4(c) image shows that only the torch region is completely saturated while the other targets are not visible. Next, the scene is attenuated by a factor of 3,200 compared to Fig. 8.4(b) resulting in the image in Fig. 8.4(d). This Fig. 8.4(d) image gives a clearer boundary of the torch region. However, the bright zones in the torch region in Fig. 8.4(d) are still saturated. Attenuating the optical irradiance from scene by a factor of 10,000 compared to Fig. 8.4(b) results in the image in Fig. 8.4(e). The Fig. 8.4(e) image gives an even clearer outline of the torch region with the bright zones of the torch falling just under the saturation limit, indicating that this is the amount of attenuation required to bring the bright torch region to the unsaturated range of the CMOS sensor. However, in Fig. 8.4(e), the filament bulb and the traffic sign are absent, indicating

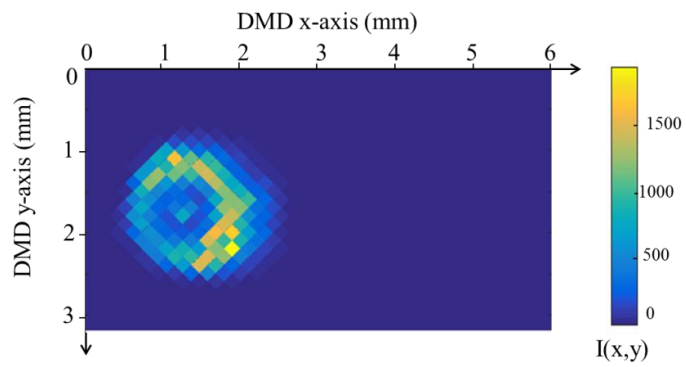
that the optical irradiance from these zones have been attenuated into the noise floor of the CMOS sensor. This conclusion is further confirmed by viewing Fig. 8.4(f) that shows the logarithmic scale image of the irradiance data from the Fig. 8.4(e) image. Thus the CMOS mode of the CAOS-CMOS camera fails to register at the same time both the bright region of the torch and the dim regions of the traffic sign and the filament of the viewed scene. Nevertheless, the CMOS-mode of the camera has provided the camera system with the locations (within the CMOS sensor pixel grid) of scene regions where a possible yet to be seen target may exist. With this CMOS-mode provided scene intelligence, the high DR CAOS mode of the CAOS-CMOS camera is deployed. Specifically, one can use smart CAOS-mode scanning of these possible target-free regions such as by performing DMD programmed horizontal and vertical slit scans over a given sub-region to quickly identify regions of the scene with possible low light level targets. If the fast scans indicate presence of such low light level targets, the DMD can be programmed in the agile pixel pin-hole CAOS mode to spatially resolve the specific pixel-grid locations of these targets in the viewed scene. It is important to note that the CAOS-CMOS camera is a fully programmable adaptive system that efficiently engages both the CMOS-mode and the CAOS-mode to search for targets with the high DR scene environment and no *a priori* scene information is required for successful imaging operations. Such coordinated operations also speed up the CAOS mode target search operations of the proposed hybrid camera. In summary, compared to a CAOS-only mode camera, the CAOS-CMOS camera has the ability to speed-up CAOS-mode operations by only scanning the scene regions where the CMOS-mode failed to register seeing a target.

For the present experiment where we already know the locations of the deployed high brightness and low light level test targets, we do not require a CAOS mode target search operation using the CMOS-mode provided Fig. 8.4(f) image data. Thus to implement a complete experimental image acquisition comparison of the CMOS mode versus the CAOS mode, an agile pixel pin-hole scan of the entire scene is done using the CAOS mode. For this CAOS mode implementation, there is no attenuation installed in SM1. The target scene consists of the torch on and the filament on, i.e., the same setting which resulted in the CMOS mode giving a saturated image in Fig. 8.4(b). In the experimental demonstration, the PD signal  $i_A(t)$  is digitized using the ADC in the  $\mu\text{C}$  and stored in the Laptop. This allows the Fourier Transform operation to be conducted using MATLAB, in which the Fast Fourier Transform (FFT) function is utilized. Additionally, the number of simultaneously coded agile pixels on the DMD chip is 2 (i.e.,  $N = 2$ ). This is due to hardware limitations of speed and

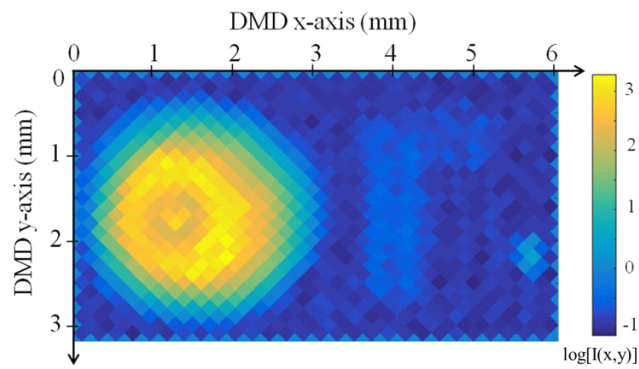
memory imposed by the low cost DMD board and the interfacing between the DMD circuitry,  $\mu\text{C}$  and the laptop. Because of this limitation, image reconstruction in the CAOS mode is accomplished using a hybrid FDMA and TDMA mode of operations. First, two simultaneously time-frequency FDMA coded agile pixels modulate and direct the coded light to the PD. After the PD signal is digitized and transferred to the laptop, the next set of two agile pixels at different locations from the previous set of pixels is modulated with the same unique frequency codes as the previous set, and the corresponding PD signal is acquired and stored. This is repeated in time (implementing TDMA) until all the PD signals from all agile pixels covering the desired scan zone have been acquired. Note that ideally, the image can be acquired almost instantly in the FDMA mode, given that all the pixels modulate with different codes at the same time. In the CAOS mode demonstration, the programmed agile pixel has dimensions of  $20 \times 20$  micromirrors, resulting in a pixel dimension of  $152 \mu\text{m} \times 152 \mu\text{m}$ . This  $20 \times 20$  micromirror pixel size is chosen to ensure that adequate irradiance emanating from the passive traffic sign region in the scene is captured to register an irradiance reading above the noise floor of the system. It is also important not to saturate the ADC input voltage limit when choosing the pixel size and number of pixels. For example, the ADC in the experiment has a 3 V limit, which means the PD voltage resulting from the PD current to voltage conversion circuitry must have a peak value of less than 3 V in to avoid saturation of the ADC readings. It turns out that when using the  $20 \times 20$  micromirror pixel and with  $N = 2$ , the maximum voltage reading from the ADC in the demonstration (which occurs when the agile pixels are located at the brightest zone of the torch in the scene) is 2.8 V. Note that if  $N = 3$  is chosen, the ADC in the present experimental setting will saturate when the pixels are located in the torch region. In such a scenario an ADC with a higher input voltage limit could be used, a smaller agile pixel size could be deployed,  $G_A$  can be reduced or  $N$  can be adjusted. Therefore, the choice of these parameters is important from the CAOS performance point of view. Using the chosen  $20 \times 20$  micromirror pixel size and  $N = 2$ , a total of 868 agile pixels (i.e., 434 separate agile dual-pixel sets) are modulated on the DMD chip in the hybrid FDMA-TDMA mode to obtain the complete image of the Fig. 8.3 scene. The 868 pixel scan consists of 28 rows and 31 columns in the DMD's diamond arrangement of micromirrors. The two frequency codes chosen are  $f_1 = 133.4 \text{ Hz}$  and  $f_2 = 200.2 \text{ Hz}$ . This choice of frequency codes ensures that the resulting intermodulation products between the frequencies and their harmonics do not affect the frequency domain amplitudes at  $f_1$  and  $f_2$ .

The steps implemented to extract the optical irradiance data at each pixel of the image using the CAOS mode are:

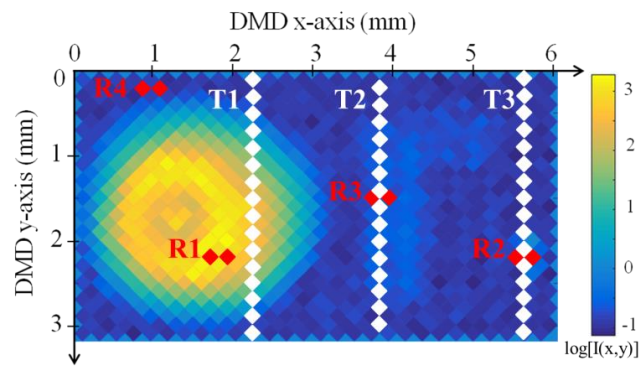
1. Using the hybrid FDMA-TDMA mode, the point PD sequentially (TDMA) acquires the optical irradiance signals from all 434 agile pixel sets modulating at FDMA codes  $f_1$  and  $f_2$ .
2. The resulting PD voltage values for all sets are sampled at 2.4 kHz using the ADC and stored into the laptop memory as 434 “.txt” files (one per modulating dual-pixel set).
3. For each file, the resulting digitized signal is subject to the FFT operation in MATLAB.
4. In the resulting frequency domain plots of  $|S(f)|$  vs.  $f$  in MATLAB for each file, the magnitude of  $S(f)$  at  $f_1 = 133.4$  Hz and  $f_2 = 200.2$  Hz are recorded. Note that these  $|S(f_1)|$  and  $|S(f_2)|$  values for all 434 dual-pixel sets give the relative optical irradiance strength at their respective agile pixel locations.
5. All  $|S(f_1)|$  and  $|S(f_2)|$  values acquired for all files are assigned to the corresponding 868 agile pixel locations to obtain the complete DMD plane optical irradiance map  $I(x, y)$ .



(a)



(b)



(c)

Fig. 8.5. 2-D image reconstruction of the target scene using the CAOS mode of the CAOS-CMOS camera. (a) scaled irradiance map  $I(x,y)$  is shown, (b) scaled irradiance map of the logarithm of  $I(x,y)$  values is shown, and (c) same plot as in (b) but with additional labels of regions R1, R2, R3 and R4 as well as location of traces T1, T2 and T3 used for quantitative image analysis purposes.

Figure 8.5(a) shows the acquired 2-D image reconstruction  $I(x, y)$  of the target scene imaged on the DMD plane using the CAOS mode. The color coding in the Fig. 8.5(a) plot indicates the scaled relative intensity of the acquired  $I(x, y)$  map, and is reported in the manuscript for visual illustration purpose only. Figure 8.5(a) is plotted in the diamond coordinates of the DMD chip micromirror layout. The Fig. 8.5(a) image map shows the shape of the torch region and is comparable to the CMOS sensor acquired image in Fig. 8.4(e). The Fig. 8.5(a) CAOS mode obtained scaled  $I(x, y)$  map includes both the traffic sign as well the filament bulb data, but these are not visible due to the limited DR of the mechanism (e.g., computer display, printed hand copy on paper) to display the irradiance map. To enable high DR viewing of the scene, the logarithm of scaled  $I(x, y)$  data is taken and plotted as Fig. 8.5(b) to reveal the true power of the CAOS mode. In Fig. 8.5(b), the torch, traffic sign and filament regions are simultaneously “seen”, demonstrating the presence of two more targets in the field of view of the camera that were otherwise unseen by the CMOS mode of the hybrid camera.

For an analysis of the Fig. 8.5(b) CAOS-mode acquired image, different sets of two pixels are marked in Fig. 8.5(c), which is the same plot as Fig. 8.5(b), as regions R1, R2, R3 and R4. R1 covers a segment of the torch, R2 has one pixel covering the filament and one in the background, R3 samples the traffic sign irradiance while R4 is on the black background and acts as a comparison. Figure 8.6 shows the resulting FFT plots in MATLAB for all four regions R1, R2, R3 and R4. Note that in the Fig. 8.6 frequency domain plots, only the peaks at frequencies 133.4 Hz and 200.2 Hz are of interest since these correspond to the modulation codes of the pixels. The 150 Hz peak labelled in each of the Fig. 8.6 plots is present due to the photodetection of light sources (including room lighting and torch) powered by the mains electricity supply. 150 Hz is the 3<sup>rd</sup> harmonic of the 50 Hz mains electricity supply [36] and is picked up in the FFT operation over all agile pixels. However, this 150 Hz peak does not carry  $I(x, y)$  data since the peaks at FDMA code frequencies of 133.4 Hz and 200.2 Hz are the ones of interest. Figure 8.6(a) plots the frequency domain amplitude for R1, giving heights of  $|S(f)| = 1940$  for  $f_1 = 133.4$  and  $|S(f)| = 401.7$  for  $f_2 = 200.2$  Hz. The peak at  $f_1$  of frequency domain amplitude = 1940 is the highest recorded peak in the CAOS mode acquired image.



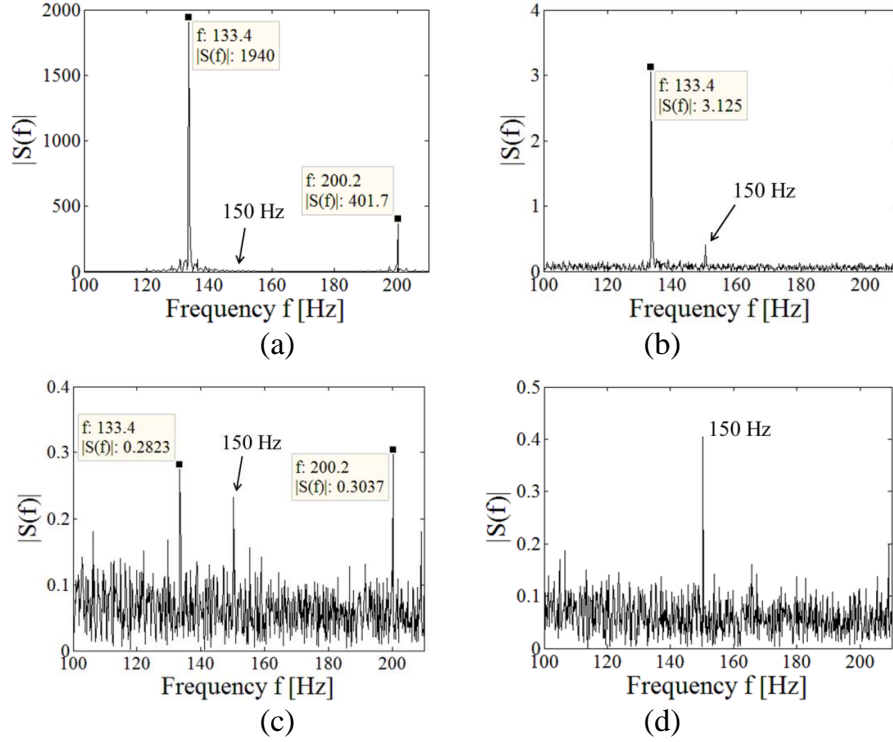


Fig. 8.6. The frequency domain plots of chosen CAOS acquired signals at regions (a) R1 covering a segment of the torch, (b) R2 covering the filament, (c) R3 covering the traffic sign, and (d) R4 covering the black background. Note that only  $|S(f_1)|$  peaks at frequencies  $f_1 = 133.4$  Hz and  $f_2 = 200.2$  Hz indicate the scaled relative optical irradiance at the corresponding agile pixels. The peak at 150 Hz appearing in each plot is due to the 3<sup>rd</sup> harmonic of the 50 Hz electricity mains supply.

Figure 8.6(b) plots  $|S(f)|$  for R2 covering the filament. In Fig. 8.6(b), the amplitude  $|S(f_1)| = 3.125$  indicates the pixel covering the filament while the pixel covering the scene background has a relative irradiance of  $|S(f_2)| \sim 0.1$ . Figure 8.6(c) plots  $|S(f)|$  for R3 covering the traffic sign, giving  $|S(f_1)| = 0.2823$  and  $|S(f_2)| = 0.3037$ . Figure 8.6(d) plots  $|S(f)|$  for R4 covering the background of the scene. Figure 8.6(d) shows that no significant irradiance is being picked up by the frequency domain plot at the two frequencies of interest, i.e.,  $|S(f_1)|$  and  $|S(f_2)| \sim 0.1$ , which is the noise floor of the experimental system. Also marked in Fig. 8.5(c) are line traces T1, T2, and T3. Trace T1 passes through the torch region, T2 passes through the traffic sign region while T3 passes through the filament region. The 1-D optical irradiance  $I(y)$  along the  $y$ -direction of the DMD chip for traces T1, T2, and T3 are shown in Figs. 8.7(a), 8.7(b), and 8.7(c), respectively. These Fig. 8.7 plots illustrate the variation of optical irradiance along different line regions of the image.

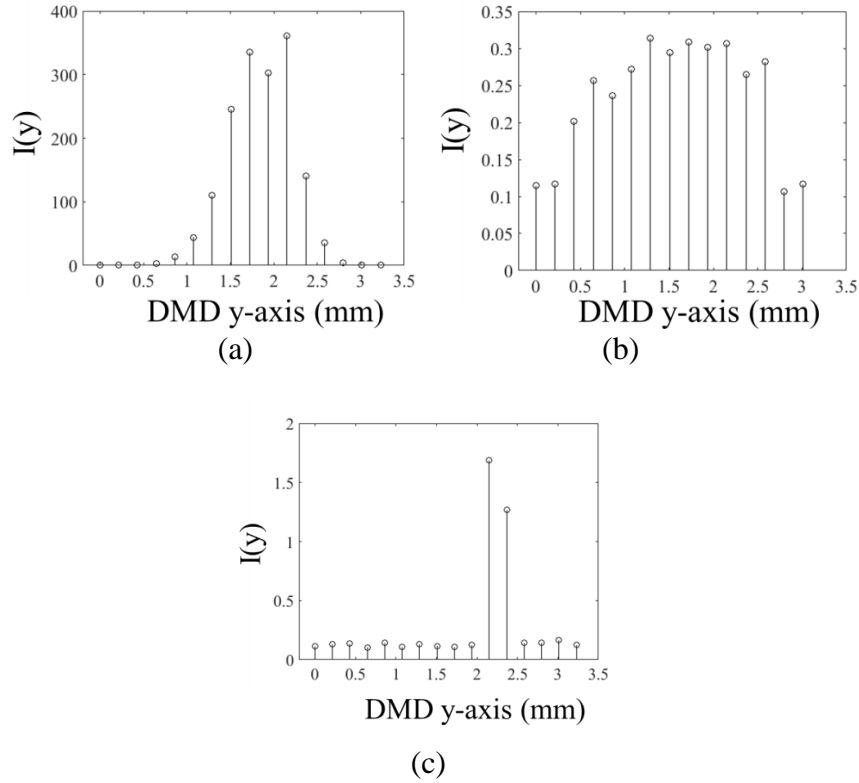


Fig. 8.7. Plots showing the measured scaled irradiances along Fig. 8.5(c) labeled traces (a) T1, (b) T2, and (c) T3.

To evaluate the Dynamic Range of the Fig. 8.5 CAOS mode acquired image, note that the highest measured relative irradiance value ( $|S(f)|$ ) is 1940 which is for the torch region of the scene. Whereas, the lowest recorded “signal” (above the noise floor of  $\sim 0.1$ ) is measured to be  $|S(f)|$  0.153. Using these values, the DR of the CAOS mode is computed to be  $20 \log(1940/0.153) = 82.06$  dB. Note that this result matches the DR of 82.0668 dB calculated earlier for the point PD used in the experiment. Therefore, the DR obtained by the CAOS mode is limited by the DR of the point PD. In the experiment, due to the weak optical irradiance for the traffic sign portion of the scene, the 70 dB gain setting of the point PD amplifier is deployed. If, for example, the lower gain 30 dB setting of the PD VGA is used which provides  $G_A = 0.75 \times 10^4$  V/A,  $NEP(970 \text{ nm}) = 2.34 \times 10^{-12}$  W/ $\sqrt{\text{Hz}}$  and  $BW = 5.5$  MHz, the point PD DR is computed to be 100.7432 dB, a near 19 dB improvement in camera DR compared to the 70 dB VGA gain setting. However, the trade-off for getting higher DR using the reduced VGA gain means lower photocurrent from reduced optical irradiance scene regions such as the traffic sign in Fig. 8.3. In such a scenario, another parameter which can be adjusted is the agile pixel size. In the experimental demonstration, a  $20 \times 20$  micromirror pixel

size is deployed. Using a larger pixel size increases the per pixel coded optical irradiance striking the point PD, increasing the likelihood of detection of weak light irradiances although at the expense of output image resolution. In this case, one must also be careful not to exceed the voltage limit of the ADC as increasing the agile pixel size also increases the light irradiance collected from the bright regions of the scene. Note that there is also a trade-off between the CAOS-mode imaging speed and  $N$ , the number of simultaneously sampling agile pixels as  $N$  increases. In other words, to operate the camera at faster imaging speed, the larger number of modulating agile pixels can result in a stronger total optical irradiance striking the point PD. In order to avoid saturation of the point PD, the VGA gain needs to be reduced and this affects the detection of weak irradiance regions in the viewed scene.

The smart operation of the hybrid camera uses the fast speed acquisition CMOS-mode acquired images that undergoes threshold image processing to first identify the spatial locations of any high brightness targets. To implement a fast operations CAOS-mode, a search mode is implemented to look for low optical irradiance targets such as by using orthogonal direction line (slit) scans, e.g., along  $x$  and  $y$  directions of the DMD plane. For the case in the experiment, the right-hand side of the CMOS-mode image (see Fig. 8.4(c)) appears dark that is about half the image frame. Considering a slit width of 20 micromirrors, there are 15 and 28 slit positions covering the  $x$  and  $y$  direction scans, respectively. Using a slit reset time of 5 seconds (includes modulating and loading time), the experimental system takes 75 seconds to generate a  $x$ -slit scan and 140 seconds to generate a  $y$ -slit scan. Via image processing, the acquired 2-D slit data provides zoomed locations of possible weak irradiance targets. For the experiment, the 2-D slit scan mode indicates presence of weak irradiance targets in the zoomed  $15 \times 28$  agile pixel count region. With  $N = 2$ , 420 ( $15 \times 28$ ) agile pixels, FDMA modulation in sets of 2 agile pixels, a set loading and acquisition time of 6 seconds (presently highly limited by our non-optimized electronic boards), a 21 minutes image acquisition time is required. For a full DR analysis and comparison between the CMOS-mode image and the CAOS mode image of the hybrid camera, a complete CAOS-mode scan of the DMD chip ( $28 \times 31$  agile pixels) is acquired as shown in Fig. 8.5. Deploying CMDA codes using a current state-of-the-art 32 kHz frame rate DMD-based CAOS mode [37], one can estimate much faster image generation time. Assuming a scanning grid of 1000 agile pixels on the DMD plane, one can deploy 100 different CDMA orthogonal or pseudo-random codes [38] with each code having a length of 100 bits and each code assigned to a certain agile pixel in a 100 agile pixels grouping. Given a 32 kHz frame rate, a single bit time duration is  $1/(32$

$\times 10^3$ ) s = 31.25  $\mu$ s. A code of 100 bits has a duration of 31.25  $\mu$ s  $\times$  100 = 3.125 ms. Thus in 3.125 ms, irradiance data from 100 simultaneously modulating codes programmed to spatially specific 100 agile pixels is acquired. To use 100 CDMA codes for 1000 agile pixels, TDMA is deployed to modulate 100 agile pixels at a time to cover the scan region, using 100 separate codes for each 100 agile pixel sets. Therefore, the total irradiance acquisition duration becomes 3.125 ms  $\times$  10 = 31.25 ms, similar to what is considered real-time video rates. Note that if TDMA is not deployed and a 100 pixel image is desired, 100 CAOS coded pixels can be simultaneously deployed, giving a total imaging time of 3.125 ms or an image refresh rate of near 300 Hz. Thus using the programmability feature of the CAOS mode and even faster frame rate DMDs, one can expect faster image acquisition. This statement assumes that the CMOS/PDA sensor has image refresh rates that match or exceed the CAOS-mode imaging rate and with today's CMOS optical sensor technology, this is indeed the case. Ultimately, image smear of fast moving targets depends on the speed of the target and the proposed imager can be programmed to avoid or reduce image smear.

Today, fast (> 65 MHz) sampling rate 14-bits ADCs are available [39] for digitizing the point PD signal to implement fast decoding and image processing. Note that in the deployed CAOS mode, inter-pixel crosstalk effects are minimal. There is zero crosstalk between the time multiplexed pixel data sets acquired using the TDMA mode as the pixel sets are acquired at different instants in time. In the CAOS mode deploying orthogonal CDMA codes, one minimizes the inter-pixel crosstalk by using orthogonal codes [38], while frequency codes in a pixel set in the CAOS FDMA mode are selected suitably to avoid spectral overlap. This pixel readout mechanism is unlike CMOS/CCD sensors where the optical and electrical crosstalk effects are ever-present due to the hardwired pixel array structure and charge readout architectures, thus limiting inter-pixel crosstalk performance in these cameras.

In summary, camera programmable parameters such as point PD VGA gain and bandwidth, number of simultaneous agile pixels, agile pixel size, total agile pixels in sampled scene, SM settings as well as incident lighting levels of the sampled scene zones all affect the performance of the CAOS mode. Used in conjunction with the CMOS mode processed image data, a search mode with a quick raw scan using larger agile pixels is used to provide a coarse resolution irradiance distribution map before optimizing the different camera parameters for the different scene zones to implement smart image reconstruction via the CAOS mode.

## 8.4 CONCLUSION

For the first time, proposed and demonstrated is a CAOS-CMOS camera that combines the time-frequency agile pixel CAOS imager with the traditional CMOS camera architecture to realize a powerful, high dynamic range imaging platform. The CAOS-CMOS camera design deploys a DMD chip which receives the incoming optical irradiance from a target scene and selectively directs it towards the CAOS arm and the CMOS arm of the camera. In the experimental demonstration, a target scene consisting of a bright light source and two dim light sources near the CAOS-mode noise floor are used to investigate the performance limits of both the CAOS and CMOS operational modes of the hybrid camera. The CMOS camera, rated at 51.3 dB DR according to the manufacturer, is experimentally shown to provide an image having insufficient dynamic range, whereas the CAOS-mode camera exhibited a DR of 82.06 dB under the experimental conditions and successfully reconstructed the target scene completely. This experimental 82.06 dB DR value of the CAOS operational mode is limited due to the components used in the demonstration. Much higher DR values are obtainable using the CAOS mode of the camera using different programmable settings of the camera smart components plus the improved electronic capabilities of the ADC, and/or by deploying coherent detection via phase-locked loop amplification. The high DR imaging performance of the CAOS-CMOS camera has diverse applications across the fields of astronomy, machine vision, safety and surveillance, undersea observations and marine science, medical imaging and extreme environment imaging.

## REFERENCES

- [1] Point Grey White Paper Series, “Sony Pregius Global Shutter CMOS Imaging Performance,” (Point Grey Research, 2015). Available at URL: <http://www.ptgrey.com/white-paper/id/10795> (visited on 06/10/2017).
- [2] M-W. Seo, S-H. Suh, T. Iida, T. Takasawa, K. Isobe, T. Watanabe, S. Itoh, K. Yasutomi, and S. Kawahito, “A low-noise high intrascene dynamic range CMOS image sensor with a 13 to 19b variable-resolution column-parallel folding-integration/cyclic ADC,” *IEEE J. Solid-State Circuits*, vol. 47, no. 1, pp. 272-283, (2012).
- [3] S. Sukegawa, T. Umebayashi, T. Nakajima, Hiroshi Kawanobe, Ken Koseki, Isao Hirota, Tsutomu Haruta, M. Kasai, K. Fukumoto, T. Wakano, and K. Inoue, “A 1/4-inch 8Mpixel back-illuminated stacked CMOS image sensor,” in *Proceedings of IEEE Conference on Solid-State Circuits Conference Digest of Technical Papers (ISSCC) (IEEE, 2013)*, pp. 484-485.
- [4] S. Sumriddetchkajorn and N. A. Riza, “Micro-electro-mechanical system-based digitally controlled optical beam profiler,” *Applied Optics*, vol. 41, no. 18, pp. 3506-3510, (2002).
- [5] N. A. Riza and M. J. Mughal, “Optical power independent optical beam profiler,” *Optical Engineering*, vol. 43, no. 4, pp. 793-797, (2004).
- [6] N. A. Riza and F. N. Ghauri, “Super resolution hybrid analog-digital optical beam profiler using digital micromirror device,” *IEEE Photonics Technology Letters*, vol. 17, no. 7, pp. 1492-1494, (2005).
- [7] M. Gentili and N. A. Riza, “Wide aperture no moving parts optical beam profiler using liquid crystal displays,” *Applied Optics*, vol. 46, no. 4, pp. 506-512, (2007).
- [8] M. Sheikh and N. A. Riza, “Demonstration of pinhole laser beam profiling using a digital micromirror device,” *IEEE Photonics Technology Letters*, vol. 21, no. 10, pp. 666-668, (2009).
- [9] N. A. Riza, S. A. Reza, and P. J. Marraccini, “Digital micro-mirror device-based broadband optical image sensor for robust imaging applications,” *Optics Communication*, vol. 284, no. 1, pp. 103-111, (2011).
- [10] N. A. Riza, P. J. Marraccini, and C. Baxley, “Data efficient digital micromirror device-based image edge detection sensor using space-time processing,” *IEEE Sensors Journal*, vol. 12, no. 5, pp. 1043-1047, (2012).

- [11] M. J. Amin, J. P. La Torre, and N. A. Riza, "Embedded optics and electronics single digital micromirror device-based agile pixel broadband imager and spectrum analyser for laser beam hotspot detection," *Applied Optics*, vol. 54, no. 12, pp. 3547-3559, (2015).
- [12] S. Selivanov, V. N. Govorov, A. S. Titov, and V. P. Chemodanov, "Lunar station television camera," (Reilly Translations): NASA CR-97884, (1968).
- [13] F. O. Huck and J. J. Lambiotte, "A performance analysis of the optical-mechanical scanner as an imaging system for planetary landers," NASA TN D-5552, (1969).
- [14] D. Takhar, J. N. Laska, M. B. Wakin, M. F. Duarte, D. Baron, S. Sarvotham, K. F. Kelly, and R. G. Baraniuk, "A new compressive imaging camera architecture using optical-domain compression," *Proceedings SPIE 6065*, 606509, (2006).
- [15] J. H. Shapiro, "Computational ghost imaging," *Physics Review A*, vol. 78, no. 061802(R), (2008).
- [16] O. Katz, Y. Bromberg, and Y. Silberberg, "Compressive ghost imaging," *Applied Physics Letters*, vol. 95, no. 131110, (2009).
- [17] M. J. E. Golay, "Multi-slit spectrometry," *Journal Optics Society of America*, vol. 39, pp. 437-444, (1949).
- [18] P. Gottlieb, "A television scanning scheme for a detector-noise limited system," *IEEE Transactions on Information Theory*, vol. 14, no. 428-433, (1968).
- [19] E. E. Fenimore, "Coded aperture imaging: predicted performance of uniformly redundant arrays," *Applied Optics*, vol. 17, no. 22, pp. 3562-3570, (1978).
- [20] W. T. Cathey, and E. R. Dowski, "New paradigm for imaging systems," *Applied Optics*, vol. 41, no. 29, pp. 6080-6092, (2002).
- [21] N. A. Riza and M. A. Arain, "Code multiplexed optical scanner," *Applied Optics*, vol. 42, no. 8, pp. 1493-1502, (2003).
- [22] K. Kearney and Z. Ninkov, "Characterization of a digital micro-mirror device for use as an optical mask in imaging and spectroscopy," *Proceedings SPIE 3292*, pp. 81-92, (1998).
- [23] J. Castracane and M. Gutin, "DMD-based bloom control for intensified imaging systems," *Proceedings SPIE 3633*, pp. 234-242, (1999).
- [24] S. Nayar, V. Branzoi, and T. Boulton, "Programmable imaging using a digital micro-mirror array," in *Proceedings of IEEE on Computer Vision and Pattern Recognition (IEEE, 2004)*, pp. 436-443.

- [25] N. A. Riza, M. J. Amin and J. P. La Torre, "Coded Access Optical Sensor (CAOS) Imager," *Journal of the European Optical Society-Rapid Publications*, vol. 10(15021), (2015).
- [26] N. A. Riza, "Coded Access Optical Sensor (CAOS) imager and applications," *Proceedings SPIE 9896*, (2016).
- [27] N. A. Riza, "Compressive optical display and imager," *US Patent 8783874 B1* (2014).
- [28] T. Scheimpflug, "Improved Method and Apparatus for the Systematic Alteration or Distortion of Plane Pictures and Images by Means of Lenses and Mirrors for Photography and for other purposes," *GB Patent No. 1196* (1904).
- [29] K. Lee, S. Huang, Y. Joo, W. A. Doolittle, S. Fike, N. Jokerst, M. Brooke, and A. Brown, "Design of a smart pixel multispectral imaging array using 3D stacked thin film detectors on Si CMOS circuits," in *Proceedings of IEEE Conference on Electronic-Enhanced Optics, Optical Sensing in Semiconductor Manufacturing, Electro-Optics in Space, Broadband Optical Networks* (IEEE, 2000), pp. 157-158.
- [30] D. Y. Kim, T-H. Lai, J. W. Lee, J. R. Manders and F. So, "Multi-spectral imaging with infrared sensitive organic light emitting diode," *International Journal of Scientific Reports*, vol. 4, no. 5946, (2014).
- [31] IDS  $\mu$ Eye LE camera datasheet, IDS, Germany. Product description available at URL: <https://en.ids-imaging.com/store/products/cameras/usb-2-0-cameras/ueye-le.html> (visited on 06/10/2017).
- [32] D. V. Blerkom, C. Basset, and R. Yassine, "CMOS DETECTORS: New techniques recover dynamic range as CMOS pixels shrink," *Laser Focus World*, vol. 46, no. 6, (2010).
- [33] PDA36A datasheet, Thorlabs, (2015). Product description available at URL: <https://www.thorlabs.com/thorProduct.cfm?partNumber=PDA36A> (visited on 06/10/2017).
- [34] Photodetector technical documents, Thorlabs, Germany. Product description available at URL: <https://www.thorlabs.com/thorproduct.cfm?partnumber=FDS100> (visited on 06/10/2017).
- [35] V. Mackowiak, J. Peuplelmann, Y. Ma, and A. Gorges, "NEP-Noise Equivalent Power", White Paper, Thorlabs.
- [36] J. Arrillega, D. A. Bradley and P. S. Bodger, *Power System Harmonics*, John Wiley and Sons, 1985.



- [37] DLP7000 DLP 0.7 XGA datasheet, Texas Instruments, USA (2015). Product description available at URL: <http://www.ti.com/product/DLP7000> (visited on 06/10/2017).
- [38] S. P. Kim and M. J. Kim, "A constant amplitude coding for code select CDMA system," in Proceedings of IEEE TENCON Conference on Computers, Communications, Control and Power Engineering, pp. 1035-1038, (2002).
- [39] ADC ADS52J90, Texas Instruments, USA. Product description available at URL: <http://www.ti.com/product/ADS52J90/datasheet> (visited on 06/10/2017).

## CHAPTER 9

### DEMONSTRATION OF 136 DB DYNAMIC RANGE CAPABILITY FOR A SIMULTANEOUS DUAL OPTICAL BAND CAOS CAMERA<sup>9</sup>

#### 9.1 INTRODUCTION

The real world is rich in color and irradiance distributions creating a massive data set of extreme contrast irradiance values spread across various optical spectral bands. Smartly mining for a full irradiance range scene image data set with desired color information is a challenge for today's dominant multi-pixel camera technology [1] where the limited instantaneous dynamic range (e.g., < 80 dB) and spectral sensitivity of the camera can fail to capture the true scene data that may be vital to the application. Industrial machine vision [2], food processing [3], archaeology and art conservation [4] along with biology, military, undersea environmental monitoring, material (e.g., soil) composition inspection, mining and mineralogy, and astronomy, are example imaging scenarios where data sets can exist with extreme optical contrast (e.g., 10<sup>7</sup>:1) bright targets across multiple simultaneous broad spectral bands, e.g., Ultra-Violet (UV) + Visible or UV + Near Infrared (NIR), or Visible + Near IR or visible and Short Wave IR (SWIR). For example, a scene can exist with two simultaneous and spatially adjacent targets, one being a very bright visible-NIR target and the other being a very low brightness visible-NIR target. Under these dual-band extreme contrast conditions, target recovery becomes a challenge for prior-art multispectral imaging instruments that deploy wavelength sensitive optics, e.g., gratings and mechanically or electronically tunable filters combined with traditional Photo-Detector Arrays (PDAs) such as CCD, CMOS, and Focal Plane Array (FPA) multi-pixel devices [5-10]. Specifically, it is mainly the PDA in the spectral imager that limits its dynamic range performance. This is because a bright target will saturate the pixel in the multi-pixel detector as each pixel in the PDA has a limited quantum well capacity, i.e. the amount of charge that the pixel can hold

---

<sup>9</sup> N. A. Riza and J. P. La Torre, "Demonstration of 136 dB dynamic range capability for a simultaneous dual optical band CAOS," *Optics Express*, vol. 24, no. 26, pp. 29427-29443, (2016).

before saturation. In addition, due to spillover effects, the bright target creates crosstalk noise in the neighboring pixels of the PDA. As an example, one commercial multispectral imager offers a 60 dB dynamic range which is inadequate for extreme contrast spectral imaging [11]. To counter the pixel saturation problem and extract a higher dynamic range from the limited dynamic range PDA, a High Dynamic Range (HDR) processing technique has been applied to multispectral imaging where gradual optical attenuation is applied to the scene to acquire multiple images and electronic imaging processing is used to reach an unsaturated final image [12-13]. Although this HDR approach and other methods (e.g., increasing pixel size, controlling pixel integration time, resetting pixel output voltage or using non-linear amplification at each pixel site) can improve the dynamic range of a camera under overall bright light scene conditions [14], a fundamental problem can occur when further attenuation of the weak light target in the scene will send the PDA pixel irradiance information into the noise floor of the limited instantaneous dynamic range PDA. Thus, a spectral camera that avoids or limits the use of scene light attenuation and also avoids calibration and control of the many individual pixels in a PDA is highly desirable for obtaining true high (e.g. > 130 dB) contrast images. Furthermore, it would also be highly beneficial that this extreme (e.g. > 130 dB) instantaneous dynamic range imager has simultaneous dual-broadband channel detection with all-optical or electronic domain fine tuning capabilities within each band and additionally provides a low (e.g. < -50 dB) inter-pixel isolation and inter-band isolation levels. Such an imager can be envisioned to work in unison with traditional prior-art PDA-based multispectral and/or hyperspectral imagers to extract the desired application specific pixel data for smart spectral imaging.

Therefore, to put things in context, earlier we proposed and demonstrated an agile pixel imager (called by some as a single pixel camera/imager) using a Texas Instruments (TI) Digital Micromirror Device (DMD) that deploys a point Photo-Detector (PD) and agile pixel programming to spatially map an incident irradiance pattern [15]. In effect, the large micro-mirror count (e.g., 1 million micro-mirrors) DMD when combined with the large quantum well capacity point PD forms a PDA. Furthermore, an agile pixel programmed as a desirable shaped and positioned light sampler on the DMD extracts the incident irradiance on the DMD and transfers it for capture by the point PD, thus forming the agile pixel imager. To add operational robustness, a two point PD design has also been proposed and demonstrated for this agile pixel imager [16]. This starrng-mode imager has been demonstrated for various spectral bands including UV, visible, and NIR [17], plus a design has been demonstrated that

enables imaging plus optical spectrum analysis [18]. Recently, we have also shown how our original DMD imager can deploy space-time-frequency agile pixel processing to realize a much improved near 80 dB dynamic range imager called the Coded Access Optical Sensor (CAOS) camera [19-23]. Specifically, the CAOS imager assigns independent time-frequency codes to selected agile pixels in the image and simultaneously detects all the light and uses Radio Frequency (RF) wireless type time-frequency domain signal processing in-parallel to decode all agile pixel irradiances of the selected image pixels. The CAOS imaging mode is similar to operations of a mobile phone wireless network where specific telephone numbers are assigned to mobile phone users within a network of many simultaneous users where extreme sensitivity electronic signal processing is used to recover phone data from the very weak RF signal picked up by the phone's electronic receiver. CAOS exploits the same extreme sensitivity and detection principles used in RF wireless networks to greatly enhance the dynamic range of our original agile pixel imager. Furthermore, simultaneous agile pixels detection via CAOS-mode can improve imaging speed. Note that the basic starring mode DMD imager design has also been used for compressive sensing-based imaging [24] where image recovery is based on image projection measurements and iterative algorithm image processing. In contrast, the imaging works described by us [15-23] and demonstrated in this chapter directly sample and preserve the true optical irradiances of the incident image and the imaging procedures are not based on compressive sensing techniques. One must also appreciate that both coding of light (e.g. via rotating patterned gratings for spectroscopy [25] and a moving reticle for television pictures [26]) and single PD irradiance map detection date back to over 50 years [27-28] and advances in devices and techniques within the modern wired and wireless optical and electronic communications and display infrastructure are seeding the CAOS imaging platform. In addition, DMDs have been used with CCD/CMOS imagers for spectrometry [29] plus control of camera parameters such as blooming [30], Field of View (FOV) and pixel level irradiance integration times [31].

Building on our prior works in two point PD DMD-based imaging and the CAOS camera, this chapter for the first time provides the workings of the desired extreme contrast bright multi-spectral target scenario dual optical band CAOS imager design that features extreme ( $> 130$  dB) instantaneous dynamic range as well as low (e.g.  $< -50$  dB) inter-pixel and inter-channel crosstalk. A proof-of-concept dual-band imager is experimentally demonstrated using visible and near infrared LED targets in a viewed scene. All-optical narrowband filtering as well as CAOS-mode RF domain filtering is engaged for the first time with the

CAOS-mode encoded image pixel data to extract finer wavelength content from the imaged agile pixel. Compared to our previous 80 dB CAOS mode dynamic range performance [19-20], it is shown for the first time how using a higher resolution ADC with both amplitude range and sampling duration control along with a larger dataset DSP implementation extends the imager dynamic range to a desired 136 dB level. This chapter provides the detailed design and experimental analysis of the proposed simultaneous dual band CAOS imager.

## 9.2 SIMULTANEOUS DUAL OPTICAL BAND CAOS CAMERA DESIGN

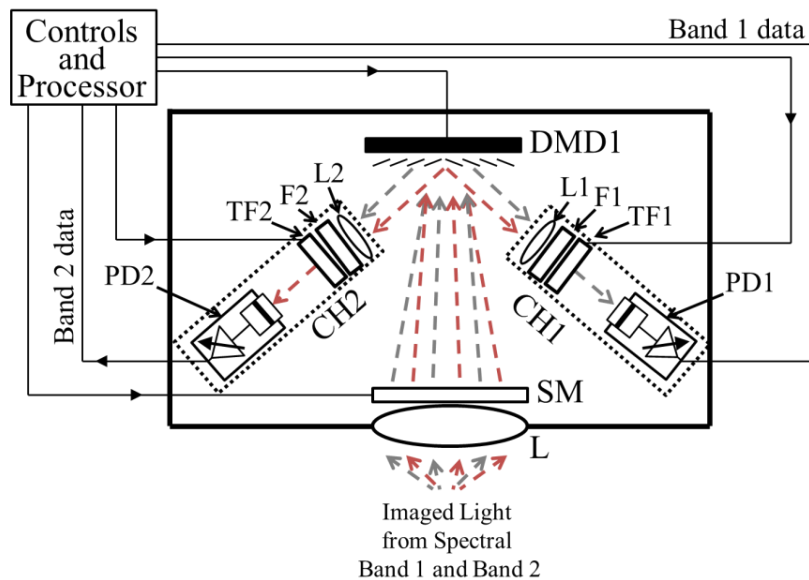


Fig. 9.1. Proposed simultaneous dual optical band CAOS imager design.

Shown in Fig. 9.1 is the proposed simultaneous dual optical band CAOS camera design. Multi-wavelength light passes through imaging lens L and a Smart Module (SM) optic to be incident on the DMD1 plane. The SM optic can contain light conditioning optics such as variable focal lenses, variable apertures, variable attenuators, and polarizers. The user decides the components make-up of the SM optics as well as on the two different spectral bands for camera operations called spectral band 1 and spectral band 2. Given the spectral band 1 and 2 wavelengths, the user selects the appropriate point PD unit detector technology deployed in the camera.

The PD unit as shown can also use a Variable Gain Amplifier (VGA) module or engage optical amplification before photo-detection. Selected agile pixels on the DMD1 plane are time-frequency modulated with specific CAOS-mode codes enabling the image irradiance to acquire different RF codes, much like different telephone numbers assigned to different pixels in the optical image. The TI DMD1 micromirror has two tilt states causing the optical image time-frequency modulated light signals to simultaneously show up in both PD channels of the CAOS camera. As the DMD1 is a digital-only spatial light modulator, each agile pixel time-frequency modulation produces its CAOS-mode specific square wave electrical signal at the point PD outputs. L1 and L2 act as imaging lenses between the DMD1 and PD1/PD2 planes. For multispectral imaging operations, F1 and F2 are fixed broadband spectral filters matched to spectral bands 1 and 2, respectively. For hyperspectral imaging operations, TF1 and TF2 are tunable spectral filters matched to spectral bands 1 and 2, respectively. For example, F1, TF1 and PD1 in channel 1 of the camera can deploy visible channel devices while F2, TF2 and PD2 in channel 2 arm can use NIR wavelength selection components. Because the TI DMD1 operates between approximately 320 nm to 2500 nm wavelengths [32], a variety of dual bands can be realized for the proposed camera. There are various options for the required TF1/TF2 modules such as designs using bulk Acousto-Optical Tunable Filters (AOTFs), DMD, volume Bragg gratings, and liquid crystals [33-36]. PD1 and PD2 units provide RF signals whose RF spectra contain CAOS coded agile pixel irradiance data for the optical filtered light from the two different spectral bands of the camera. Specifically, PD1 and PD2 provide spectral image data for spectral bands 1 and 2, respectively. Decoding this detected RF spectra using time-frequency electronic signal processing recovers the agile pixel irradiance values for the selected wavelengths. RF signals from both PD1 and PD2 are recorded simultaneously and subjected to high speed electronic processing.

There are a number of innovative design features of the Fig. 9.1 imager design that create enhanced imaging performance in terms of dynamic range, inter-pixel crosstalk, inter-band crosstalk, and within broadband channel spectral channel crosstalk. Note the DMD time-frequency modulation CAOS-mode operation instantaneously sends selected agile pixels input image light to both optical detection channels of the imager. Because the two detection channels are physically separated, fixed broadband optical filters (F1/F2) matched to the point PD (PD1/PD2) broad wavelength band can be deployed to greatly reject the unwanted band light, implementing spatially powered optical spectral filtering. The CAOS-

mode creates agile pixel light signals with RF modulation, each pixel having its unique electronic RF spectral signature that is decoded after photo-detection using RF wireless-style processing. Furthermore, note that TF1/TF2 can be programmed in an additional CAOS-mode to time-frequency modulate selected hyperspectral wavelength channels within agile pixels, allowing the use of RF spectral processing to detect specific narrow spectral band image data. Because RF domain signal processing can operate with extreme dynamic ranges, electronic filtering can be used to further reject optical spectral crosstalk within a broadband optical channel. Thus the proposed Fig. 9.1 imager can engage both optical and electronic filtering to reject unwanted optical wavelengths. In the same spirit, spatial crosstalk between agile pixels in the image can also be reduced using RF domain electronic processing.

Another innovative feature that is empowered by the CAOS-mode is the use of controlled ADC and DSP operations to extend the instantaneous dynamic range of the imager and in-turn improve image spatial and spectral crosstalk performance. Specifically, proposed and shown experimentally for the first time in this chapter is how using a higher resolution ADC with both amplitude range and sampling duration control along with a higher data set DSP implementation extends the imager dynamic range by creating significant signal processing gain and noise floor suppression. This electronic digital domain feature is possible because of the CAOS mode agile pixel operations via point PD detection that naturally produces an RF spectrum rich data set that can engage the power of wireless-style DSP processing. For example, consider an N-bit ADC using a sampling rate of  $f_s$  kilo-samples/second with an agile pixel sampling duration time of  $t_s$  seconds. The voltage range of such an ADC can also be programmable and can be set between various voltage ranges to create a zoomed in extreme resolution detection of a weak signal. The output of the N-bit ADC then undergoes DSP, for example, spectrum analysis via DSP Discrete Fourier Transform (DFT) operation computed by the FFT algorithm implemented in a dedicated processor. The DFT produces processing gain resulting in noise suppression. Specifically, FFT-based processing gain in dB is equal to  $10 \times \log(M/2)$  where M is the number of points in the FFT [37,38]. Given that the output of a point PD has a designed Dynamic Range (DR) of A dB, subjecting the point PD signal to FFT processing leads to a final output enhanced camera DR of  $A+10 \times \log(M/2)$  dB. For example, a two million point FFT can produce an additional 60 dB processing gain for the imager, enabling exceptional agile pixel image and spectral map capture.

As described in our prior CAOS related work [20], the speed of operation of a CAOS platform-based imager depends on a number of factors associated with using the CAOS mode. These factors include the frame rate of the DMD1, response time of the point PDs, the number of activated simultaneous agile pixels on the DMD1, the time-frequency modulation code temporal parameters (e.g. code duration and frequency), ADC sampling rate and total sampling duration of an activated agile pixel, the speed of DSP to compute agile pixel irradiance values, number of hyperspectral channels, and speed of operation of the hyperspectral channel selection optical devices. Thus, one must optimize the CAOS camera parameters to meet the application specific imaging requirements. Also note that the spectral image pixel maximum dynamic range obtained via our imager depends not only on the mentioned optical control and electronic processing parameters, but inherently depends on the sampled scene spectral content and its spatial irradiance map. Hence the dynamic range and speed of the imaging operation should be optimized using initial scans by the proposed dual-band CAOS imager working in unison with image spatial and spectral intelligence gathered via prior-art spectral sensor systems and other CAOS camera hardware-based computational imaging methods.

### **9.3 VISIBLE-NIR SIMULTANEOUS DUAL OPTICAL BAND CAOS CAMERA EXPERIMENT**

The proposed CAOS camera design for simultaneous dual-band imaging is implemented in the laboratory for the visible and NIR bands. The camera optical assembly uses a low cost DLP3000 TI DMD chip having a micromirror pitch of  $7.637 \mu\text{m}$ , a  $608 \times 684$  micromirror array arranged in a diamond configuration and a micromirror tilt angle  $\theta = \pm 12^\circ$  with respect to the DMD normal. This DMD1 with its controls has a frame update rate up to 4000 Hz. Lenses L, L1, L2 have focal lengths of 5 cm, 2.54 cm, and 2.54 cm, respectively. Distances for experiment are: L to DMD1 = 5.3 cm; DMD1 to L1 = 8.4 cm; DMD1 to L2 = 8.4 cm; L1 to PD1 = 3.7 cm; and L2 to PD2 = 3.7 cm. The camera visible band Channel 1 (CH1) uses a PD1 that is a Thorlabs switchable gain silicon detector model PDA36A with an active area of  $3.6 \text{ mm} \times 3.6 \text{ mm}$ . The NIR Channel 2 (CH2) of the camera uses PD2 that is a Thorlabs switchable gain germanium detector model PDA50B with an active area having a 5 mm diameter. Fundamentally, PD1 silicon PD technology covers the spectral range from 350 nm to 1100 nm whereas PD2 based on germanium-based photo-detection covers wavelengths



from 800 nm to 1800 nm. The visible channel in the camera deploys a Thorlabs bandpass color filter F1 model FGS900M having 315 nm to 710 nm transmission wavelength range. The NIR channel in the camera uses a Thorlabs high pass filter F2 model FEL0800 having 800 nm cut-off lower wavelength and a recommended upper wavelength of 2200 nm. To conduct the first basic narrowband imaging tests in the visible band, narrow bandwidth Thorlabs filters representing TF1 are mechanically deployed in the visible channel of the camera. Specifically FB450-40, FB550-40, FB620-10 filters have wavelengths centered at 450 nm, 550 nm, and 620 nm and Full Width Half Maximum (FWHM) bandwidths equal to 40 nm, 40 nm and 10 nm, respectively. The CAOS visible-NIR simultaneous dual optical band imager is first setup using 50  $\Omega$  PD signal terminations, a STMicroelectronics STM32F4 microcontroller board using 12-bit ADCs and a Personal Computer (PC) that implements the FFT DSP. The control and synchronization of these components along with the DMD1 is done through the developed in-house Graphic User Interface (GUI) software.



Fig. 9.2. Shown is the Visible-NIR bands target scene created using 3 visible LEDs and 1 NIR LED. Photos show LEDs off (left) and LEDs on (right). These photos are taken with a Nikon D3300 DSLR visible camera.

The CAOS visible-NIR simultaneous dual optical band imager is deployed to image the scene shown in Fig. 9.2 made up by four bright LEDs having central wavelengths of 450 nm, 525 nm, 625 nm and 1450 nm with FWHM values of 20 nm, 25 nm, 14 nm, and 105 nm, respectively. These blue, green, red, and NIR LEDs have optical powers of 7 mW, 4 mW, 12 mW, and 5 mW, respectively. Both PD1 and PD2 units have VGAs with variable gain settings from 0 dB to 70 dB. To register the photo-detected signals, these gains are set to 70 dB. To acquire viewed images by the camera for the visible band and NIR band, the camera is programmed in CAOS-mode so that two simultaneously agile pixels on the DMD1 are

used to time-frequency modulate the dual-band optical image irradiance falling in the DMD1 chip. Each agile pixel is square shaped and programmed to have a 152.74  $\mu\text{m}$  (20 micromirrors) agile pixel side. These two simultaneously agile pixels are programmed in the Frequency Division Multiple Access (FDMA) CAOS-mode [19] to oscillate at the RF frequencies of  $f_1 = 133.4$  Hz and  $f_2 = 200.2$  Hz. Both PD1 and PD2 generate these coded RF signals that undergo analog-to-digital conversion using the 12-bit ADCs operating at a sampling rate of 2.4 kilo-samples/second and a total sampling time duration of 6 seconds. Square wave signal frequencies  $f_1$  and  $f_2$  are selected such that their harmonics do not overlap in the frequency space to create inter-pixel crosstalk. The 6 seconds PD sampling time is chosen to produce a sampled signal with a time-bandwidth product that closely matches  $M$ , the number of points in the implemented FFT. With the deployed point PD modules, the generated photodetector photocurrent  $i_{PD}(t)$  is given by:

$$i_{PD}(t) = \sum_{n=1}^N i_n(t), \quad (9.1)$$

where  $i_n(t)$  is the photo-current produced by the CAOS-mode  $n^{\text{th}}$  agile pixel amongst the set of  $N$  agile pixels simultaneously falling on the point PDs.

The photo-current  $i_n(t)$  is given by:

$$i_n(t) = c_n(t) \times I_n(x, y) \times A_n \times R(\lambda) \times D(\lambda), \quad (9.2)$$

where  $I_n(x,y)$  is the spatially averaged irradiance in  $\text{W}/\text{m}^2$  at the  $n^{\text{th}}$  agile pixel location centered at the  $x_n, y_n$  coordinates of the image map incident on the DMD1. Irradiance averaging is done over  $A_n$ , the area of the  $n^{\text{th}}$  agile pixel on the DMD1.  $c_n(t)$  is the time-frequency CAOS code used for the  $n^{\text{th}}$  agile pixel.  $R(\lambda)$  is the point PD responsivity value in units of  $\text{A}/\text{W}$  for a given wavelength  $\lambda$ .  $D(\lambda)$  ranges between 0 and 1 (1 is for 100% micro-mirror reflectivity) and is the optical attenuation factor due to the CAOS-mode DMD1 (or DMDs when TF1/TF2 contains a DMD) for a given wavelength  $\lambda$ . Recall that the DMD has a broadband spectral response from 320 nm to 2500 nm [32]. However the reflectance of the DMD window material is not uniform in this range. In [32] TI demonstrated that for the visible region range of 420 nm to 700 nm, the typical transmittance observed for the deployed DMD is approximately 97% indicating that  $D(\lambda) \sim 1$  for the 3 LED visible colours used in our experiment. Regarding the NIR wavelength region, the transmittance varies according to the specific NIR wavelength. For the test target LED having a 1450 nm wavelength, the

transmittance is approximately 72% giving a  $D(\lambda) \sim 0.72$ . To compute the true DMD1 plane incident spectrally distributed image irradiance,  $D(\lambda)$  is considered in the post-processing for image generation.

The VGA voltage output  $v_n(t)$  at the ADC input due to the  $n^{\text{th}}$  agile pixel current contribution  $i_n(t)$  is given by:

$$v_n(t) = i_n(t) \times G_A, \quad (9.3)$$

where  $G_A$  is the trans-impedance gain of the VGA. Thus  $v_n(t)$  can be computed as:

$$v_n(t) = c_n(t) \times I_n(x, y) \times A_n \times R(\lambda) \times D(\lambda) \times G_A. \quad (9.4)$$

The FFT DSP is implemented on the  $v_n(t)$  signal which is a scaled version of the agile pixel optical irradiance as one can write  $v_n(t)$  as:

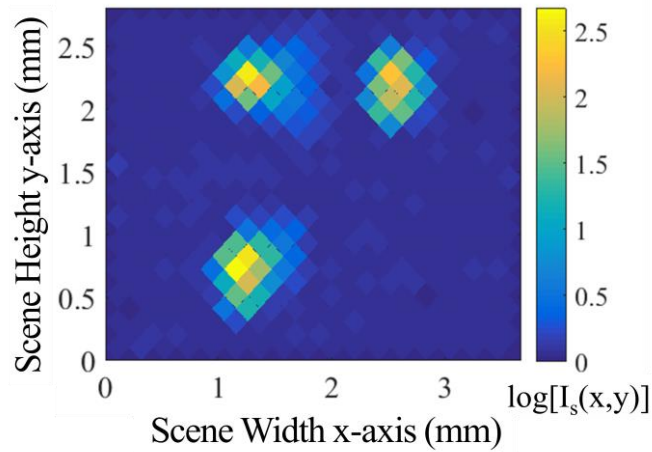
$$v_n(t) = K \times I_n(x, y), \quad (9.5)$$

where the scaling factor  $K$  is:

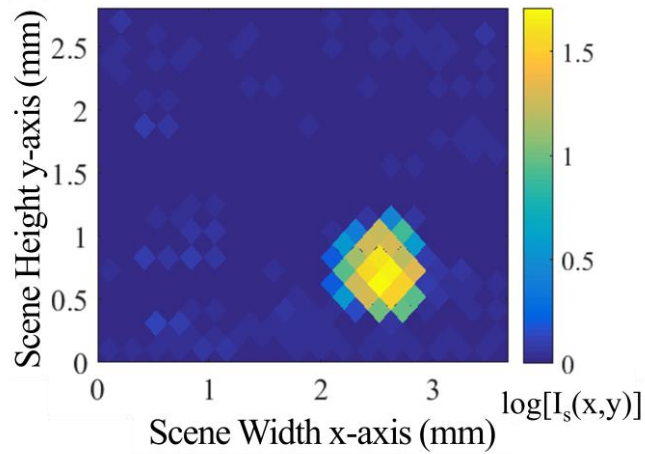
$$K = c_n(t) \times A_n \times R(\lambda) \times D(\lambda) \times G_A. \quad (9.6)$$

The FFT DSP value for the  $n^{\text{th}}$  agile pixel is given as  $|S_n(f)| = \text{FFT}[v_n(t)]$  with frequency  $f$  in Hz. The digital data from the ADC representing  $v_n(t)$  is fed to the PC that implements 16384 point FFT-based agile pixel decoding to recover the visible band and NIR band irradiance values at the selected agile pixels.

To cover the entire scene being projected on the DMD1 chip plane, a total of 442 individual agile pixels are programmed and scanned in time sequence with  $N = 2$  agile pixels per PD1/PD2 detection time slot. For the CAOS-mode FDMA codes,  $c_1(t)$  and  $c_2(t)$  are unity amplitude square wave signals with time periods of  $1/f_1$  and  $1/f_2$ , respectively. Line-by-Line scanning is used giving a total agile pixel line scan length of 442 (number of pixels)  $\times$  216  $\mu\text{m}$  (pixel diagonal) = 95.48 mm. Presented in Fig. 9.3 is the scaled irradiance data acquired via FFT processing as cameras typically provide scaled irradiance images.



(a)



(b)

Fig. 9.3. (a) Visible scaled irradiance map obtained using the CAOS visible-NIR simultaneous dual optical band imager visible channel. (b) NIR scaled irradiance map obtained using the CAOS camera infrared channel.

Figure 9.3(a) shows the visible scaled irradiance map obtained using the CAOS camera visible channel while Fig. 9.3(b) shows the NIR scaled irradiance map obtained using the CAOS camera infrared channel. In both cases shown in Fig. 9.3, the base 10 logarithm of the experimentally obtained scaled irradiance map  $I_s(x,y) = K \times I(x,y)$  is plotted along the scene x-y axes. Figure 9.3 shows that indeed the CAOS dual optical band imager has correctly located the positions of the 3 visible targets and 1 NIR target in the viewed scene.

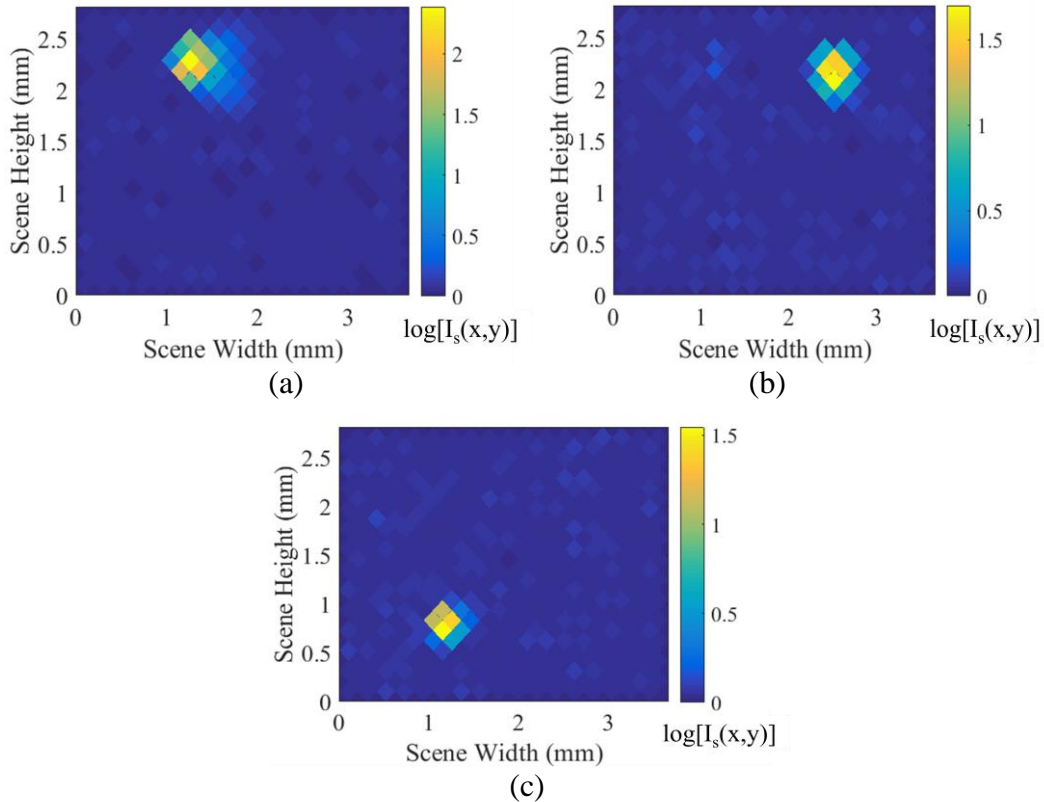


Fig. 9.4. Narrower spectral channel CAOS visible-NIR simultaneous dual optical band imager scaled irradiance maps at (a)  $\lambda = 450$  nm with FWHM of 40 nm, (b)  $\lambda = 550$  nm with FWHM of 40 nm and (c)  $\lambda = 620$  nm with FWHM of 10 nm.

Note that at this stage of camera operations, one has not conducted narrow spectral channel imaging within desired spectral channels for the detected dual-band images. To do so, the camera switches to its narrower band operations spectral camera mode by engaging TF1 and TF2 fine channel wavelength tuning in the two independent broadband channels in the camera. Specifically, since we are using 3 different color visible targets, the visible channel is tested for hyperspectral imaging by mechanically inserting a specific color wavelength filter (specifications of filters defined earlier) within the visible light channel of the camera. Figure 9.4 shows the experimentally obtained CAOS narrow spectral band irradiance maps at (a)  $\lambda = 450$  nm with FWHM of 40 nm, (b)  $\lambda = 550$  nm with FWHM of 40 nm and (c)  $\lambda = 620$  nm with FWHM of 10 nm. The electronic FFT processed signal shown in Fig. 9.5 shows the detected light location (on the agile pixel scan line) and its normalized irradiance. Specifically, Fig. 9.5(a) plot is generated from PD2 while Fig. 9.5(b) plot is generated from PD1. This Fig. 9.5 data shows that the unwanted wavelength band falls in the noise floor of the FFT trace giving a measured inter-spectral band optical isolation of  $10 \log [1/(2.88 \times 10^{-4})] = -35.3$  dB (or an electrical isolation of -70.6 dB) between the visible and

NIR bands for PD1. Regarding the measured inter-spectral band optical isolation for CH2, its value is computed as  $10 \log [1/(9.97 \times 10^{-4})] = -30 \text{ dB}$  (or an electrical isolation of  $-60 \text{ dB}$ ). Note that the inter-spectral band camera isolation can be further improved if cascading of multiple F1 and F2 filters is used in the CH1 and CH2 paths, respectively.

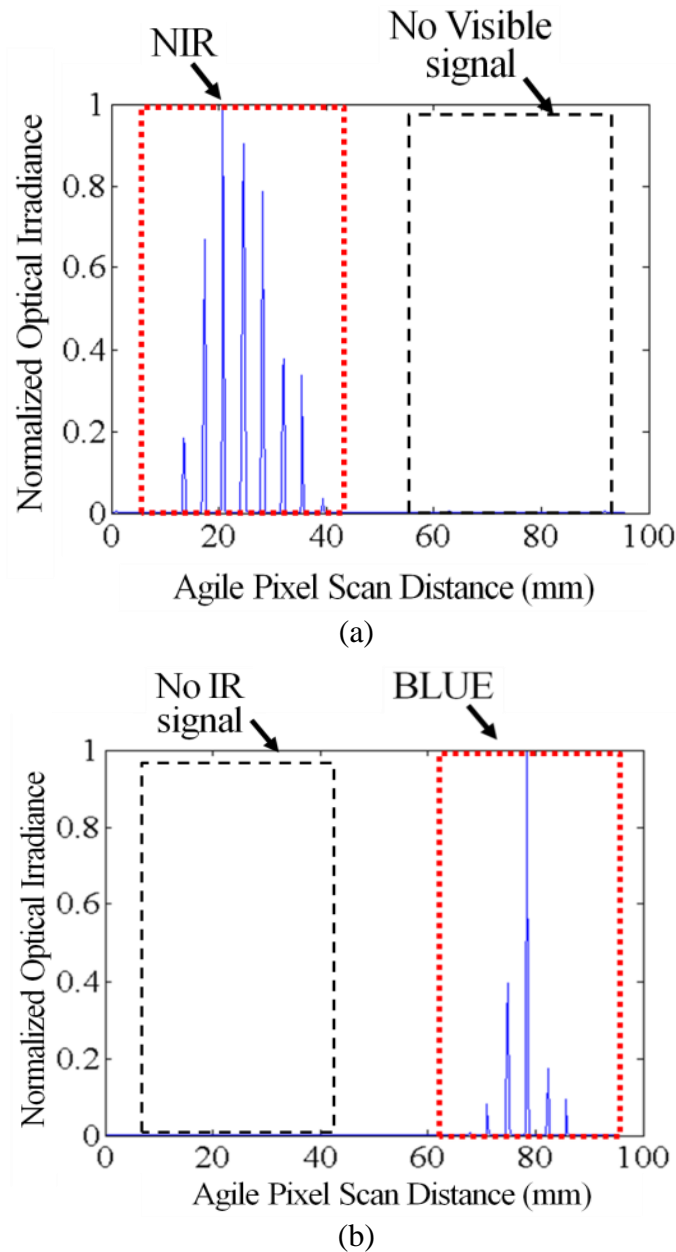


Fig. 9.5. Shown is the normalized optical irradiance plotted versus agile pixel scan distance as the agile pixel conducts a line-by-line scan over the DMD1 plane making 442 agile pixels. Plot in (a) is generated from PD2 (NIR channel) while plot in (b) is generated from PD1 (Visible channel). Note that (b) is obtained by unrolling into a 1-D array, the 2-D array data shown in Fig. 9.4(b).

Note that one can compute the optical (and electronic) contrast of the detected narrow spectral channel images by using the experimentally measured agile pixel irradiance values via the FFT spectral trace  $|S(f)|$  data. One can compute the image electrical contrast  $DR_{im}$  in dB as:

$$DR_{im} = 20 \times \log \left( \frac{|S(f)_{max}|}{|S(f)_{min}|} \right). \quad (9.7)$$

Here  $|S(f)|_{max}$  and  $|S(f)|_{min}$  are the maximum and minimum values of the electronically processed FFT signal for a given narrow spectral band image map. For the experimental narrow spectral band images at 450 nm, 550 nm, 625 nm, and 1450 nm,  $|S(f)|_{max}$  values are 510.5, 110.4, 788.9, and 58.15, respectively. At 450 nm, 550 nm, 625 nm, and 1450 nm, the  $|S(f)|_{min}$  values are 0.1473, 0.1587, 0.1315, and 0.1578, respectively. Given these values, the narrow spectral band images at 450 nm, 550 nm, 625 nm, and 1450 nm have measured electrical contrast ratios of 70.78 dB, 57.125 dB, 75.56 dB, and 51.32 dB, respectively. Note that the measured narrow spectral band image contrast value is strongly dependent on the various camera parameters such as optical filter and PD spectral responses.

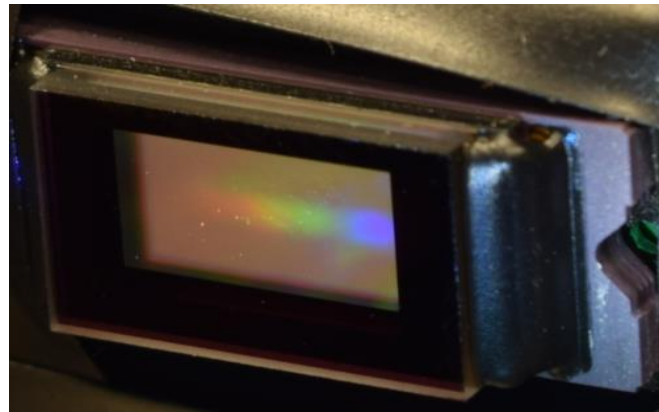
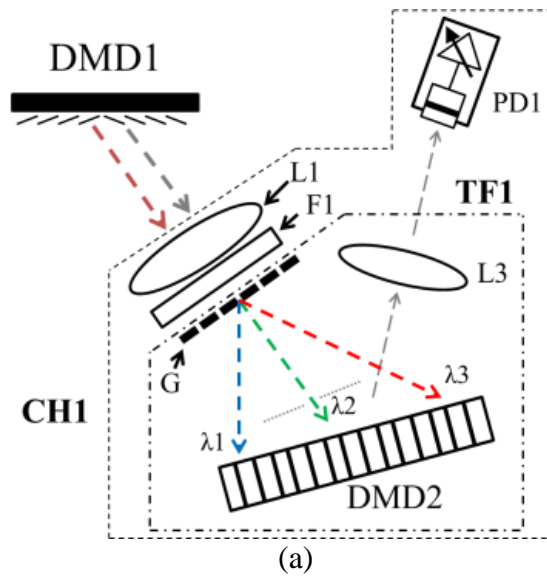


Fig. 9.6. (a) Shown is the design of the DMD2-based TF1 module used in Channel 1 of the CAOS camera that implements CAOS-mode narrower wavelength optical spectral detection. (b) Photograph of the DMD2 plane spatially distributed visible spectrum produced by light coming from the DMD1 programmed CAOS-mode white light agile pixel.

As described in the design section, the proposed dual band CAOS imager can also engage the CAOS-mode in a suitable TF1/TF2 module to bring the power of RF domain signal processing and filtering into effect for in-band wavelength analysis for the selected agile pixels in the imaged scene. To demonstrate this imager feature, a TF1 filter based on the DMD spectral filter design, described in [33], is placed within the CAOS imager implemented in the laboratory. This TF1 design is shown in Fig. 9.6(a) and uses a 500 lines/mm visible band transmission amplitude grating G with another DMD called DMD2 (same technical specifications as DMD1) and an lens L3 of focal length of 3 cm that images the DMD2 plane onto the PD1 plane. The distance between L3 and PD1 is 4 cm. G is placed



just after the lens L1 in the Channel 1 assembly to produce a spatially distributed white light spectrum (showing the main red, green, blue wavelength bands across ~400-700 nm) along the DMD2 horizontal axis (see Fig. 9.6(b)) covering a length of ~4.5 mm (the chip length is 6.57 mm). To create a suitable white light agile pixel on the imager DMD1 plane, a 5 W LED white light torch having a luminosity of 180 lumens [37] placed 60 cm from L with a focal length of 7.5 cm is imaged on to the imager DMD1 plane where a 1.527 mm×1.527 mm CAOS mode agile pixel is formed at a  $f_0 = 400$  Hz test code frequency. This pixel's entire white light irradiance shows up as spatially separated wavelength channels on DMD2 plane, all carrying a carrier code of 400 Hz that are summed up at PD1. The white light pixel generated current undergoes 2,097,152 points FFT signal processing to produce a white light agile pixel scaled irradiance data signal shown in Fig. 9.7(a). The data acquisition parameters using a higher performance ADC are: 16 bit resolution ADC, sampling rate of 20 kilo-samples/sec and sampling duration of 60 seconds.

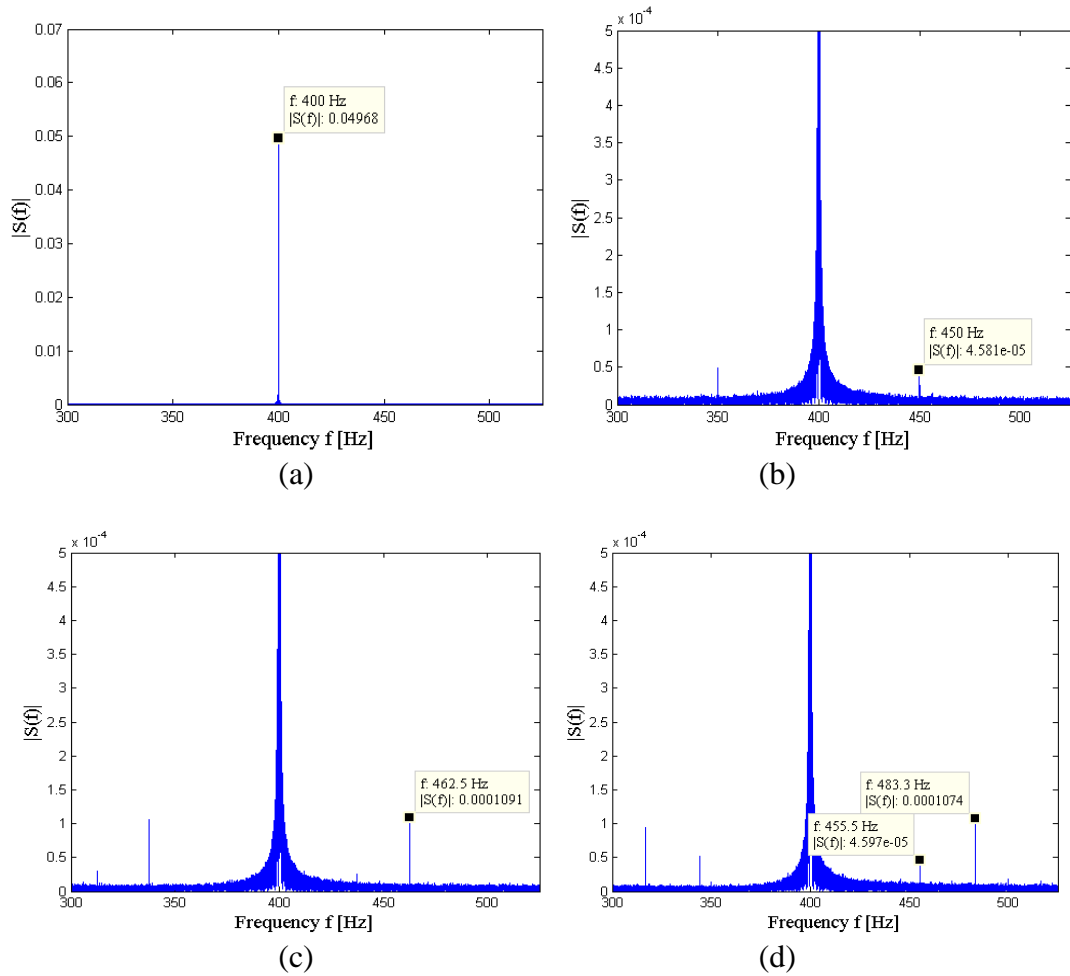


Fig. 9.7. Shown are the detected RF spectrum peaks  $|S(f)|$  for different visible band spectral selections programmed by the CAOS-mode of DMD2 in TF1. (a)  $|S(f = f_0)| = 49.68 \times 10^{-4}$  obtained when the entire DMD2 is programmed to direct all spectral components of the white light agile pixel at  $f = f_0 = 400$  Hz CAOS-mode to PD1. (b)  $|S(f_0 + f_3)| = 0.4581 \times 10^{-4}$  obtained when DMD2 is programmed to direct only the red color spectral band light to PD1 using a  $f_3 = 50$  Hz CAOS-mode. (c)  $|S(f_0 + f_2)| = 1.091 \times 10^{-4}$  obtained when DMD2 is programmed to direct only the green color spectral band light to PD1 using a  $f_2 = 62.5$  Hz CAOS-mode. (d)  $|S(f_0 + f_3)| = 0.4597 \times 10^{-4}$  and  $|S(f_0 + f_1)| = 1.074 \times 10^{-4}$  obtained when DMD2 is programmed to simultaneously direct the red and blue color spectral band light components to PD1 using  $f_3 = 55.5$  Hz (red) and  $f_1 = 83.3$  Hz (blue) CAOS-mode.

To independently monitor the color content of this white light agile pixel, different CAOS codes are assigned to the different color/spatial zones defined as a second set of time-frequency CAOS mode agile pixels with frequencies  $f_1$ ,  $f_2$ ,  $f_3$  for blue ( $\lambda_1$ ), green ( $\lambda_2$ ), and red ( $\lambda_3$ ) spectral bands, respectively. The spatial size of the agile pixel on DMD2 determines the spectral bandwidth of the spectral selection. DMD2 is programmed with a square agile pixel with a side length of 382  $\mu\text{m}$  and a diagonal length (along the wavelength spread axis) of 540  $\mu\text{m}$ . Given the 500 lines/mm grating period and a distance of 4.8 cm between G and DMD2, each agile pixel of a 540  $\mu\text{m}$  width on DMD2 makes a spectral filter bandpass of  $(0.54 \text{ mm}/4.5 \text{ mm}) \times 300 \text{ nm} = 36 \text{ nm}$ . In contrast to the CAOS coding of the agile pixels in the image space on DMD1, the DMD2 agile pixels simultaneously implement wavelength coding for the multi-color light for all agile pixels on DMD1. Figure 9.7 highlights the detected peaks  $|S(f)|$  for different visible band spectral selections programmed by the CAOS-mode of DMD2 in TF1. Figure 9.7(a) gives  $|S(f = f_0)| = 49.68 \times 10^{-4}$  obtained when the entire DMD2 is programmed to direct all spectral components of the white light agile pixel at  $f = f_0 = 400 \text{ Hz}$  CAOS-mode to PD1. In this case, DMD2 does not time-frequency modulate the incident light, creating a strong carrier signal at 400 Hz observed in the FFT spectrum. Figure 9.7(b) gives  $|S(f_0 + f_3)| = 0.4581 \times 10^{-4}$  obtained when DMD2 is programmed to direct only the red color spectral band light to PD1 using a  $f_3 = 50 \text{ Hz}$  CAOS-mode. In this case, the double CAOS-mode implementation using DMD1 and DMD2 produces double sideband time-frequency optical modulation, creating at  $f_0 + f_3$  and  $f_0 - f_3$  the FFT spectrum sidebands around the carrier  $f_0$ . It is adequate to use either sideband spectral strength to determine the relative spectral strength of the incident multispectral light. Similarly, Fig. 9.7(c) gives  $|S(f_0 + f_2)| = 1.091 \times 10^{-4}$  obtained when DMD2 is programmed to direct only the green color spectral band light to PD1 using a  $f_2 = 62.5 \text{ Hz}$  CAOS-mode and Fig. 9.7(d) gives  $|S(f_0 + f_1)| = 1.074 \times 10^{-4}$  and  $|S(f_0 + f_3)| = 0.4581 \times 10^{-4}$  obtained when DMD2 is programmed to simultaneously direct only the blue and red color spectral band light components to PD1 using  $f_1 = 83.3 \text{ Hz}$  (blue) and  $f_3 = 55.5 \text{ Hz}$  (red) CAOS-mode. This white light agile pixel blue ( $\lambda_1, f_1$ ), green ( $\lambda_2, f_2$ ), red ( $\lambda_3, f_3$ ) color data indicates that compared to the red light content, blue and green light spectral contents are a factor of  $\sim 2.3$  larger, a result also confirmed using optical power and filter-based direct spectral measurements of the light exiting the white light LED. Thus the deployment of a programmable CAOS-mode TF1 and TF2 modules within the proposed dual band CAOS imager empowers spectral imaging, allowing the user to sift out desired simultaneous spectral features via electronic domain signal processing for high dynamic range spectral monitoring.

## 9.4 CAOS CAMERA EXTREME DYNAMIC RANGE ANALYSIS AND EXPERIMENT

The camera dynamic range DR in dB is defined as:

$$DR(dB) = 20 \log \times \left[ \frac{P_{\max}}{P_{\min}} \right], \quad (9.8)$$

DR (dB) = 20×log(P<sub>max</sub>/P<sub>min</sub>) where P<sub>min</sub> is the minimum detectable optical power by the PD and P<sub>max</sub> is the maximum detectable optical power by the PD. To determinate the DR of both PD1 and PD2 modules in the optical design shown in Fig. 9.1, one must note that each point PD-VGA module has its own electrical characteristics such as the PD G<sub>A</sub>, PD bandwidth (BW), and PD Noise Equivalent Power (NEP). These PD module parameters are dependent on the VGA switchable gain setting used during the optical image acquisition operation via the CAOS-mode agile pixels sampling. Considering an ADC having a maximum input voltage limit V<sub>max</sub>, the PD's maximum current output i<sub>max</sub> can be found as i<sub>max</sub> = V<sub>max</sub>/G<sub>A</sub>. G<sub>A</sub> varies according to the impedance termination used which can be either a high impedance (Hi-Z) such as used in the CAOS camera extreme dynamic range test to be described next or the 50 Ω impedance termination such as used previously in the microcontroller-based imaging system test setup in the dual band imager experiment. The maximum detectable optical power P<sub>max</sub> at a point PD can be found as P<sub>max</sub> = i<sub>max</sub>/R(λ). To compute the DR for the point PD, it is necessary to first compute the minimum detectable optical power P<sub>min</sub> at the point PD. In order to do so, the NEP value of the PD needs to be considered. The NEP, which is the sensitivity of the PD device, represents the minimum optical signal that can be optically detected per square root bandwidth with units of W/√Hz. The NEP value is wavelength dependent and to compute its value the following generalized formula is used:

$$NEP(\lambda) = NEP_{\min} \times \left[ \frac{R_{\max}}{R(\lambda)} \right], \quad (9.9)$$

where NEP<sub>min</sub> corresponds to the NEP value at the PD's peak wavelength λ<sub>p</sub> and R<sub>max</sub> is the responsivity value at the peak wavelength. By knowing the NEP value at the detected wavelength it is possible to compute the minimum detectable optical power P<sub>min</sub> as:

$$P_{\min} = NEP(\lambda) \times \sqrt{BW}, \quad (9.10)$$

where BW is the measurement electrical bandwidth of the PD unit. With both  $P_{\max}$  and  $P_{\min}$  values determined, the point PD DR and hence the *raw* camera DR is computed.

To obtain the designed DR values for the wavelengths used in the dual band CAOS imager experiment, the following considerations are taken into account. The maximum voltage value  $V_{\max}$  that the 12-bit ADC is able to sense is equal to 3 V. This 3 V value represents the PD1/PD2 optical saturation limitation for the dual band CAOS imager. The demonstrated imager PD1/PD2 units have VGA gains set to 70 dB with PD1 data sheet specified bandwidth  $BW_1 = 5 \times 10^3$  Hz and PD2 bandwidth  $BW_2 = 210$  Hz. Both PDs are designed to have  $50 \Omega$  termination impedances giving data sheet specified gains  $G_{A1} = G_{A2} = 2.38 \times 10^6$  V/A. Via datasheets,  $\lambda_p = 970$  nm and  $R_{\max} = 0.65$  A/W for PD1 and  $\lambda_p = 1550$  nm and  $R_{\max} = 0.85$  A/W is for PD2.  $NEP_{\min}$  corresponds to the NEP value at the PD's peak wavelength  $\lambda_p$ . For PD1,  $NEP_{\min}$  is equal to  $2.10 \times 10^{-12}$  [W/ $\sqrt{\text{Hz}}$ ] whereas for PD2,  $NEP_{\min}$  is equal to  $4.63 \times 10^{-12}$  [W/ $\sqrt{\text{Hz}}$ ]. The hyperspectral imager experimental test wavelengths  $\lambda_1 = 450$  nm,  $\lambda_2 = 550$  nm,  $\lambda_3 = 625$  nm, and  $\lambda_4 = 1450$  nm have computed responsivity values  $R(\lambda_1) = 0.114$  A/W,  $R(\lambda_2) = 0.22$  A/W,  $R(\lambda_3) = 0.299$  A/W, and  $R(\lambda_4) = 0.8175$  A/W, respectively. The computed maximum detectable optical power at the specific wavelengths is  $P_{\max1} = 1.10 \times 10^{-5}$  W,  $P_{\max2} = 5.73 \times 10^{-6}$  W,  $P_{\max3} = 4.21 \times 10^{-6}$  W and  $P_{\max4} = 1.54 \times 10^{-6}$  W. Using the computed  $NEP(\lambda)$  values for the 4 wavelengths, the computed minimum detectable optical power by PD1 at the specific wavelengths is  $P_{\min}(\lambda_1) = 8.46 \times 10^{-10}$  W,  $P_{\min}(\lambda_2) = 4.39 \times 10^{-10}$  W,  $P_{\min}(\lambda_3) = 3.23 \times 10^{-10}$  W, and  $P_{\min}(\lambda_4) = 6.97 \times 10^{-11}$  W. Using the calculated  $P_{\max}$  and  $P_{\min}$  values, the designed PD DR values in dB for the test wavelengths gives  $DR(\lambda_1) = DR(\lambda_2) = DR(\lambda_3) = 82.3$  dB and  $DR(\lambda_4) = 86.88$  dB. Indeed, these designed DR values are more than adequate to capture the deployed hyperspectral image targets that register at best an experimentally measured electrical contrast of 75.56 dB for the red LED target.

In order to test the extreme DR range (and image contrast) performance of the presented CAOS camera, a super bright target in the form of a 15 mW 633 nm Melles Griot He-Ne laser is deployed as a target in the viewed scene. In this experimental setup, Thorlabs Neutral Density (ND) filter-based variable optical attenuators are deployed to attenuate the laser light to simulate a high contrast target that reaches an extreme optical contrast ratio of  $10^7:1$  (or an equivalent camera electrical DR of 140 dB). By deploying x-y slit scanning on the DMD1 plane, the spatial location of the deployed CAOS agile pixel is positioned to sample the high brightness laser target so that PD1 generates the maximum signal. A CAOS-mode modulation frequency of  $f = f_1 = 400$  Hz is used in the experiment with  $N = 1$  as there

is one agile pixel. Given the red wavelength, only the PD1 channel of the camera is engaged. Specifically, the PD1 output is connected to a high termination impedance Data Acquisition (DAQ) card model 6211 from National Instrument that has programmable high speed 16-bit ADCs [38]. PD1 can handle extreme optical power levels to produce maximum 10 V output signals and the DAQ card has a specified  $V_{\max} = 10$  V. Given the presence of a strong bright source (a laser beacon) in the target scene, the PD1 VGA gain is set to 0 dB which in-turn as per datasheet sets the PD1 unit BW = 10 MHz and PD gain to  $G_A = 1.51 \times 10^3$  V/A for the high termination impedance setting. The computed  $R(\lambda = 633\text{nm}) = 0.312$  A/W and the computed maximum detectable optical power using  $V_{\max} = 10$  V is  $P_{\max} = 21 \times 10^{-3}$  W. At 0 dB setting,  $NEP_{\min} = 2.91 \times 10^{-11}$  [W/ $\sqrt{\text{Hz}}$ ] and  $NEP(\lambda = 633\text{nm}) = 6.06 \times 10^{-11}$  [W/ $\sqrt{\text{Hz}}$ ] giving a computed minimum detectable optical power is  $P_{\min} = 1.92 \times 10^{-7}$  W. Using PD1, the designed *raw* DR capability of the CAOS camera when using the maximum acceptable DAQ voltage range of 10 V is computed to be 100.88 dB. However, using the deployed laser with the agile pixel size matched to the multispectral imaging experiments agile pixel size of  $20 \times 20$  micromirrors, ( $152.74 \mu\text{m} \times 152.74 \mu\text{m}$ ), an approximately 2 V signal is produced from PD1, i.e., a factor of 5 below the PD1 total light detection capacity. In effect, the designed PD1 DR for the CAOS camera extreme DR test is 86.9 dB. It is well known that the Signal-to-Noise Ratio (SNR) in dB for a P-bit ADC is given by  $SNR(\text{dB}) = 6.02 \times P + 1.76$  [39]. With  $P = 16$  bits, the deployed DAC has an SNR of 98.08 dB that is adequate for capturing the direct output of PD1 with a designed DR of 86.9 dB. Another point to note is that about 1/5 of the full well capacity of PD1 is used in our experiment implying that one could simultaneously detect 5 such extremely bright agile pixels in the scene by using up the full 10 V range of the PD1 output. Of course, one can decrease the agile pixel sampling area, thus reducing the total optical power collected by PD1 which leads to simultaneously registering a larger number of agile pixels in the image space. It is important to point out that the CAOS camera inherently makes the best and most efficient use of the relatively large full quantum well capacity of the point detectors PD1 and PD2. Such is not the case in prior-art PDA-based cameras where an incident bright extreme contrast image causes the many high spatial resolution smaller capacity quantum wells to be partially filled while many other quantum wells in the PDA are over filled and create spill over to nearby wells, thus causing pixel saturation and inter-pixel crosstalk noise. In short, CAOS is also quantum well capacity efficient.

The 16-bit DAC uses a sampling rate  $f_s$  of 20 kilo-samples/second with a DAQ card sampling duration time  $t_s$  set to 5 seconds. The voltage range of the DAQ is programmable and set to the -10 to +10 V range. The output of the 16-bit DAC undergoes RF spectrum analysis via DSP DFT operation computed by the FFT algorithm implemented in the PC. As mentioned earlier, the DFT produces processing gain resulting in noise suppression and the CAOS camera employs this special DFT capability to pull out the desired agile pixel data signal from the noise background created under extreme image contrast conditions. Specifically, FFT-based processing gain in dB is equal to  $10 \times \log(M/2)$  where  $M$  is the number of points in the FFT [39, 40].  $M$  is first calculated as  $M = f_s \times t_s$  and subsequently increased to a power of 2 number for computational efficiency purposes so that the algorithm complexity decreases from  $O(n^2)$  to  $O(n \log n)$  where “O” stands for *order of* [41]. For the first stage of the high dynamic range experiment,  $f_s \times t_s = 100,000$ . With  $M = 2^{17} = 131,072$  satisfying the algorithm efficiency condition for the FFT implemented in MATLAB gives a designed processing gain  $G_{\text{FFT}} = 10 \log (M/2) = 48.16$  dB. Given that the output of PD1 has a designed DR of 86.9 dB, subjecting the PD1 signal to FFT processing leads to a final output designed camera DR of  $86.9 + 48.16 = 135.06$  dB.

To initiate the extreme dynamic range test to reach this 135.06 dB camera DR, optical attenuation of the laser beam is gradually increased using the optical ND filters starting with Optical Density (OD) values of 1, 3, 4, 5, 5.3 and 5.5 giving photo-detected output electrical signal attenuations of 20 dB, 60 dB, 80 dB, 100 dB, 106 dB and 110 dB, respectively. Here electrical attenuation in dB is equal to  $20 \times \log(10^{\text{OD}})$ . The signal FFT spectral traces for laser light optical attenuations of 0 dB, 50 dB, and 55 dB are shown in Figs. 9.8(a), 9.8(b), and 9.8(c), respectively. Note that when optical attenuation reaches 55 dB, the fundamental RF  $f = f_1 = 400$  Hz FFT spectral peak due to the photo-detected square wave signal disappears into the spectrum trace noise floor. At this stage, the CAOS camera has demonstrated a camera dynamic range near 100 dB ( $50 \text{ dB} \times 2$ ) where camera DR is  $20 \times \log(|S(f_1)|_{\text{max}}/|S(f_1)|_{\text{min}})$  with  $|S(f_1)|_{\text{max}}$  determined at the zero optical attenuation setting and  $|S(f_1)|_{\text{min}}$  determined when the RF spectral peak almost disappears in the spectral trace noise floor. Specifically, the Fig. 9.8(b) data gives an experimental DR = 98.6 dB, nearly matching the expected DR of 100 dB using the 50 dB optical attenuator. At the 55 dB optical attenuation of the target light, the camera produces the Fig. 9.8(c) FFT spectral signal where no clear  $f_1$  peak is seen. In this instance, the DAQ is switched to its -200 mV to +200 mV super-resolution 50X DAC range compression mode. Doing so produces the Fig. 9.8(d) FFT spectral trace result where the

peak is again clearly visible indicating a recovered camera DR of 110 dB. This recovery is possible because the DAC signal sampling resolution is improved by a factor of 50, changing from 30 mV to 6  $\mu$ V allowing finer signal quantization, thus improving the digitization quality of the very weak RF signal produced by PD1.

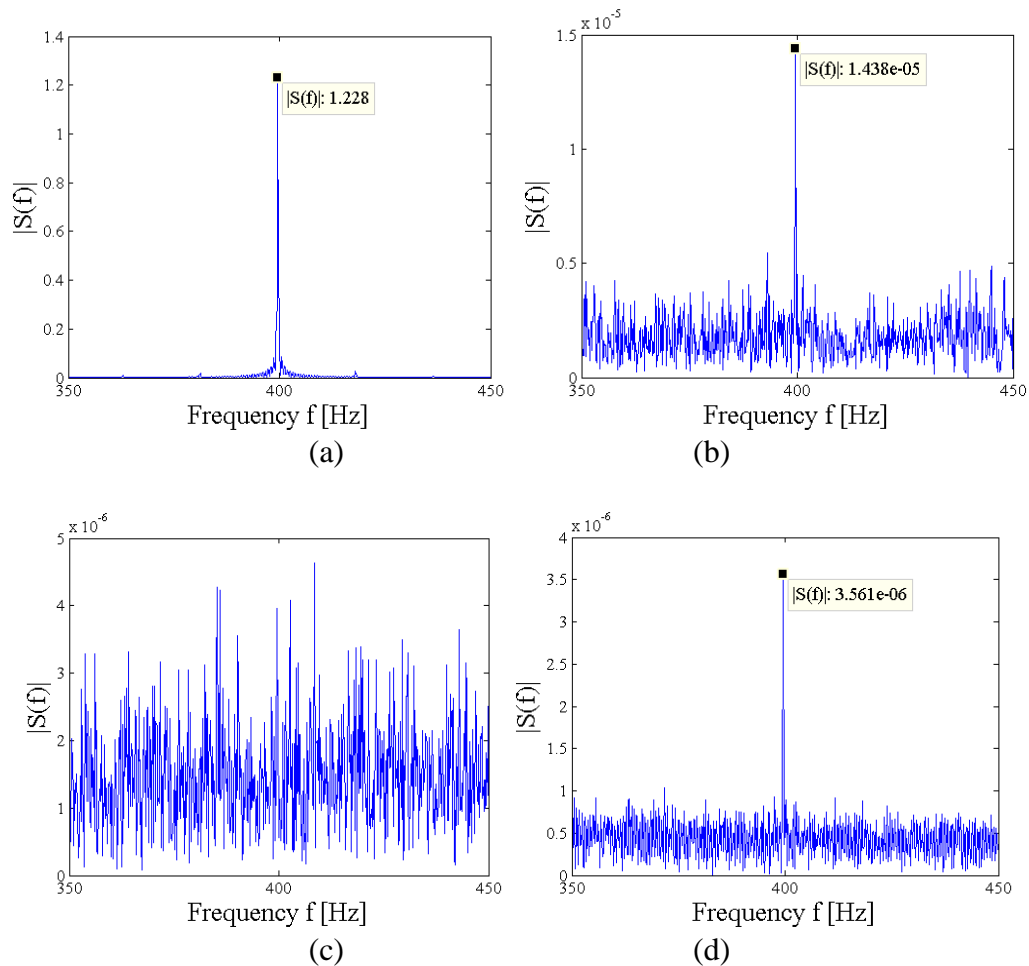


Fig. 9.8. Highlighted are the detected peak  $|S(f_1)|$  for different optical attenuation, DAQ voltage range configuration, and sampling duration time. (a)  $|S(f_1)| = 1.228$  obtained for a 10 V DAQ range setting when no optical attenuation is used and  $t_s = 5$  s. (b)  $|S(f_1)| = 1.43 \times 10^{-5}$  obtained for a 10 V DAQ range setting when ND filter is equal to OD = 5 and  $t_s = 5$  s. (c) Peak at  $f_1$  buried in system noise floor for a 10 V DAQ range setting when ND filter is equal to OD = 5.5 and  $t_s = 5$  s. (d)  $|S(f_1)| = 3.56 \times 10^{-6}$  obtained for a 200 mV DAQ range setting when ND filter is equal to OD = 5.5 and  $t_s = 5$  s.



The Fig. 9.9(a) FFT trace giving a measured DR of 116.2 dB is obtained when a PD signal electrical attenuation of 120 dB is implemented using a ND filter with an OD of 6. An increase of the target light attenuation using a ND filter with a 6.3 OD (which is equal to 126 dB electrical attenuation) results in the FFT trace shown in Fig. 9.9(b) where once more the FFT spectral peak carrying the irradiance information of the CAOS-mode agile pixel signal is buried in the spectrum noise. In order to extract the CAOS pixel irradiance information from the FFT spectral peak, the sampling duration acquisition time parameter of the DAC is increased by a factor of 12, i.e., from 5 seconds to 60 seconds. For the MATLAB FFT, this increase in integration time increases the M value to  $2^{21} = 2,097,152$  giving a FFT processing gain of  $G_{\text{FFT}} = 60.2$  dB. As it is shown in Fig. 9.9(c), using this increased processing gain recovers the FFT peak which is well visible with respect to the noise floor giving an experimental CAOS camera DR of 125.7 dB. With the increased  $G_{\text{FFT}}$ , the designed camera  $\text{DR} = 86.9 + 60.2 = 147.1$  dB. Next the attenuation is further increased to a value of 6.6 OD which corresponds to a PD signal electrical attenuation of 132 dB. For this attenuation, Fig. 9.9(d) gives an experimental CAOS camera DR value of 130.5 dB. As shown in Fig. 9.9(e), by further increasing the applied optical attenuation to a value of 6.9 OD which is equivalent to 138 dB PD signal attenuation, one can no longer recover the super weak CAOS pixel irradiance signal since it is hidden in the FFT spectrum noise floor. From Fig. 9.9(e) a  $|S(f_1)|_{\text{min}} = 2 \times 10^{-7}$  just above the noise floor gives an experimental CAOS camera DR of 136 dB. This extreme DR number of 136 dB showcases the power of the proposed wavelength sensitive CAOS camera technology.

Do note that the approximately 11 dB difference in experimental versus designed camera DR is due to several factors that includes error tolerances of optical and electronic components specifications from the datasheets, measurement errors due to deployed test instruments, and drift from the perfect linearity assumed for the point PD responses as well as their built-in trans-impedance amplifiers. Specifically, the deployed point PDs are designed for an ideal linear response in regions sufficiently far from the PD saturation point and the PD noise floor [42]. In an optimized CAOS camera design for application-specific field deployment, the experimental camera can be appropriately calibrated to produce true image irradiance data.

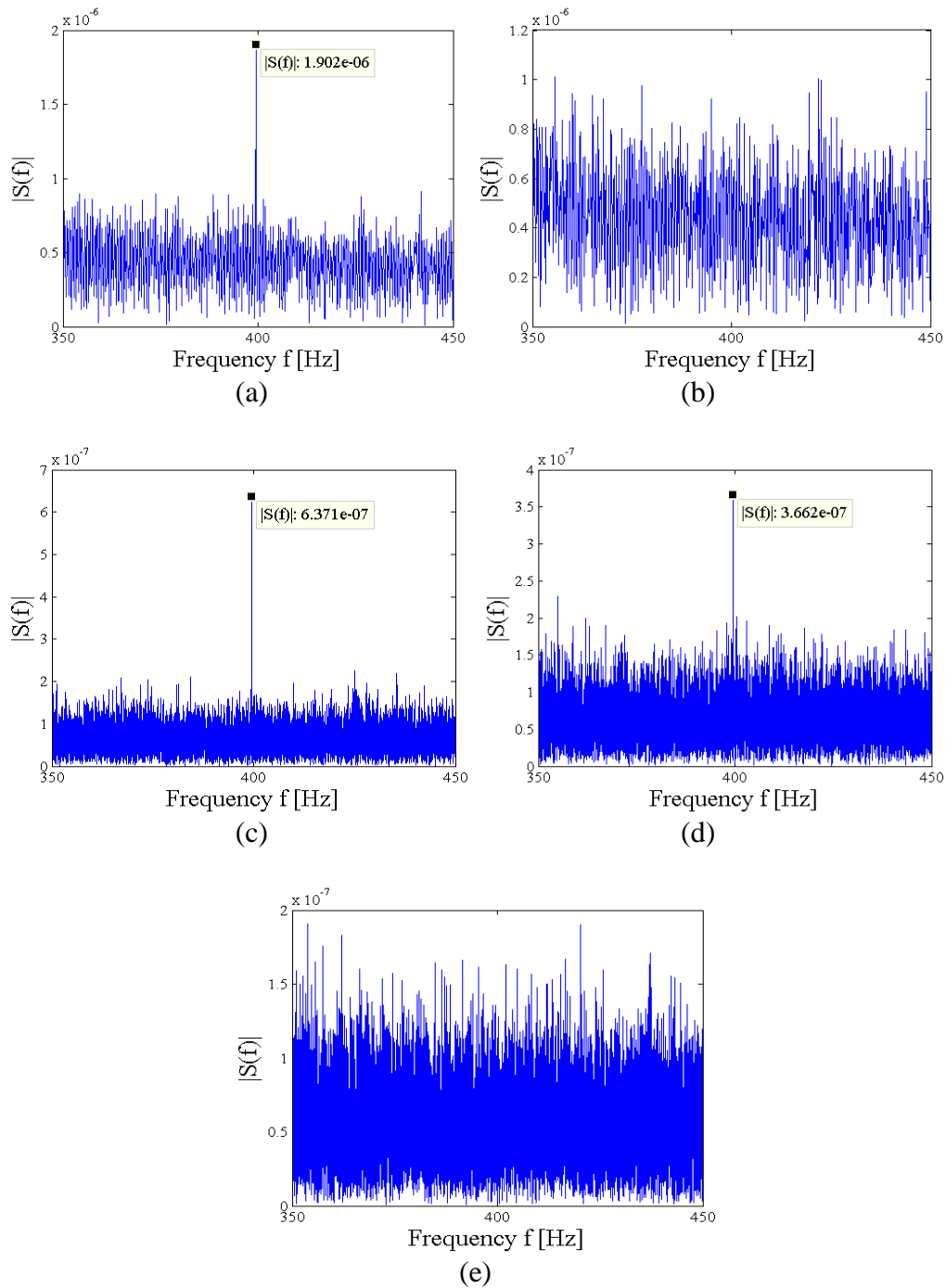


Fig. 9.9. (a)  $|S(f_1)| = 1.902 \times 10^{-6}$  obtained for a 200 mV DAQ range setting when ND filter is equal to OD = 6 and  $t_s = 5$  s. (b) Peak at  $f_1$  buried in system noise floor for a 200mV volts DAQ range setting when ND filter is equal to OD = 6.3 and  $t_s = 5$  s. (c)  $|S(f_1)| = 6.371 \times 10^{-7}$  obtained for a 200 mV DAQ range setting when ND filter is equal to OD = 6.3 and  $t_s = 60$  s. (d)  $|S(f_1)| = 3.662 \times 10^{-7}$  obtained for a 200 mV DAQ range setting when ND filter is equal to OD = 6.6 and  $t_s = 60$  s. (e) Peak at  $f_1$  buried in system noise floor for a 200mV volts DAQ range setting when ND filter is equal to OD = 6.9 and  $t_s = 60$  s.

## 9.5 CONCLUSION

For the first time, proposed and demonstrated is a novel spectral CAOS camera design that has the inherent capability to provide very high dynamic range with simultaneous dual-band spectral imaging. The imager features low inter-pixel and spectral channel crosstalk via application dependent agile-pixels CAOS-mode programmability that allows electronic signal processing-based optical irradiance monitoring and filtering both in the image spatial domain as well as the optical spectral domain. When used with classic multispectral and hyperspectral imagers, this camera can extract useful spectrum specific irradiance image pixel data required by the end user. In effect, the proposed spectral CAOS camera can be programmed as a precision spatial and spectral irradiance sifter that pulls out otherwise unseen image data. Because the CAOS camera hardware allows the placement of programmable spatial masks on the DMDs, for certain sparse data set scenarios, the compressive sensing algorithm implementation is possible by first using the proposed camera's non-CAOS staring mode [15] to record the point PD voltage value for each spatial mask in a sequence of  $P$  masks and then combining this point PD data set with the spatial mask data set via numerical optimization based post-processing to produce an estimate of the imaged scene. Thus after iterative computation using higher  $P$  values and modified optimization criteria, one gets an improved estimated sparse image data set of a limited dynamic range that can also be used to assist the camera CAOS-mode extreme dynamic range region of interest imaging operations. In such a hybrid design case, the agile pixel can be thought of as a space-time-frequency representation that combines time-frequency encoding/decoding of CAOS with spatial-coding of classic transform and compressive sensing as well as ghost imaging [43]. Speed of CAOS camera sifting operations depends on various factors including agile pixel size, pixel count, detector integration time, DSP algorithm and PC speed, as well as application dependent conditions and the parameters of the imager. Experiments for the first time using the proposed spectral imager have been successfully conducted with a 4 LED spatially distributed multi-colour (3 visible LEDs and 1 IR LED) test target observed using the CAOS-mode to spatially sample the image space and mechanically placed narrowband spectral filters to determine the specific target spectral bands. Images of the targets for the visible and NIR bands show a better than -60 dB inter-band measured electrical isolations. Fully programmable CAOS-mode spectral filtering implemented with a DMD-based narrowband filter placed within the CAOS imager demonstrates simultaneous wavelength filtering and monitoring of red, green, and blue bands

of a white light LED target. Therefore, the power of dual CAOS-mode operations is demonstrated here, one CAOS-mode for the image space and one CAOS-mode for the optical spectral space. To increase camera dynamic range, proposed is the use of a higher resolution ADC with both range and sampling duration parameter control along with a larger data set electronic DSP to extract higher DSP gain and realize additional noise suppression. Specifically, by experimentally engaging programmable 16-bit ADC control and the 60 dB DSP gain of a near 2 million point FFT applied to the point PD signal, an extreme dynamic range of 136 dB has been demonstrated for the CAOS camera agile pixel using an optical variable attenuator irradiance controlled visible laser target. These fundamental experiments point to the power of the CAOS camera for diverse applications in imaging. Future work using a much higher speed (e.g., 32 kHz frame rate) DMD relates to the optimization and extensions of the proposed dual band CAOS camera design to application specific demonstrations in multispectral and hyperspectral imaging including hybrid (H) CAOS camera designs engaging prior-art spectral imagers as well as prior-art computational imaging methods within the CAOS hardware platform.

## REFERENCES

- [1] Point Grey White Paper Series, “Sony pregius global shutter CMOS imaging performance,” (Point Grey Research, 2015). Product description available at URL: <http://www.ptgrey.com/white-paper/id/10795> (visited on 06/10/2017).
- [2] Allied Vision Technologies White Paper, “Seeing beyond the visible - short-wave infrared (SWIR) cameras offer new application fields in machine vision,” Allied Vision Technologies GmbH, Germany, (2014).
- [3] A. Gowen, C. P. O'Donnell, P. J. Cullen, G. Downey, and J. M. Frias, “Hyperspectral imaging - an emerging process analytical tool for food quality and safety control,” *Trends in Food Science and Technology*, vol. 18, no. 12, pp. 590-598, (2007).
- [4] R. S. Berns, Y. Zhao, L. A. Taplin, J. Coddington, C. McGlinchey, and A. Martins, “The use of spectral imaging as an analytical tool for art conservation,” *American Institute of Conservation, Annual Meeting, United States* (2009).
- [5] N. Hagen and M. W. Kudenov, “Review of snapshot spectral imaging technologies,” *Optical Engineering*, vol. 52, no. 9, 090901, (2013).
- [6] P. Gonzalez, K. Tack, B. Geelen, B. Masschelein, W. Charle, B. Vereecke, and A. Lambrechts, “A novel CMOS-compatible, monolithically integrated line-scan hyperspectral imager covering the VIS-NIR range,” *Proceedings SPIE 9855, 98550N*, (2016).
- [7] T. Egloff, J. Knobbe, S. Sinzinger, and H. Gröger, “Design of a micro-opto-electro-mechanical-system-based near-infrared hyperspectral imager,” *Applied Optics*, vol. 48, no. 34, pp. 6583-6593, (2009).
- [8] Y. Murakami, M. Yamaguchi, and N. Ohyama, “Hybrid-resolution multispectral imaging using color filter array,” *Optics Express*, vol. 20, no. 7, pp. 7173-7183, (2012).
- [9] P. Mouroulis, B. Van Gorp, R. O. Green, H. Dierssen, D. W. Wilson, M. Eastwood, J. Boardman, B. Gao, D. Cohen, B. Franklin, F. Loya, S. Lundeen, A. Mazer, I. McCubbin, D. Randall, B. Richardson, J. I. Rodriguez, C. Sarture, E. Urquiza, R. Vargas, V. White, and K. Yee, “Portable remote imaging spectrometer coastal ocean sensor: design, characteristics, and first flight results,” *Applied Optics*, vol. 53, no. 7, pp. 1363-1380, (2014).
- [10] C. Goenka, J. Semeter, J. Noto, J. Baumgardner, J. Riccobono, M. Migliozzi, H. Dahlgren, R. Marshall, S. Kapali, M. Hirsch, D. Hampton, and H. Akbari,

- “Multichannel tunable imager architecture for hyperspectral imaging in relevant spectral domains,” *Applied Optics*, vol. 55, no. 12, pp. 3149-3157, (2016).
- [11] IMEC Hyperspectral Snapshot Imager datasheet, Belgium (2013). Product description available at URL: <https://www.imec-int.com/en/hyperspectral-imaging> (visited on 06/10/2017).
- [12] J. Brauers, N. Schulte, A. A. Bell, T. Aach, “Multispectral high dynamic range imaging,” *Proceedings SPIE 6807*, 680704, (2008).
- [13] B. Tan, N. Liao, L. Tian, J. Wang, Y. Lianry, “High dynamic range multispectral imaging using liquid crystal tunable filter,” *Proceedings SPIE 7850*, 78502A, (2010).
- [14] D. V. Blerkom, C. Basset, and R. Yassine, “CMOS DETECTORS: New techniques recover dynamic range as CMOS pixels shrink,” *Laser Focus World*, vol. 46, no. 6, (2010).
- [15] S. Sumriddetchkajorn and N. A. Riza, “Micro-electro-mechanical system-based digitally controlled optical beam profiler,” *Applied Optics*, vol. 41, no. 18, pp. 3506-3510, (2002).
- [16] N. A. Riza and M. J. Mughal, “Optical power independent optical beam profiler,” *Optical Engineering*, vol. 43, no. 4, pp. 793-797, (2004).
- [17] N. A. Riza, S. A. Reza, and P. J. Marraccini, “Digital micro-mirror device-based broadband optical image sensor for robust imaging applications,” *Optics Communication*, vol. 284, no. 1, pp. 103-111, (2011).
- [18] M. J. Amin, J. P. La Torre, and N. A. Riza, “Embedded optics and electronics single digital micromirror device-based agile pixel broadband imager and spectrum analyser for laser beam hotspot detection,” *Applied Optics*, vol. 54, no. 12, pp. 3547-3559, (2015).
- [19] N. A. Riza, M. J. Amin, and J. P. La Torre, “Coded Access Optical Sensor (CAOS) Imager,” *Elsevier Journal of the European Optical Society: Rapid Publication (JEOS:RP)*, vol. 10(15021), (2015).
- [20] N. A. Riza, J. P. La Torre, and M. J. Amin, “CAOS-CMOS camera,” *Optics Express*, vol. 24, no. 12, pp. 13444-13458, (2016).
- [21] N. A. Riza, “Coded Access Optical Sensor (CAOS) imager and applications,” *Proceedings SPIE 9896*, 98960A, (2016).
- [22] N. A. Riza and J. P. La Torre, “CAOS-CMOS multispectral and hyperspectral camera,” *OSA Congress on Light, Energy and the Environment, Topical Meeting:*

- Hyperspectral Imaging and Sounding of the Environment (HISE), Proceedings Paper, Germany, (2016).
- [23] N. A. Riza, "H-CAOS camera," Year in Optics Special Issue, OSA Optics and Photonics News (OPN) Magazine, (2016).
  - [24] D. Takhar, J. N. Laska, M. B. Wakin, M. F. Duarte, D. Baron, S. Sarvotham, K. F. Kelly, and R. G. Baraniuk, "A new compressive imaging camera architecture using optical-domain compression," Proceedings SPIE 6065, 606509, (2006).
  - [25] M. J. E. Golay, "Multi-slit spectrometry," Journal of the Optical Society of America, vol. 39, no. 6, pp. 437-444, (1949).
  - [26] P. Gottlieb, "A television scanning scheme for a detector-noise limited system," IEEE Transactions on Information Theory, vol. 14, no. 3, pp. 428-433, (1968).
  - [27] S. Selivanov, V. N. Govorov, A. S. Titov, and V. P. Chemodanov, "Lunar station television camera," (Reilly Translations): NASA CR-97884, (1968).
  - [28] F. O. Huck, and J. J. Lambiotte, "A performance analysis of the optical-mechanical scanner as an imaging system for planetary landers," NASA TN D-5552, (1969).
  - [29] K. Kearney, and Z. Ninkov, "Characterization of a digital micro-mirror device for use as an optical mask in imaging and spectroscopy," Proceedings SPIE 3292, 81, (1998).
  - [30] J. Castracane, and M. Gutin, "DMD-based bloom control for intensified imaging systems," Proceedings SPIE 3633, 234, (1999).
  - [31] S. Nayar, V. Branzoi, and T. Boulton, "Programmable imaging using a digital micro-mirror array," Proceedings of IEEE Conference on Computer Vision and Pattern Recognition 1, pp. 436-443, (2004).
  - [32] Wavelength Transmittance Considerations for DPL DMD Window, DLPA031C, Texas Instrument Technical Documentation, (2014). Document available at URL: [www.ti.com/lit/an/dlpa031c/dlpa031c.pdf](http://www.ti.com/lit/an/dlpa031c/dlpa031c.pdf) (visited on 06/10/2017).
  - [33] N. A. Riza and M. J. Mughal, "Broadband optical equalizer using fault tolerant digital micromirrors," Optics Express, vol. 11, no. 13, pp. 1559-1565, (2003).
  - [34] N. A. Riza and J. Chen, "Ultra-high -47 dB optical drop rejection multi-wavelength add-drop filter using spatial filtering and dual bulk acousto-optic tunable filters," Optics Letters, vol. 23, no. 12, pp. 945-947, (1998).
  - [35] S. Blais-Ouellette, O. Daigle, and K. Taylor, "The imaging Bragg tunable filter: a new path to integral field spectroscopy and narrow band imaging," Proceedings SPIE 6269, 62695H, (2006).

- [36] W. Wang, C. Li, E. W. Tollner, G. C. Rains, and R. D. Gitaitis, "A liquid crystal tunable filter based shortwave infrared spectral imaging system: Design and integration," *Computers and Electronics in Agriculture Journal*, vol. 80, pp. 126-134, (2012).
- [37] Rolson 61641 LED torch. Product description available at URL: <http://www.rolsontools.com/5w-z2-aluminium-torch.html> (visited 06/10/2017).
- [38] National Instrument 6211 DAQ card, National Instrument, Texas, USA. Product description available at URL: <https://www.ni.com/pdf/manuals/371931f.pdf> (visited 06/10/2017).
- [39] W. Kesler, "Taking the mystery out of the infamous formula, "SNR=6.02+1.76 dB," and why you should care," Analog Devices White paper, MT-001, (2008).
- [40] R. Lyons, *Understanding Digital Signal Processing*, Prentice Hall, pp. 93-97, (2001).
- [41] J. Cooley, P. Lewis, and P. Welch, "Historical notes on the fast Fourier transform," *Proceedings of the IEEE*, vol. 55, pp. 165-1677 (1967).
- [42] Photodetector technical documents, "Photodiode saturation and noise floor," Thorlabs, Germany. Document available at URL: [https://www.thorlabs.com/images/TabImages/Photodetector\\_Lab.pdf](https://www.thorlabs.com/images/TabImages/Photodetector_Lab.pdf) (visited on 06/10/2017)
- [43] J. H. Shapiro, "Computational ghost imaging," *Physics Review A*, vol. 78, no. 6, 061802, (2008).





## CHAPTER 10

### CONCLUSIONS

To summarize, this thesis is focused on innovations in two macro research fields namely, shape sensing and imaging. Specifically, proposed and experimentally demonstrated are smart and elegant optical and electronic system designs to existing real world problems in the shape sensing and imaging domains. In each chapter, I present the detailed design and experiments for each innovation as the research builds over the thesis work to improve the system performances for both the shape sensing and imaging applications.

Starting from the shape sensing field, my thesis has proposed system design solutions based on different optical components emphasizing the use of an electronically controlled variable focus lens (ECVFL) for beam forming operations. Using the ECVFL and an illumination laser light source, it has been successfully demonstrated how starting from simple elements a 3-D shape sensor can be designed and experimentally demonstrated. Strengths of the proposed sensor are its highly programmable working range and its small transverse resolution. Depending on the application, improvements in the sensor design are proposed by change of the optical beam parameters of the light source. First a laser spot sampling was deployed to shape sense. Next, laser line sampling was used to enable faster shape sensing while keeping a flexible working range and the smallest transverse resolution. For these two presented designs, further improvements can be achieved with the use of a more efficient and robust image processing algorithm as well as better performing optical devices having faster response. It is also shown how the key components in the shape sensing sensor can be embedded into a projection system that forms a smart art display. Traditional projection systems are designed to display content information onto a flat 2-D surface. However, when the surface presents irregularities or it is a multi-distance conformal screen, current projection technologies have limitations. I have shown using experimental demonstrations how the projected image suffers distortion, losses its sharpness and presents artefacts that have a negative impact on the desired image projection. On the other hand, when using the proposed projection system design in this thesis, it is shown that one can obtain a clear and in-sharp image projection onto a multi-distance conformal surface over a designed programmable working range. The proposed design can be deployed in an artistic scenario where irregularities are common and user interaction is required for better user

visual perception. Here, the proposed display design can be improved using better performing ECVFLs and faster x-y scan mirrors. Additionally, by using the combination and synchronization of many laser wavelengths in the proposed display system, one can enrich the viewed output projection quality.

The second part of the thesis involves extensive use of a DMD chip device for the realization of smart imaging modules. First I present the DMD-based module that is a programmable Young's double slit interferometer. I show a successful demonstration of experiments with Young's interference fringes. The thesis next presents for the first time the design and implementation of a novel embedded smart agile pixel imager suitable for laser beam imaging. The simplicity of the design and functionality is based on a cost-effective microcontroller device. Several applications require the laser monitoring for verifying particular features, e.g. laser beam width. It is well known that because of the strong laser irradiance intensity levels, monitoring such spatial features in a beam is not a trivial task and current imaging technology requires strong optical attenuation that can spoil a beam's true spatial content. By adopting the imager design proposed in this thesis, one can image the laser beam automatically with electronic control without any optical attenuation. Another imager design introduced and experimentally demonstrated in this thesis is the CAOS camera. Both coherent (laser) and incoherent (white light scene) imaging operations have been studied with the CAOS camera. The CAOS camera is special because it can achieve extremely high imaging dynamic ranges and experiments I conducted showed an extreme linear dynamic range of 136 dB. This result is a major advance in imaging technology when compared to state-of-art imaging sensor technologies. I also demonstrated the CAOS imager as a multi-spectral and hyper-spectral imager showcasing its multi-wavelength capabilities.

I would like to conclude this thesis by saying that the CAOS camera has great potential for imaging applications in science and industry. The CDMA mode of the camera mentioned in the thesis could significantly improve the camera performance in terms of speed. In addition, the CAOS smart camera that uses the hybrid imager design by combining with CMOS sensors holds great promise. In terms of software improvements in the CAOS camera, benefits can be derived by using machine learning algorithms. Finally, the deployed DMD chip device and board used in this thesis was from a low cost DMD projector unit and has extra unnecessary hardware. Therefore, the development of a custom Application Specific Integrated Circuit (ASIC) for the CAOS camera is required and it will further reduce the hardware complexity of the overall system. It is expected that with the fast pace of

development of today's electronics, CMOS sensors, programmable optical devices and computational algorithms, the proposed smart design modules in this thesis can benefit many real-world scenarios.